The Institute of Photonic Sciences

Universitat Politècnica de Catalunya

Multiple light scattering in atomic media: from metasurfaces to the ultimate refractive index

Doctoral Thesis

Author:
Francesco Andreoli

Supervisor:
Prof. Dr. Darrick Chang

A thesis submitted in fulfillment of the requirements for the

Degree of PhD in Photonics

Barcelona, February 2023

Francesco Andreoli

Multiple light scattering in atomic media: from metasurfaces to the ultimate refractive index

Barcelona, February 2023

This project has received funding from the European Union's Horizon 2020 research and innovation programme, under the Marie Skłodowska-Curie grant agreement No. 713729.

Alla mia famiglia e a chi
mi è sempre vicino.

Solo nei resoconti di Marco Polo, Kublai Kan riusciva a discernere, attraverso le muraglie e le torri destinate a crollare, la filigrana d'un disegno così sottile da sfuggire al morso delle termiti.

– Italo Calvino, *Le città invisibili*

Abstract

Our ability to confine, guide, and bend light has led to astonishing technological achievements, playing a fundamental role in diverse fields like microscopy, photochemistry, telecommunications or material design. The key property of materials that allows to control light is the refractive index. Notably, regardless of very different microscopic structures, all natural materials exhibit a modest, near-unity index of refraction, $n \sim 1$. This universality suggests the existence of some simple, ubiquitous origin, whose complete characterization from microscopic considerations, surprisingly, is still missing. Moreover, one can wonder which principles might allow to synthesize a material with an ultra-high index $n \gg 1$, to boost the performance of photonic devices.

In this thesis, we address these questions from an atomic-physics standpoint, exploring if the macroscopic optical properties can be related to simple, electrodynamical processes occurring between well-separated atoms, which only interact via light scattering. Standard theories neglect that light can be scattered multiple times, and lead to unphysical predictions when strong interference occurs between the coherent atomic emission, such as in dense atomic ensembles or ordered lattices. We here develop new techniques to address the physics of multiple light scattering, with the ultimate goal of understanding the fundamental limits to the refractive index, as well as proposing unexpected photonic applications. Our results are divided in three parts.

First, we investigate an ensemble of ideal atoms with increasing atomic density, starting from the dilute gas limit, up to dense regimes where a non-perturbative treatment of multiple scattering and near-field interactions is required. In this situation, we find that these effects limit the index to a maximum value of $n \approx 1.7$, in contrast with standard theories. We propose an explanation based upon strong-disorder renormalization group theory, in which the near-field interactions combined with random atomic positions result in an inhomogeneous broadening of the atomic resonance frequencies. This basic mechanism ensures that regardless of the physical atomic density, light at any given frequency only interacts with at most a few near-resonant atoms per cubic wavelength, thus limiting the index attainable.

Afterwards, we show that a radically different behavior is expected for an ideal, atomic crystal. As long as the inter-atomic interactions are only mediated by multiple scattering, each 2D array of the crystal exhibits a lossless, single-mode response, which builds up a very large and purely real refractive index. To address the limits to this picture, we extend our theoretical analysis to much higher densities, where the electronic orbitals on neighboring nuclei begin to overlap. We develop a minimal model to include the onset of this regime into our non-perturbative analysis of multiple light scattering, arguing that the emergence of quantum magnetism, density-density correlations and tunneling dynamics of the electrons effectively suppresses the single-mode response, decreasing the index back to unity. Nonetheless,

right before the onset of chemistry, our theory predicts that an ultra-high index ($n \approx 30$) and low-loss material could in principle be allowed by the laws of nature.

Finally, inspired by the impressive optical response of atomic arrays, we propose their use as a more complex optical device, namely a thin lens. The building blocks of this "atomic metalens" are composed of three consecutive 2D arrays, whose distance and lattice constants are suitably chosen to guarantee a high transmission of light, as well as an arbitrary phase shift. To characterize its efficiency and prove its robustness against losses, we perform large-scale numerical simulations, on a number of atoms ($N \sim 5 \times 10^5$) between one and two orders of magnitude larger than comparable works.

Resumen

Nuestra capacidad de confinar y guiar la luz nos ha llevado a logros tecnológicos asombrosos, jugando un papel fundamental en campos tan diversos como la fotoquímica, las telecomunicaciones o el diseño de materiales. La propiedad clave de un material para controlar la luz es su índice de refracción. En particular, todos los materiales naturales exhiben un índice de refracción modesto, cercano a la unidad, $n \sim 1$. Esta universalidad sugiere la existencia de algún origen simple y ubicuo, cuya caracterización completa a partir de consideraciones microscópicas, sorprendentemente, aún falta. Además, para aumentar el rendimiento de los dispositivos fotónicos, es crucial entender si los principios físicos permiten o prohíben la síntesis de materiales con índices más altos, $n \gg 1$.

En esta tesis, abordamos estas cuestiones desde un punto de vista atómico, estudiando si las propiedades ópticas macroscópicas pueden deberse a procesos electrodinámicos entre átomos bien separados, que solo interactúan a través de la dispersión de la luz. Las teorías estándar ignoran que la luz puede dispersarse varias veces y conducen a predicciones erradas en situaciones de fuerte interferencia, como en redes cristalinas o conjuntos densos de átomos. Aquí, desarrollamos nuevas técnicas para tratar la dispersión múltiple de la luz, con el objetivo final de comprender los límites fundamentales del índice de refracción, así como proponer aplicaciones fotónicas innovadoras. Nuestros resultados se dividen en tres partes.

Primero, investigamos un conjunto desordenado de átomos con densidad creciente, hasta regímenes donde se requiere un tratamiento completo de la dispersión múltiple y de las interacciones de campo cercano. En esta situación, encontramos que estos efectos limitan el índice de refracción a un valor máximo de $n \approx 1,7$. Proponemos una explicación basada en la teoría del grupo de renormalización, en la que las interacciones de campo cercano, combinadas con posiciones atómicas aleatorias, desarrollan una ampliación no homogénea de las frecuencias atómicas de resonancia. Este mecanismo asegura que, independientemente de la densidad atómica, la luz (para cualquier frecuencia dada) solo interactúa con unos pocos átomos resonantes por unidad cúbica de longitud de onda, limitando la respuesta óptica.

Un comportamiento radicalmente diferente se manifiesta en una red cristalina de átomos. Siempre que las interacciones solo estén mediadas por dispersión múltiple, cada capa del cristal exhibe una respuesta monomodo sin pérdidas, que genera un índice de refracción muy grande y puramente real. Para abordar los límites de esta respuesta física, ampliamos nuestro análisis teórico hasta densidades tan altas que los orbitales electrónicos de los núcleos vecinos comienzan a superponerse. Desarrollamos un modelo para incluir el inicio de este régimen en nuestro análisis, argumentando que la aparición del magnetismo cuántico, las correlaciones de densidad y la dinámica de efecto túnel de los electrones suprimen efectivamente la respuesta monomodo, bajando nuevamente el índice a la

unidad. No obstante, justo antes del inicio de los procesos químicos, nuestra teoría predice la posibilidad teórica de sintetizar un material con un índice de refracción sorprendentemente alto ($n \approx 30$) y pérdidas bajas.

Por último, inspirándonos en la impresionante respuesta óptica de las redes atómicas, proponemos su uso para imitar un dispositivo óptico complejo, a saber, una lente delgada. El componente básico de esta "metalente atómica" está compuesto por tres redes atómicas bidimensionales consecutivas, cuyas distancias y constantes de red se eligen adecuadamente para garantizar una alta transmisión de la luz, así como un cambio de fase arbitrario. Para caracterizar su eficiencia y probar su robustez frente a pérdidas, realizamos simulaciones numéricas incluyendo un gran número de átomos ($N \sim 5 \times 10^5$), entre uno y dos órdenes de magnitud mayor que en trabajos comparables.

Acknowledgements

It is well known that the acknowledgements are the hardest part to write in any thesis. I was convinced that I was going to spare myself this additional stress, but then I realized that many people really deserved, at least, a few words on this white page.

First of all, I want to thank my supervisor, Darrick. A PhD is a long journey, and it can often be tough. You've always been available to discuss, anytime I needed. I wouldn't be here, depositing my thesis, if it weren't for your support and for all I learnt from you. I'm really grateful for all of this.

I would also like to thank our collaborators, who always provided new insights and challenging questions. It has been a real pleasure to work with you.

I want to thank all my colleagues, the ones that I still have the pleasure to see (almost) every day, and those who have spent time in the group and continued their journey somewhere else. I could list all the qualities that I admire about you all, but I'll just say that your generosity and kindness stand out among them, which I think is rare and precious. I wish you all the best of the best in your future.

Odi et amo. Quare id faciam, fortasse requiris. Catullus wrote. He was definitely referring to something different, but I can probably stretch this quote to describe my relationship with ICFO. I want to thank all the friends that this place gifted me. I grew up so much spending time with you, and we lived so many experiences together that no amount of words could do enough justice. You're definitely the *amo* part of this quote.

Infine, vorrei ringraziare la mia famiglia e quelle persone che mi sono sempre vicine, sia fisicamente che nonostante le distanze. Date un senso a questi giorni, quelli più luminosi come quelli più bui. Questa tesi, tutta questa lunga lista di concetti e faticose parole, è per voi.

List of acronyms

DFT Density-Functional Theory

DL Drude-Lorentz model

LL Lorentz-Lorenz model

MB Maxwell-Bloch theory

NZI Near-Zero-Index of refraction

OD Optical Depth

RAM Random Access Memory

RG Renormalization Group

SiV Silicon-Vacancy center in diamond

SM Spin Model formalism for atom-light interaction

List of publications

The results of this thesis led to the preparation of the following manuscripts:

- **F. Andreoli**, M. J. Gullans, A. A. High, A. Browaeys and D. E. Chang. *Maximum refractive index of an atomic medium*. Physical Review X 11, 011026 (2021).
- **F. Andreoli**, B. Windt, S. Grava, G.M. Andolina, M. J. Gullans, A. A. High and D. E. Chang. *Maximum refractive index of an atomic crystal – from quantum optics to quantum chemistry*. Paper in preparation (2023).
- **F. Andreoli**, A. A. High and D. E. Chang. *Metalens formed by structured, sub-wavelength atomic arrays*. Paper in preparation (2023).

Some numerical simulations have been performed with original codes written in Julia [1]. Part of these codes can be found in the GitHub repository:

- https://github.com/frandreoli/atoms_optical_response

A supplementary result of the PhD, not included in this thesis, is given by:

- Z. Li, X. Guo, Y. Jin, **F. Andreoli**, A. Bilgin, D. D. Awschalom, N. Delegan, F. J. Heremans, D. E. Chang, G. Galli, A. A. High. *Manipulating charge states at the nanoscale with coherent atomic antennas*. Paper in preparation (2023).

Contents

Part I

Introduction

1 - Light-matter interfaces

Chapter Contents

1.1 The limits to the refractive index

Light played a crucial role in the development of our world. By mainly irradiating in the visible spectrum, the sunlight constantly supplies an essential energetic balance to our ecosystem. Plants, through photosynthesis, provide a method to harness this energy, to sustain and proliferate life.

In the history of humanity, light has represented our preferential means (along with sound) to acquire information on the physical reality. Eyesight stands out among our senses, and the first designs of telescopes and microscopes furnished it with the keys into (otherwise inaccessible) macroscopic and microscopic worlds. On the other hand, both lighthouses and signal fires can be interpreted as an effort to reverse this paradigm, using visible light to communicate and spread information. Similarly, one of the first attempts to actively manipulate physical objects with light (and *viceversa*) dates back to the ancient times, when Archimedes is said to have used gigantic mirrors to burn ships attacking Syracuse.

Despite the remarkable promises that it embodies, it is then rather surprising that a systematic use of light as a technological tool, i.e. the field of photonics, only emerged in the recent years, coming after both heat (18-19th century) and electricity (19-20th century) [2]. Historically, this process was effectively boosted by the invention of lasers, which guaranteed an on-demand generation of coherent light. Similarly, optical fibers represented a supplementary pivotal step, enabling the efficient transport of photons over long distances. Nonetheless, one of the main, intrinsic limitations of light-matter interfaces is still given by the low ability of natural materials to manipulate and interact with light without experiencing extreme losses or dissipation, as quantified by a refractive index n that never exceeds the order unity, in any transparent spectral region [3, 4]. Moreover, while we typically utilize materials far from their natural electronic resonances, this

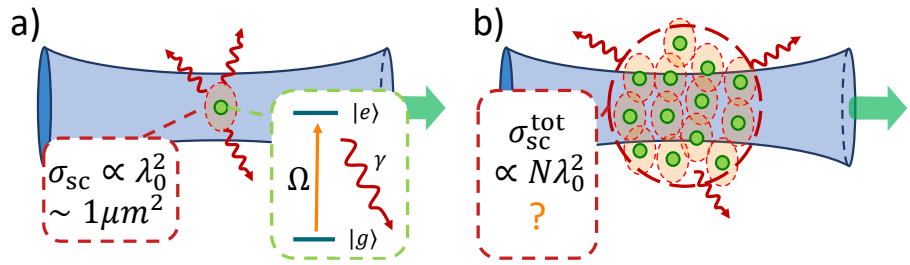

Figure 1.1: Schematic representation of the scattering cross section. a) Scattering cross section $\sigma_{sc} \propto \lambda_0^2$ of a two-level atom, illuminated by a laser beam. b) Additive estimation of the overall response, given a set of N atoms.

observation even holds true close to resonance [5–12], suggesting that a widespread, fundamental reason should exist.

Due to the extremely broad nature of these observations, one might speculate that a trace of this common behaviour could be encoded in the most minimal model of a light-matter interface, as constituted by an isolated atom in vacuum, illuminated by an external light beam. Surprisingly, the standard predictions of atomic physics are hard to reconcile with the empirical evidence of the macroscopic indices of refraction. In particular, a single atom with two electronic levels $|g\rangle$ and $|e\rangle$ is a non-absorbing object whose interaction with near-resonant light is exquisitely understood, and characterized by an extraordinarily large resonant scattering cross section [13], given by the square of the resonant wavelength of its transition $\sigma_{sc} \sim \lambda_0^2$, as pictorially shown in Fig. 1.1-a. This effective scattering size (considering that $\lambda_0 \sim 1\mu$m, in the visible range) is orders of magnitude larger than the physical size of the atom, as characterized by the Bohr radius $a_0 \sim 0.05$nm. Its infinitesimal extension (from an optical standpoint) implies that the atom responds to a photon as an ideal, point-like dipole, explaining why its scattering area must be reasonably dictated by the only relevant length scale: the resonant wavelength[1] λ_0. Intuitively, this mismatch of scales can lead to non-trivial phenomena, when many atoms are placed so near that their cross sections largely overlap. When considering a collection of N atoms, indeed, if the scattering or interaction with light

[1] More concretely, the cross section can be calculated by the ratio $\sigma_{sc} = \mathcal{P}_{sc}/I_0$ between the power of the scattered field and the intensity of the input light. If we decompose an incident plane wave into a superposition of in-going, vector spherical waves (each associated to a different order in the multipole expansion), the atom will then perfectly absorb and re-emit the component related to the electric dipole. This allows to estimate the scattered power as the product $\mathcal{P}_{sc} \propto \lambda_0^2 I_0$ of the input intensity and the smallest focusing area of that field component, which is bounded to $\sim \lambda_0^2$ by diffraction.

were multiplicative, the collective cross section would grow as $\sigma_{\text{sc}}^{\text{tot}} \propto N\sigma_{\text{sc}}$ [14], as portrayed in Fig. 1.1-b. Naively then, if one simply filled a cubic wavelength with $\sim 10^2 - 10^3$ atoms (still orders of magnitude more dilute than a rarified gas, such as air), then one might expect that such a system already allows for an extreme index of refraction.

The heuristic description provided above in fact coincides with conventional models of the optical response of an atomic medium. As detailed later, these models then predict an indefinite growth of the susceptibility[2] $\chi(\omega)$ with the atomic density N/V, scaling as $\chi(\omega) = (N/V)\alpha_0(\omega)$. Here, the quantity $\alpha_0(\omega)$ describes the polarizability of a single atom, and it is typically related to a real part of the index that is either high $n_{\text{re}} > 1$ (for frequencies $\omega < \omega_0$), or low $n_{\text{re}} < 1$ (when $\omega > \omega_0$). As the usual magnitude of the polarizability is characterized by the optical volume of a single atom $|\alpha_0(\omega)| \sim \lambda_0^3/(2\pi)^3 = 1/k_0^3$, at the aforementioned densities $\eta = N/(Vk_0^3) \gg 1$ these theories would predict an index which extremely deviates from that in vacuum. This is pictorially represented in Fig. 1.2, where the orange line shows the standard predictions for the maximum index of an atomic ensemble $n_{\text{re}}^{\max} \sim \sqrt{\eta}$, as a function of the atomic density η. Although these methods well describe the experimental evidence in the "low-density" regime of quantum optics (orange region), they become deeply unrealistic (up to $n_{\text{re}}^{\max} \sim 10^5$ at solid densities), when extrapolated outside.

At the other side of Fig. 1.2, when the atomic densities are comparable to those of real solids $\eta \sim 1/(a_0 k_0)^3 \sim 10^9 - 10^{10}$, the atoms cannot be approximated anymore as independent scatterers, and must be rather treated jointly. In this regime, a large variety of physical phenomena can potentially take place (such as electron tunneling, Pauli exclusion, orbital hybridization, molecular/crystalline bounds, insulator/metal transitions, Fermi's sea of electrons, electronic conduction or valence bands, etc.) depending on the specific atomic species, on their spatial ordering, on the overall temperature and on many other physical factors. In the rest of the thesis, we will group this broad set of phenomena under the name of "quantum chemistry". Within this field, many methods have been developed, such the as the Hartree-Fock method [15], the Quantum Monte Carlo approach [16] or the most common Density-Functional Theory (DFT) [17], which are able to model and precisely describe the optical properties of a large variety of materials [18–20] (as pictorially portrayed by the blue line of Fig. 1.2).

[2] In classical optics, the susceptibility $\chi(\omega)$ describes how much the index in a material differs from that in vacuum, given $n(\omega) = \sqrt{1 + \chi(\omega)}$.

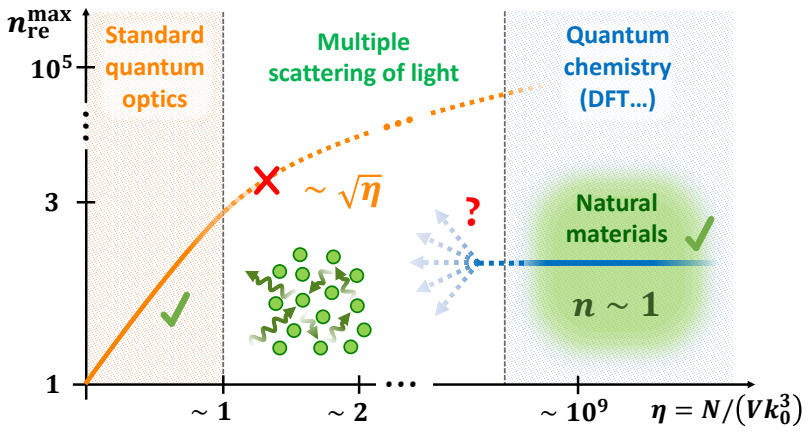

Figure 1.2: Illustrative depiction of the standard predictions for the maximum (real) index $n_{\mathrm{re}}^{\max}$, given different regimes of density $\eta = N/(Vk_0^3)$. The orange (solid and dotted) line is associated to the standard models of quantum optics, which well describe an idealized atomic medium in the dilute regime of $\eta \ll 1$ (orange region). On the other side, the blue region describes the typical densities of actual solid materials $\eta \sim 1/(a_0 k_0)^3$. In that case, the atoms cannot be considered anymore as isolated scatterers, and usual quantum-chemistry techniques, such as Density-Functional Theory (DFT), must be used. Both models well-describe the experimental evidences in their respective regimes of validity, but fail or are undefined in the intermediate zone, where multiple scattering of light dominates (pictorial inset). In that region, the average inter-atomic distance is lower than the radius of the cross section, which imposes a non-perturbative treatment of the optical response. Finally, the green area is a pictorial representation of where natural materials would sit in such a plot.

These approaches, however, are designed to solve an extremely complex many-body problem, which motivated focusing on the physical regime of real solids (represented by the blue solid line in Fig. 1.2), without further analysis into hypothetical, intermediate regimes where specific photonic effects could still be relevant (blue, dotted arrows).

In sight of these observations, it is clear that these two opposite directions are well-defined within their specific limits, but don't easily reconcile in the halfway region. In particular, no clear method exists to draw a continuous line which could connect their predictions and simultaneously describe the intermediate area between them. In this thesis, we aim to provide a first step towards this long-term direction. To do so, we realize that both approaches neglect that light scattering is actually a wave phenomenon, and the potential complexity that emerges due to multiple scattering of photons and interference. It is well-known, however, that multiple scattering of light

through disordered media can give rise to complex and disruptive effects such as Anderson localization of light [21], or make the goal of focusing and imaging through turbid media an outstanding technological challenge [22–24]. In the central, white region of Fig. 1.2, a non-perturbative description of these effects becomes imperative, as the average inter-atomic distance becomes smaller than the size of the cross section. The same issue doesn't arise in the low-density regime $\eta \ll 1$ of standard quantum optics[3], given that atoms are farther apart. At the same time, we suspect that the optical cross section is dramatically reduced at the onset of quantum chemistry, as studied in Chapter 4, which would motivate why such a non-perturbative analysis of photon scattering can be neglected, when predicting the optical properties of natural solids in the quantum-chemistry regime.

In sight of these reasons, in this thesis we will describe new techniques in order to address the physics of multiple scattering of light, with the ultimate goal of understanding the fundamental limits to the index of refraction, as well as developing new photonic applications which exploit the complexity of wave interference.

1.1.1 The impact of an extreme refractive index

One might wonder what technological consequences an extreme index of refraction would imply. Within linear optics, a medium can drastically alter the state of light as long as its photonic response $n = n_{\mathrm{re}} + i n_{\mathrm{im}}$ strongly differs from that of vacuum $n = 1$. At the same time, one usually needs that the optical dynamics is not trivially suppressed by a high absorption of photons (as quantified by the imaginary part of the refractive index n_{im}). As discussed in [3, 4, 26, 27], however, no natural material exhibits both low losses $n_{\mathrm{im}} \sim 0$ and either a ultra-high $n_{\mathrm{re}} \gg 1$ or a near-zero $n_{\mathrm{re}} \sim 0$ index of refraction, in the visible or near-visible spectral range. As we are interested in the potential implications of such transparent materials, for the rest of this section we assume that $n_{\mathrm{im}} \approx 0$, so that $n \approx n_{\mathrm{re}}$.

The natural bounds to the refractive index impose strong limitations on even the simplest optical device: a bulk, refractive lens [31]. In its simplest definition, an optical lens is a transparent object that curves the wavefront of an incident light beam (with initial waist w_{in}), to focus it on a smaller spot w_{out}, with a focal length[4] of f. Considering monochromatic light

[3] This becomes more subtle when strict spatial order is added, due to perfect interference patterns of the scattered light. This is the case, for instance, of Bragg gratings in classical electromagnetism [25].

[4] The focal spot is placed at a distance $z_{\mathrm{f}} = [1 - (w_{\mathrm{out}}/w_{\mathrm{in}})^2] f$ from the lens, which

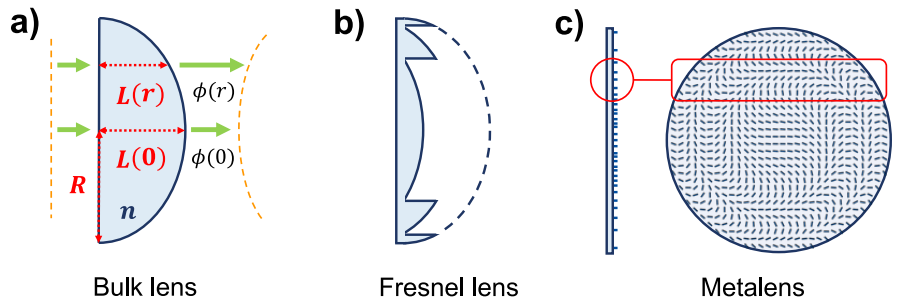

Figure 1.3: Pictorial representation of different types of lenses. a-b) Classical refractive lenses, which exploit a spatially variable optical path to induce a phase delay which curves the incident wavefront, to make it focus at the established distance. Specifically, we show a bulk lens (a) and a Fresnel, refractive lens (b), where the phase is induced modulo 2π. c) Schematic structure of a metalens, where microscopic nano-antennas act as discrete phase shifters, with subwavelength thickness. Specifically, here we depict the case of rotated nano-fins [28], but other typical structures include nano-rods [29] or nano-disks [30].

with wavevector $k_{\text{vac}} = \omega/c$ in vacuum, the lens must impress a spatially dependent phase shift of $\Delta\phi(r) \equiv \phi(r) - \phi(0) = k_{\text{vac}}(f - \sqrt{r^2 + f^2})$, where r is the transverse, radial coordinate [28, 32]. This is accomplished by varying the optical path inside the lens, which induces the phase delay $\Delta\phi(r) = k_{\text{vac}}(n-1)[L(r)-L(0)]$, where $L(r)$ is the thickness of the lens, as shown in Fig. 1.3-a. From these simple considerations, one can immediately notice that the overall thickness of a bulk, refractive lens is bounded by $L(0) \geq (\sqrt{f^2 + R^2} - f)/(n-1)$, where $2R$ is the transverse diameter of the lens. To design thinner lenses, one can realize that the phase delay can be defined modulo 2π, which leads to the *so-called* Fresnel geometry[5], which is characterized by the typical, discontinuous profile portrayed in Fig. 1.3-b. The reduction in thickness, however, is obtained at the expenses of a strong chromatic aberration [33], as well as an overall reduction of the imaging quality, due to the higher manufacturing challenges. Nonetheless, this scheme allows to understand a more fundamental limit, as the thickness of the lens now reads $L_{\text{Fr}} = 2\pi/[(n-1)k_{\text{vac}}] = \lambda_{\text{vac}}/(n-1)$, which is ultimately bounded only by the low value of the refractive index. Due to this restraint, in the last decade the concept of metalens was developed (see Fig. 1.3-c), where the phase is locally tailored by specifically designed nano-elements, as will be further discussed in the next sections.

depends on both the focal length and the waist of the input and output light.

[5] Fresnel lenses are often referred to as *diffractive lenses*, in particular when approximated by a finite set of flat, concentric rings [33, 34].

The minimum thickness is not the only constrain imposed by $n \sim 1$ to a lens. Specifically, its focusing ability is inevitably restricted by the very general diffraction limit, which emerges from the fundamental, wave nature of light. Let us consider a source of monochromatic light, placed in front of a lens and surrounded by a transparent material with positive, real index n. Without loss of generality, the emitted field admits the 2D Fourier decomposition $E(\mathbf{k}_{\mathrm{xy}}, z) = f(\mathbf{k}_{\mathrm{xy}}) e^{i\mathbf{k}_{\mathrm{xy}}\cdot\mathbf{r} + ik_{\mathrm{z}}z}$, where the longitudinal wavevector is constrained by the Maxwell equations to be $k_{\mathrm{z}} = \sqrt{k^2 - |\mathbf{k}_{\mathrm{xy}}|^2}$, with $k = n\omega/c$ accounting for the surrounding material. Since no evanescent field can propagate to the lens, only the components with $|\mathbf{k}_{\mathrm{xy}}| \leq k$ can be effectively observed, leading to an optimal transverse resolution of $\delta r \sim 2\pi/k = \lambda_{\mathrm{vac}}/n$ [35]. This explains why *near-field* microscopy, which captures evanescent waves, can partially defeat the diffraction limit [36].

These two examples well illustrate the notable properties that a transparent, ultra-high index $n \gg 1$ would imply. They can both be summarized with the notion that the wavelength of a monochromatic wave inside a material shrinks by a factor $\lambda = \lambda_{\mathrm{vac}}/n$. Due to this reason, a high index of refraction wouldn't only increase the attainable phase shift per unit length, but would have strong implications in all the technologies which require a strong confinement of light. This is the case, for instance, of optical fibers, which have already revolutionized the human ability to transmit information. Intuitively, the propagating light inside the fiber still has to obey the diffraction limit for the medium, which sets a fundamental constraint to the fiber diameter, given by[6] $d \gtrsim \lambda_{\mathrm{vac}}/(2n)$.

If one thinks of a single photon, carrying a fixed energy $E = \hbar\tilde{\omega}$, the overall reduction of the optical scale inside the medium to $\tilde{\lambda} = \tilde{\lambda}_{\mathrm{vac}}/n = 2\pi c/(\tilde{\omega} n)$, intuitively means an enhancement of the spatial density of energy. Since nonlinear effects require remarkably high intensities, an ultra-high index could potentially trigger nonlinearities with few photons [38], a phenomenon which up to now has been only observed using near-resonant atom-light interactions, either at the single [39–41] or many atom [42, 43] level. The overall possibilities offered by high indices are broad [44, 45] and encompass many fields of research, ranging from solar panels [46] and super-resolved microscopy [47–49] to ink-free color printing [50] or optical

[6] More concretely, a fiber is compose of an internal core with an index n_{co} that is bigger than that of the external cladding $n_{\mathrm{cl}} < n_{\mathrm{co}}$, thus confining the light via total internal reflection [25]. For the fundamental mode of a planar geometry the minimum thickness can be calculated analytically, reading $d > \lambda_{\mathrm{vac}}/\left(2\sqrt{n_{\mathrm{co}}^2 - n_{\mathrm{cl}}^2}\right)$ [37]. The cylindrical case is described by more complicated Bessel functions, but it exhibits an identical qualitative behaviour.

lithography [51]. They include, as well, the modification of the spontaneous decay rate of a two-level, quantum emitter inside a homogeneous, transparent dielectric [52, 53]. These considerations, then, explain the efforts to design materials with an enhanced refractive index [44, 54–57], as reported in Fig. 1.4.

In addition to the case of $n \gg 1$, various interesting effects have been theorized (and partly demonstrated) for near-zero $n \sim 0$ indices of refraction as well [26, 27]. The existence of an index lower than unity is not forbidden by special relativity [76], since the phase velocity $v_{\mathrm{ph}} = c/n$ describes the propagation of an ideal, infinitely extended, plane wave, which cannot transport information due to its perfect spatial homogeneity. Nonetheless, causality imposes a bound on the group velocity[7] $v_{\mathrm{g}} = \partial\omega/\partial k = c/(n + \omega\partial n/\partial\omega) \leq c$ of a lossless material, which in turns limits the dispersion relation of a lossless, zero-index medium to $\partial n/\partial\omega \geq 1/\omega$. More generally, one can show that the causal order introduces a stricter relation between how small a near-zero index can be, and the bandwidth over this can be sustained [79]. A qualitatively similar result, for the case of ultra-high indices $n > 1$, was recently derived in [80].

Inside a material with $n \sim 0$, the wavelength of light becomes (almost) infinite. This property is similar to that of a quantum-wave particle with energy $E = k^2/(2m)$ tunneling inside a low potential barrier $U \gtrsim E$, where the evanescent transfer is associated to typical lengths $\propto 1/\sqrt{U - E}$ larger than the initial wavelength $\propto 1/\sqrt{E}$. As we will see, the propagation of light in a Near-Zero-Index (NZI) material closely resembles this analogy.

Due to the very large wavelength $\lambda = \lambda_{\mathrm{vac}}/n \sim \infty$, light doesn't acquire any spatial phase of propagation [81, 82]. This means that spatial and temporal variations are decoupled [26, 83], and that the electromagnetic field feels every point in space as if they were the same point. It is not surprising then, that the transport of light in a NZI medium happens via tunneling from one end of the material to the other, as first theorized by [84] and experimentally shown in the microwaves [85–87] and infrared [88]. This also explains why no diffraction pattern can emerge from a double-slit experiment inside a NZI material [89], and it shows that scattering processes are suppressed. At the level of classical optics, light transfer indeed resembles a near-field effect (which doesn't possess any spatial phase profile), but with

[7] The quantity bounded by c is the speed at which information propagates [77]. This, however, is usually equivalent to the group velocity, unless one is dealing with anomalous dispersion, where $\partial n_{\mathrm{re}}/\partial\omega < 0$ [78], or strongly dispersive media [37]. Both situations can happen in a material around its resonance, which is usually accompanied by non-negligible losses $n_{\mathrm{im}} > 0$.

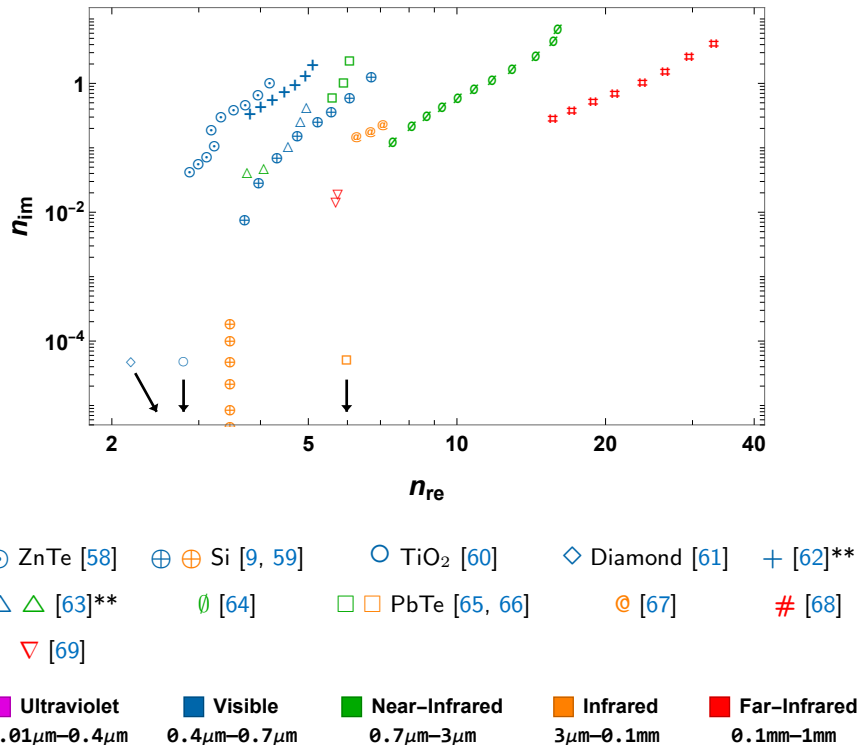

Figure 1.4: Natural and artificial materials with ultra-high, low-loss refractive index. Values of n_{im} and $n_{\text{re}} \gg 1$, given different frequencies. In some occasions, the data are extracted via the freely available software of [70], while for some natural materials we refer to [71]. Natural materials or composites are named, while metamaterials are only defined by their reference. Those metamaterials marked with one (two) asterisk(s) refer to systems with reduced dimensions (respectively, 1D or 2D), where the bulk properties can only be effectively inferred. We choose those transparent natural materials with the highest positive index [3, 4]. We don't include the results of [72–74], as they operate in the microwaves. Titanium dioxide (TiO_2) is birefringent [60], so we only considered the index along its ordinary axis. The data of [62] refer to the ensemble of gold (Au) nano-particles, which has a higher real index and lower imaginary part. The refractive index of [64] is retrieved from the nano-sphere configuration, where the effective, bulk refractive index is estimated through the method of [75]. For [68], we select the 5-layer configuration, rather than the single-layer one, as we believe that it better approximates the concept of a "bulk" material. Furthermore, we focus on the experimental data with frequencies $\gtrsim 0.75$THz, where both the real index n_{re} and the figure-of-merit $n_{\text{re}}/n_{\text{im}}$ are higher and less noisy. From [69], we only plot the sample with thickness ~ 2mm (given that similar data are shown for the other sample), and we neglect those data in the microwave regime.

a characteristic optical length so extended that it encompasses the whole macroscopic material.

Intuitively, this peculiar behaviour makes light completely insensitive of the shape of the material boundaries. This means that light can be squeezed and tunnel inside a very narrow (even subwavelength [84, 88]) channel filled with NZI and surrounded by a reflective coating, which leaves only two possible apertures [87]. This can lead to ideal optical interconnects, which are not affected by sharp or irregular bends [90–93]. Inside such channels, light would propagate similarly to a superfluid with zero viscosity, as highlighted in [94] and experimentally addressed in [95]. Similarly to the outer boundaries, light cannot be scattered or diffracted by a reflective impurity placed inside the NZI material. This property has potential applications for cloaking designs, which aim to make an object invisible with respect to the environment, as was first envisioned in [96] and experimentally shown in [86]. As discussed in [76], this property can be understood by recalling that the optical resolution in a medium scales as $\delta r \sim \lambda_{\mathrm{vac}}/n$, which means that two different sources can never be distinguished when $n \sim 0$ (regardless of how far they are), allowing to hide any object in the NZI material.

Due to this same reason, imaging inside a bulk, isotropic NZI medium is impossible. Nevertheless, radically different results can be obtained by tailoring the index anisotropically, with $\epsilon_{\mathrm{z}} \neq 0$ and $\epsilon_{\mathrm{xy}} = 0$. In that case, indeed, light travelling in the $\widehat{\mathbf{z}}$ direction experiences a zero index, so that, optically, the material behaves as if the front and back surfaces were directly in contact [97]. Since this applies to all the spectral components (due to the peculiar dispersion relation), *de facto*, this medium can reproduce a "perfect" copy of the initial image from one side to the other, which can be stretched and enlarged by exploiting curved surfaces [98, 99]. This means that an image can be magnified in its near field by the NZI device, before the diffraction effects of free-space propagation take place [98], which can lead to far-field imaging beyond the diffraction limit, as experimentally addressed in [100] for a spherical geometry.

On top of these considerations, many optical applications (such as those based on total internal reflection) require a large contrast ratio n_1/n_2 between indices [4, 112], meaning that a near-zero index would produce similar or higher enhancement than the ultra-high case [113] (with the further possibility of combine it with existing high-index materials, like silicon $n \approx 3.5$). In general, the idea of combining high-index $n > 1$ and low-index $n < 1$ materials enables interesting perspectives, including transformation-based cloak designs, as discussed in [114, 115] and experimentally demonstrated in [116]. Nonetheless, many applications of near-zero indices have been pro-

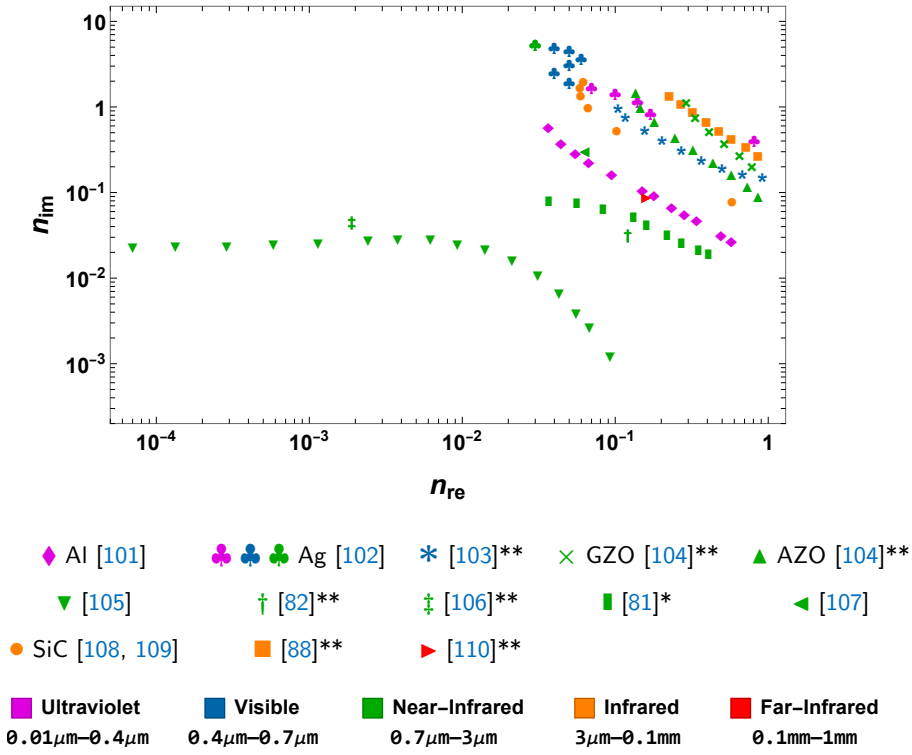

Figure 1.5: Natural and artificial materials with near-zero, low-loss refractive index. Values of n_{im} and $n_{\text{re}} \ll 1$, given different frequencies. In some occasions, the data are extracted via the freely available software of [70], while for some natural materials we refer to [71]. Natural materials or composites are named, while metamaterials are only defined by their reference. Those metamaterials marked with one (two) asterisk(s) refer to systems with reduced dimensions (respectively, 1D or 2D), where the bulk properties can only be effectively inferred. The NZI natural materials reported are those with the lowest associated losses [26]. In [103], we select the data of the *slab 1*, whose index is inferred through the *method 2* (based on [75]). The GZO (gallium-doped zinc oxide) thin film of [104] has a 4% doping, but a similar curve can be obtained from [111], where a 6% doping is used. The AZO (aluminium-doped zinc oxide) has a 2% doping. For the metamaterials in [82, 106], we cannot properly infer the scaling of n_{im} as a function of n_{re}, so we only consider the fixed frequency that is explicitly mentioned in the texts. Similar considerations apply for [107, 110], where instead we focus on the value with the lowest, positive index. In [81], the finite length of the waveguide imposes a measurement floor of $n_{\text{re}} \sim 0.05$, so we restrict to the experimental points above this value. Moreover, we only consider the case without the supplementary cladding with a photonic band-gap material. The data for the SiC are taken from the formula shown in [108], which refers to the theoretical calculations of [109].

posed [117], including time-varying mirrors [118], optical solitons [119], all-optical switching [120], wavefront patterning [121] (as well as lensing [86]), frequency modulation [122–124], optomechanics [125] or highly-directional [112, 126] and unconventional [127, 128] antennas.

Notwithstanding, high losses still represent a serious limitation to the development of NZI optics [4]. As an example, some implementations exploit metals or doped semiconductors near their plasma frequency $\omega \sim \omega_{\mathrm{p}}$, where the relative permittivity reads $\epsilon/\epsilon_0 \sim 1-(\omega_{\mathrm{p}}/\omega)^2 \sim 0$ [112]. However, in this simplified formula we neglect losses, which become particularly relevant around the plasmonic resonance [129, 130]. This issue is evident in Fig. 1.5, where many experimental realizations of NZI media are compared, showing that the condition $n_{\mathsf{re}} \sim n_{\mathsf{im}} \sim 0$ is still out of range.

1.1.2 Extreme indices and artificial materials

As we commented in the previous section, several works focused on the idea of designing structures whose macroscopic behaviour could emulate an extreme index of refraction.

The effects of a NZI, for example, are mimicked when light travels inside an artificial material whose dispersion relation allows for a vanishing wavevector $k \sim 0$ at a non-vanishing frequency $\omega > 0$. This was experimentally investigated using waveguides operating near their cut-off frequency [87, 131]. More concretely, this condition can be specifically engineered with a photonic crystal. Such a device is constituted by a periodic pattern of materials with alternated indices of refraction, so that light can be scattered at their interfaces [2]. The photonic modes are subjected to the Bloch theorem, which permits to quantify how the multiple scattering can radically alter the dispersion relation of light.

For example, anisotropic NZI can be experimentally emulated using a stack of alternated slabs with thicknesses $z_{a,b}$ and indices $n_{a,b}$, as long as the condition $z_a n_a^2 \simeq -z_b n_b^2$ is satisfied [97–100]. This recipe requires an index $n_b^2 < 0$, which is typical of plasmonic metals[8], whose losses are nonetheless relevant. At the same time, two-dimensional photonic crystals have been explored as well [86, 105, 106], showing that a NZI can be emulated with tailored geometric designs of all-dielectric elements.

The idea of using ordered geometries of scatterers was analogously explored to obtain ultra-high indices [67, 132]. To this aim, a large, resonant response of the constitutive elements is necessary, which favoured the use of

[8] We recall that plasmonic metals are characterized by $n^2/\epsilon_0 \sim 1-(\omega_{\mathrm{p}}/\omega)^2$ (neglecting losses). For frequencies below ω_{p}, one can have $n^2 < 0$.

cut metallic nano-antennas[9] [68, 72, 133–136], metallic gratings [69] or colloidal superlattices of metallic nanoparticles [62, 64]. Nonetheless, some of the main constraints of these latter approaches are the multipolar behaviour of the metallic scatterers and large plasmonic losses in the metals.

On the contrary, an ideal light scatterer would be inherently lossless, behave as a point-like dipole, and posses an optical scattering cross section much bigger than its physical size. All these qualities are satisfied by two-level atoms, so that, intuitively, one might expect that an ordered atomic lattice could represent the ultimate platform for extreme refractive indices. In Chapter 4, we suggest that this may be the case.

1.1.3 Flat optics and metasurfaces

The works described in the previous section are applications of the more general idea of engineering microscopic structures to exhibit a target optical response. A similar spirit motivates the the field of flat optics, where specific optical phenomena are tailored in an artificial material to reproduce the properties of a thin optical device, with a subwavelength thickness.

Namely, in Section 1.1.1 we already discussed the case of refractive lenses, where a specific phase profile was obtained by locally changing the optical path of light inside the material, where it experiences a higher refractive index. We argued that such a tailored phase pattern can shape the wavefront of the input light, to make the beam focus at the desired distance. What emerges is that locally controlling the phase shift impressed in transmission can drastically alter the macroscopic, photonic behaviour. A metasurface (or a metalens for the specific lensing application), then, is a device which can locally impress a variable phase retardation, in a thickness smaller than the wavelength of light, and possibly smaller than the bound $L_{\mathrm{Fr}} \sim \lambda_{\mathrm{vac}}/(n-1)$ to Fresnel lenses [33, 137]. This is accomplished by designing specific nano-elements, acting as discrete building blocks of the metasurface, which aim to ideally satisfy the following conditions:

- They should be as lossless as possible, with low energy dissipation.
- Normally incident light should be transmitted in the same direction (directional emission/scattering).
- The impressed phase shift should be tunable over the whole 2π range, by changing some constituent parameter. Full tunability should be ensured given a fixed frequency of light, so that the wavefront of a (nearly) monochromatic beam can be arbitrarily shaped.

[9] A similar approach was associated to near-zero indices as well [82, 107, 110].

The first demonstrations of these concepts came from the field of plasmonics, where metallic nano-antennas and nano-resonators where designed to fulfill that scope [138]. This included the realization of lenses, vortex beam generators and holography [139]. Nonetheless, as we discussed, such systems are heavily bounded by their losses [129, 130], which limit their applicability. To overcome this problem, the idea emerged of designing all-dielectric metamaterials [45], whose building blocks can exploit various physical phenomena. Specifically, we can mention the case of dielectric nano-rods, which act as truncated waveguides with an effective index of refraction, controllable by changing their diameter [29]. Alternatively, anisotropic dielectric cuboids, called nano-fins, exploit their intrinsic birefringence to impress a variable phase shift, depending on the angle of rotation around their main axis [28]. Devices built upon these paradigms were proven to efficiently behave as low-loss lenses, with a thickness often smaller than what Fresnel lenses achieve [33, 137]. Nonetheless, such dielectric devices still need to obey the fundamental law of diffraction, which imposes a bound that approximately scales as $L \gtrsim \lambda_{\mathrm{vac}}/n$ [140].

Notably, these nano-structures are often referred to as "meta-atoms" to describe their ability to strongly manipulate light over very small spatial scales [141]. This aspect indeed reminds the optical properties of single atoms, which are characterized by a gigantic optical cross section, compared to their physical size. One may wonder, then, if an "atomic metalens" can be analogously conceived by means of actual atoms, with a well-defined dipole transition. Unfortunately, two-level atoms do not naturally satisfy the points two and three of the list mentioned above. Specifically, they have a non-directional, 4π emission and the impressed phase shift is uniquely determined by the frequency of the incident photon, without further tunability.

In Chapter 5, we argue that these problems can be solved by spatially ordering the atoms. In particular, we employ subwavelength, inter-atomic distances to suppress non-zero diffraction orders and ensure directionality. At the same time, we exploit the collective atomic response to locally tune the phase shift, by varying the lattice constants over distances $\lesssim \lambda_0$, which are analogous to the discretization scales of common metalenses.

1.2 Outline of the thesis

In this introduction, we discussed the role of the refractive index in photonic technologies, as well as their intrinsic limitations due to its low order of magnitude. At the same time, we described the emergence of novel ap-

proaches, namely flat optics and metasurfaces, to efficiently deal with these universal limits.

Given the constrains that $n \sim 1$ imposes on optical devices, it is important to understand what are the fundamental limits to how large refractive index can be. From Fig. 1.2, we see that even an answer to this question seems elusive, given the failure of existing theories to describe the transition from dilute gases to real solids, while accounting for non-perturbative multiple scattering of light. In the rest of this thesis, we explore how its study can give more insights into the microscopic meaning of the refractive index, as well as representing an interesting tool for optical technologies.

To this aim, in Chapter 2 we first revise the standard methods to describe light-matter interfaces, from the perspectives of both solid state physics and quantum optics. Then, we underline the breakdown of these theories, in the regime where multiple light scattering is dominant. We finally discuss an alternative approach which naturally accounts for this latter, reporting some novel phenomena that it enables to predict, including the possibility of building up a mirror out of a 2D atomic array. Eventually, in Part II we discuss our work, which is divided into the following chapters.

- First, in Chapter 3, we focus on the emergence of the concept of refractive index in an ideal medium composed of randomly positioned atoms. The results of this chapter are published in [142]. Given a resonant wavelength $\lambda_0 = 2\pi/k_0$, we theoretically and numerically investigate its optical properties as a function of density $\eta = N/(k_0^3 V)$, finding that multiple scattering prohibits the indefinite growth of the index with η predicted by conventional models (orange, dashed line of Fig. 1.6) and that the index saturates to a "real-life" maximum value of $n \approx 1.7$ (green curve). We develop a non-perturbative Renormalization Group (RG) theory to understand its origin, where we show that multiple scattering and granularity effectively produce a process of inhomogeneous broadening, whose amount linearly scales with density. This ensures that, regardless of the physical atomic density, light at any given frequency only interacts with at most a few near-resonant atoms per cubic wavelength, thus resulting in the maximum index $n \approx 1.7$. This limit arises purely from electrodynamics, as it occurs at densities far below that where chemical processes become important. Nonetheless, we speculate that this process might dominate the optical response at higher densities as well (green, dotted line).

- In Chapter 4, we then analyze the case of atoms ordered in a lattice.

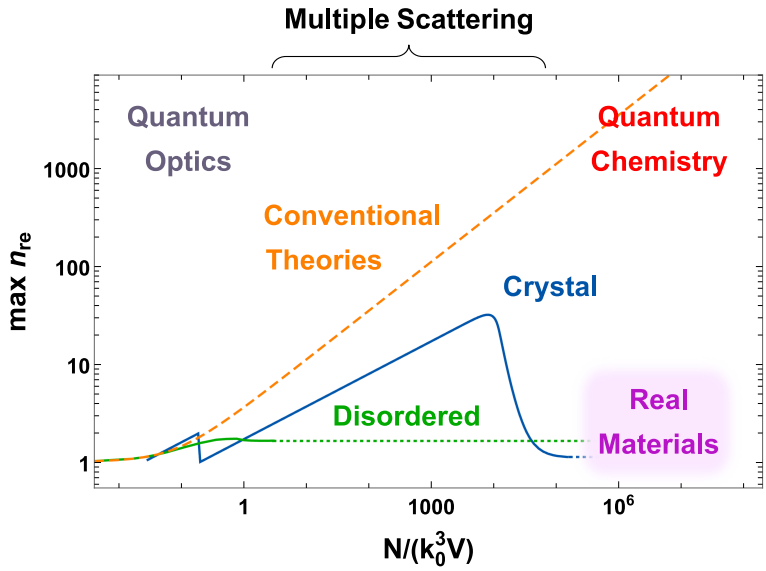

Figure 1.6: Schematic plot of the maximum real part of the refractive index versus density of atoms $\eta = N/(k_0^3V)$. The density is in units of the reduced wavelength $k_0^{-1} = \lambda_0/(2\pi)$ of the atomic transition. Conventional theories predict a maximum index that scales with density as $n \sim \sqrt{\eta}$ (orange, dashed curve). In the "quantum optics" regime, atoms are sufficiently far apart that they can be considered isolated objects, which only interact via the electromagnetic field. For sufficiently high densities, one enters the "quantum chemistry" regime where the overlap of electronic orbitals between different atoms becomes non-negligible and chemical interactions occur. In a vast intermediate regime of densities, ranging from $\eta \sim 1$ through the onset of quantum chemistry, a non-perturbative treatment of multiple scattering of light is needed to correctly predict the index. For a disordered atomic medium in the quantum optics regime, we show in Chapter 3 that the maximum index is limited to $n \approx 1.7$. This is shown by the solid, green curve, while the dotted, green curve represents our suggestion that this phenomenon might dominate at higher densities as well. In Chapter 4, we show that a perfect atomic crystal exhibits a purely real index scaling as $n \sim \eta^{1/3}$ in the quantum optics regime, and the maximum attainable value is limited by effects arising from quantum chemistry (blue curve). The discontinuity of the blue curve at low densities arises from interference effects, as discussed in Section 4.2.3.

Specifically, we aim to characterize the intermediate region between the typical "low-density" regime $\eta = N/(k_0^3V) \ll 1$ of standard quantum optics and that of "high densities" $\eta \gg 1$ which characterizes solid state physics (see Fig. 1.6). At dilute densities, this problem falls into the realm of pure optics, where atoms behave as isolated, point-like scatterers of light. On the other hand, when the lattice

constant d becomes comparable to the Bohr radius a_0, the electronic orbitals centered on different nuclei begin to overlap and strongly interact, giving rise to quantum chemistry. We thus discuss a minimal model for a unifying theory of index spanning the quantum optics and quantum chemistry regimes. A key aspect of this theory is the proper treatment of multiple light scattering, which can be highly non-perturbative over a large density range.

We first focus on the regime of pure quantum optics. Differently from the disordered case, we show that ideal light-matter interactions can have a single-mode, narrowband nature, which allows for a purely real maximum index that grows with density as $n_{\max} \propto \lambda_0/d \propto \eta^{1/3}$ (blue, solid curve of Fig. 1.6). At the same time, we discuss how this system ideally allows to reach the zero-index condition $n_{\min} = 0$.

This single-mode behaviour is rooted in the perfect translational symmetry of the 2D layers composing the lattice, which are sequentially encountered by normally incident light. From an optical perspective, we first identify two possible mechanisms that could suppress this ideal response within each 2D layer, later providing a minimal model of how those processes should spontaneously arise at the onset of quantum chemistry. Specifically, these corresponds to the situations when an atom of the array is either selectively driven or removed, to create a defect. In both cases, we show that the single-mode response of the array is drastically affected, due to the excitation of supplementary atomic modes.

When $d \sim a_0$, we identify two quantum-chemical mechanism (namely, excited-electron tunneling-dynamics and ground-state density-density correlations), which optically act as incoherent sources of either distinguishable excitations or off-resonant defects. Due to this reason, these processes naturally open up inelastic and spatial multi-mode light scattering processes, thus reducing the index back to order unity while simultaneously introducing absorption. Furthermore, we prove that around $d \sim a_0$ they allow to perturbatively recover the standard theories of solid-state optics, due to the suppression of multiple light scattering. Nonetheless, right before the onset of chemistry, our theory predicts that low-loss materials with both ultra-high ($n_{\mathrm{re}} \sim 30$) and near-zero ($n_{\mathrm{re}} \sim 0$) index could in principle be allowed by the laws of nature, albeit within a small bandwidth around the atomic resonance frequency.

- Finally, in Chapter 5, we study some potential applications of the complex interference patterns of the light scattered by atoms. Inspired by the approach of metasurfaces to optics, we specifically wonder if atoms can behave as an efficient optical device, when carefully positioned in free space. In particular, we start from the intuition that a 2D atomic array can act as an efficient mirror, to broaden this idea into a more complex optical device: a microscopically thin lens. As we discussed, flat optics is based on building blocks which require high transmission of light and the possibility of locally tailoring the impressed phase shift. We argue that this can be fulfilled by using two 2D arrays in series, and by properly designing the lattice constant. In particular, the choice of the transverse lattice constants d_{x}, d_{y} permits to control the phase over the full 2π range, while the distance d_{z} between the layers can ideally ensure a 100% transmission. While this method works only in the ideal, lossless case, we show that the addition of a third layer can make the system robust against the noise. Eventually, we show how these building blocks can be assembled to form an atomic metalens, characterizing its focusing efficiency against noise and imperfections via large-scale ($N \sim 5 \times 10^5$) numerical simulations. We note that this number of simulated atoms is approximately between one and two orders of magnitude larger than comparable works in literature.

2 - Multiple scattering of light

Chapter Contents

2.1 Smooth-field theories of standard optics

The quantum interactions between multiple atoms and light can be an extremely complex problem, involving a large number of particles interacting through a continuum of electromagnetic modes. At the same time, this represents a powerful playground, leading to many proposed protocols for quantum technologies [14, 38]. While the quantum regime cannot be possibly covered in the scope of this introduction, we can still examine the classical, linear optical limit, to characterize the notion of refractive index.

In this regime, the optical problem is largely simplified by a number of photons that is much lower than the number of atoms. The atomic system is weakly excited, and the intrinsic nonlinearity in the atomic levels can be neglected, meaning that their optical behaviour simplifies to that of classical scattering dipoles. In principle, however, to exactly solve such a problem one would still need to account for multiple scattering of light, which makes the complexity of the problem scale linearly with the number of atoms N. Due to these reasons, this scenario still requires unfeasible computational efforts, if one attempted to account for the realistic numbers of atoms typical of macroscopic system.

This complexity led to the development of simplified equations, which ignore the granularity of atomic positions and instead treat them as a smooth macroscopic medium, thus neglecting multiple light scattering. In this section, we review the most prominent of these methods, both from the perspective of solid-state physics (such as the Drude-Lorentz (DL) theory) and from that of pure optics (starting from the quantum, Maxwell-

Bloch (MB) equations and then focusing on their classical limit), mentioning one of the most famous and well-established attempts (namely, the Lorentz-Lorenz (LL) model) to locally correct the standard theories by partially accounting for multiple scattering. We show that these simplified approaches manifest evident discrepancies when extrapolated beyond their limited regimes of applicability, in a vast region where multiple scattering is dominant. We thus report an established method to exactly include multiple light scattering, discussing the specific example of a 2D atomic array, whose distinctive optical response cannot be predicted with standard smooth-medium theories.

To conclude, we stress that here, and throughout our thesis, the analysis will be limited to optical/near-optical frequencies, which motivates the specific assumption that only the electronic response contributes to the refractive index. This neglects phenomena of molecular re-organization into permanent dipoles, such as the case of water in the radio frequencies [143].

2.1.1 Solid-state index: Drude-Lorentz and beyond

The DL theory represent the most established, textbook description of light inside a material, whose roots dates back to the seminal works of Drude and Lorentz at the beginning of the 20^{th} century. It is based on a classical toy model, which is meant to describe the optical response of electrons and atomic nuclei in terms of smooth, macroscopically averaged quantities [25]. Specifically, let us start by explicitly focusing on a non-magnetic and electrically neutral medium. Semi-classically, one can consider that each j-th atom responds to light with its electric dipole moment $\mathbf{d}_j$, due to those electrons bound to the atomic nuclei. Clearly, this represents the typical behaviour of a dielectric medium, and one can define a macroscopic polarization $\mathbf{P}(\mathbf{r},t)$ as the volume density of such electric dipoles. At the same time, a generic material can exhibit free electrons as well, whose motion can be accounted for via the current density $\mathbf{J}_{\text{free}}(\mathbf{r},t)$, defined as the electric current per unit area. Intuitively, this latter mechanism characterizes the optical response in a conductor. From Maxwell's equations, these quantities fully characterize the propagation of an electromagnetic wave, via[1]

$$\nabla \times (\nabla \times \mathbf{E}) + \frac{1}{c^2}\partial_t^2 \mathbf{E} = -\mu_0 \partial_t \left(\partial_t \mathbf{P} + \mathbf{J}_{\text{free}}\right). \tag{2.1}$$

[1] Here, we indicate with $\mathbf{J}_{\text{free}}$ the current induced by unbound electrons moving inside the medium, but one can easily realize that the contribution due to the bounded electrons can be interpreted as an additional current, namely $\mathbf{J}_{\text{bound}} = \partial_t \mathbf{P}$.

This expression is very generic, and the granularity in the positions of atoms and electrons could in principle be included if $\mathbf{P} = \sum_j \mathbf{d}_j \delta(\mathbf{r} - \mathbf{r}_{\mathrm{n}}^j)$ and $\mathbf{J}_{\mathrm{free}} = q_{\mathrm{e}} \sum_i \dot{\mathbf{r}}_{\mathrm{e}}^i \delta(\mathbf{r} - \mathbf{r}_{\mathrm{e}}^i)$ were defined by means of delta functions centered at the particle positions (here, the indices j and i span the positions of respectively the atomic nuclei and the free electrons, while q_{e} is the electronic charge [144]). Nonetheless, to avoid the issues described earlier, a simpler classical estimation is performed, which ignores granularity.

- **Free charges.** First we study the limit where the effect of $\mathbf{P}$ is negligible compared to $\mathbf{J}_{\mathrm{free}}$. The current density can be then approximated by the smooth function $\mathbf{J}_{\mathrm{free}} \approx (N_{\mathrm{e}}/V) q_{\mathrm{e}} \dot{\mathbf{r}}_{\mathrm{e}}$ (where N_{e}/V is the density of the electrons), which obey the simple transport equation[2] $\ddot{\mathbf{r}}_{\mathrm{e}} + \gamma' \dot{\mathbf{r}}_{\mathrm{e}} = q_{\mathrm{e}} \mathbf{E}/m_{\mathrm{e}}$ with the rate γ' describing the effects of frictional dissipation. At the steady state, one gets the solution $\mathbf{J}_{\mathrm{free}}(\mathbf{r}, \omega) \approx -i\omega\epsilon_0 \chi_{\mathrm{cond}}(\omega) \mathbf{E}(\mathbf{r}, \omega)$, with

$$\chi_{\mathrm{cond}}(\omega) = \frac{\omega_{\mathrm{p}}^2}{-\omega^2 - i\gamma'\omega}, \tag{2.2}$$

  where we defined the plasma frequency $\omega_{\mathrm{p}} = \sqrt{(N_{\mathrm{e}}/V) q_{\mathrm{e}}^2/(m_{\mathrm{e}}\epsilon_0)}$.

- **Bound charges.** On the contrary, when all electrons are tightly bounded to the nuclei, one can neglect the current density due to free electrons $\mathbf{J}_{\mathrm{free}} \sim 0$, and estimate the atomic dipole moments $\mathbf{d}_j$ by means of a classical toy model. Specifically, let us define the displacement $\mathbf{r}_{\text{e-n}}$ of an electron from its equilibrium position. This approach roughly models the change in the electron orbitals when going from the ground to a target excited state, and allows us to write $\mathbf{d}_j \approx \mathbf{d} \equiv Z_{\mathrm{e}} q_{\mathrm{e}} \mathbf{r}_{\text{e-n}}$, where Z_{e} is the atomic number. The dynamics of $\mathbf{r}_{\text{e-n}}$ is then modeled as a classical, damped harmonic oscillator of resonant frequency ω_0 and damping rate γ_0', which is meant to account for the finite lifetime of the excited state. After solving for $\mathbf{r}_{\text{e-n}}$ at the steady state, we can approximate the macroscopic polarization as the smooth quantity $\mathbf{P} \approx (N/V)\mathbf{d} = (N_{\mathrm{e}}/V) q_{\mathrm{e}} \mathbf{r}_{\text{e-n}}$, where $N_{\mathrm{e}}/V = Z_{\mathrm{e}} N/V$. In Fourier space, one obtains $\mathbf{P}(\mathbf{r}, \omega) \approx \epsilon_0 \chi_{\mathrm{res}}(\omega) \mathbf{E}(\mathbf{r}, \omega)$, where we define the susceptibility

$$\chi_{\mathrm{res}}(\omega) = \frac{\omega_{\mathrm{p}}^2}{\omega_0^2 - \omega^2 - i\gamma_0'\omega}. \tag{2.3}$$

[2] In principle, the Lorentz force $q_{\mathrm{e}} \dot{\mathbf{r}}_{\mathrm{e}} \times \mathbf{B}$ should be similarly included, but this latter would be typically smaller than $q_{\mathrm{e}}\mathbf{E}$ by a factor $\sim \dot{\mathbf{r}}_{\mathrm{e}}/c \ll 1$, justifying its neglect [145].

To include the possibility for electrons to be excited into many excited states, one usually defines the total dielectric susceptibility $\chi_{\rm res}^{\rm tot}(\omega) = \sum_j f_j \chi_{\rm res}^j(\omega)$, where each resonance has its how frequency ω_j and decay rate γ_j', while the fractions f_j are called *oscillator strengths*.

To describe materials such as poor conductors or semiconductors, both contributions of $\mathbf{P}$ and $\mathbf{J}_{\rm free}$ must be included. Using the fact that $\mathbf{P} \propto \mathbf{E}$ and $\mathbf{J}_{\rm free} \propto \mathbf{E}$, and that no net charge is present in the material, we plug $\nabla \times (\nabla \times \mathbf{E}) = -\nabla^2 \mathbf{E}$ inside Eq. 2.1, leading to the refractive index [25]

$$\begin{aligned} n_{\rm DL}(\omega) &= \sqrt{1 + \chi_{\rm DL}(\omega)} \\ \chi_{\rm DL}(\omega) &= \chi_{\rm cond}(\omega) + \sum_j f_j \chi_{\rm res}^j(\omega), \end{aligned} \tag{2.4}$$

where the susceptibility $\chi_{\rm DL}(\omega)$ must satisfy the very general Kramers–Kronig relations, which relate its real and imaginary parts. From Eq. 2.4 one can identify the meaning of the plasma frequency $\omega_{\rm p}$: given a low-loss conductor (with $\gamma' \ll \omega_{\rm p}$ and $f_j \approx 0$), at $\omega \simeq \omega_{\rm p}$ one has $\chi_{\rm cond}(\omega \simeq \omega_{\rm p}) \approx -1$ and $n_{\rm DL}(\omega \simeq \omega_{\rm p}) \approx 0$. Finally, if one resonance ω_0 is extremely dominant around $\omega \sim \omega_0$, the index further simplifies into [37]

$$n_{\rm DL}(\omega \sim \omega_0) \approx \sqrt{1 + \frac{f_0 \omega_{\rm p}^2/(2\omega_0)}{-\omega + \omega_0 - i\gamma_0'/2}}. \tag{2.5}$$

The classical DL model must ascribe its success to its simplicity and to its ability of qualitatively (and to some extent quantitatively) describing empirical evidence. Many works, for example, well succeed in fitting the experimental data with the DL predictions, where the resonance frequencies ω_j, decay rates γ_j and strengths f_j are used as free parameters [146]. Nonetheless, it is also true that, mathematically, any optical response can be well approximated with a sufficient number of resonances [80].

Notably, the DL model already provides a rough intuition of why the index of a dielectric, transparent material should be limited to $n \sim 1$, as discussed in [4, 74]. Specifically, let us start from Eq. 2.3, and consider the typical transparency region of $\omega \ll \omega_0$, where $\chi_{\rm res} \sim \omega_{\rm p}^2/\omega_0^2$. By approximating an electronic orbital as a sphere of volume $V_{\rm e}$, one can estimate the resonance frequency by means of classical electrostatic considerations, leading to $\omega_0 \sim \sqrt{q_{\rm e}^2/(3\epsilon_0 V_{\rm e} m_{\rm e})}$. This allows to write $\chi_{\rm res} \sim 3N_{\rm e}V_{\rm e}/V$, where the quantity $N_{\rm e}V_{\rm e}/V$ describes (within this naive classical model) the average orbital occupancy, thus meaning that $0 \leq N_{\rm e}V_{\rm e}/V \leq 2$ due to Pauli

exclusion and spin degeneracy. This very rough, semi-classical argument, then, already provides a range of indices $1 \leq n \leq \sqrt{7} \simeq 2.6$ [4], which is surprisingly accurate compared to the primitiveness of this approach. On top of that, an elegant work recently placed a more refined boundary between the maximum index of a transparent material and the bandwidth where it can be sustained [80], although it didn't directly address how large the index might be. Furthermore, the argument described above explicitly focuses on very off-resonant responses, while several experimental papers explored the refractive index of materials over broad frequency ranges, showing that the index is similarly bounded by $n \sim 1$ around the resonances [5–12].

The DL theory is a purely classical model. To overcome the limitations emerging due to the quantum nature of particles, theories and methods were suggested based on the laws of quantum mechanics. This is particularly true for the case of crystals, where the Bloch theorem allows to infer the optical properties from quantum considerations. Specifically, one can describe the electronic state in terms of bands, where the Fermi level defines the energy of occupancy at zero temperature. Depending on its value, one can have different solid-state properties. In a metal, the Fermi energy is within a (conduction) band, so that this latter is semi-filled and the electrons can be easily accelerated by an external field, developing a current. In an insulator, this is in the middle of a large bandgap, so that the electrons fill a lower (valence) band and cannot be easily excited to the empty, upper band, due to the broad energy gap. In a semi-conductor, typically, the bandgap is small, meaning that electrons can in principle hop from the valence to the conduction band, so that this latter is not empty at a finite temperature.

The optical properties of a conductor are then related to transitions within the conduction band [146]. To this aim, free electrons models are usually adopted, which lead to results similar to Eq. 2.2, where a reduced electron mass m_{e}^{*} locally approximates the conduction band with the parabolic dispersion relation typical of free particles. On the contrary, the resonant properties are associated to transitions between the valence $\psi_{\mathrm{v}}(\mathbf{k},\mathbf{r})$ and the conduction $\psi_{\mathrm{c}}(\mathbf{k},\mathbf{r})$ band, with an energy difference of $\hbar\omega_{\mathrm{cv}}(\mathbf{k})$. After solving for the band structure via DFT (or equivalent methods), one can then estimate the transition rate due to the coupling $\hat{\mathcal{H}}_{\mathrm{int}} = -(q_{\mathrm{e}}/m_{\mathrm{e}})\hat{\mathbf{p}}\cdot\mathbf{A}$ with light[3], where this latter is treated as a classical

[3] The minimal coupling Hamiltonian, with $\hat{\mathcal{H}}_{\mathrm{int}} = -(q_{\mathrm{e}}/m_{\mathrm{e}})\hat{\mathbf{p}}\cdot\mathbf{A}$, in this regime should be equivalent to that in the dipole gauge (i.e. $\hat{\mathcal{H}}_{\mathrm{int}} = -\hat{\mathbf{d}}\cdot\mathbf{E}$). Nonetheless, a technical problem emerges in the calculation of $\langle\hat{\mathbf{d}}\rangle$ in an extended periodic lattice, given by the contrast between the local definition of the dipole moment (which is related to a positional displacement from each atomic center) and the global defini-

field. In sight of Fermi's golden rule, one can infer the absorption coefficient as [147, pp. 149-155]

$$\text{Im } \chi_{\text{res}}^{\text{cv}}(\omega) = \frac{8\pi^2 q_{\text{e}}^4}{m_{\text{e}}^2 \omega^2} \int_{\text{BZ}} \frac{d\mathbf{k}}{(2\pi)^3} |\mathbf{p}_{\text{cv}}(\mathbf{k})|^2 \delta(\hbar\omega_{\text{cv}}(\mathbf{k}) - \hbar\omega), \tag{2.6}$$

where $\mathbf{p}_{\text{cv}}(\mathbf{k}) = \int_{\text{UC}} \psi_{\text{c}}^*(\mathbf{k}, \mathbf{r})(-i\hbar\nabla)\psi_{\text{v}}(\mathbf{k}, \mathbf{r})d\mathbf{r}$ is the electron momentum matrix element associated with the chosen transition, in Bloch space. The real part of the susceptibility can be then computed by plugging Eq. 2.6 into the Kramers-Kronig relation, leading to

$$\text{Re } \chi_{\text{res}}^{\text{cv}}(\omega) = \frac{16\pi q_{\text{e}}^4}{m_{\text{e}}^2} \int_{\text{BZ}} \frac{d\mathbf{k}}{(2\pi)^3} \frac{|\mathbf{p}_{\text{cv}}(\mathbf{k})|^2/\omega_{\text{cv}}(\mathbf{k})}{\omega_{\text{cv}}(\mathbf{k})^2 - \omega^2}. \tag{2.7}$$

This expression closely resembles Eq. 2.3, and indeed some works include a phenomenological decay term $-i\gamma'\omega$ at the denominator, to emulate inelastic losses [56], such as phononic excitations. Differently from the case of single atoms or molecules, however, here the (localized) orbitals are broadened into bands, and one has to account for the contribution of transitions over the whole Brillouin zone [4].

Within this formalism, some arguments can partially explain why extreme indices of refraction are unlikely, when considering typical energies of the bands and of the bandgaps [4, 55–57]. These results, along with those of the more naive DL model, might suggest that the search for extreme indices should focus on the intermediate region between quantum optics and solid-state physics, where the response is dominated by the multiple scattering of light. In particular, in Chapter 4 we will try to address this idea. For the moment, in the next section we review the most common model to describe the opposite limit of pure quantum optics, namely MB theory.

2.1.2 Maxwell-Bloch equations of an atomic ensemble

Nowadays, the cornerstone of our understanding and description of quantum atom-light interfaces is constituted by the MB equations [14]. Differently from the classical DL model, they retain the quantum nature of atoms and

tion of the Bloch modes (extended over the whole lattice) [4]. One has indeed that $\mathbf{d}(\mathbf{k}) = e\int_{\text{UC}} \psi_{\text{c}}^*(\mathbf{k}, \mathbf{r})\ \mathbf{r}\ \psi_{\text{v}}(\mathbf{k}, \mathbf{r})d\mathbf{r}$ would wrongly depend on the arbitrary definition of the unit cell of integration. The momentum space of $\mathbf{p}$, on the other hand, is global by definition, allowing to solve this discrepancy.

light[4], aiming to capture its behaviour via macroscopic quantum operators. Specifically, its predictions well describes disordered ensembles of quantum emitters, such as an ultra-cold gas of atoms, as long as the validity of its approximations doesn't break down. Its drastic simplifications, indeed, have caused many essential aspects of atom-light interactions to be largely ignored, particularly when multiple scattering comes into play [148]. These effects are only starting to be appreciated again, given the emergence of ordered atomic lattices [149–152] or dense atomic clouds [153–159], where multiple scattering plays a preeminent role.

Similarly to the previous section, the full wave-equation of the electric field operator in the presence of N quantum dipoles (atoms) reads

$$\nabla \times \left(\nabla \times \hat{\mathbf{E}} \right) + \frac{1}{c^2} \partial_t^2 \hat{\mathbf{E}} = -\mu_0 \partial_t^2 \sum_{j=1}^{N} \hat{\sigma}_{\mathrm{ge}}^j \mathbf{d}_0 \delta(\mathbf{r} - \mathbf{r}_j), \tag{2.8}$$

where now $\hat{\mathbf{E}}$ is the quantum operator associated to the electric field, while the terms $\hat{\sigma}_{\mathrm{ge}}^j \equiv |g_j\rangle \langle e_j|$ stand for the quantum coherence operators of the j-th atom[5] and $\mathbf{d}_0$ is the dipole matrix element associated with the transition between ground state $|g\rangle$ and excited state $|e\rangle$ (here, for simplicity, we focus on a two-level atom). The quantities $\hat{\sigma}_{\mathrm{ge}}^j \mathbf{d}_0$ represent the quantum operators associated to the atomic dipoles $\mathbf{d}_j$.

Within the MB approximation, the granularity of atomic positions is ignored and the discrete set of atomic dipoles is replaced by a macroscopic smooth polarization field $\hat{\mathbf{P}}_{\mathrm{ge}}(\mathbf{r})$, which is defined by assuming a uniform atomic distribution, namely $\sum_i^N \delta(\mathbf{r} - \mathbf{r}_j) \hat{\sigma}_{\mathrm{ge}}^j \mathbf{d}_0 \simeq (N/V) \hat{\mathbf{P}}_{\mathrm{ge}}(\mathbf{r})$. The polarization operator $\hat{\mathbf{P}}_{\mathrm{ge}}(\mathbf{r})$ evolves under the usual dipole Hamiltonian, along with independent emission, and its dynamics read

$$i\partial_t \hat{\mathbf{P}}_{\mathrm{ge}} = -\Gamma_0 \left(\Delta + \frac{i}{2} \right) \hat{\mathbf{P}}_{\mathrm{ge}} - \frac{\mathbf{d}_0^* \cdot \hat{\mathbf{E}}}{\hbar} \left[\hat{\mathbf{P}}_{\mathrm{gg}} - \hat{\mathbf{P}}_{\mathrm{ee}} \right], \tag{2.9}$$

where we defined the dimensionless detuning parameter $\Delta = (\omega - \omega_0)/\Gamma_0$, between the light frequency ω and the atomic resonance $\omega_0 \equiv k_0 c$, and where the densities of population of the ground $\hat{\mathbf{P}}_{\mathrm{gg}}(\mathbf{r})$ and excited $\hat{\mathbf{P}}_{\mathrm{ee}}(\mathbf{r})$ states are smoothly defined analogously to the coherence operator $\hat{\mathbf{P}}_{\mathrm{ge}}(\mathbf{r})$. In these equations, the atoms are assumed to spontaneously emit at an independent rate, quantified by the rate $\Gamma_0 = k_0^3 |\mathbf{d}_0|^2/(3\pi\hbar\epsilon_0)$, which is

[4] This is possible because atomic ensembles are simpler compared to solid-state systems, where a long list of quantum-chemical effects cannot be neglected.

[5] In the rotating frame of the incoming light.

identical to the spontaneous emission rate of a single atom in vacuum.

Typically, Eq. 2.8 (with the sum of the atomic dipoles replaced by $\hat{\mathbf{P}}_{\mathrm{eg}}$) and Eq. 2.9 are used to address the quantum state of light, including nonlinear effects due to the coupling with atoms. These quantum-operator equations are still challenging to solve generally, and in our work we are interested in the regime where Eq. 2.9 is simplified by the assumption of weak nonlinearities. This corresponds to studying the linear, optical response associated to the refractive index, and it is motivated by the observation that the number of absorbed photons is typically much lower than the number of atoms, allowing to write $|\langle\hat{\mathbf{P}}_{\mathrm{ee}}\rangle| \ll |\langle\hat{\mathbf{P}}_{\mathrm{gg}}\rangle| \simeq 1$. Taking further the classical limit, where operators are replaced by their mean values, one can define the polarization density $\mathbf{P}(\mathbf{r}) = (N/V)\langle\hat{\mathbf{P}}_{\mathrm{ge}}(\mathbf{r})\rangle$, arriving to the linear response $\mathbf{P}(\mathbf{r}) = (N/V)\alpha_0(\Delta)\mathbf{E}(\mathbf{r})$, which is characterized by the atomic polarizability $\alpha_0(\Delta) = 3\pi\epsilon_0/[(-\Delta - i/2)k_0^3]$. In turn, this permits to easily solve the Maxwell equations for monochromatic plane waves, predicting a refractive index given by

$$n_{\mathrm{MB}}(\Delta) = \sqrt{1 + \frac{N}{V\epsilon_0}\alpha_0(\Delta)} = \sqrt{1 + \frac{3\pi\eta}{-\Delta - i/2}}, \tag{2.10}$$

where we recall the definition of the dimensionless density $\eta \equiv N/(Vk_0^3)$. This formula is completely analogous to Eq. 2.5, which described the DL index, when one single resonance dominates the optical response. This is no coincidence, given that atoms have a very narrowband and strongly resonant response, and that we are focusing on the classical limit of linear atomic response.

The result of Eq. 2.10 means that the index of refraction indefinitely grows with η, reaching for instance resonant values of $n_{\mathrm{MB}} \sim 10^2 \div 10^3$ at the typical density of air. This prediction is directly related to the simplifications adopted by the MB model. It is assumed, indeed, that at each point in space the polarization field decays with a constant decay rate Γ_0, independently from the effects of other surrounding atoms in the cloud. This results in an additive response, where the overall susceptibility is simply N times the polarizability that one atom would have if no other atoms were present. Atoms, however, are non-absorbing scatterers, and it is well-known in other branches of optics that light propagating through a dense medium of scatterers produces a highly complex *speckle* pattern in the output intensity (see Fig. 2.1), due to multiple scattering and wave interference of light [23, 24]. As there must be a direct correspondence between the intensity in this complex pattern and the emission of the atoms, one can conclude that

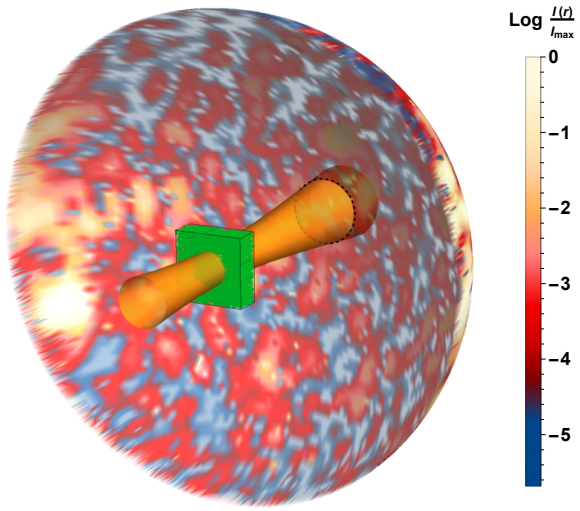

Figure 2.1: Illustration of a typical speckle pattern given a fixed random atomic ensemble. 3D reconstruction of the forward scattered intensity $I(\mathbf{r})/I_0 = |\mathbf{E}(\mathbf{r})/E_0|^2$ over a hemispherical surface far from the sample. The intensity value is described in terms of the color bar on the right, while the atomic ensemble is depicted in terms of green points, placed inside a pictorial box. The input Gaussian beam is characterized by its waist, which is portrayed with an orange surface. The optical behaviour is numerically calculated by means of the coupled-dipole formalism, which will be defined in the next section.

the true model for atomic decay must be more complex than independent emission. Furthermore, as such speckle cannot arise without granularity, we can also conclude that a more accurate model must take granularity into account.

2.1.3 Lorentz-Lorenz approximation

Historically, the LL (or Clausius-Mossotti) model represented one early attempt to approximate the local corrections due to multiple scattering, and it remains widely used today, both in the context of solid-state and atomic physics. Within this model, one considers a local field $\mathbf{E}_{\text{loc}}(\mathbf{r})$ acting on each atom, which is different from the macroscopic field $\mathbf{E}(\mathbf{r})$, due to the light re-radiated by the surrounding atoms. This effective field $\mathbf{E}_{\text{loc}}(\mathbf{r})$ is estimated by defining a small empty sphere[6] that separates each atom from the rest of the material, which is approximated as a smooth medium, and then solving the problem by means of classical electrostatics [160–162].

[6] Often referred to as the Lorentz sphere.

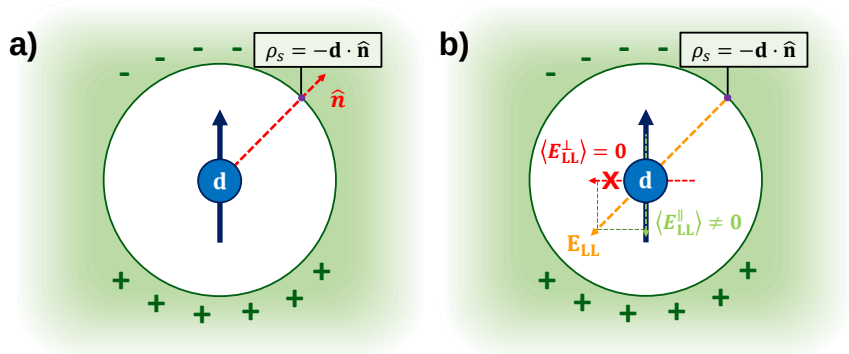

Figure 2.2: Pictorial representation of the LL correction inside the Lorentz sphere. a) Surface charge density induced by the polarization at the interface, due to the presence of an empty sphere inside a smooth medium. b) Contribution to the electric field felt at the center of the Lorentz sphere (i.e. where the atomic dipole is placed), due to the presence of the surface bound charges. When integrating all the contributions, the part of the field perpendicular to the atomic dipole vanishes, as represented by a red cross.

Specifically, at the interface between the empty sphere and the rest of the medium, the atomic dipole induces a local surface density of charges, which provides a supplementary, corrective field back to the atom (a schematic representation of this process is depicted in Fig. 2.2). This leads to the new definition of $\mathbf{P}(\mathbf{r}) = \epsilon_0\chi(\omega)\mathbf{E}_{\text{loc}}(\mathbf{r})$, with the local field given by

$$\mathbf{E}_{\text{loc}}(\mathbf{r}) = \mathbf{E}(\mathbf{r}) + \frac{\mathbf{P}(\mathbf{r})}{3\epsilon_0}, \tag{2.11}$$

which results in a different prediction for the refractive index, reading

$$n_{\text{LL}}(\Delta) = \sqrt{1 + \frac{\chi(\omega)}{1 - \chi(\omega)/3}}. \tag{2.12}$$

Here, the value of $\chi(\omega)$ depends on the underlying physical model, which is usually either DL or MB. For this latter case, one has that $\chi(\omega) = (N/V)\alpha_0(\Delta)/\epsilon_0$, which leads to [163]

$$n_{\text{LL}}(\Delta) = n_{\text{MB}}(\Delta + \pi\eta) = \sqrt{1 + \frac{3\pi\eta}{-(\Delta + \pi\eta) - i/2}}. \tag{2.13}$$

An analogous result can be inferred starting from the resonant limit of the DL index, which was discussed in Eq. 2.5. Despite representing a partial correction to the MB equations, the LL model is still only phenomenolog-

ical in origin. In particular, it simply results in a shift of all spectra by an amount $\Delta \to \Delta + \pi\eta$, and the maximum index of refraction will still scale as $\sim \sqrt{\eta}$. In the context of dipole ensembles, indeed, successful agreements between LL predictions and experimental results were historically obtained in regimes of low optical response $(N/V)\alpha_0(\Delta)/\epsilon_0 < 1$, where the approximated arguments of this model can be sufficient [164].

2.2 The problems with smooth theories

Smooth-field models have a well-established list of successes in predicting optical phenomena, in situations where the multiple scattering of light is weak. Nonetheless, in the last decade optical experiments with cold atomic clouds have started to explore regimes where the average inter-atomic distances become comparable or smaller than the resonant, optical cross section $\sigma_0 \propto \lambda_0^2$ of single atoms, so that multiple light scattering cannot be ignored anymore[7]. A list of some prominent examples is given in Table 2.1, where the first two columns report the peak density $\eta = N/(Vk_0^3)$ and the temperature T. These works were able to study densities as high as $\eta \sim 1$ or fraction of unity, which represent the onset of the regime of $\eta \gtrsim 1$ where multiple scattering is expected to completely dominate the optical response. In particular, in Table 2.1 we report their analysis of the optical response as a function of increasing densities (given a fixed size of the ensemble). These experiments already observe a relevant number of discrepancies between their results and that predicted by traditional, smooth-medium theories. These include the saturation of the optical scattering per unit length, which is experimentally quantified by studying the Optical Depth (OD), i.e. the quantity OD $\sim n_{\mathrm{im}} k_0 L$, for ensembles with a fixed length L (in the direction of light propagation), and increasing density (third column). At the same time, they also witnessed an abnormal shift of the resonance frequency (fourth column) or broadening of the optical linewidth (fifth column). Some supplementary analysis of can be found in [165, 169, 170].

On top of that, multiple scattering of light can be equivalently interpreted as a phenomenon of wave interference between the light scattered by each atom. Interference effects can be expected to be prominent in ordered arrays, where destructive or constructive interference might be maximized. For example, great interest was recently gathered by the theoretical possibility of exploiting these processes to build a perfect mirror out of a single 2D

[7] At higher temperatures (such as with hot atomic vapours) Doppler broadening would suppress the resonant effects of multiple scattering [165–168].

Ref.	η	T(μK)	Saturation of OD	Resonance shift $\delta\omega$	Linewidth
[153]	0.5	100	Depends on ω	$\delta\omega < 0$	$\propto \eta^{0.08}$
[154]	0.9	110	Yes	$\delta\omega \sim 0$	Broadens
[155]	0.9	110	–	$\delta\omega \sim 0$	–
[156] [157]	$\lesssim 0.4$	120	Yes	$\delta\omega < 0$	$\propto \eta$
[158]	0.3	0.3	Yes	$\delta\omega > 0$	$\propto \eta$
[159]	0.15	150	–	$\delta\omega < 0$	Broadens

Table 2.1: Experimental evidence of deviations from mean-field models, with dense cold atomic clouds. Table comparing the results of various experimental references (first column), studying the optical properties of a cold atomic ensemble. The second and third column represent the peak atomic density $\eta = N/(k_0^3 V)$ (in units of k_0^{-3}) and temperature T. The notation "–" stands for "not analyzed in the paper". Some of the main results are also listed, showing discrepancies with MB and LL when increasing the atomic density, which include witnessing a saturation of the OD (defined as the total losses, i.e. the imaginary part of the index multiplied by the length of the ensemble in the direction of light propagation OD $= n_{\mathrm{im}} L$), the shift of the central resonance frequency or the broadening of the total linewidth.

atomic array [149, 150], as was experimentally addressed in [171]. Finally, other works have explored the effects of multiple scattering on different optical phenomena, such as collective resonance shifts [163, 166, 167, 172, 173], cooperative scattering properties [174–176], emergence of sub- and superradiance [151, 177–181], and Anderson localization of light [182, 183].

2.3 Atoms in free space: a spin model formalism

The full description of atoms in free space interacting with light must account for all the mutual interactions due to multiple scattering in a continuum of directions, spanning the whole solid angle. To accomplish that, one historical approach has been a Spin Model (SM) formalism [151, 184–187], which we discuss here.

Given an atomic cloud illuminated by an external light beam, the total

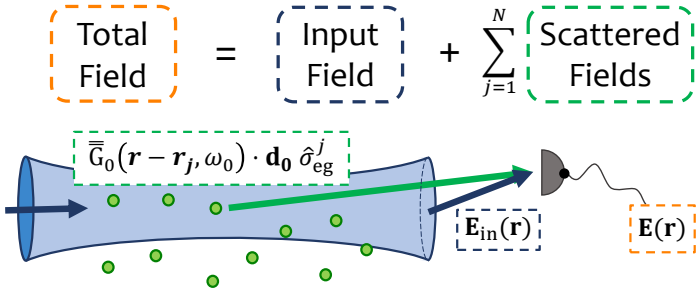

Figure 2.3: Pictorial representation of the total field reconstruction. The total field at a given point (orange boxes) is given by the sum of the input field shone onto the atomic ensemble (blue boxes) and the various fields scattered by the different atoms (green boxes).

field can be directly expressed as the linear sum of the input field $\mathbf{E}_{\mathrm{in}}(\mathbf{r})$ and the field scattered by the various atomic dipoles, as pictorially depicted in Fig. 2.3. Assuming that the atoms respond to near-resonant light as two-level systems, with a dipole matrix element $\mathbf{d}_0$, this reads

$$\hat{\mathbf{E}}(\mathbf{r},\omega) = \hat{\mathbf{E}}_{\mathrm{in}}(\mathbf{r},\omega) + \frac{k_0^2}{\epsilon_0}\sum_{j=1}^{N}\bar{\bar{\mathbf{G}}}(\mathbf{r}-\mathbf{r}_j,\omega_0)\cdot\mathbf{d}_0\,\hat{\sigma}^j_{\mathrm{ge}}. \tag{2.14}$$

The emission pattern of each single atom at position $\mathbf{r}_j$ is given by the Dyadic Green's tensor $\bar{\bar{\mathbf{G}}}(\mathbf{r}-\mathbf{r}_j,\omega_0)$, which has the form

$$\bar{\bar{\mathbf{G}}}(\mathbf{r},\omega_0) = k_0\frac{e^{i\rho}}{4\pi}\left[\left(\frac{1}{\rho}+\frac{i}{\rho^2}-\frac{1}{\rho^3}\right)\mathbb{I}+\left(-\frac{1}{\rho}-\frac{3i}{\rho^2}+\frac{3}{\rho^3}\right)\frac{\boldsymbol{\rho}\otimes\boldsymbol{\rho}}{\rho^2}\right], \tag{2.15}$$

where we defined $\rho \equiv |\boldsymbol{\rho}| \equiv |k_0\mathbf{r}|$, with $k_0 = \omega_0/c$. This tensor represents the full vectorial field emitted by a $\mathbf{d}_0$-polarized dipole. Its radiation pattern is composed of several terms, which can be related to interaction strength at different ranges of distance. In particular, one can distinguish between a far-field behaviour and a near-field term, characterized, respectively, by the $\sim 1/\rho$ and the $\sim 1/\rho^3$ scalings. Due to the non-absorbing nature of atoms, each atomic excitation gets converted into an electromagnetic scattered field, as encoded by the presence of the quantum dipole operators $\hat{\sigma}^j_{\mathrm{ge}}$.

The formula presented in Eq. 2.14 is valid in the Markovian regime, which allows to approximate $\bar{\bar{\mathbf{G}}}(\mathbf{r}-\mathbf{r}_j,\omega) \simeq \bar{\bar{\mathbf{G}}}(\mathbf{r}-\mathbf{r}_j,\omega_0)$, so that the Fourier transformation becomes local in time [151]. This is justified by the very narrowband optical response of atoms (with a typical width of $\Gamma_0 \ll$

ω_0), and its physical meaning can be clarified in the time domain. This assumption, indeed, expresses the idea that light travels between different atoms so quickly, that it can be approximated as instantaneous, compared to the typical time-scale $\sim 1/\Gamma_0$ of the atomic dynamics. Specifically, this corresponds to $1/\Gamma_0 \gg |\mathbf{r}_j - \mathbf{r}_i|/c$, which is fulfilled as long as $|\mathbf{r}_j - \mathbf{r}_i| \lesssim 1\mathrm{m}$, for typical magnitudes of the spontaneous emission rate [151]. Eventually, we remark that Eq. 2.14 is completely equivalent (except for the Markovian assumption) to the Maxwell's wave equation[8] of Eq. 2.8.

The input-output equation of Eq. 2.14 permits to efficiently reconstruct the complete field at a given point, in terms of only the atomic spins $\hat{\sigma}^j_{\mathrm{ge}}$. In turn, the atomic quantum state is driven by the field itself, which depends on all other atoms. It can be shown that the full dynamics of the atomic density matrix $\hat{\rho}$ evolving under the re-scattered fields are given by [148, 151, 188]

$$\begin{aligned} \frac{d\hat{\rho}}{dt} &= -\frac{i}{\hbar}\left(\hat{\mathcal{H}}_{\mathrm{eff}}\hat{\rho} - \hat{\rho}\hat{\mathcal{H}}^{\dagger}_{\mathrm{eff}}\right) + \mathcal{J}\left[\hat{\rho}\right], \\ \hat{\mathcal{H}}_{\mathrm{eff}} &= \hat{\mathcal{H}}_0 - \frac{k_0^2}{\epsilon_0}\sum_{j,k=1}\mathbf{d}_0^* \cdot \bar{\bar{\mathbf{G}}}(\mathbf{r}_j - \mathbf{r}_k, \omega_0)\cdot \mathbf{d}_0\ \hat{\sigma}^j_{\mathrm{eg}}\hat{\sigma}^k_{\mathrm{ge}}, \\ \mathcal{J}[\hat{\rho}] &= \frac{2k_0^2}{\epsilon_0\hbar}\sum_{j,k=1}\mathbf{d}_0^* \cdot \mathrm{Im}\ \bar{\bar{\mathbf{G}}}(\mathbf{r}_j - \mathbf{r}_k, \omega)\cdot \mathbf{d}_0\ \hat{\sigma}^k_{\mathrm{ge}}\hat{\rho}\hat{\sigma}^j_{eg}, \end{aligned} \tag{2.16}$$

where the effective Hamiltonian $\hat{\mathcal{H}}_{\mathrm{eff}}$ is a non-Hermitian operator (i.e. includes emission into the photonic bath), while the Liouvillian super-operator $\mathcal{J}[\hat{\rho}]$ describes the "population recycling" terms, i.e. the terms which increase the ground state population when an excitation gets lost. Intuitively, the terms $\hat{\sigma}^j_{eg}\hat{\sigma}^k_{\mathrm{ge}}$ in $\hat{\mathcal{H}}_{\mathrm{eff}}$ describe the exchange of excitations between two different atoms j and k, which can be physically interpreted as a multiple scattering event involving emission of a photon by one atom and re-absorption by another atom. By accounting for all of these events, then, the model is able to completely capture the full multiple scattering problem, providing a complete description of the many atoms-field system.

2.3.1 Linear limit of coupled-dipoles equations

The SM equations of the previous section provide a reliable formalism, which includes the full quantum dynamics of the atomic ensemble interacting with

[8] This can be easily verified by recalling the mathematical definition of the Dyadic Green's tensor $\bar{\bar{\mathbf{G}}}(\mathbf{r}, t)$, which reads $\nabla \times [\nabla \times \bar{\bar{\mathbf{G}}}(\mathbf{r}, t)] + \partial_t^2 \bar{\bar{\mathbf{G}}}(\mathbf{r}, t)/c^2 = \delta(\mathbf{r})\mathbb{I}$.

the electromagnetic field. Nevertheless, finding general solutions of Eq. 2.16 for any 3D random configuration is a hard task, since the dimension of the full atomic Hilbert space grows exponentially as 2^N. Due to this reason, one can truncate the Hilbert space to those states where only one atom is excited at a time, which is valid in the linear response regime of low-intensity input fields. The dimension of the single excitation manifold, then, only grows linearly in N, allowing to efficiently treat the equations while still retaining the complexity of the full multiple scattering many-body problem. The atomic quantum state can thus be written as $|\psi\rangle \simeq |g\rangle + \sum_j^N \beta_j |e_j\rangle + \mathcal{O}(|\beta|^2)$, where the ground state coefficient, due to the small amount of excitation, was approximated as ~ 1. In the equations of motion, the jump operator $\mathcal{J}[\hat{\rho}] \sim \mathcal{O}(|\beta|^2)$ is then negligible, so that the steady-state solution of Eq. 2.16 reduces to a $N \times N$ purely algebraic problem, which reads

$$
\begin{aligned}
-\Delta \left(\frac{\Gamma_0}{\Omega_0} \beta_j \right) - \sum_{k=1}^{N} G_{jk} \left(\frac{\Gamma_0}{\Omega_0} \beta_k \right) &= \frac{\mathbf{d}_0^* \cdot \mathbf{E}_{\text{in}}(\mathbf{r}_j)}{|\mathbf{d}_0| E_0}, \\
\mathbf{E}(\mathbf{r}) &= \mathbf{E}_{\text{in}}(\mathbf{r}) + E_0 \sum_{j=1}^{N} \mathbf{G}_j(\mathbf{r}) \left(\frac{\Gamma_0}{\Omega_0} \beta_j \right).
\end{aligned}
\tag{2.17}
$$

Here, we defined the Rabi frequency $\Omega_0 = E_0 |\mathbf{d}_0|/\hbar$ in terms of the magnitude scale $E_0 = E_{\text{in}}(0)$ of the field, as well as the rate of spontaneous decay $\Gamma_0 = k_0^3 |\mathbf{d}_0|^2/(3\pi\epsilon_0\hbar)$. At the same time, we recall that the dimensionless detuning is defined as $\Delta = (\omega - \omega_0)/\Gamma_0$. In Eq. 2.17, the Green's tensors are encoded in the definitions of the parameters $\mathbf{G}_j(\mathbf{r}) \equiv (3\pi/k_0)\bar{\bar{\mathbf{G}}}(\mathbf{r} - \mathbf{r}_j, \omega_0) \cdot \mathbf{d}_0/|\mathbf{d}_0|$ and $G_{jk} \equiv \mathbf{d}_0^* \cdot \mathbf{G}_j(\mathbf{r}_k)/|\mathbf{d}_0|$. There, we define $G_{jj} = i/2$, recovering the single-atom decay rate (in units of Γ_0), and regularizing the divergent self-energy associated to Re $\bar{\bar{\mathbf{G}}}(\mathbf{r} \to 0, \omega_0)$.

In this limit, the nonlinear nature of the atomic energy levels is ignored, and the atoms respond as classical, harmonic oscillators. This motivates the use of this formalism to study the emergence of the refractive index, which quantifies the linear optical response of the atomic medium. At the same time, this also explains why Eq. 2.17 is mathematically equivalent to those equations describing a system of N classical dipoles $\mathbf{d}_j = \beta_j \mathbf{d}_0$ with polarizability $\alpha_0(\Delta) = 3\pi\epsilon_0/[(-\Delta - i/2)k_0^3]$.

2.3.2 2D atomic arrays

When free-space atoms are positioned in an ordered geometry the dipole-dipole interactions can radically alter the overall atomic response. This is the

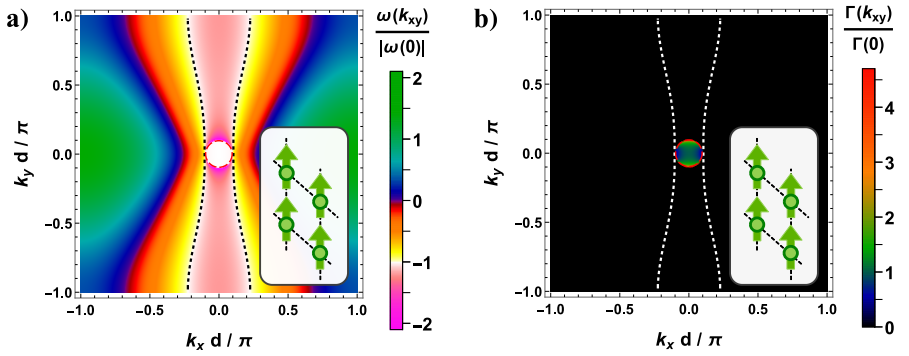

Figure 2.4: Complex eigenvalues $\omega(\mathbf{k}_{\rm xy})-i\Gamma(\mathbf{k}_{\rm xy})/2$ of a 2D atomic array in free space. The array extends in the $\hat{\mathbf{x}}$-$\hat{\mathbf{y}}$ plane, and the atomic dipoles are aligned along $\hat{\mathbf{x}}$. The red, dashed lines describe the edge of the light cone $|\mathbf{k}_{\rm xy}|\leq k_0$, while the black (a) and white (b) dotted lines correspond to the isoenergetic curves $\omega(\mathbf{k}_{\rm xy})=\omega(0)$. The lattice constant is $d_{\rm z}=0.05\lambda_0$.

case of 2D atomic arrays, that we review in the two-level, single-excitation limit of Eq. 2.17. Rich physics was indeed highlighted in this regime, such as the possibility of exponentially improving the storage efficiency of quantum memories based on electromagnetically induced transparency [151, 152].

Atoms in free space can talk to a continuum of electromagnetic modes, spanning the whole solid angle. Usually, this means that the energy can spontaneously escape outside the atomic ensemble. Nonetheless, when they are neatly ordered, the dipole-dipole interactions cause the appearance of collective guided modes, as long as the translational symmetry is preserved. The reason is not surprising, as can be derived in the limit of an infinite array. In that regime the Bloch theorem defines the eigenmodes $\left|E_{\mathbf{k}_{\rm xy}}\right\rangle=\sum_j^N e^{i\mathbf{k}_{\rm xy}\cdot\mathbf{R}_j}\left|e_j\right\rangle/\sqrt{N}$ of the interaction matrix G_{jk} of Eq. 2.17, where we identify with $\mathbf{R}_j$ the atomic positions. These modes are associated to a continuum of complex eigenvalues $\omega(\mathbf{k}_{\rm xy})-i\Gamma(\mathbf{k}_{\rm xy})/2=-\Gamma_0\sum_j G_{j0}e^{i\mathbf{k}_{\rm xy}\cdot\mathbf{R}_j}$, whose imaginary part quantifies the rate of photon losses out of the array. To emit in free space, however, each Bloch mode must satisfy the dispersion relation $|\mathbf{k}_{\rm xy}+k_{\rm z}\hat{\mathbf{z}}|=k_0$. As shown in Fig. 2.4 for a square lattice of constant d with $\hat{\mathbf{x}}$-aligned dipoles, those Bloch modes outside the light cone $|\mathbf{k}_{\rm xy}|=k_0$ (red, dashed circle) are then associated to evanescent normal components $k_{\rm z}\in\mathbb{C}^2$, which cannot propagate in the $\hat{\mathbf{z}}$ direction and remain confined inside the array [151]. Since the Brillouin zone is given by $k_{\rm x,y}\leq\pi/d$, the condition $|\mathbf{k}_{\rm xy}|>k_0$ requires $d\leq\lambda_0/\sqrt{2}$.

In addition, it is interesting to study the optical scattering. When illuminated by a plane wave at normal incidence, the light can only excite the

mode $\left|E_{\mathbf{k}_{\mathrm{xy}}=0}\right\rangle$ (with $\mathbf{k}_{\mathrm{xy}}=0$) to conserve the symmetry, which effectively reduces the array to a single-mode system. When this collective mode decays, the output field can be calculated via Eq. 2.17. The atomic array is then equivalent to an optical grating, which from classical optics is characterized by a discrete set of diffraction orders given by $\mathbf{k}_{\mathrm{z}}=\sqrt{k_0^2-|\mathbf{g}_{mn}|^2}$, where $\mathbf{g}_{mn}=(2\pi/d)(m\widehat{\mathbf{x}}+n\widehat{\mathbf{y}})$ are the reciprocal lattice vectors. If the array is subwavelength $d<\lambda_0$, then all the orders become evanescent (i.e. Im $k_{\mathrm{z}}>0$) except $\mathbf{g}_{mn}=0$, thus reducing the problem to transmission or reflection into the same 1D direction $\widehat{\mathbf{z}}$ of the input light[9], as quantified by the complex coefficients t and r. Due to the single-mode nature of this problem, when the input light is resonant at $\omega(0)$ with the collective mode $\left|E_{\mathbf{k}_{\mathrm{xy}}=0}\right\rangle$, the system becomes perfectly reflecting (with $|r|^2=1$) due to perfect destructive interference [149, 150], as experimentally addressed by [171]. More generally, this reflects the lossless nature of this single-mode response, as certified by the relation $|t|^2+|r|^2=1$, which retains valid for any frequency of the input light.

The properties introduced above have a relevant role in Chapter 4, where we analyze the refractive index of a 3D lattice of atoms in terms of 2D planes. Specifically, we show that the key ingredient of single-mode, lossless response can give rise to extreme (both ultra-high and near-zero) and purely real indices of refraction. At the same time, in Chapter 5 we discuss how two (or more) consecutive 2D arrays can be engineered to transmit light with an arbitrary phase shift, acting as the building blocks of an "atomic metalens".

[9] When $d<\lambda_0/2$ a similar argument applies to any incident angle of the input light [150].

Part II

Results

3 - Refractive index of a disordered atomic medium

Chapter Contents

3.1 Introduction

All the optical materials that we know of, with a positive index of refraction at visible wavelengths, universally have an index of order unity $n \sim \mathcal{O}(1)$, either off resonance or closer to resonance [5–12]. Yet, despite the profound implications of an extreme refractive index (as detailed in Section 1.1.1), a deep understanding of the origin of this apparently universal behavior seems to be lacking. Furthermore, this property of real materials is not readily reconciled with the fact that a single, isolated atom exhibits a giant scattering cross-section $\sigma_{\text{sc}} \sim \lambda_0^2$ for photons resonant with an atomic transition of wavelength λ_0 (Fig. 3.1-a), which far exceeds both the physical size of the atom or the typical lattice constant of a solid.

As we discussed in Section 2.1, in standard optical theories [189, 190], the macroscopic index of an atomic medium (Fig. 3.1-b) is constructed

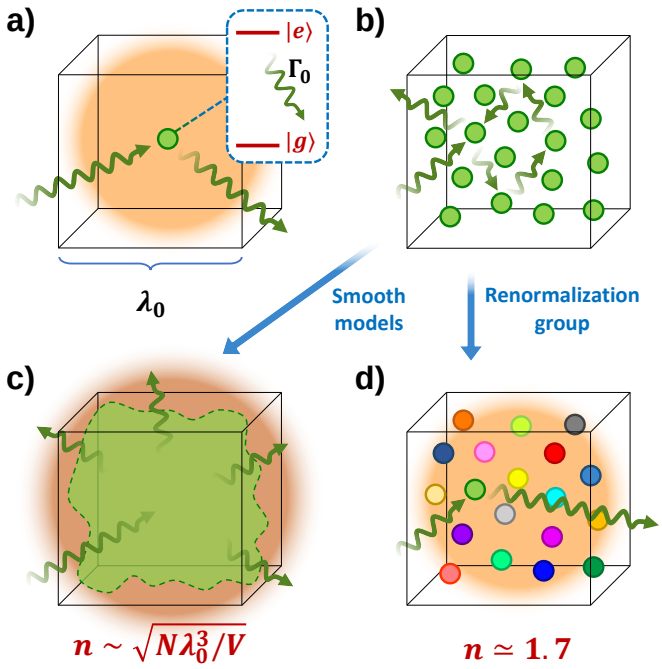

Figure 3.1: Optical response of an atomic medium. a) Illustration of a single atom with a dipole-allowed optical transition between ground and excited states $|g\rangle$ and $|e\rangle$, characterized by a transition wavelength λ_0 and spontaneous emission rate Γ_0. Such an atom exhibits a scattering cross section (illustrated by the shaded region) of $\sigma_{\text{sc}} \sim \lambda_0^2$ for a single resonant photon (wavy green arrows). b) In a dense ensemble with many atoms per cubic wavelength λ_0^3, the scattering of an incident photon can involve multiple scattering and interference between atoms. c) In conventional theories of macroscopic optical response, the atoms are approximated by a smooth medium, and the index is derived from the product of single-atom polarizability and density. The maximum index n near the atomic resonance then scales with atomic density like $n \sim \sqrt{N\lambda_0^3/V}$. d) In our renormalization group theory, we retain multiple scattering and granularity, showing that the optical properties of the ensemble are determined by a hierarchy of nearby atomic pairs that strongly interact via their near fields. These interactions effectively produce an inhomogeneously broadened ensemble, where the amount of broadening scales with density (with the different colors of atoms representing the different resonance frequencies in the figure). An incident photon of a given frequency thus sees only ~ 1 near-resonant atom per reduced cubic wavelength to interact with, regardless of atomic density. This results in a maximum index of $n \approx 1.7$.

from the product of the single-atom polarizability and the atomic density, and around resonance its value $n \sim \sqrt{N\lambda_0^3/V}$ extrapolates to a maximum of $\sim 10^5$ at solid densities (Fig. 3.1-c). It is well-known that this argument

neglects multiple scattering of light and photon-mediated dipole-dipole interactions [169, 191], and substantial work has been devoted to explore their effects on various optical phenomena, as summarized in Section 2.2. In particular, we recall that this includes theoretical and experimental evidence that the optical response of dense gases can be much smaller than standard predictions [153, 159, 169, 174, 192] or even reach limiting values [154, 156–158, 165, 170, 193]. However, an underlying physical explanation is still missing, and our goal here is to understand better the mechanisms that might limit the index even when operating close to resonance.

Specifically, we investigate in detail the optical response of an ideal ensemble of identical, stationary atoms, as a function of density starting from the dilute limit, and well within the regime where the atoms do not interact chemically. The atoms are assumed to be ranomly positioned in space, with a uniform distribution. In large scale numerics (involving up to ~ 25000 atoms, about an order of magnitude larger than comparable works [154, 157–159, 165, 166, 169, 170, 173–176]), we find that the maximum index does not indefinitely grow with density, and saturates to a maximum value of $n \approx 1.7$, when the typical distance between atoms becomes smaller than the length scale associated with the resonant cross section, i.e. $d < \lambda_0$. Furthermore, we introduce an underlying theory based upon strong-disorder RG, which has been a very successful technique to deal with highly varying interaction strengths in a wide variety of condensed matter systems [194–201]. In the context of our particular problem, the combination of strong near-field ($\sim 1/r^3$) optical interactions and random atomic positions enables one to characterize the optical response of the system in terms of a hierarchy of strongly interacting, nearby atomic pairs. The shifts of the resonance frequencies arising from the near-field interactions then effectively yield an inhomogeneously broadened optical medium, where the amount of broadening linearly scales with density. This implies that light of any given wavelength only interacts with at most ~ 1 near-resonant atom per reduced cubic wavelength $\lambda_0^3/(2\pi)^3$, regardless of the physical atomic density, thus limiting the optical response (Fig. 3.1-d).

Our results are potentially significant on a number of fronts. First, in the context of disordered ensembles, they provide a convincing picture of why typical theories for optical response, based upon a smooth density approximation, fail for dense, near-resonant atomic media, due to the important role of granularity and strong interactions of any given atom with a particularly close-by, single neighbour. Furthermore, our results show the promise of a bottom-up approach to understanding the physical limits of refractive index, starting from objects (isolated atoms) whose optical responses

are both huge and exquisitely understood. Separately, the existence of a fundamental mechanism that results in inhomogeneous broadening (i.e. dephasing) and saturation of optical properties at high densities, which occurs even for perfect, stationary atoms, should impose fundamental bounds on the maximum densities and minimum sizes of atom-light interfaces needed to realize high-fidelity quantum technologies. Finally, while we focus here on the linear optical response of a dense atomic medium, we believe that the validity of RG is quite general, and can constitute a versatile new tool for the generally challenging problem of multiple scattering in near-resonant disordered media [158, 159, 165, 169, 170, 175, 182, 192, 202–204], including in the nonlinear and quantum regimes [205].

This chapter is structured as follows. First, we present our large-scale numerical simulations, describing a few implementation details that allow the index to be efficiently calculated, and show that the index eventually saturates with increasing density to a maximum value of $n_{\mathrm{re}} \approx 1.7$. Then, we introduce our RG theory, which highlights the importance of granularity and nearby atomic pairs on the macroscopic optical response, before concluding with an expanded discussion of future interesting directions to investigate.

3.2 Coupled-dipole simulations

We consider a minimal system consisting of N identical, stationary two-level atoms. The atoms are assumed to have an electronic ground and excited state $|g\rangle$, $|e\rangle$, with frequency difference ω_0 and associated wavelength $\lambda_0 = 2\pi c/\omega_0$, and which have an electric dipole transition with a dipole matrix element along a fixed axis (say $\hat{\mathbf{x}}$), as depicted in Fig. 3.1-a. The excited states of the atoms decay purely radiatively, with a rate of Γ_0 for a single, isolated atom. Moreover, we recall that we define the resonant wavevector $k_0 = 2\pi/\lambda_0$, as well as the dimensionless detuning $\Delta \equiv (\omega - \omega_0)/\Gamma_0$ and atomic density $\eta = N/(k_0^3 V)$.

As we are specifically interested in the linear refractive index, it is sufficient to treat atoms in the limit of classical, polarizable, radiating dipoles. In order to investigate the frequency-dependent index $n(\omega)$, we consider that the atoms are driven by a monochromatic, linearly-polarized input beam $\mathbf{E}_{\mathrm{in}}(\mathbf{r},\omega) = E_{\mathrm{in}}(\mathbf{r},\omega)\hat{\mathbf{x}}$, whose polarization aligns with the polarizability axis of the atoms. Each atom j acquires a dipole moment $\mathbf{d}_j(\omega) = d_j(\omega)\hat{\mathbf{x}}$, as a result of being driven by the total field, which consists of the sum of the incident field and fields re-scattered from other atoms, as described by the

coupled-dipole equations of Eq. 2.17, that we introduced in Section 2.3.1.

Although in our regime these equations are formally exact, we already mentioned how their computational complexity fostered the development of simplified, smooth theories (Fig. 3.1-c) for the macroscopic response, such as the MB equations [190] of Eq. 2.10 or the LL model of Eq. 2.13, which introduces the frequency shift $n_{\mathrm{LL}}(\Delta) = n_{\mathrm{MB}}(\Delta + \pi\eta)$. Notably, for an optimum detuning, both models predict a maximum real part of the index that scales as $\sim \sqrt{\eta}$.

3.2.1 Retrieving the index

The equations in Eq. 2.17 are ubiquitously used to model multiple scattering and interference effects involving a moderate number of point-like scatterers. Here, we briefly introduce some key details of our implementation, which allows us to perform simulations on very high atom number and efficiently extract the index.

First, one direct way to extract the complex refractive index of a material would be to take a slab of thickness L and large transverse extent, and investigate the phase shift and attenuation of a quasi-plane-wave incident field upon transmission. We approximately realize such a situation by taking atoms with a fixed density in a cylindrical volume centered around the origin, illuminated by a weakly focused, near-resonant Gaussian beam (see Fig. 3.2). Decomposing the position $\mathbf{r} = \{\mathbf{r}_\perp, z\}$ in terms of a transverse component $\mathbf{r}_\perp$ and axial component z, the beam amplitude within the paraxial approximation is given by $\mathbf{E}_{\mathrm{in}}(\mathbf{r}) = \mathbf{E}_{\mathrm{gauss}}(\mathbf{r}, w_0)$, where

$$\mathbf{E}_{\mathrm{gauss}}(\mathbf{r}, w_0) = E_0 \left(\frac{w_0}{w(z)}\right) \exp\left[-\left(\frac{r_\perp}{w(z)}\right)^2 + ik_0 z + i\varphi(\mathbf{r}, w_0)\right] \widehat{\mathbf{x}}, \tag{3.1}$$

where $w(z) = w_0\sqrt{1+(z/z_{\mathrm{R}})^2}$ describes the transverse extension of the beam, while $w_0 = w(0)$ is the beam waist at the focal plane and $\varphi(\mathbf{r}, w_0) = -\arctan(z/z_{\mathrm{R}}) + k_0 r_\perp^2/\{2z[1+(z_{\mathrm{R}}/z)^2]\}$ accounts for the curvature of the wave-front and for the Gouy phase, assuming $z_{\mathrm{R}} = k_0 w_0^2/2$ [190]. Given that the intensity of the beam drops off rapidly for transverse distances larger than $w(z)$, the parameters are chosen such that $w(z)$ is small compared to the radius of the cylinder, so that diffraction effects from the edges are negligible. Finally we avoid very tight focusing $w_0 \lesssim \lambda_0$, where non-paraxial effects could emerge.

We must also specify a practical definition of index, for a granular system as ours. In particular, since our atoms are purely scattering and have no

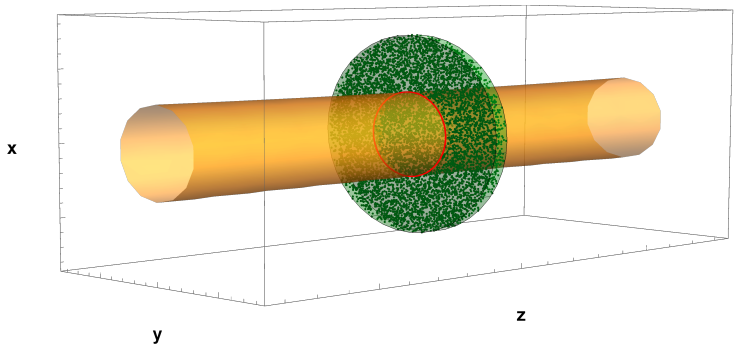

Figure 3.2: Simulated physical system. A cylindrical ensemble of randomly distributed atoms (green points) is illuminated by a z-directed Gaussian beam, whose beam waist $w(z) \gg \lambda_0$ is represented in orange. The transverse radius of the cylinder is chosen to be much larger than the beam waist, to avoid edge diffraction.

absorption, it is well-known [175, 202, 203, 206] that for a fixed random spatial configuration, an input as in Fig. 3.2 produces a complex "speckle" pattern in the outgoing intensity when the system is optically dense, due to multiple scattering and interference, as exemplified in the introduction of this thesis with Fig. 2.1. To isolate the part of the field that possesses a well-defined phase relationship with the incident field from realization to realization, we project the total field $\mathbf{E}(\mathbf{r})$ (that we defined in Eq. 2.17) back into the same Gaussian mode as the input, as can be experimentally enforced by recollecting the transmitted light through a single mode fiber. The physical and mathematical meaning of this process is better detailed in Appendix A. This results in a transmission coefficient $t(\Delta)$ given by [152, 170]

$$t(\Delta) = 1 + \frac{3i}{(w_0 k_0)^2} \sum_{j=1}^{N} \frac{E_{\text{in}}^*(\mathbf{r}_j)}{E_0} c_j(\Delta), \tag{3.2}$$

where E_0 is the input field amplitude at the beam focus. Here, for convenience, we have defined re-scaled dipole amplitudes $c_j = \Gamma_0 \beta_j / \Omega_0$, with β_j representing the excited-state coefficients defined in the coupled-dipole equations of Eq. 2.17. Similar considerations can be made to infer the reflection coefficient

$$r(\Delta) = \frac{3i}{(w_0 k_0)^2} \sum_{j=1}^{N} \frac{E_{\text{in}}(\mathbf{r}_j)}{E_0} c_j(\Delta). \tag{3.3}$$

Within this dimensionless formalism the coupled-dipole equations of Eq. 2.17

become

$$-\Delta c_i(\Delta) - \sum_{j=1}^{N} G_{ij} c_j(\Delta) = \frac{E_{\text{in}}(\mathbf{r}_i, \omega_0)}{E_0}, \tag{3.4}$$

where we recall that we define $G_{ij} \equiv (3\pi/k_0)\hat{\mathbf{x}} \cdot \bar{\bar{\mathbf{G}}}(\mathbf{r}_i, \mathbf{r}_j, \omega_0) \cdot \hat{\mathbf{x}}$ and $G_{jj} = i/2$, which coincides with the single-atom decay rate in units of Γ_0, while regularizing the divergent self-energy associated with the real part of $\bar{\bar{\mathbf{G}}}$. Note that, for simplicity, the Green's function $\bar{\bar{\mathbf{G}}}(\mathbf{r}_i, \mathbf{r}_j, \omega_0)$ is only evaluated at the atomic resonance frequency, in order to ease the computational cost as the detuning is varied. We remind that ignoring the dispersion of $\bar{\bar{\mathbf{G}}}$ is an excellent approximation for near-resonant atoms, as the optical dispersion and delay of such a system is dominated by the atomic response itself rather than from the vacuum [207]. Similarly, we approximate the near-resonant input field as $E_{\text{in}}(\mathbf{r}_i, \omega) \simeq E_{\text{in}}(\mathbf{r}_i, \omega_0)$.

The expression in Eq. 3.2 represents a useful closed-form definition of the transmission coefficient $t(\Delta)$, which avoids a numerically expensive point-by-point evaluation of the scattered field $\mathbf{E}(\mathbf{r}, \omega)$, as nominally prescribed by Eq. 2.17. We can extrapolate the complex index of refraction $n(\Delta)$ from the relation

$$\langle t(\Delta) \rangle = \exp\left\{ i \left[n\left(\Delta\right) - 1 \right] k_0 L \right\}. \tag{3.5}$$

where the averages are performed over $\sim 10^3 - 10^4$ sets of random positions, for each fixed density. Unlike in a smooth medium, we have that $|\langle t(\Delta) \rangle|^2 \neq \langle |t(\Delta)|^2 \rangle$. Nevertheless, our definition of the index coincides with that often used within atomic physics (e.g. in phase contrast or absorption imaging of a Bose-Einstein condensate [208, 209]).

3.2.2 Numerical results

In Fig. 3.3, we plot our numerical results for the real and imaginary parts of $n(\Delta)$, as a function of the input field detuning Δ, and for various densities. For comparison, we also plot the index as predicted by the MB equations, which starts to appreciably deviate from the full numerical results for dimensionless densities $\eta \gtrsim 0.1$. Interestingly, for sufficiently high densities, we observe that the computed spectra collapse onto the same curve when plotted as a function of the re-scaled detuning Δ/η, as shown in the insets of Fig. 3.3, which include all plots in the range $2 \lesssim \eta \lesssim 3$. The invariance of $n(\Delta/\eta)$ for $\eta \gtrsim 2$ directly indicates that both the maximum real index and the attenuation per unit length acquire fixed values with increasing density, and that density only determines a linear broadening in the spectra. Notably, the maximum real index saturates to a "real-life" value of ~ 1.7,

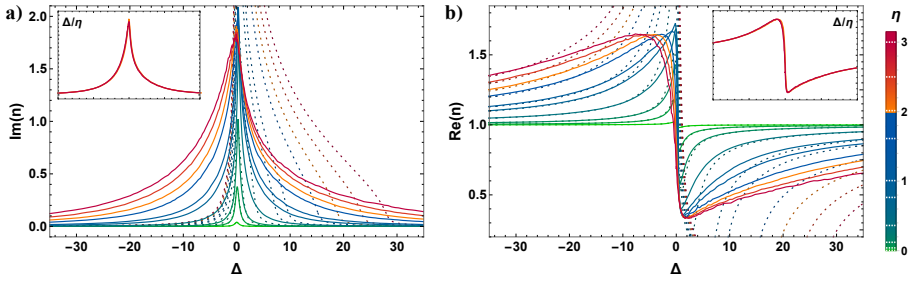

Figure 3.3: Frequency-dependent refractive index for different atomic densities. The solid lines portray the imaginary (subfigure a) and real (subfigure b) part of the refractive index versus dimensionless detuning Δ, obtained through Eq. 3.2, while the dotted lines show the MB predictions. The colors denote different atomic densities (colorbar on right), with the specific values indicated by the dotted white lines. The refractive index is inferred by averaging the complex transmission coefficient $t(\Delta)$ over $\sim 10^3 - 10^4$ atomic configurations. Other system parameters are: thickness $L = 0.4\lambda_0$, transverse radius $5 \leq R_{\mathrm{cyl}}/\lambda_0 \leq 7$, beam waist $2.5 \leq w_0/\lambda_0 \leq 3$. The insets show the curves at the 3 highest densities as a function of the rescaled detuning Δ/η.

in contrast to the indefinite growth predicted by both MB and LL.

We note that a number of experiments involving dense cold atomic clouds have observed both a saturation of the index [154, 156, 158] and the emergence of an anomalous broadening of the linewidth [153–155, 157, 159], including a linear scaling with density [156, 158]. A maximum index of $n \approx 1.26$ has also been observed in experiments involving dense, hot atomic vapours [193], which has been attributed to atomic collisions. However, while complex collision dynamics necessitate semi-phenomenological models [210], here, our mechanism for saturation is quite fundamental, and occurs even for perfectly identical, stationary atoms.

3.2.2.1 Macroscopic behaviour of the index

In this technical subsection, we validate the independence of the calculated index from the thickness L, which is implicitly assumed in Eq. 3.5. We also discuss how, alternatively, one might assume that the calculated $\langle t(\Delta)\rangle$ approximately coincide with the finite-slab Fresnel coefficients for a smooth material [211], which would produce an alternative way to extrapolate the index, yielding closely similar results.

Our operative definition of the complex index of refraction is given by Eq. 3.5. Since the refractive index is an intensive property by definition, it must not depend upon the thickness L that we choose in our numerics.

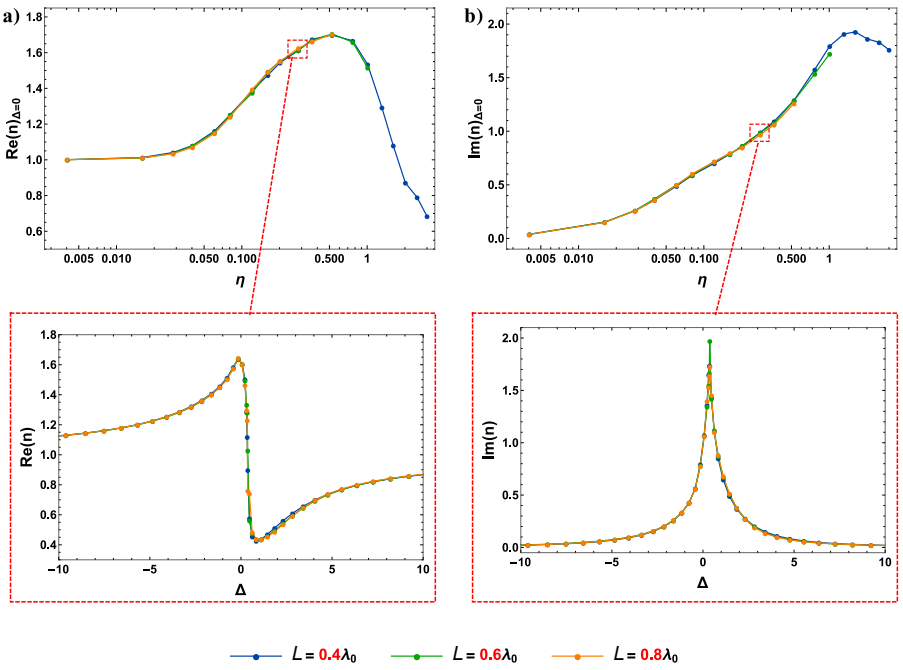

Figure 3.4: Independence of the refractive index from the thickness of the ensemble. Given the physical system of Fig. 3.2 (with $w_0 = 2.5\lambda_0$, $R_{\rm cyl} = 5\lambda_0$), we compare the resonant ($\Delta = 0$) refractive index as a function of the density, for various ensemble thicknesses: $L = 0.4\lambda_0$ (in blue), $L = 0.6\lambda_0$ (in green) and $L = 0.8\lambda_0$ (in orange). Subfigures a) and b) illustrate the real and imaginary parts of the index, respectively. The insets show the full spectra $n(\Delta)$ at a fixed density $\eta \simeq 0.28$. All data are obtained by averaging $\langle t(\Delta)\rangle$ over > 1000 configurations.

Here, we show that our operative definition satisfies this condition. We consider the same physical system described in Fig. 3.3, with $w_0 = 2.5\lambda_0$, $R_{\rm cyl} = 5\lambda_0$ and different values of the thickness L. By applying Eq. 3.2 and Eq. 3.4, we compute the resonant ($\Delta = 0$) refractive index for growing values of the density η, and we plot its real (imaginary) part in Fig. 3.4-a(b). The simulated values of the thickness are: $L = 0.4\lambda_0$ (as Fig. 3.3, here in blue), $L = 0.6\lambda_0$ (in green) and $L = 0.8\lambda_0$ (in orange). Moreover, for the point at $\eta \simeq 0.28$, we evaluate the full spectra $n(\Delta)$, as represented in the insets of the figure. All curves show the same behaviour, independently of L, both on resonance and when varying the detuning.

From the standpoint of classic optics, given a dielectric slab of length

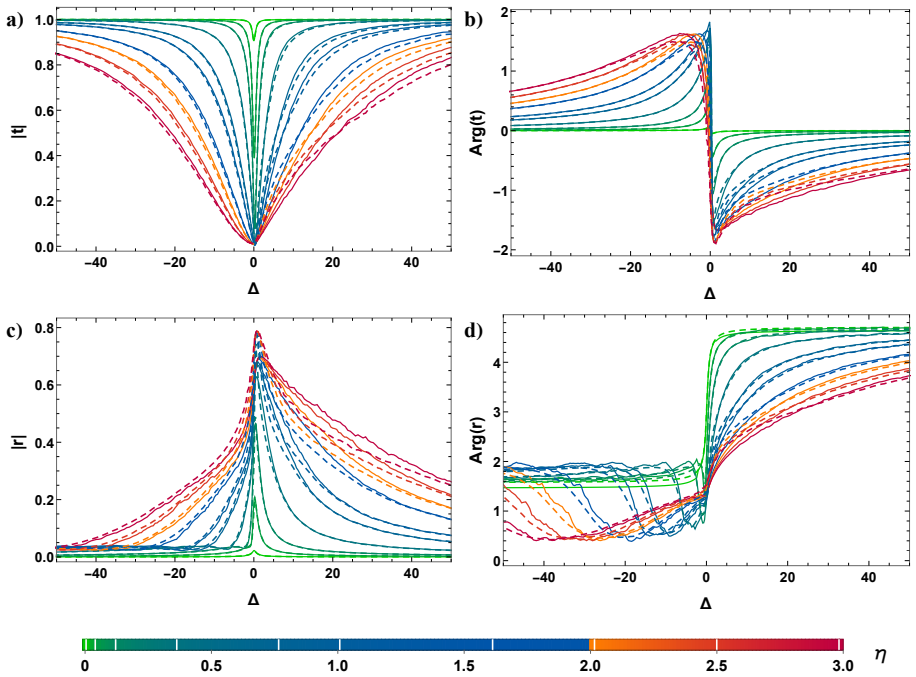

Figure 3.5: Recovering the reflection and transmission coefficients via Fresnel law. We solve the coupled-dipole equations of Eq. 3.2, Eq. 3.3 and Eq. 3.4 to compute the transmission and reflection of the atomic medium, which are averaged over many configurations (solid lines). Each color relates to a different value of the atomic density, as denoted by the color bar (the white marks identify the exact densities of the simulations). We then compute the refractive index $n(\Delta)$ from the phase of transmission, by means of Eq. 3.5 (similarly to Fig. 3.3). To verify the consistency of this prediction, we plug the value of $n(\Delta)$ inside the Fresnel laws of Eq. 3.6, which describe in classical optics the transmission and reflection of a macroscopic slab with index $n(\Delta)$, and plot these results with dashed lines.

L and (complex) refractive index $n(\Delta)$, the Fresnel equations predict

$$t_{\mathrm{Fr}}(\Delta) = \frac{4n(\Delta)e^{in(\Delta)k_0L}}{[1+n(\Delta)]^2 - e^{2in(\Delta)k_0L}[n(\Delta)-1]^2},$$
$$r_{\mathrm{Fr}}(\Delta) = \frac{[n(\Delta)^2-1]\left(e^{2in(\Delta)k_0L}-1\right)}{[1+n(\Delta)]^2 - e^{2in(\Delta)k_0L}[n(\Delta)-1]^2}, \tag{3.6}$$

due to the index mismatch at the interfaces with free space. As a consistency check of our predictions for $n(\Delta)$ (which were shown in Fig. 3.3), we plug these values into the Fresnel equations, aiming to reproduce the initial transmission and reflection resulting from the coupled-dipole simulations of

Eq. 3.2, Eq. 3.3 and Eq. 3.4. This is shown in Fig. 3.5, where the solid lines represent the values of $\langle t(\Delta)\rangle$ and $\langle r(\Delta)\rangle$ computed by solving the coupled-dipole equations (and averaging over many configurations), while the dashed lines display the Fresnel predictions.

Their agreement confirms our interpretation of the index. Physically, our simplified method is valid because the non-negligible, near-resonant absorption $n_{\rm im} > 0$ suppresses the multiple bouncing inside the slab between its two interfaces, so that the Fresnel transmission in Eq. 3.6 approximately reduces to Eq. 3.5.

3.3 Renormalization group approach

The analytic description of multiple scattering is a complex problem, even in the linear regime. Differently from diagrammatic approaches [212, 213] or from other attempts to treat the dipole-dipole interactions with a mean-field models (such as the case of the "cooperative Lamb shift" [214]), we focus on a non-perturbative analysis of the strongly correlated atomic system. This is necessary in the high-density regime where the average inter-atomic distance is much smaller than the size of the atomic cross section.

3.3.1 Physical intuition and definition of the scheme

Our RG theory is based upon the key intuition gained in the collective scattering of just two atoms, to build up an understanding of the many-atom problem in a hierarchical manner. To be specific, let us consider the problem of two identical atoms, whose distance is much smaller than a wavelength, $\rho_{12} \equiv k_0|\mathbf{r}_1 - \mathbf{r}_2| \ll 1$. Applying Eq. 3.2 and Eq. 3.5, we can calculate the imaginary part of the "index" of the two-atom system, as illustrated in Fig. 3.6-a. One can see that the characteristic two-atom spectrum (blue line) is not twice the response of a single, isolated atom (green dashed curve), but instead consists of two, well-separated peaks with different linewidths and shifted resonances.

To understand this behavior, we consider the normal modes of the two-atom system, as encoded in the eigenstates of the dimensionless matrix G, whose elements G_{ij} were introduced in Eq. 3.4. When $\rho_{12} \ll 1$, G is dominated by its off-diagonal components $G_{12} = G_{21}$, and in particular, by the purely real $1/\rho_{12}^3$ near-field term (which we denote by $G_{12}^{\rm near}$). Specifically, in spherical coordinates $\boldsymbol{\rho}_{ij} \equiv \rho_{ij}\,(\cos\theta\,\widehat{\mathbf{x}} + \sin\theta\cos\phi\,\widehat{\mathbf{y}} + \sin\theta\sin\phi\,\widehat{\mathbf{z}})$, one

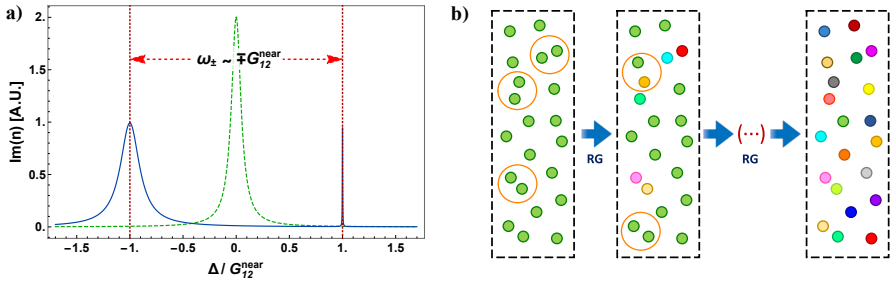

Figure 3.6: Renormalization group scheme. a) Representative optical response of two identical atoms separated by a distance $\rho_{12} \ll 1$. Here, we plot the absorption spectrum (blue curve), which consists of two well-separated Lorentzians. The positions of the resonances are given by $\sim \mp G_{12}^{\text{near}}$, where $G_{12}^{\text{near}} \propto 1/\rho_{12}^3$ is the near-field component of the Green's function. To compare, we also plot twice the response of a single, isolated atom (green dashed line). b) Pictorial representation of the RG scheme for a many-atom system. At each step of the RG flow the nearby pairs (identified by orange circles) that mostly strongly interact via their near fields are identified, and replaced with atoms with different resonance frequencies (indicated by different colors) in such a way to produce an equivalent optical response. At the end of the RG process (last panel) the overall system is equivalent to an inhomogeneously broadened ensemble of weakly interacting atoms.

obtains

$$G_{ij}^{\text{near}} = \frac{3}{4\rho_{ij}^3}(-1 + 3\cos^2\theta). \tag{3.7}$$

This describes the strong, coherent, near-field coupling between the two dipoles. This produces symmetric and anti-symmetric eigenstates whose dimensionless normal mode frequencies (real parts of the eigenvalues) are shifted as $\omega_\pm \approx \mp G_{12}^{\text{near}}$, and align with the resonant peaks seen in Fig. 3.6-a. Given that Im G is also a 2×2 matrix with equal diagonal entries and equal off-diagonal entries, its eigenstates are also the same symmetric and anti-symmetric modes. This results in renormalized linewidths for these modes (given by the eigenvalues of Im G) of $\Gamma_+ \approx 2$ and $\Gamma_- \approx \rho_{12}^2$, which is simply the two-atom limit of the famous Dicke superradiance model [178]. The key insight is that due to the large splitting, the total response in Fig. 3.6-a is characterized by two well-separated resonances, which, although arising from the strong interaction of identical atoms, resemble the case of two, inhomogeneous and *non-interacting* atoms, which were assigned these resonance frequencies and linewidths to start. This concept is at the heart of the RG approach for the many-atom case.

We now discuss how strong, coherent $1/\rho_{ij}^3$ near-field interactions in a many-atom system can be treated, by successively replacing strongly inter-

acting pairs by optically equivalent, non-interacting atoms. Here, we will focus on the main conceptual steps of our RG scheme, while additional justification of this scheme can be found in Section 3.3.3. Given the discussion above, we anticipate that the scheme generates an optically equivalent ensemble containing atoms with different renormalized resonance frequencies ω_i. Contrary to the two-atom case, however, the linewidths will *not* be renormalized within our RG scheme (see Section 3.3.3). At any step of the RG flow, each pair of atoms can either interact, or not, through the near-field coupling, depending on the previous RG steps. The normal modes of such a system are given by the eigenstates of the generalized $N \times N$ matrix $\mathcal{M} = \mathrm{diag}(\boldsymbol{\omega}) - \tilde{G}$, where the elements $\tilde{G}_{ij}$ are defined as $\tilde{G}_{ij} = \mathcal{L}_{ij} G_{ij}^{\mathsf{near}} + (G_{ij} - G_{ij}^{\mathsf{near}})$. Here, $\mathrm{diag}(\boldsymbol{\omega})$ is a diagonal matrix containing the individual resonance frequencies $\boldsymbol{\omega} = (\omega_1, \ldots, \omega_N)$, while $\mathcal{L}_{ij} = 1$ or 0 dictates whether pair i, j is allowed to interact via the near field. At the beginning of the RG process, the optically equivalent ensemble corresponds to the physical one, and thus all atoms are allowed to interact ($\mathcal{L}_{ij} = 1$ for all pairs) and $\omega_i = \omega_0$. In three dimensions, the $1/\rho^3$ scaling of the near-field interaction implies that if an atom has a particularly close-by and near-resonant neighbour, this pair will interact much more strongly between themselves than with any other nearby atoms [194]. Suppose that atoms i, j (with $\mathcal{L}_{ij} = 1$) are identified as the most strongly interacting pair, by a prescription given below. Then, we can re-write $\mathcal{M}$ as $\mathcal{M} = \mathcal{M}_{\mathsf{pair}} + (\mathcal{M} - \mathcal{M}_{\mathsf{pair}})$, where the only non-zero elements of $\mathcal{M}_{\mathsf{pair}}$ involve atoms i, j. This effective 2×2 matrix reads

$$\mathcal{M}_{\mathsf{pair}} = \langle \omega \rangle_{ij} \mathbb{I} + \begin{pmatrix} \delta\omega_{ij} & -G_{ij}^{\mathsf{near}} \\ -G_{ij}^{\mathsf{near}} & -\delta\omega_{ij} \end{pmatrix}, \tag{3.8}$$

where $\langle \omega \rangle_{ij} = (\omega_i + \omega_j)/2$ and $\delta\omega_{ij} = (\omega_i - \omega_j)/2$, and where we have included the coherent near-field interaction in $\mathcal{M}_{\mathsf{pair}}$. The remaining far-field interactions between atoms i and j, as well as near- and far-field interactions involving all other atoms, are included in $(\mathcal{M} - \mathcal{M}_{\mathsf{pair}})$. The large near-field interaction motivates diagonalizing $\mathcal{M}_{\mathsf{pair}}$ first, while treating $(\mathcal{M} - \mathcal{M}_{\mathsf{pair}})$ as a perturbation.

From the structure of $\mathcal{M}_{\mathsf{pair}}$, we define the pairwise interaction parameter $\mathcal{K}_{ij} = \mathcal{L}_{ij} |G_{ij}^{\mathsf{near}}| / (|\delta\omega_{ij}| + 1)$. A large value of $\mathcal{K}_{ij}$ (which requires $\mathcal{L}_{ij} = 1$) implies that the strong near-field interaction is able to strongly split the original resonances, including overcoming any possible differences in resonance frequencies $\delta\omega_{ij}$ of the pair. We thus identify the most strongly

interacting pair as that with the largest value of $\mathcal{K}_{ij}$, as pictorially depicted in the first panel of Fig. 3.6-b. Diagonalization of $\mathcal{M}_{\text{pair}}$ results in two, new interacting resonance frequencies $\omega_{\pm} = \langle\omega\rangle_{ij} \mp \sqrt{\delta\omega_{ij}^2 + (G_{ij}^{\text{near}})^2}$. We can then obtain an approximately equivalent system by replacing the two original resonance frequencies $\omega_{i,j}$ with the new values $\omega_{\pm}$ (second panel of Fig. 3.6-b). While the resulting normal modes are in principle delocalized between atoms i, j, to facilitate the RG, we randomly assign ω_+ to either atom i or j, while ω_- is then assigned to the other atom (see Appendix B on the issue of replacing atoms i, j with two new atoms placed at the midpoint of the original locations). This new system is described by a renormalized interaction matrix $\mathcal{M}_{\text{eff}} = \text{diag}(\boldsymbol{\omega}_{\text{eff}}) - \tilde{G}_{\text{eff}}$, where $\boldsymbol{\omega}_{\text{eff}} = (\omega_1, \ldots, \omega_+, \ldots, \omega_-, \ldots \omega_N)$ contains the two renormalized resonance frequencies, and where $\tilde{G}_{\text{eff}}$ includes the new set of allowed near-field interactions $\mathcal{L}_{\text{eff}}$, which both forbid the renormalized pair from interacting again (i.e. $\mathcal{L}_{ij}^{\text{eff}} = 0$) and prevent any backflow of the RG process (see Appendix B for more details). The RG process can be iteratively repeated by identifying, at each step, the most strongly interacting pairs, and ends once $\mathcal{K}_{ij} \leq \mathcal{K}_{\text{cut-off}} \sim 1$, i.e. when all strong near-field interactions have been removed. In the numerics presented here, we take a cutoff parameter of $\mathcal{K}_{\text{cut-off}} = 1$. Other choices result in minor quantitative corrections, while the overall conclusions remain the same. The final result, as suggested in the third panel of Fig. 3.6-b, is that the original, homogeneous system can be mapped to an optically equivalent system that is inhomogeneously broadened, with a smooth probability distribution of resonance frequencies $P(\omega_{\text{eff}})$.

3.3.2 Results of the renormalization

To validate the RG approach, we can use Eq. 3.2 and Eq. 3.4 (with the near-field interactions of renormalized atoms suitably removed, see Appendix B) to calculate the maximum real index (optimized over detunings) as a function of density η of the ensemble with renormalized resonance frequencies. This is plotted in Fig. 3.7-a (green), along with exact numerical simulations (blue) of Eq. 3.2 for the original system of identical atoms. These curves show good agreement for all densities, and in particular, reveal a maximum index of $n \approx 1.7$ at high densities. For comparison, the maximum index of the MB and LL equations (orange) increase indefinitely with density.

Furthermore, motivated by our previous observation that high-density spectra collapse onto the same curve when the detuning is rescaled by density (insets of Fig. 3.3 and Fig. 3.7-a), in Fig. 3.7-b, we plot the rescaled probability distribution of effective resonance frequencies $P(\omega_{\text{eff}}/\eta)$

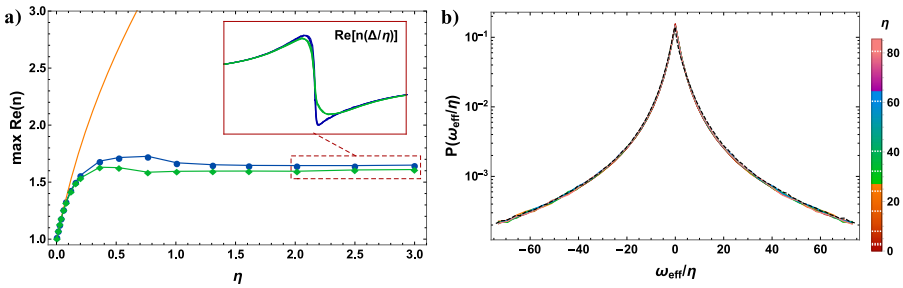

Figure 3.7: Renormalization group analysis. a) Comparison between the maximum real refractive index predicted by the full coupled-dipole simulations of identical atoms (blue points), and index of the equivalent, inhomogeneously broadened ensemble predicted by RG (green). For each value of density, the maximum index is obtained by optimizing over detuning. For comparison, the MB and LL models both predict a maximum index given by the orange curve. The inset compares the rescaled spectra Re $n(\Delta/\eta)$ of the RG (green) and full coupled-dipole (blue) simulations, given the points at densities $\eta \gtrsim 2$. b) Rescaled probability distribution of effective, inhomogeneously broadened resonance frequencies $P(\omega_{\text{eff}}/\eta)$ obtained from the application of the RG scheme. Given 9 different values of the density η (ranging from $\eta \approx 2.5$ up to $\eta \approx 80$), the distributions of effective resonance frequencies are plotted with a different color, according to the bar on the right. The exact values chosen for the curves are emphasized by dotted white lines in the color-bar. The curves at $\eta \approx 2.5$ and $\eta \approx 3$ are calculated using the cylindrical system studied in Fig. 3.3 (with thickness $d = 0.4\lambda_0$ and transverse radius $l_{\text{cyl}} = 5\lambda_0$), while the distributions $P(\omega_{\text{eff}}/\eta)$ at densities $\eta > 3$ are evaluated using a spherical geometry of radius $r_{\text{sph.}} = 0.55\lambda_0$. Finally, for the case of density $\eta \approx 3$ we plot (black dashed curve) the many-atom distribution of the eigenvalues of the near-field matrix $-G_{\text{near}}$ (also rescaled by a factor of $1/\eta$ for consistency), as discussed further in Section 3.3.3. All distributions are obtained by accumulating results from ~ 100 different configurations of atomic positions.

predicted by RG. For all densities considered ($2.5 \lesssim \eta \lesssim 80$), we see that a single universal curve results, i.e. the amount of broadening grows directly with density. Based on this curve, we find that the number of near-resonant atoms per reduced cubic wavelength $(\lambda_0/2\pi)^3 = k_0^{-3}$, within a range $\pm\Gamma_0$ of the original atomic resonance frequency, is approximately ~ 0.3. The limited number of near-resonant atoms for light to interact with, regardless of how high the physical density is, directly explains the saturation of the maximum achievable index. We note that obtaining $P(\omega_{\text{eff}})$ by RG does not require solving the coupled equations of Eq. 3.4, but only the diagonalization of 2×2 pairwise matrices, and we can calculate this distribution for much higher densities up to $\eta \sim 80$. Furthermore, as RG only involves the "short-range" near-field interaction (see Eq. 3.8), we expect the rescaled distribution to

be unique in the bulk of the atomic medium. That is, it should not depend sensitively on the specific geometry, provided that the system is sufficiently large that boundary effects are negligible. In Fig. 3.7-b, the curves for $\eta \leq 3$ are obtained by a cylindrical geometry (the highest densities that we can compare to full coupled-dipole simulations, as in Fig. 3.7-a). For higher densities $\eta > 3$, when comparing with coupled-dipole simulations is no longer feasible, the extreme aspect ratio of the cylindrical geometry makes it inefficient to explore significantly higher densities using RG. We then find it more efficient to switch to atoms within a spherical geometry, which has the smallest surface area to volume ratio.

Within the language of RG, the universal distribution $P(\omega_{\text{eff}}/\eta)$ constitutes the (numerically obtained) fixed point, as the interaction parameter of a system flows toward $\mathcal{K}_{ij} \to 1$. While it might be desirable to write down and analytically solve the RG flow equation for $P(\omega_{\text{eff}})$, this appears quite challenging in our case. This is because $\mathcal{K}_{ij}$ not only depends on the distance between atoms, but also their spatial orientation (as the near field is anisotropic) and the difference in resonance frequencies.

As mentioned earlier, it is rather inconvenient to derive key optical properties of a system, like index, by solving a set of equations (Eq. 3.4) as large as the number of particles. At the same time, the RG approach clearly shows why conventional models (such as MB and LL) that treat atoms as a smooth medium fail at high densities [166, 169, 173], since the optical properties depend highly on granularity and on the strong interaction between an atom and a single, particularly close-by neighbor. Interestingly, RG also provides a basis to develop a more accurate smooth medium model. In particular, after the system is mapped to an inhomogeneously broadened distribution, $P(\omega_{\text{eff}})$, where near-field interactions and the influence of single neighbors are seen to be strongly reduced, one can finally apply a smooth medium approximation. Specifically, the MB equation (i.e. Eq. 2.10) for index can be readily generalized to an inhomogeneously broadened ensemble

$$n(\Delta) = \sqrt{1 + 3\pi\eta \int \frac{P(\omega_{\text{eff}})}{-\Delta + \omega_{\text{eff}} - i/2} d\omega_{\text{eff}}}. \tag{3.9}$$

Substituting the distribution found in Fig. 3.7-b, at high densities $\eta \gg 1$, this equation predicts a maximum index of $n \approx 1.8$, in qualitative agreement with full results. We stress that the emergence of a finite bound to the maximum index predicted by Eq. 3.9 can be directly related to the invariance of the distribution $P(\omega_{\text{eff}}/\eta)$, and thus to the linear growth of broadening with density.

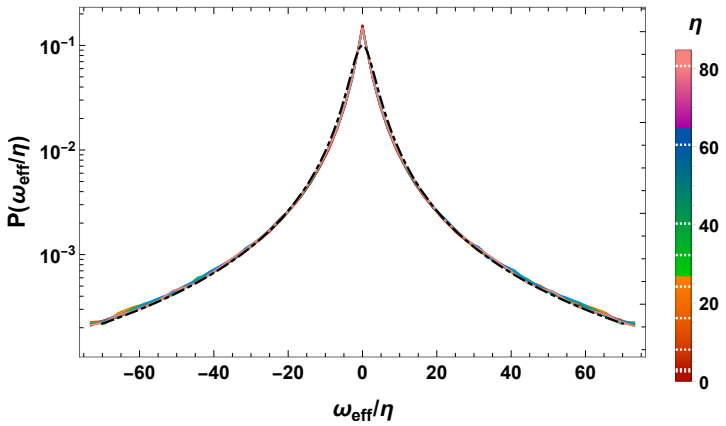

Figure 3.8: Fitting the RG distribution $P(\omega_{\text{eff}}/\eta)$ with a Lorentzian. The solid, colored lines show the rescaled, RG distributions $P(\omega_{\text{eff}}/\eta)$ as equally represented in Fig. 3.7-b. Here, the black, dot-dashed line is a Lorentzian fit of the universal function $P(\omega_{\text{eff}}/\eta)$.

This can be intuitively visualized by approximating the RG distribution with a Lorentzian function $P(\omega_{\text{eff}}) \approx 1.1\eta/(\omega_{\text{eff}}^2 + 10.8\,\eta^2)$ (via least-square fitting), which simplifies Eq. 3.9 to $n(\Delta) \approx \sqrt{1 + 3\pi/[-(\Delta/\eta) - i\pi]}$. The validity of this approximation is addressed in Fig. 3.8.

3.3.3 Microscopic justification of the scheme

In the previous sections, we have established that our RG procedure reproduces well the dependence of refractive index on density. We now present additional numerical and physical arguments that justify this approach and its approximations. Casual readers can consider skipping this section and jump to Section 3.4. In this section, we will specifically answer the following questions:

1. Strictly speaking, RG is an approximate diagonalization of the many-atom near-field interaction matrix G_{near}, in terms of pairwise blocks. In sight of that, how well does our RG prescription reproduce the entire eigenvalue distribution of G_{near}?

2. In our RG prescription, the collective symmetric and anti-symmetric modes of two strongly interacting atoms are replaced by two new effective atoms with electric dipole transitions and modified resonance frequencies. However, this seemingly ignores the possibility that these modes (in particular the anti-symmetric one) could have a higher order multipolar character. Then, why is such a replacement valid?

3. As a related point, these collective modes can be renormalized again if they strongly interact with a third nearby atom. As a higher order multipolar mode can have a different scaling of the near field ($\sim 1/\rho^4$ in the case of the anti-symmetric mode), why does our replacement scheme with an electric dipole transition and a $\sim 1/\rho^3$ near-field interaction work?

4. Our RG prescription focuses on the strong interaction between nearby pairs due to the near field, but the $\sim 1/\rho$ far field associated with a radiating dipole might suggest that the large number of atoms *far away* from a given atom might have a dominant effect in the interactions. What justifies treating the near field first over the far field?

5. As seen in the case of just two interacting atoms (Fig. 3.6-a), both the resonance frequencies and linewidths of the collective modes are modified. Thus, why is it incorrect to renormalize both resonance frequencies and linewidths pairwise in the many-atom problem?

6. In the coupled-dipole numerics of Fig. 3.3, we choose a cylindrical shape of the atomic medium, to minimize the computational cost of the simulations. When calculating the RG distribution $P(\omega_{\text{eff}})$, as in Fig. 3.7-b, we instead opt for a spherical ensemble for densities $\eta > 3$. How do these two scenarios relate? Is the "universal" function $P(\omega_{\text{eff}})$ dependent on the system shape?

3.3.3.1 Comparison with eigenvalue distribution

First, while we have previously focused on the observable quantity of refractive index, we note that mathematically, the RG approach is an attempt to approximately diagonalize the many-atom, near-field interaction matrix $G_{ij}^{\text{near}} = 3(-1 + 3\cos^2\theta)/(4\rho_{ij}^3)$, in terms of pairwise blocks. We can thus test its accuracy by comparing the probability distribution of effective resonance frequencies $P(\omega_{\text{eff}})$ obtained by RG, with the probability distribution of the eigenvalues of $-G_{\text{near}}$ obtained by exact diagonalization of a many-atom, dense system. A remarkable agreement can be observed in Fig. 3.7-b, where the rescaled distribution of effective resonances $P(\omega_{\text{eff}}/\eta)$ is compared with the eigenvalue distribution of $-G_{\text{near}}$ (also rescaled by the density, black dashed curve), as calculated for the highest feasible density $\eta \approx 3$ of our cylindrical system. We separately checked that different (higher) densities and different geometries give similar results. Although subtle, we point out for future work the presence of a slight asymmetry

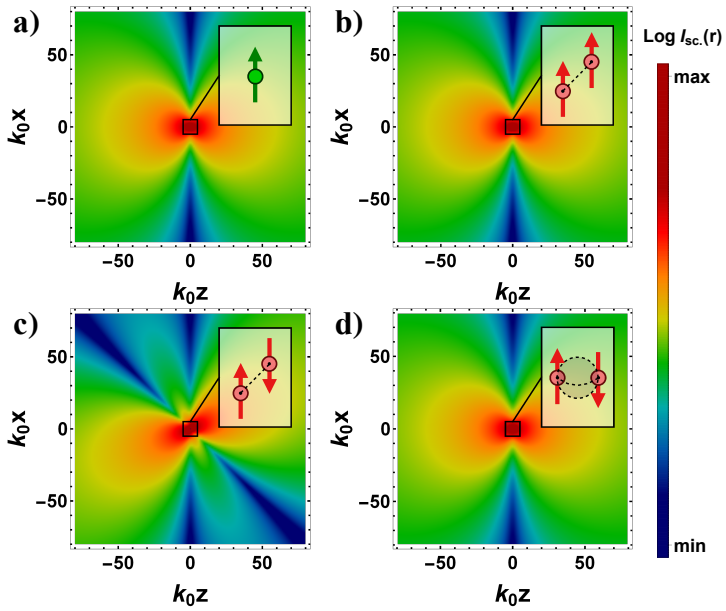

Figure 3.9: Radiation pattern of a single dipole, compared to that of two in-phase or out-of-phase dipoles. a) Given an isolated dipole $\mathbf{d}$ of fixed dipole amplitude d_0 and direction $\widehat{\mathbf{x}}$, which is placed at $\boldsymbol{\rho} = 0$ and radiates light at the frequency ω_0, we plot the intensity of the radiated field $I_{\text{sc.}}(\mathbf{r}) = |\mu_0\omega_0^2\bar{\bar{\mathbf{G}}}(\mathbf{r},\omega_0)\cdot\mathbf{d}|^2/(2\mu_0 c)$ in the $\widehat{\mathbf{x}}$-$\widehat{\mathbf{z}}$ plane, with the value indicated in the colorbar. b-c) Radiation pattern $I_{\text{sc.}}(\mathbf{r}) = |\mu_0\omega_0^2\sum_{j=1,2}\bar{\bar{\mathbf{G}}}(\mathbf{r}-\mathbf{r}_j,\omega_0)\cdot\mathbf{d}_j|^2/(2\mu_0 c)$ for two near-positioned dipoles of fixed amplitude d_0 and direction $\widehat{\mathbf{x}}$, oscillating either in-phase (b) or out-of-phase (c) with one another (i.e. $\mathbf{d}_1 = \pm\mathbf{d}_2 = d_0\widehat{\mathbf{x}}$), and placed at positions $\boldsymbol{\rho}_1 = -\boldsymbol{\rho}_2 = 0.1(\widehat{\mathbf{x}}+\widehat{\mathbf{z}})/\sqrt{2}$. d) Intensity radiated by two out-of-phase dipoles averaged over all possible inter-atomic orientations, keeping fixed the mutual distance $|\boldsymbol{\rho}_1 - \boldsymbol{\rho}_2| = 0.2$. This pattern closely resembles that of a single oscillating dipole.

in the exact eigenvalue spectrum around $\omega_{\text{eff}} = 0$, which doesn't appear in the RG-derived distribution $P(\omega_{\text{eff}})$. This might arise from higher order corrections to RG (e.g. rare triplets of nearly equidistant atoms, where the pairwise picture fails).

3.3.3.2 Multipolar nature of collective modes

Even if RG accurately predicts the resonance frequencies of a strongly interacting pair (e.g., the positions of the resonant peaks in Fig. 3.6-a), one can wonder what is the justification of associating these two collective modes with two new individual atoms, which we implicitly assumed up to now to be characterized by electric dipole transitions like the original atoms.

To frame the issue, we recall from Section 3.3.1 that two strongly in-

teracting, identical atoms are diagonalized by a symmetric and an anti-symmetric collective mode, where the two atomic electric dipoles respectively oscillate in phase or out of phase with one another. Clearly, the symmetric mode retains an electric dipole character, as the two individual dipoles add to produce a dipole of doubled amplitude. This can be observed in Fig. 3.9, where we compare the intensity pattern radiated by one single dipole $\mathbf{d} = d_0\widehat{\mathbf{x}}$ of fixed amplitude and direction (Fig. 3.9-a) with that of two in-phase, close-by dipoles $\mathbf{d}_1 = \mathbf{d}_2 = d_0\widehat{\mathbf{x}}$ (Fig. 3.9-b). The case of the anti-symmetric mode, however, is visibly more complex (Fig. 3.9-c). Intuitively, the two out-of-phase dipoles produce a vanishing electric dipole response, and are instead a hybrid of magnetic dipole and electric quadrupole modes. Interestingly, though, while the radiation pattern of Fig. 3.9-c depends sensitively on the relative orientation of the two out-of-phase dipoles, if one averages over orientations, the pattern again closely resembles that of a single, electric dipole (see Fig. 3.9-d). More concretely, in Section B.3 we show that the orientation-averaged resonant scattering cross section associated to the anti-symmetric mode is $\langle\sigma_{\mathsf{sc}}^{-}\rangle \approx 0.94\sigma_{\mathsf{sc}}$, where we recall that $\sigma_{\mathsf{sc}} = 3\lambda_0^2/(2\pi)$ is the resonant cross section of a single atom with electric dipolar response. To sum up, the anti-symmetric mode on average is seen to behave almost identically to a single atom with electric dipole response, justifying such a replacement in our RG prescription. Furthermore, we show in Section B.3 that this agreement is even stronger when considering pairs of strongly interacting atoms with different resonance frequencies $\delta\omega_{ij} \neq 0$, which is a situation typically encountered in an actual RG flow.

3.3.3.3 Near-field between renormalized atoms

Having argued that the anti-symmetric mode has an average optical response resembling that of a single electric dipole, we now turn to a second, related issue. Namely, since the anti-symmetric mode is a hybrid of magnetic dipole and electric quadrupole modes, it should have a near-field of $\sim 1/\rho^4$ at distances ρ much larger than the separation between the two composing atoms and much smaller than the optical wavelength. As the RG flow proceeds, a third atom that interacts strongly with this mode would then see such a scaling law at this distance (see Fig. 3.10-a). However, our RG prescription assumes that any new effective resonance has electric dipole character, and in particular, a $\sim 1/\rho^3$ near-field interaction with the third atom. We now argue that the RG prescription is a good approximation, because as the RG flow continues, it is likely that the third atom actually sits *closer* to one of the atoms in the pair (say atom 1), than the

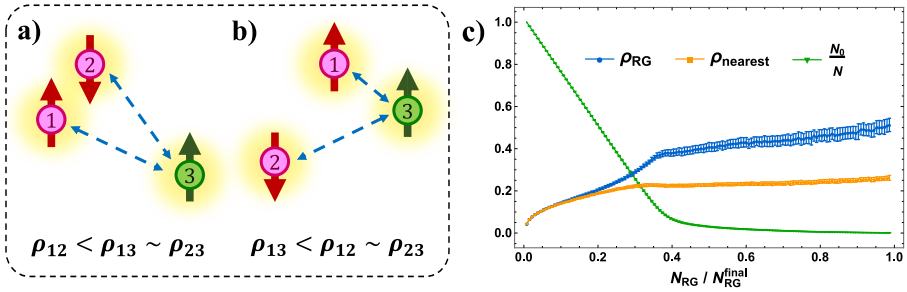

Figure 3.10: Microscopic analysis of the renormalization of the anti-symmetric modes. a) Pictorial representation of the near-field interaction between the anti-symmetric mode of a pair (represented by two out-of-phase dipoles, pink circles labeled 1 and 2) and a third atom (green circle, with label 3), which may sit very far from the pair (characterized by the distances $\rho_{12} < \rho_{13} \sim \rho_{23}$). In this case, the interaction strength scales like $\sim 1/\rho_{13}^4$, reflecting the higher order multipole nature of the out-of-phase dipoles. b) A similar illustration for the case where the third atom sits closer to one atom of the pair (say atom 1) than the pair separation itself ($\rho_{13} < \rho_{12} \sim \rho_{23}$). The interaction strength then scales like $\sim 1/\rho_{13}^3$. c) System properties during the RG flow. The horizontal axis quantifies how many pairs N_{RG} have been renormalized, from the beginning ($N_{\text{RG}} = 0$) towards the end ($N_{\text{RG}} = N_{\text{RG}}^{\text{final}}$) of the algorithm. As one atom can be renormalized more than once, typically $N_{\text{RG}}^{\text{final}} > N/2$. The blue circles represent the average inter-atomic distance ρ_{RG} of those pairs that get renormalized, while the orange squares shows the average distance ρ_{nearest} between the atoms of those pairs and their respective nearest atom, chosen among those that are still allowed to interact (i.e. with $\mathcal{L}_{ij} = 1$). The green triangles display the fraction of atoms N_0/N that have never been renormalized up to that moment of the flow. The data represents the average over ~ 300 runs over different random atomic positions, uniformly sampled inside a sphere of radius $R_{\text{sph.}} = 0.55\lambda_0$ and density $\eta \approx 32$. The bars show one standard deviation in the accumulated statistics.

pair separation itself (Fig. 3.10-b). In that case, the effective interaction strength between the anti-symmetric mode of the pair and the third atom will scale as $\sim 1/\rho_{13}^3$, exactly as if this mode was replaced by an electric dipolar atom. Mathematically, this is possible because the interaction parameter $\mathcal{K}_{ij} = |G_{ij}^{\text{near}}|/(|\delta\omega_{ij}|+1)$ that governs when atoms are renormalized does not depend only on closest distance of separation (via G_{ij}^{near}), but on the detunings $\delta\omega_{ij}$ as well. To quantify this picture, we have run ~ 300 RG flows over random configurations of a dense medium ($\eta = 32$) within a spherical geometry of radius $r_{\text{sph.}} = 0.55\lambda_0$. In Fig. 3.10-c, we plot several salient properties throughout the RG flow, averaged over the various runs. The horizontal axis denotes the relative position within the flow ($0 \leq N_{\text{RG}}/N_{\text{RG}}^{\text{final}} \leq 1$). In particular, $N_{\text{RG}}^{\text{final}}$ is the total number of pairs

renormalized during the entire RG (starting from a homogeneous atomic medium, until one reaches $\mathcal{K}_{ij} < \mathcal{K}_{\text{cut-off}} = 1$ for all pairs), while N_{RG} denotes the total number of renormalized pairs at any point in between. We recall that it is possible for an atom to be renormalized more than once, so that in general $N_{\text{RG}}^{\text{final}} > N/2$ for a dense medium. For reference, in green, we plot the fraction N_0/N of atoms that have never been renormalized up to that point. Notably, the fact that N_0/N reaches nearly zero when $N_{\text{RG}}/N_{\text{RG}}^{\text{final}} \sim 0.4$ indicates that almost all renormalization events beyond this stage involve previously renormalized (and thus inhomogeneous) atoms. Separately, with blue circles, we show the average value of the inter-atomic distance between atoms comprising the renormalized pairs at that stage, and we compare it with the average distance between each atom of these pairs and its own nearest neighbour, as portrayed by the orange squares. As we are interested in the interaction between atoms which will possibly be renormalized in some subsequent RG step, we only count the nearest neighbours where $\mathcal{L}_{ij} = 1$. The figure shows that we can roughly divide the RG flow into two parts. Before the critical value of $N_{\text{RG}}/N_{\text{RG}}^{\text{final}} \sim 0.4$, many atoms are still homogeneous, so that the algorithm mostly renormalizes pairs of identical, nearest neighbour atoms (as confirmed by the coincidence of the blue and orange curves). On the contrary, when $N_{\text{RG}}/N_{\text{RG}}^{\text{final}} \gtrsim 0.4$, almost all atoms have already been renormalized at least once, and in particular, an effective atom representing an anti-symmetric mode can potentially be renormalized again. In this regime, however, the nearest, interacting neighbour to the two original atoms forming this mode is on average significantly closer than the distance between these two atoms, as evidenced by the blue curve being significantly higher than the orange. This confirms that the intuitive picture of Fig. 3.10-b constitutes a typical case, which preserves the $\sim 1/\rho^3$ scaling of the near-field interaction.

3.3.3.4 Near-field vs far-field interactions

Separately, we want to underline the importance of separating the effects of near-field and far-field interactions, which occur in an atomic medium. To this aim, we point out the historic work of [194], which used RG to understand the properties of permanent, *static* dipoles, which only experience a near-field $1/\rho^3$ interaction. Given only a near-field interaction in three dimensions, the interaction of a dipole with its nearest neighbour is then indeed dominant. However, we have a qualitatively different system, of driven, radiating dipoles. Naively then, a similar argument considering the $1/\rho$ far field would suggest that atoms within a shell of radius ρ and

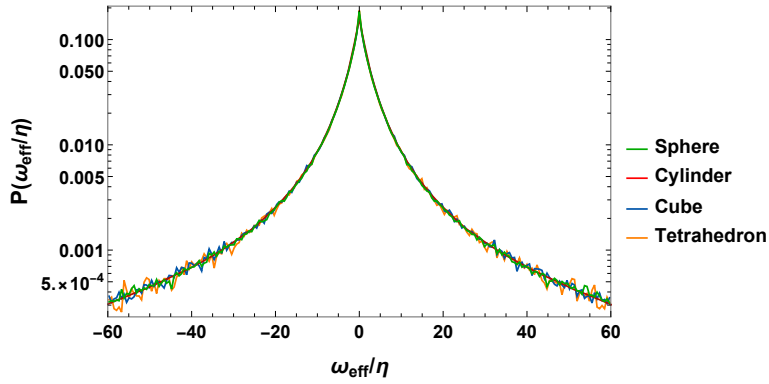

Figure 3.11: Renormalization group analysis, given different geometries. Similar plot as Fig. 3.7-b, but for a fixed density $\eta = 3$ and different geometrical shapes of the atomic ensemble.

$\rho + d\rho$ of one atom at the origin would contribute an interaction strength of $\sim \rho d\rho$, such that the *furthest* atoms actually play the strong role. We argue that an RG process based on the near field is still the correct prescription, as the index should be a local property. Instead, the apparent "dominance" of the far field simply reflects the fact that the macroscopic geometry of an optical system (e.g., if it is shaped as a lens or prism) can drastically alter the overall optical response, but not the index.

3.3.3.5 Linewidths in the RG prescription

At this point, we note that although the problem of just two atoms (Fig. 3.6-b) can be interpreted in terms of renormalized resonance frequencies and linewidths, in the many-atom case, we *only* renormalize the resonance frequencies. As we discussed, the interaction between atoms is described by the dimensionless matrix G (as defined in Eq. 3.4), whose real part Re G determines the coherent part of the interaction (i.e. the collective resonance frequencies), while its imaginary part Im G is associated to the dissipative phenomena, thus dictating the collective linewidths. In the case of two identical atoms, Re G and Im G are both naturally and exactly diagonalized by the same symmetric and anti-symmetric modes. However, in a many-atom ensemble, the different mathematical structures and physical origins of Re G and Im G become important. In particular, we recall that the $\sim 1/\rho_{ij}^3$ near-field component of the Green's function, G_{ij}^{near}, is purely real and strongly divergent as two atoms approach each other, which motivates our RG theory based on diagonalizing these terms first. Physically, Im G does not contain a near-field term (recall that Im $G_{ij} \to 1/2$ as $\rho_{ij} \to 0$),

since dissipation is associated with the radiation of energy into the far field. The absence of a near-field term implies that Im G does not yield an especially strong interaction between close atomic pairs, and thus cannot be approximately diagonalized pairwise. Again, this makes sense physically, because the emitted power by a collection of dipoles depends on the global interference between all dipoles, and does not generally decompose into the sum of powers radiated by pairs. Separately, we have checked that if our RG prescription were modified to renormalize resonance frequencies *and* linewidths pairwise, it would predict a non-physical optical response that tends to decrease ($n \to 1$) in the limit of high densities, in contrast with the full numerical simulations.

3.3.3.6 Independence of geometry

Finally, we remark how the choice of the cylindrical geometry in Fig. 3.3 was aimed to optimize the computational complexity of the coupled-dipole calculations. The Gaussian input beam (of waist w_0) has a rotational symmetry, and choosing a cylinder with the same symmetry ensures that the atoms at the edges couple with equal strength to light. At the edge this coupling must be small, in order to avoid unwanted edge diffraction effects. We find that $R_{\mathrm{cyl}} \sim 2w_0$ is sufficient to achieve this. With a rectangular-box geometry, corresponding width would be $4w_0$, meaning that the atoms at the corners would sit at a larger distance $2\sqrt{2}w_0$ from the beam axis. These would not affect the optical response but would be accounted for in the numerics, representing a "waste" of numerical resources that would undermine our goal to calculate very high densities and atom number.

In Fig. 3.6-d, on the contrary, the evaluation of the effective probability distribution of resonance frequencies $P(\omega_{\mathrm{eff}})$ purely by RG does not involve any external field or full coupled-dipole simulations, so that we don't have the same geometrical constraint as before. For consistency, we decide to still compute $P(\omega_{\mathrm{eff}})$ for the same cylindrical shape up to the maximum densities $\eta \simeq 3$ where we could also run coupled dipole simulations. We note, however, that these cylinders have an extreme aspect ratio, being several wavelengths in radius but sub-wavelength in thickness. At densities much higher than $\eta \simeq 3$, this aspect ratio becomes inefficient and impractical. As the RG scheme only involves short-range, near-field interactions, we expect the distribution $P(\omega_{\mathrm{eff}})$ to be unique in the bulk, and thus the results to be independent of the exact geometry, as long as the system is big enough to minimize boundary effects (as characterized by the system surface area to volume ratio). In Fig. 3.11, we check this statement by calculating $P(\omega_{\mathrm{eff}})$

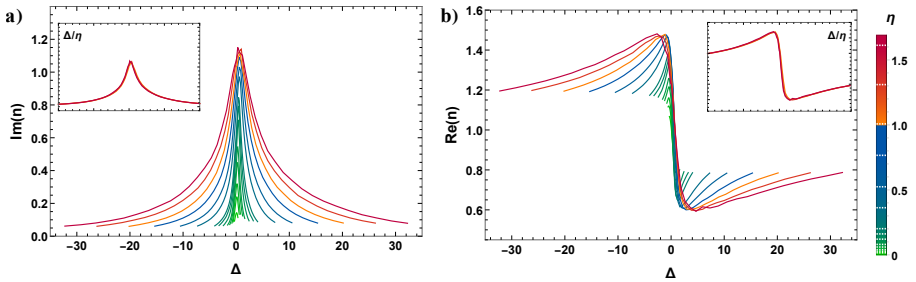

Figure 3.12: Spectrum of the refractive index, assuming isotropic atoms. The scheme of the figure is analogous to Fig. 3.3, but here we solve the coupled-dipole equations assuming that the atomic dipoles can isotropically align in all directions (isotropic scenario).

for four different geometries, at the fixed density $\eta = 3$.

3.4 Isotropic atoms

Conceptually, the case where atoms have a fixed polarization axis is the simplest, minimal model that one can consider. Usually, the atomic dipoles tend to align along the polarization of the external, input field, which typically validates this approximation. At the same time, we also notice that a fixed polarization axis does serve to model well various solid-state impurity emitters, which can have a reduced symmetry due to their surrounding crystal environment. Nonetheless, it is true that a realistic, isolated atom might be more precisely modelled by an isotropic polarizability. In this subsection, we discuss how our physical conclusions are affected when the atomic dipoles are allowed to align in any direction, from the perspective of both the coupled-dipole numerics and of our theoretical RG formalism.

- When dealing with isotropic atoms the coupled-dipole equations of Eq. 2.17 must be modified by associating three degrees of freedom to each atomic dipole, i.e. $\mathbf{d}_j = \sum_{a=x,y,z} \beta_j^a d_0 \hat{\mathbf{a}}$. This leads to the well-known equations

$$\begin{aligned} \mathbf{d}_i &= \alpha_0(\Delta) \left[\mathbf{E}_{\text{in}}(\mathbf{r}_i) + \mu_0 \omega_0^2 \sum_{j \neq i} \bar{\bar{\mathbf{G}}}(\mathbf{r}_i, \mathbf{r}_j, \omega_0) \cdot \mathbf{d}_j \right], \\ \mathbf{E}(\mathbf{r}) &= \mathbf{E}_{\text{in}}(\mathbf{r}) + \mu_0 \omega_0^2 \sum_{j=1} \bar{\bar{\mathbf{G}}}(\mathbf{r}, \mathbf{r}_j, \omega_0) \cdot \mathbf{d}_j, \end{aligned} \tag{3.10}$$

which are shown in the their very common formulation of dipoles with a polarizability $\alpha_0(\Delta) = 3\pi\epsilon_0/[(-\Delta - i/2)k_0^3]$. Numerically, a fixed polarization axis is then favourable as it results in the smallest number of degrees of freedom for large-scale numerics, scaling as the number of atoms N, rather than $3N$ as one would obtain with isotropic atoms. We believe that our simplified model of two-level atoms well captures the main physical processes involved in building up the index. To show this, we numerically solve Eq. 3.10 for a medium of isotropic atoms, inferring the transmission and the index analogously to Eq. 3.2 and Eq. 3.5. In Fig. 3.12, we show the refractive index over an extended range of near-resonant frequencies, given increasing densities. The data confirm our conclusion that the index of refraction saturates at high densities, although our computational resources don't allow us to reach the same densities and atom number as we currently do in the case of fixed polarization. In the case of isotropic dipoles, the saturation value of the index approximately reads $n_{\mathrm{re}} \sim 1.5$, showing that the precise value of $n_{\mathrm{re}} \sim 1.7$ discussed in the previous sections should not be considered as a universal, exact threshold, but rather as the result of a fundamental physical process which fixes the the correct magnitude of the index.

- Theoretically, one would have to modify the specific RG rules, accounting for the fact that a pair of isotropic atoms strongly interacting via their near-fields now has six eigenstates instead of two. Moreover, the natural polarizability axes of these six eigenstates will be oriented either parallel or perpendicular to the "molecular" axis defined as the vector pointing from one atom to the other. This axis generally does not coincide with the polarization of the input field, which requires one to then calculate the projected responses. We believe that this extension of RG should be valid, but it is challenging to compare and verify with exact numerics on dense ensembles, given realistic computational resources.

3.5 Conclusions and outlook

To summarize, we have shown that despite the large resonant scattering cross section of a single atom, a dense atomic medium does not exhibit an anomalously large optical response. Rather, strong near-field interactions between atomic pairs combined with spatial disorder results in an effective inhomogeneous broadening mechanism, which occurs even if the atoms are

otherwise perfect, and yields a maximum index of $n_{\mathrm{re}} \approx 1.7$. The key role of atomic granularity in this process also illustrates why conventional smooth medium approximations fail to describe the near-resonant response.

While we have focused on the linear refractive index, we believe that our RG formalism is valid in general for resonant disordered atomic media, and constitutes a versatile new tool to study multiple scattering. Within the linear regime, RG might be used to provide additional insight to the question of whether an Anderson localization transition exists in a 3D ensemble, and under what conditions [182, 183, 204, 215–217]. Furthermore, it would be interesting to explore the usage of RG toward the challenging problem of quantum, nonlinear scattering. As previously mentioned, the multiple scattering problem is formally encoded in a non-Hermitian Hamiltonian that describes light-mediated dipole-dipole interactions between atoms. In the limit of linear response, the resulting equations are equivalent to our coupled-dipole equations of Eq. 3.10, but beyond that, one is faced with the challenge of dealing with the exponentially large Hilbert space associated with N two-level atoms. Perturbative diagrammatic approaches have only recently been developed to treat the dilute atom limit [205], but our understanding of the nonlinear physics beyond this regime is very limited. To this end, we hypothesize that a diagrammatic theory can also be developed in the dense, strong scattering regime, where strong interactions between nearby pairs are first non-perturbatively summed via RG, while remaining interactions can be treated perturbatively.

Our results could also have interesting implications for quantum technologies based on atomic ensembles. In particular, the total optical depth of system, given by the product of the imaginary part of the index and system length, OD $\sim n_{\mathrm{im}} k_0 L$, is a fundamental resource [14, 218, 219], with its magnitude establishing fundamental error bounds for most applications. As the imaginary part of the index also saturates with increasing density, this could place minimum size constraints on systems in order to achieve a given fidelity. Likewise, constraints on the maximum density could arise due to the induced inhomogeneous broadening, which typically constitutes an undesirable dephasing mechanism.

Finally, it would be interesting to understand more fully how the optical properties of a dilute atomic medium eventually transform into the low refractive index of actual optical materials, as the density is increased. Specifically, for a disordered ensemble, we have seen that the maximum index already saturates, at densities that are approximately six orders of magnitude before the onset of chemical processes. We hypothesize that the onset of chemistry, and the phase transition toward a real material,

does not qualitatively alter the optical response, provided that the system remains disordered and the electrons tightly bound. Separately, it would be interesting to explore the same questions and transition for spatially ordered atomic systems, where RG breaks down and one expects very different qualitative behavior, due to the possibility of strong constructive and destructive interference in light scattering. This will be the topic of the next chapter.

4 - Refractive index of an ordered atomic crystal

Chapter Contents

4.1 Introduction

In the previous chapter, we studied the concept of refractive index in a disordered atomic medium, observing the emergence of strict bounds imposed by the electrodynamics of multiple light scattering. Here, we introduce a minimal physical model that elucidates how extreme one *might expect* the index to become in an ordered atomic crystal, under ideal circumstances.

Specifically we want to study what index might be achievable as a function of the atomic density, spanning a wide range of physical regimes. As long as the atomic nuclei are too far separated for electronic orbitals on different nuclei to directly interact (which we term the "quantum-optics" regime), the atoms only interact via electromagnetic fields, and the index should solely be a function of the atomic distance and the single-atom polarizability. At very dilute densities, moreover, one expects that conventional macroscopic theories hold, as discussed in Chapter 2. Nonetheless, when increasing the densities (still within this quantum-optics scenario), the interatomic distance can become lower than the spatial extent of the scattering cross section of an (isolated) atom, so that multiple scattering of light can cause the breakdown of conventional theories of refractive index. In the disordered case of Chapter 3, we indeed showed that these electrodynamical effects were already guaranteeing an order of magnitude in line with empirical evidences, thus speculating that these processes might qualitatively characterize the optical response at any larger density.

Here, we show that for an ordered, atomic crystal the scenario is radically different. Specifically, we argue that multiple light scattering can build up an index that keeps growing with density, due to perfect constructive interference. This motivates our direct analysis of the "quantum-chemistry" regime, where the atomic densities are sufficiently high that electronic orbitals on neighbouring nuclei begin to overlap, in principle giving rise to a wealth of new phenomena associated with chemical interactions. We empirically know, indeed, that conventional, computational quantum chemistry (which ignores multiple light scattering) can predict the optical properties of real solids with reasonable accuracy, suggesting that multiple scattering in the full regime of chemistry is a weak effect. Due to these reasons, we develop a model to non-perturbatively study multiple scattering including the onset of quantum chemistry, showing how this latter can suppress the growth of the index mentioned above.

4.1.1 Summary of the chapter

We now summarize the scope and main results of this chapter.

- In Section 4.2 we analyze the refractive index of an atomic crystal in the quantum optics limit. We first review the result of Section 2.3.2, that a single two-dimensional (2D) array of atoms can provide a large, lossless and cooperatively enhanced response to light near resonance, as characterized by large reflectance and large phase shift in transmission [149, 150, 171]. At the same time, we re-phrase the equations in

an equivalent, operatorial manner, which might allow in the following sections to include the effects of quantum chemistry more directly. By considering a three-dimensional (3D) crystal as a sequence of 2D arrays separated by lattice constant d_z, we then show that the 2D properties directly translate into a refractive index near resonance that can be purely real, and which scales as $n_{\max} \propto \lambda_0/d_z$. At the same time, the dispersion relation of the array allows for the lossless index $n_{\min} \sim 0$. The key property enabling this behavior is the *single-mode nature* of the light-matter interaction, both in the 2D and 3D arrays, where light excites only a single collective mode of the atoms, *and* this collective mode only re-radiates light elastically back in the same $\mathbf{k}_{xy} = 0$ direction, to produce a maximal and lossless response.

- To counteract the physical processes that build up the index, one would need to suppress this single-mode nature of the response. In Section 4.3, we study from a purely optical perspective what mechanisms might be required to fulfil this scope. Specifically, one would need to break down the perfect translational symmetry within each 2D array. We thus first study the case of an atom in the array that is selectively driven, to make it distinguishable from the others. Afterwards, we discuss the effects of a missing atom at a particular site, acting as a defect. In both cases, we show that these hypothetical scenarios allow for spatial multi-mode response, suppressing the coherent emission in the relevant, $\hat{\mathbf{z}}$-directed mode.

- In Section 4.4.1, we finally introduce a model to tackle the onset of quantum-chemistry. In particular, our analysis focuses on an expansion around a large lattice constant compared to the Bohr radius, $d/a_0 \gg 1$. Then, quantum chemistry can be treated perturbatively, while multiple scattering must still be treated non-perturbatively (given $d/\lambda_0 \ll 1$). Considering the simplest model of a lattice of hydrogen atoms, we identify two mechanisms stemming from a combination of quantum magnetism, electronic density-density correlations, and chemistry of photo-excited electrons dominate at large d/a_0. Specifically, we argue that these effects modify the optical response similarly to selectively driven atoms or defects in the array. We quantify how these processes lead to a maximum allowed real part of the refractive index, and the growth of the imaginary part associated with absorption. Our model suggests that an ultra-high index material of $n \sim 30$ with low losses is not fundamentally forbidden by the laws of nature. Similarly, our ideal scheme would predict a near-zero index $n \sim 0$

around a specific frequency.

- Although our quantitative model deals with hydrogen atoms, in Section 4.5 we also discuss possible realistic routes toward extreme-index materials, such as high-density arrays of solid-state quantum emitters [220–222] or van der Waals heterostructures [223], and we qualitatively show that the extreme indices are robust to some degree of additional imperfections (e.g., implementation-dependent inhomogeneities, or additional inelastic mechanisms). Finally, in Section 4.6 we provide an outlook of future research questions to explore.

4.2 Optical properties of a 3D lattice

We derive the refractive index of a perfect atomic lattice in the quantum-optics limit, where quantum-chemistry interactions between atoms are ignored and each atom is seen as a point dipole from the standpoint of optics. Similarly to Chapter 3, we consider the relevant levels of the atom to consist of an electronic ground state and first excited state, connected by an electric dipole transition of frequency ω_0 and corresponding wavevector $k_0 = \omega_0/c$ and wavelength $\lambda_0 = 2\pi/k_0$. The atoms can also be driven by a weak coherent input field of frequency ω_{L}, with a polarization $\widehat{\mathbf{x}}$ that aligns with the dipole matrix-element $\mathbf{d}_0 = d_0\widehat{\mathbf{x}}$ of the atomic transition. The excited state can only decay by emitting a photon, at a rate $\Gamma_0 = k_0^3 d_0^2/(3\pi\epsilon_0\hbar)$.

Although our conclusions in this section are completely general to any atom with the properties specified above, here we re-write the SM and coupled-dipole formalism of Section 2.3 in a second-quantized notation of the atomic degrees of freedom, to be consistent with our later model including quantum chemistry. Specifically, there we will consider hydrogen atoms whose ground and excited states are then the 1s and $2p_x$ orbitals. Moreover, we treat the near-resonant input field as a classical field $\mathbf{E}_{\mathrm{in}}$. In the rotating frame relative to this driving field and in the long-wavelength limit, the Hamiltonian describing the atom-light interactions is given by

$$\begin{aligned}\hat{\mathcal{H}}_{\mathrm{QO}} &= \hat{\mathcal{H}}_0 + \hat{\mathcal{H}}_{\mathrm{dip-dip}} + \hat{\mathcal{H}}_{\mathrm{drive}} \\ &= -\delta\sum_{i,\sigma}\hat{b}^{\dagger}_{pi\sigma}\hat{b}_{pi\sigma} - \Gamma_0\sum_{ij,\sigma\sigma'}G_{ij}(\hat{b}^{\dagger}_{pi\sigma}\hat{b}_{si\sigma})(\hat{b}^{\dagger}_{sj\sigma'}\hat{b}_{pj\sigma'}) \\ &\quad -\sum_{i,\sigma}\left[\Omega_i\hat{b}^{\dagger}_{pi\sigma}\hat{b}_{si\sigma} + h.c.\right],\end{aligned} \tag{4.1}$$

where we define the detuning $\delta = \omega_{\rm L} - \omega_0$ the Rabi frequency $\Omega_i = \mathbf{d}_0 \cdot \mathbf{E}_{\rm in}(\mathbf{r}_i)/\hbar$, and the fermionic operator $\hat{b}_{\alpha i\sigma}$ that annihilates an electron of orbital α and spin σ on atom i, whose nucleus is at position $\mathbf{r}_i$. We recall that the dipole-dipole interaction $\hat{\mathcal{H}}_{\rm dip-dip}$ describes the electronic excitation $(\hat{b}^\dagger_{pi\sigma}\hat{b}_{si\sigma})$ of an atom from its s to its p-orbital at site i, and the de-excitation $(b^\dagger_{sj\sigma'}\hat{b}_{pj\sigma'})$ of another at site j. This describes electromagnetic field mediated interactions once the photons are integrated out within the Born-Markov approximation, with $G_{ij} = (3\pi/k_0)\hat{\mathbf{x}} \cdot \bar{\bar{\mathbf{G}}}(\mathbf{r}_i - \mathbf{r}_j, \omega_0) \cdot \hat{\mathbf{x}}$ being proportional to the electromagnetic Green's function at frequency ω_0 (as in Eq. 2.17). In this formalism, the positive-frequency component of the electric field operator (as shown in Eq. 2.14 of Section 2.3) reads

$$\hat{\mathbf{E}}(\mathbf{r}) = \mathbf{E}_{\rm in}(\mathbf{r}) + \frac{k_0^3}{3\pi\epsilon_0}\sum_{i\sigma}\bar{\bar{\mathbf{G}}}(\mathbf{r}-\mathbf{r}_i,\omega_0)\cdot\mathbf{d}_0\,\hat{b}^\dagger_{si\sigma}\hat{b}_{pi\sigma}, \tag{4.2}$$

which formally expresses the total field at any spatial point, in terms of the input field and that scattered by the atoms. At this level of discussion, $\hat{\mathcal{H}}_{\rm QO}$ and the relevant Hilbert space can just as well be written in terms of the pseudospin-$1/2$ objects $\hat{\sigma}_{\rm eg}$ introduced in Section 2.3 [151, 178, 185]. We avoid that here, to prevent confusion with the actual electronic spins σ and to more naturally extend to the inclusion of quantum chemistry.

We want to remark that, since G_{ij} is complex, the Hamiltonian $\hat{\mathcal{H}}_{\rm dip-dip}$ is non-Hermitian. Its Hermitian and non-Hermitian components describe coherent energy exchange between atoms, and collective spontaneous emission arising from interference of light emission, respectively. To the extent that Eq. 4.1 and Eq. 4.2 can be solved exactly, they fully incorporate the effects of non-perturbative multiple scattering of light and wave interference in emission.

4.2.1 Review of a 2D array

While the equations for a 3D lattice absent driving can in principle be (numerically) diagonalized [224, 225], one can arrive at a better physical understanding of the refractive index by first considering a single, 2D square array of lattice constant d, located in the $z = 0$ plane. The brief review of this subsection is aimed to expand the discussion of Section 2.3.2.

We write the total wave function $|\Psi(t)\rangle = |\psi_{\rm 2D}(t)\rangle \otimes |\sigma\rangle$ in terms of the orbital $|\psi_{\rm 2D}(t)\rangle$ and electronic spin $|\sigma\rangle$ wave functions, the latter of which is time independent and irrelevant in the quantum optics limit, as atom-light interactions and thus $\hat{\mathcal{H}}_{\rm QO}$ are decoupled from spin. In the single-excitation

limit (containing exactly one p-orbital), the discrete translational symmetry implies that all eigenstates of $\hat{\mathcal{H}}_{\mathrm{dip-dip}}$ of the 2D array are Bloch modes with corresponding Bloch wavevector $\mathbf{k}_{\mathrm{xy}}$, $|E_{\mathbf{k}_{\mathrm{xy}}}\rangle = N^{-1/2}\sum_i e^{i\mathbf{k}_{\mathrm{xy}}\cdot\mathbf{R}_i} b_{pi}^\dagger b_{si}|G\rangle$. The ground state consists of all atoms in the s orbitals, $|G\rangle = \Pi_i b_{si}^\dagger|\mathrm{vac}\rangle$. Here, we have suppressed the spin index given its decoupling from dynamics, and $N \to \infty$ represents the number of atoms in the 2D array.

We write the complex eigenvalues of the Bloch modes in the form $\omega(\mathbf{k}_{\mathrm{xy}}) - i\Gamma(\mathbf{k}_{\mathrm{xy}})/2 = -\Gamma_0\sum_{i,j} G_{ij}e^{i\mathbf{k}_{\mathrm{xy}}\cdot\mathbf{R}_{ij}}$, which can be calculated by discrete Fourier transform of the Green's function [149, 150]. The dispersion relation $\omega(\mathbf{k}_{\mathrm{xy}})$ represents the energy shift of each Bloch mode relative to the bare atomic resonance ω_0, due to dipole-dipole interactions, and can be evaluated numerically. The collective emission rate admits an analytic solution given by [151, 226]

$$\Gamma(\mathbf{k}_{\mathrm{xy}}) = \frac{3\lambda_0^2\Gamma_0}{4\pi d^2} \sum_{\substack{m,n \\ |\mathbf{k}_{\mathrm{xy}}+\mathbf{g}_{mn}|\le k_0}} \frac{k_0^2 - [(\mathbf{k}_{\mathrm{xy}}+\mathbf{g}_{mn})\cdot\hat{\mathbf{x}}]^2}{k_0\sqrt{k_0^2 - |\mathbf{k}_{\mathrm{xy}}+\mathbf{g}_{mn}|^2}}, \tag{4.3}$$

and is modified from the single-atom value due to interference in the emitted light from different atoms [150]. Here, we defined the reciprocal lattice vectors, $\mathbf{g}_{mn} = (2\pi/d)(m\hat{\mathbf{x}} + n\hat{\mathbf{y}})$. In the regime of lattice constants $d < \lambda_0/2$ that we are interested in, its expression further simplifies into

$$\Gamma(\mathbf{k}_{\mathrm{xy}}) = \frac{3\lambda_0^2\Gamma_0}{4\pi d^2}\left(\frac{k_0^2 - k_{\mathrm{x}}^2}{k_0\sqrt{k_0^2 - |\mathbf{k}_{\mathrm{xy}}|^2}}\right)\Theta(k_0 - |\mathbf{k}_{\mathrm{xy}}|), \tag{4.4}$$

where $\Theta(k_0 - |\mathbf{k}_{\mathrm{xy}}|)$ is the Heaviside step function. For the collective mode with $\mathbf{k}_{\mathrm{xy}} = 0$, one has $\Gamma(0) = 3\lambda_0^2\Gamma_0/(4\pi d^2)$. At small lattice constants, the rate is significantly enhanced relative to the single-atom value Γ_0 by an amount $\propto (\lambda_0/d)^2$ due to strong constructive interference.

We now consider driving with a plane wave at normal incidence to the 2D array (with longitudinal wavevector $k_{\mathrm{z}} = k_0$ and perpendicular wavevector $\mathbf{k}_{\mathrm{xy}} = 0$), whose spatially uniform Rabi frequency $\Omega_i = \Omega_0$ is sufficiently weak that dynamics can be restricted to the ground state and single-excitation manifold. The discrete symmetry imposes that this field will only couple to the Bloch mode $|E\rangle = |E_{\mathbf{k}_{\mathrm{xy}}=0}\rangle$, with the time-dependent wave function restricted to the form $|\psi_{\mathrm{2D}}(t)\rangle = c_{\mathrm{G}}(t)|G\rangle + c_{\mathrm{E}}(t)|E\rangle$. The wave function approach to the non-Hermitian Hamiltonian of Eq. 4.1, or more properly the full master equation, is valid within the quantum jump formalism of open systems. Nonetheless, under weak driving, quantum jumps can

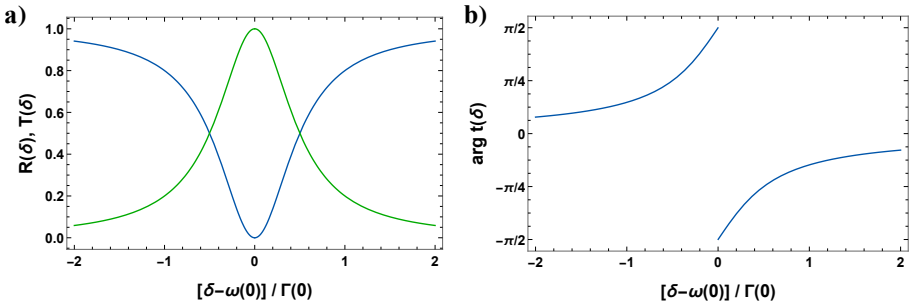

Figure 4.1: Reflection and transmission coefficients of a 2D atomic array. a) Spectrum of reflectance (blue) and transmittance (green) as a function of detuning relative to the collective resonance frequency of the array $\delta - \omega(0)$, and in units of the collective linewidth $\Gamma(0)$. b) Spectrum of transmission phase, $\arg\, t(\delta)$.

be neglected and $c_{\mathrm{G}}(t) \approx 1$ up to order $\sim (\Omega_0/\Gamma_0)^2$ [152]. The Schrodinger equation then leads to a steady-state amplitude of the excited state whose dependence on detuning δ goes as

$$c_{\mathrm{E}}(\delta) = \frac{\Omega_0}{-\delta + \omega(0) - i\Gamma(0)/2}. \tag{4.5}$$

We now derive the expectation value $\mathbf{E}(\mathbf{r}) = \langle \hat{\mathbf{E}}(\mathbf{r}) \rangle$ of the total field from Eq. 4.2. Given the periodic nature of the array and that only the $\mathbf{k}_{\mathrm{xy}} = 0$ Bloch mode is excited, the total field only contains transverse momentum components given by integer multiples (m, n) of the reciprocal lattice vectors, $\mathbf{g}_{mn} = (2\pi/d)(m\hat{\boldsymbol{x}} + n\hat{y})$. Specifically, we find

$$\frac{\mathbf{E}(\mathbf{r})}{E_0} = \frac{\mathbf{E}_{\mathrm{in}}(\mathbf{r})}{E_0} + \left(i\frac{\Gamma(0)}{2} \sum_{m,n} \frac{k_0^2 - (\mathbf{g}_{mn} \cdot \widehat{\mathbf{x}})^2}{k_0 k_{\mathrm{z}}^{mn}} e^{i\mathbf{g}_{mn}\cdot\mathbf{r}_\perp + ik_{\mathrm{z}}^{mn}|z|} \right) \frac{c_{\mathrm{E}}(\delta)}{\Omega_0}, \tag{4.6}$$

where $k_{\mathrm{z}}^{mn} = \sqrt{k_0^2 - |\mathbf{g}_{mn}|^2}$, and where $\mathbf{E}_{\mathrm{in}}(\mathbf{r}) = E_0 e^{ik_0 z}\widehat{\mathbf{x}}$. Note that for $d < \lambda_0$, then k_{z}^{mn} is imaginary except for $m = n = 0$. In other words, only transmission and reflection at normal incidence are radiation waves, while any other $(m, n) \neq (0, 0)$ correspond to evanescent diffraction orders (with the sign of $\mathrm{Im}\; k_{\mathrm{z}}^{mn}$ chosen such that the field decays away from the array). In the far field limit $|k_0 z| \gg 1$, one thus has

$$\mathbf{E}(\mathbf{r}) \simeq \mathbf{E}_{\mathrm{in}}(\mathbf{r}) \left[1 + i\frac{\Gamma(0)}{2}\frac{c_{\mathrm{E}}(\delta)}{\Omega_0}\Theta(z) \right] + \mathbf{E}_{\mathrm{in}}^*(\mathbf{r}) \left[i\frac{\Gamma(0)}{2}\frac{c_{\mathrm{E}}(\delta)}{\Omega_0}\Theta(-z) \right], \tag{4.7}$$

Using the steady-state amplitude in Eq. 4.5, we identify the reflection and

transmission coefficients $r(\delta) = i\Gamma(0)/[-2\delta + 2\omega(0) - i\Gamma(0)]$ and $t(\delta) = 1 + r(\delta)$. Note in particular that the array is perfectly reflecting when light is resonant with the Bloch mode, $\delta = \omega(0)$, and generally that the system is lossless with $|r|^2 + |t|^2 = 1$. These properties reflect the *single-mode nature* of the light-matter interaction for this system, where the light excites only a single collective eigenmode $|E\rangle = |E_{\mathbf{k}_{\mathrm{xy}}=0}\rangle$, *and* this collective mode only re-radiates light elastically back in the same $\mathbf{k}_{\mathrm{xy}} = 0$ direction (either forward or backward). In Fig. 4.1, we plot the reflectance and transmittance spectra and as well as the transmission phase. Notably, near resonance, the transmitted light can undergo a significant phase shift of up to $\pm\pi/2$.

4.2.2 Single-mode response and 1D formalism

We now consider a 3D array, with the lattice constant d_{z} between 2D layers allowed to be different than the intra-layer lattice constant d, as pictorially represented in Fig. 4.2. Naively, if each 2D layer can contribute a large phase shift to propagating light, then one expects a large, perfectly real index scaling like $n \sim \lambda_0/d_{\mathrm{z}}$. This naive argument does not account for multiple scattering between planes or evanescent fields, but we now present an exact calculation showing that this scaling holds.

As before, we restrict ourselves to the weak-driving limit at normal incidence. Thus, only the collective mode $|E\rangle = |E_{\mathbf{k}_{\mathrm{xy}}=0}\rangle$ of each 2D array can be excited, leading to a total wave function $|\psi_{\mathrm{3D}}(t)\rangle = c_{\mathrm{G}}(t)|G\rangle + \sum_j c_{\mathrm{E}}^j(t)|E_j\rangle$, where $c_{\mathrm{G}}(t) \approx 1$ and $|E_j\rangle$ is the collective mode associated with the 2D plane at position z_j. Within this manifold, the dynamics under $\hat{\mathcal{H}}_{\mathrm{QO}}$ of Eq. 4.1 is mathematically equivalent to a 1D problem, characterized by the matrix elements $H^{\mathrm{1D}}_{\mathrm{dip-dip},ij} = \langle E_i|\hat{\mathcal{H}}_{\mathrm{dip-dip}}|E_j\rangle$, which read

$$H^{\mathrm{1D}}_{\mathrm{dip-dip},ij} = \begin{cases} \omega(0) - \dfrac{i}{2}\Gamma(0) & i = j, \\ -i\dfrac{\Gamma(0)}{2}\displaystyle\sum_{m,n} \frac{k_0^2 - (\mathbf{g}_{mn}\cdot\hat{\mathbf{x}})^2}{k_0 k_{\mathrm{z}}^{(m,n)}} e^{ik_{\mathrm{z}}^{(m,n)}|z_i - z_j|} & i \neq j, \end{cases} \tag{4.8}$$

where we recall that $k_{\mathrm{z}}^{mn} = \sqrt{k_0^2 - |\mathbf{g}_{mn}|^2}$. Comparing Eq. 4.8 with Eq. 4.6, the off-diagonal elements $i \neq j$ between different planes can be equivalently interpreted as the Rabi frequency associated with the field scattered by one plane, as experienced by the atoms in another plane.

The structure of Eq. 4.8 defines two type of interactions between the 2D atomic layers. Specifically, the zero-th diffraction-order $(m, n) = (0, 0)$

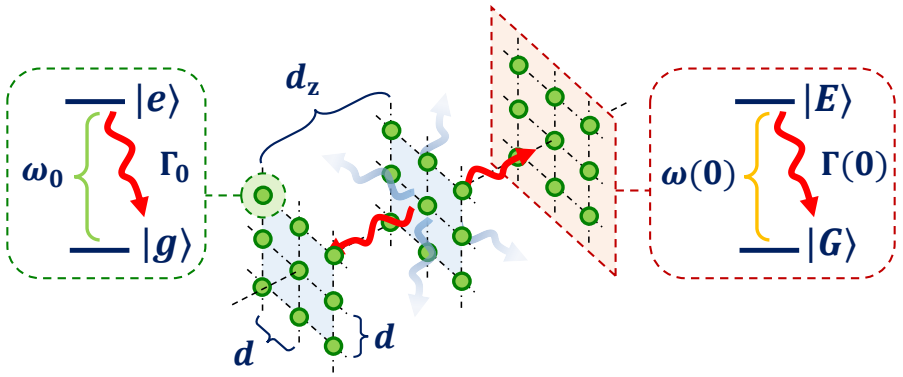

Figure 4.2: 1D model for a 3D atomic lattice, illuminated at normal incidence. We consider a 3D atomic lattice, composed of a stack of 2D arrays with constant d separated by a longitudinal distance d_z. The atoms are identical two-level systems, with a resonant frequency ω_0 between two generic states $|g\rangle$ (afterwards, in our chemistry model we consider the state $1s$ of Hydrogen) and $|e\rangle$ (state $2p_x$ of Hydrogen). The spontaneous emission rate reads Γ_0. The layers are illuminated at normal incidence, and they can re-radiate only in this same $\hat{\mathbf{z}}$ direction (red, wavy arrows), while the other diffraction orders give rise to an evanescent interaction between the arrays (blue, shaded, wavy arrows). Each 2D array only excites the collective state $|E\rangle = N^{-1/2}\sum_i b^\dagger_{pi} b_{si}|G\rangle$ with resonant frequency $\omega(0)$. This can decay back to the ground state $|G\rangle = \Pi_i b^\dagger_{si}|\mathrm{vac}\rangle$ with a radiative rate $\Gamma(0) = 3\lambda_0^2\Gamma_0/(4\pi d^2)$.

describes an infinite-range interaction $\propto \exp(ik_0|z_i - z_j|)$ mediated by radiative emission (red, wavy arrows of Fig. 4.2). On top of that, the residual diffraction orders $(m,n) \neq (0,0)$ (blue, shaded, wavy arrows of Fig. 4.2) contribute with an evanescent coupling, which is exponentially suppressed $\sim \exp(-|k_z^{mn}(z_i - z_j)|)$ with increasing distances between the layers.

4.2.3 Extreme refractive indices

Diagonalizing the matrix $H^{\mathrm{1D}}_{\mathrm{dip-dip}}$ of Eq. 4.8 then gives the optical band structure of the array at normal incidence, with dispersion relation

$$J(k_z) = \omega(0) + \frac{\Gamma(0)}{2}\left[\frac{\sin(k_0 d_z)}{\cos(k_z d_z) - \cos(k_0 d_z)} + J_{\mathrm{ev}}(k_z)\right], \tag{4.9}$$

where $|k_z| \leq \pi/d_z$ is restricted to the first Brillouin zone. We find that deriving the 3D band structure in terms of 2D planes is more elucidating for our purposes than applying previously developed techniques, such as in [225]. We recall that we are in a rotating frame, and $J(k_z)$ is thus

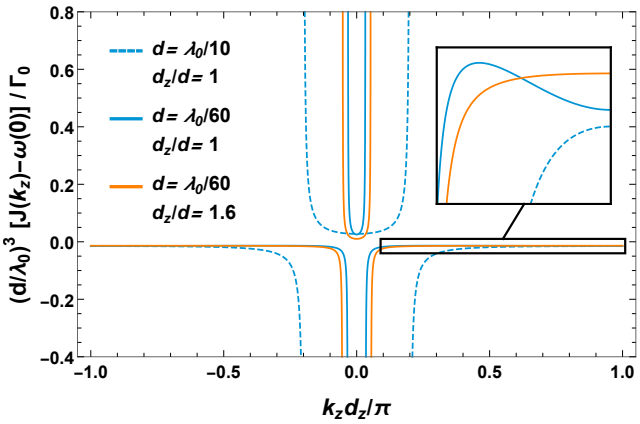

Figure 4.3: Optical band structure along $\hat{\mathbf{z}}$ of a 3D lattice. Re-scaled dispersion relation $(d/\lambda_0)^3 J(k_z)/\Gamma_0$ for Bloch waves along z with Bloch wavevector k_z, for the lattice constants d and d_z shown in the legend. The non-invertibility of the band for some values of d, d_z can be clearly seen in the inset.

the frequency relative to the bare atomic resonance frequency ω_0. Also, we will always be in a regime where the shift is small relative to the bare frequency $|J(k_z)|/\omega_0 \ll 1$. Here, $J_{\rm ev}(k_z)$ is the contribution coming from the evanescent fields of each plane, and is found to be

$$J_{\rm ev}(k_z) = -\sum_{(m,n)\neq(0,0)} \frac{(\mathbf{g}_{mn}\cdot\hat{\mathbf{x}}/k_0)^2-1}{\sqrt{|\mathbf{g}_{mn}/k_0|^2-1}} \times\left[1+\frac{\sinh\left(k_0 d_z\sqrt{|\mathbf{g}_{mn}/k_0|^2-1}\right)}{\cos(k_z d_z)-\cosh\left(k_0 d_z\sqrt{|\mathbf{g}_{mn}/k_0|^2-1}\right)}\right]. \tag{4.10}$$

Although $H^{\rm 1D}_{\rm dip-dip}$ itself is non-Hermitian, the dispersion relation is purely real, as a result of the lossless nature of the individual planes. We notice, indeed, that Eq. 4.9 is equivalent to what expected for an ideal chain of two-level atoms perfectly coupled to a lossless waveguide [187, 227], up to the supplementary, evanescent interaction term $J_{\rm ev}(k_z)$.

A typical band structure is illustrated in Fig. 4.3 for various values of d/λ_0 and d_z/d. As long as $J(k_z)$ is invertible (a single value of $|k_z|$ is associated to each value of $J(k_z)$), then the index is well-defined as the reduction of the effective wavelength of light compared to free space at the same frequency, reading $n(\delta) \approx k_z(\delta)/k_0$. Here, we inferred $k_z(\delta)$ by

inverting the relation $J(k_z) = \delta$, and we used the fact that $|J(k_z)|/\omega_0 \ll 1$. Then, the maximum index is associated to the band edge $k_z = \pi/d_z$, and reads

$$n_{\max} \approx \frac{\lambda_0}{2d_z}, \tag{4.11}$$

which is obtained at $\delta_{\max} = \omega(0) - [\Gamma(0)/2]\tan(k_0 d_z/2)$ and which grows indefinitely with shrinking lattice constant. The formula in Eq. 4.11 is valid as long as $d_z < \lambda_0/2$, while the behaviour of the index for $\lambda_0/2 \leq d_z < \lambda_0$ is discussed in Appendix C.1. At the same time, by choosing a different detuning $\delta_{\min} = \omega(0) + [\Gamma(0)/2]\cot(k_0 d_z/2)$ one can excite the central mode $k_z = 0$, leading to

$$n_{\min} \approx 0. \tag{4.12}$$

These predictions are derived from the dispersion relation. To validate them, one can check their agreement with the calculation of the phase of transmission, by numerically simulating a finite number of 2D layers (similarly to what done in Chapter 3). As discussed in Appendix C.2, this supplementary analysis shows a perfect agreement with our theoretical predictions.

In reality, the band structure is not always invertible, due to the interfering mechanisms of energy transfer between planes via radiation and evanescent waves. For fixed d_z/d, non-invertibility will arise for sufficiently small d, while for fixed d, increasing d_z/d will eventually lead to invertibility. This is illustrated in Fig. 4.3, for example, as the choices $d/\lambda_0 = 1/10$, $d_z/d = 1$ and $d/\lambda_0 = 1/60$, $d_z/d = 1.6$ are invertible, while $d/\lambda_0 = 1/60$, $d_z/d = 1$ is not. The condition for invertibility is derived in greater detail in Appendix Appendix C.3. In what follows, we will fix $d_z/d = 2.5$, where the contribution of the evanescent coupling to the band is negligible $|J_{\text{ev}}(k_z)| \ll |J(k_z)|$ down to $d \simeq \lambda_0/360$ (corresponding to $d \simeq 6a_0$ for hydrogen atoms), by which point quantum chemistry has already become significant.

4.3 Optical limits to the single-mode response

In the previous section, we showed that an atomic 3D array of ideal atoms responds to light in a single-mode manner, which builds up a large optical response characterized by both extremely high and extremely low refractive indices. As long as the single-mode behavior is preserved, this mechanism would ensure the gigantic collective response of the ordered atomic set.

In this section, we address the following question: from a purely optical standpoint, are there physical processes which can potentially suppress such single-mode nature of the atom-light interaction? For the moment, we only

focus on identifying these potential mechanisms, without analyzing why and when we expect them to appear. This will be the topic of Section 4.4.1, where we will argue that they naturally arise at small lattice constants, due to the onset of quantum chemistry. Specifically, we know from Section 4.2.1 that the single-mode response is deeply related to the perfect translational symmetry within each 2D, transverse layer. Due to this reason, we here study two scenarios where this latter is broken in a 2D array, namely the cases when a specific atom is either selectively driven or missing.

4.3.1 Selectively driven atom

The collective response of a uniformly excited array differs remarkably from the response of a single, distinguishable driven atom. Concretely, we now consider an infinite 2D array, but where a weak input field with detuning δ selectively drives just a single atom located at $\mathbf{r} = \mathbf{r}_h$, i.e. taking $\Omega_j = \Omega_h \delta_{jh}$ in Eq. 4.1, as illustrated in Fig. 4.4-a. Although this scenario might not be particularly physical by its own, it represents one of the simplest theoretical ways of breaking the perfect translational symmetry in a 2D array. Moreover, it allows us to analyze an optical mechanism that will be directly relevant for our quantum chemistry discussions later.

We consider a wave function $|\psi_{\text{2D}}\rangle = c_{\text{G}}|G\rangle + \sum_j \tilde{c}_j b_{pj}^\dagger b_{sj}|G\rangle$, where other atoms $j \neq h$ can still be excited via dipole-dipole interactions with the driven atom. Our goal is to solve for the steady-state atomic amplitudes $\tilde{c}_j(\delta)$ under Eq. 4.1, assuming that $c_{\text{G}} \approx 1$. This can be efficiently done by calculating the free propagator inside the 2D atomic array, which describes the spread of the excitation mediated by dipole-dipole interactions [228, 229]. In the rotating frame, such a propagator is given by the operator $\hat{G}_\chi(\delta) = -(\hat{\mathcal{H}}_0 + \hat{\mathcal{H}}_{\text{dip-dip}})^{-1}$, which can be explicitly computed by decomposing the single-excitation manifold into the Bloch modes $|E_{\mathbf{k}_{\text{xy}}}\rangle$ that diagonalize it. One obtains

$$\begin{aligned} \hat{G}_\chi(\delta) &= -N\left(\frac{d}{2\pi}\right)^2 \int_{\text{BZ}} \mathrm{d}\mathbf{k}_{\text{xy}} \frac{|E_{\mathbf{k}_{\text{xy}}}\rangle\langle E_{\mathbf{k}_{\text{xy}}}|}{-\delta + \omega(\mathbf{k}_{\text{xy}}) - i\Gamma(\mathbf{k}_{\text{xy}})/2} \\ &= -\sum_{jh\sigma\sigma'} \chi(\mathbf{r}_j - \mathbf{r}_h, \delta)\ (b_{pj\sigma}^\dagger b_{sj\sigma})(b_{sh\sigma'}^\dagger b_{ph\sigma'}), \end{aligned} \tag{4.13}$$

where we defined the susceptibility

$$\chi(\mathbf{r}_j - \mathbf{r}_h, \delta) = \left(\frac{d}{2\pi}\right)^2 \int_{\text{BZ}} \mathrm{d}\mathbf{k}_{\text{xy}} \frac{e^{-i\mathbf{k}_{\text{xy}}\cdot(\mathbf{r}_j - \mathbf{r}_h)}}{-\delta + \omega(\mathbf{k}_{\text{xy}}) - i\Gamma(\mathbf{k}_{\text{xy}})/2}. \tag{4.14}$$

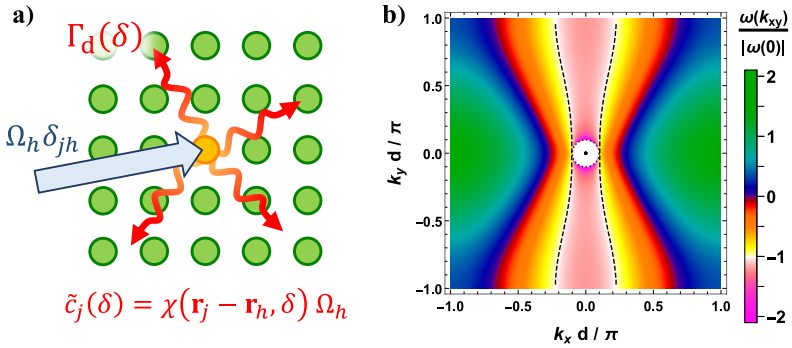

Figure 4.4: Optical properties of a 2D array. a) A single, distinguishable atom at $\mathbf{r}_h$ in a 2D array is selectively driven by a weak input field of Rabi frequency Ω_h (blue arrow). Dipole-dipole interactions between atoms allow other atoms j in the array to become excited by an amount proportional to the susceptibility $\chi(\mathbf{r}_j - \mathbf{r}_h, \delta)$. The rate of such a process is given by $\Gamma_d(\delta) = -2\text{Im}\,[\Omega_h/\tilde{c}_h(\delta)] = -2\text{Im}\,1/\chi(0,\delta)$. b) Dispersion relation $\omega(\mathbf{k}_{xy})$ of a 2D atomic array, within the first Brillouin zone. The lattice constant is chosen as $d = \lambda_0/20$, while the black, dashed line and the black point at the center represent the isoenergetic modes with $\omega(\mathbf{k}_{xy}) = \omega(0)$. The modes with $|\mathbf{k}_{xy}| < k_0$ that radiate into free space are inside the boundary given by the dotted black circle.

The physical meaning of these operators is given by the first-order expansion of the Dyson equation, which leads to the steady state $|\psi_{2D}\rangle = (1 + \hat{G}_\chi(\delta)\hat{\mathcal{H}}_{\text{drive}})\,|G\rangle$. For the case of a selectively driven atom, one has the driving field Hamiltonian $\hat{\mathcal{H}}_{\text{drive}} = -\Omega_h \sum_\sigma \left(b^\dagger_{ph\sigma} b_{sh\sigma} + h.c.\right)$, which leads to the coefficients

$$\tilde{c}_j(\delta) = \chi(\mathbf{r}_j - \mathbf{r}_h, \delta)\,\Omega_h. \tag{4.15}$$

Some of the energy provided by the drive will naturally be radiated into free space, through the excitation of collective modes $|\mathbf{k}_{xy}| \leq k_0$ with non-zero radiative decay rate $\Gamma(\mathbf{k}_{xy})$. However, at small lattice constants $d \ll \lambda_0$ this channel is negligible compared to the amount of energy that has gone into exciting non-radiative modes with $|\mathbf{k}_{xy}| > k_0$, which subsequently propagate outward from $\mathbf{r}_h$ along the array itself. To illustrate this, we first plot $\omega(\mathbf{k}_{xy})$ within the first Brillouin zone $|k_x|, |k_y| < \pi/d$ in Fig. 4.4-b for a lattice constant $d = \lambda_0/20$ that is small compared to the resonant wavelength. For $d \ll \lambda_0$, the first Brillouin zone is dominated by the region outside the light cone $|\mathbf{k}_{xy}| > k_0$.

Restricting the integration in Eq. 4.14 to this dominant region, one has $\Gamma(\mathbf{k}_{xy}) = 0$, while the energy scale is dictated by the near-field ($\sim 1/r^3$)

component of the Green's function, leading to the functional form $\omega(\mathbf{k}_{xy}) \sim \Gamma_0 f(\mathbf{k}_{xy}d/\pi)(\lambda_0/d)^3$. Considering that the region of integration scales as $\mathrm{d}\mathbf{k}_{xy} = (\pi/d)^2 \mathrm{d}(\mathbf{k}_{xy}d/\pi)$, one then obtains the final scaling[1] $\chi(\mathbf{r}_j - \mathbf{r}_h, \delta) \sim d^3/(\Gamma_0\lambda_0^3)$. In Appendix D.1, we discuss how we can verify this scaling by means of numerical simulations. We note that $\chi(0,\delta)$ can have an imaginary component describing work done by the drive on atom h. This occurs if there exists an isoenergy contour where $\omega(\mathbf{k}_{xy}) = \delta$ (see the dashed black curve in Fig. 4.4-b for the contour $\omega(\mathbf{k}_{xy}) = \omega(0)$), allowing the drive to resonantly excite a continuum of non-radiative modes. Specifically, the quantity

$$\Gamma_{\mathrm{d}}(\delta) = -2\mathrm{Im}\left[\frac{\Omega_h}{\tilde{c}_h(\delta)}\right] = -2\mathrm{Im}\left[\frac{1}{\chi(0,\delta)}\right], \tag{4.16}$$

quantifies the rate at which energy is irradiated into the atomic array via the selectively driven atom (as pictorially described by the wavy arrows in Fig. 4.4-a).

4.3.2 2D array with defects

Similarly to the previous case, we here consider a scenario where the translational symmetry is broken within a 2D atomic array, which will be helpful for the quantum chemistry problem. Specifically, we study the problem of a 2D array illuminated by a normally incident plane wave of Rabi frequency Ω_0, but with a single missing atom at site $\mathbf{r} = \mathbf{r}_h$. Such a system is pictorially represented in Fig. 4.5-a.

Working in the usual weak driving limit, it is convenient to write the steady-state, single-excitation amplitude of atom j as $c_j(\delta) = c_{\mathrm{E}}(\delta) + \tilde{c}_j(\delta)$. Here, $c_{\mathrm{E}}(\delta)$ is the solution for a defect-free, uniformly driven array given in Eq. 4.5, while $\tilde{c}_j(\delta)$ is the solution for an array with a single driven atom at $\mathbf{r}_h$ given in Eq. 4.15. This expression is valid provided that $\Omega_h = -c_{\mathrm{E}}(\delta)/\chi(0,\delta)$ is chosen such that $c_h(\delta) = c_{\mathrm{E}}(\delta) + \tilde{c}_h(\delta) = 0$. Physically, this states that the overall solution can be expressed as the coherent sum of the solution of two separate problems, of a uniformly driven perfect array and a perfect array with a single driven atom, as pictorially depicted in Fig. 4.5-b. Enforcing that $c_h(\delta) = 0$ via a proper choice of the single-atom driving amplitude Ω_h says that the atom at $\mathbf{r}_h$ has no excitation amplitude, which

[1] One can similarly prove that, in comparison, the contribution to the susceptibility $\chi(\mathbf{r}_j - \mathbf{r}_h, \delta)$ from the modes inside the light cone is negligible. Restricting the integral in Eq. 4.14 to this latter region, due to the far-field dominance we have $\omega(\mathbf{k}_{xy}) \sim \Gamma_0 f'(\mathbf{k}_{xy}/k_0)(\lambda_0/d)$. By considering $\Gamma(\mathbf{k}_{xy}) \sim \Gamma_0 g(\mathbf{k}_{xy}/k_0)(\lambda_0/d)^2$ and $\mathrm{d}\mathbf{k}_{xy} = k_0^2 \mathrm{d}(\mathbf{k}_{xy}/k_0^2)$, one can infer the scaling $\chi_{\mathrm{inside}}(\mathbf{r}_j - \mathbf{r}_h, \delta) \sim d^4/(\Gamma_0\lambda_0^4)$, so that $|\chi_{\mathrm{inside}}| \ll |\chi_{\mathrm{outside}}| \sim |\chi|$.

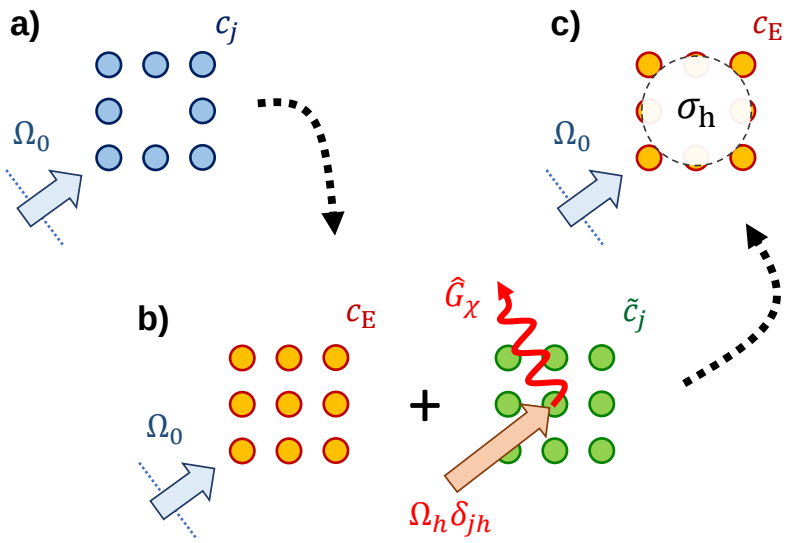

Figure 4.5: Optical response of a 2D atomic array with a hole. a) A 2D square array with coefficients c_j (blue points) and a missing atom at $\mathbf{R}_h$ is illuminated by a normally incident plane wave (blue, thick arrow), with Rabi frequency Ω_0. b) The system can be written as the sum $c_j = c_{\mathrm{E}} + \tilde{c}_j$ of a perfectly filled array with solutions c_{E} (orange points) and a perfectly filled array of coefficients $\tilde{c}_j$ where the atom placed at $\mathbf{r}_h$ is selectively driven by the Rabi frequency $\Omega_j = \Omega_h \delta_{jh}$, which is self-consistently defined to ensure that $\tilde{c}_h = -c_{\mathrm{E}}$. This distinguishable excitation spreads inside the array with a propagator $\hat{G}_\chi(\delta)$ (red, wavy arrow), which characterizes the response function $\tilde{c}_j = \chi(\mathbf{r}_j - \mathbf{r}_h)\Omega_h$. c) By accounting for the energy dispersed via $\hat{G}_\chi(\delta)$, one can finally define an effective scattering cross section $\sigma_{\mathrm{h}} \sim \lambda_0 d$ for the defect. The system is then optically equivalent to an ideal array of dipoles c_{E} with a macroscopic hole, which encompasses many lattice sites.

is equivalent to having no atom at $\mathbf{r}_h$ to begin with. The initial problem of a defect was then re-phrased as that of a selectively driven atom, already solved in Eq. 4.15. In the next subsections, we use this solution to infer some key physical insights.

4.3.2.1 Scattering cross section of a defect

To quantify the effect of a missing atom, we can calculate the scattering cross-section associated with a defect, at the (collective) resonant frequency $\omega(0)$. This latter can be calculated by means of the optical theorem [230, 231], which was already discussed in Appendix B.3. We recall that given a generic set of atomic dipoles with coefficient c_j and decay rate Γ_0, centered

around $\mathbf{r}_0$ and illuminated by Ω_j, this theorem states that the optical cross section is $\sigma = (\sigma_0/2)(\Gamma_0/\Omega_0^2)\mathrm{Im}\ \sum_j \Omega_j c_j$, where $\sigma_0 = 3\lambda_0^2/(2\pi)$ is the resonant cross section of a single atom in vacuum. As we are interested in the resonant cross section, hereafter we implicitly assume $\delta = \omega(0)$ in all the equations. For the case of a defect in a 2D array, this reduces to $\sigma_\mathrm{h} = (\sigma_0/2)(\Gamma_0/\Omega_0^2)\mathrm{Im}\ \Omega_h \tilde{c}_h = -4d^2\mathrm{Im}\ [\chi(0)\Gamma(0)]^{-1} \sim d\lambda_0$, where we have the effective coefficient of the defect $\tilde{c}_h = -c_\mathrm{E}$, and the Rabi frequency $\Omega_h = -c_\mathrm{E}/\chi(0)$, as self-consistently defined from Eq. 4.15.

It is convenient to normalize this quantity by the cross-section of a single atom in the perfect array at the same frequency, which reads $\sigma_\mathrm{a} = (\sigma_0/2)\mathrm{Im}\ [\Gamma_0 c_\mathrm{E}/\Omega_0] = 2d^2$. Their ratio $N_\mathrm{h} = \sigma_\mathrm{h}/\sigma_\mathrm{a}$ describes the number of lattice sites effectively affected by the defect, and it is given by

$$N_\mathrm{h} = \frac{\sigma_\mathrm{h}}{\sigma_\mathrm{a}} = \frac{\Gamma_\mathrm{d}(\delta = \omega(0))}{\Gamma(0)} \sim \frac{\lambda_0}{d} \gg 1, \tag{4.17}$$

where we recall that the rate of excitation of the atomic modes in the 2D array is given by $\Gamma_\mathrm{d}(\delta) = -2\mathrm{Im}\ [1/\chi(0,\delta)]$.

As pictorially shown in Fig. 4.5-d, the cross section σ_h can be interpreted as the area of the "macroscopic" hole induced by the defect (in an otherwise perfect array), as seen by resonant, incident light (similar results were suggested in [232, 233]). From Eq. 4.17, one can better understand the physical origin of such a large response due to the single defect. The quantity $\Gamma_\mathrm{d}(\delta = \omega(0))$, indeed, defines the rate of "optical losses" due to the missing atoms (at resonance). More concretely, these "losses" correspond to the energy spent in the excitation of transverse $\mathbf{k}_\mathrm{xy} \neq 0$, either non-radiative $|\mathbf{k}_\mathrm{xy}| \geq k_0$ or radiative $|\mathbf{k}_\mathrm{xy}| < k_0$ modes, which breaks down the perfect single-mode response of Section 4.2.2. In particular, the non-radiative modes will dominate at low lattice constants (as discussed in Section 4.3.1). The ratio above $\Gamma_\mathrm{d}(\delta = \omega(0))/\Gamma(0)$ then corresponds to the rate of energy effectively lost in these transverse directions, over the rate of energy actually radiated in the single-mode channel.

4.3.2.2 Optical response and self-energy

To validate the results of the previous subsection, here we analytically calculate the optical response to a normally incident plane wave of a 2D array with a missing atom at a random position $\mathbf{r}_h$. We then extend this result to the limit of many defects, under the condition that their number is much smaller than the number of total lattice sites.

We begin by considering just a single hole or removed atom in the array,

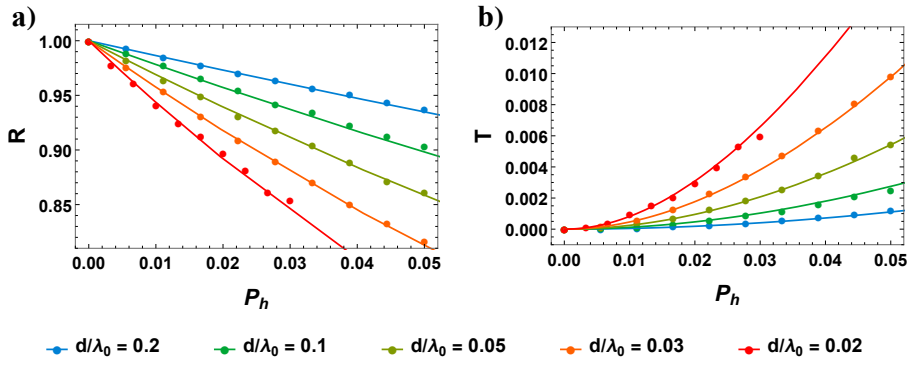

Figure 4.6: Resonant $\delta = \omega(0)$ optical response of a finite 2D array with many holes. Resonant reflectance $R = |r|^2$ (a) and transmittance $T = |t|^2$ (b), as a function of the fraction of holes P_h. Different colors are associated to different lattice constants d/λ_0. The solid lines show the predictions of our model Eq. 4.20, while the points represent the numerics, calculated for a finite system illuminated by a Gaussian beam. In this latter case, the optical properties are computed from the coupled-dipole equations, by projecting on the same mode as the input, as described in Appendix A.3. In the numerics, the response is averaged over a large number > 100 of random configurations of the positions of the defects.

at position $\mathbf{r}_h$. The solution to the excitation amplitudes of the atoms $c_j(\delta) = c_\mathrm{E}(\delta) + \tilde{c}_j(\delta)$ was provided in Section 4.3.1. Using Eq. 4.2, we can then calculate the total field. In the far field limit of $k_0|z| \gg 1$, it can be written as $\mathbf{E}(\mathbf{r}_\perp, z) \simeq \mathbf{E}_\mathrm{ideal}(z) + \mathbf{E}^h_\mathrm{defect}(\mathbf{r}_\perp, z)$, where $\mathbf{E}_\mathrm{ideal}(z)$ is the far field associated to a defect-free array, as defined in Eq. 4.7. On the other hand, the field scattered due to the defect is

$$\mathbf{E}^h_\mathrm{defect}(\mathbf{r}_\perp, z) = iE_0 \frac{\Gamma(0)}{\Omega_0} \left(\frac{d}{2\pi}\right)^2 \Omega_\mathrm{h}(\delta) \times \left[\int_{|\mathbf{k}_\mathrm{xy}|\leq k_0} \left(\frac{k_0^2 - k_\mathrm{x}^2}{k_0 k_\mathrm{z}}\right) \frac{e^{-i\mathbf{k}_\mathrm{xy}\cdot(\mathbf{r}_\perp - \mathbf{r}_h) + i|z|k_\mathrm{z}}}{-\delta + \omega(\mathbf{k}_\mathrm{xy}) - i\Gamma(\mathbf{k}_\mathrm{xy})/2} d\mathbf{k}_\mathrm{xy}\right] \widehat{\mathbf{x}}, \tag{4.18}$$

with $k_\mathrm{z} = \sqrt{k_0^2 - |\mathbf{k}_\mathrm{xy}|^2}$, and where we recall that Ω_h is self-consistently defined by Eq. 4.15. The broken translational symmetry due to the defect allows it to scatter into all directions inside the light cone, $|\mathbf{k}_\mathrm{xy}| \leq k_0$.

This result can be easily extended to the case of multiple defects, as long as they are well separated and uncorrelated, which is valid in the limit of a small fraction of defects $P_\mathrm{h} \ll 1$ over the total number of atoms. In that case, we can fairly assume that the total field is $\mathbf{E}(\mathbf{r}_\perp, z) \simeq \mathbf{E}_\mathrm{ideal}(z) + \sum_h \mathbf{E}^h_\mathrm{defect}(\mathbf{r}_\perp, z)$, implicitly stating that each defect still scatters the same

light that it would scatter if it were the only defect in the array. To infer the transmission and reflection coefficients of such a system, we first need to divide the total field into forward and backward propagating waves

$$\mathbf{E}^{+}(\mathbf{r}_{\perp},z)=\mathbf{E}_{\text{in}}(\mathbf{r})\left[1+i\frac{\Gamma(0)}{2}\frac{c_{\text{E}}(\delta)}{\Omega_0}\Theta(z)\right]+\Theta(z)\sum_h\mathbf{E}^{h}_{\text{defect}}(\mathbf{r}_{\perp},z),$$

$$\mathbf{E}^{-}(\mathbf{r}_{\perp},z)=\mathbf{E}^{*}_{\text{in}}(\mathbf{r})\left[i\frac{\Gamma(0)}{2}\frac{c_{\text{E}}(\delta)}{\Omega_0}\Theta(-z)\right]+\Theta(-z)\sum_h\mathbf{E}^{h}_{\text{defect}}(\mathbf{r}_{\perp},z). \tag{4.19}$$

Then, we calculate the fraction of power scattered into the same mode as the input light, in both directions. As discussed in Appendix A.2.1, this can be calculated as $\langle\mathbf{E}_{\text{in}}|\mathbf{E}\rangle=\int d\mathbf{r}_{\perp}\,\mathbf{E}^{*}_{\text{in}}(z)\cdot\mathbf{E}(\mathbf{r}_{\perp},z)/\int d\mathbf{r}_{\perp}\,|\mathbf{E}_{\text{in}}(z)|^2$, which naturally applies to the case of paraxial Gaussian beams [152, 234, 235] or interfaces with optical fibers [156, 157], as well as for input plane waves [170]. These latter, however, have a nominally infinite power, and we account for it by calculating $\langle\mathbf{E}_{\text{in}}|\mathbf{E}\rangle$ for a finite, square system of size L^2, so that the projection correctly renormalizes to a finite value at any scale L. In the limit of $L\to\infty$, we then obtain

$$\begin{aligned}t(\delta)=\langle\mathbf{E}_{\text{in}}|\mathbf{E}^{+}\rangle&=1+i\frac{\Gamma(0)}{2}\frac{c_{\text{E}}(\delta)}{\Omega_0}\left(1+P_{\text{h}}\frac{\Omega_{\text{h}}(\delta)}{\Omega_0}\right)\\&\simeq 1+\frac{i\Gamma(0)/2}{-\delta+\omega(0)-i\Gamma(0)/2+\Sigma_{\text{h}}(\delta)},\end{aligned} \tag{4.20}$$

as well as the reflection $r(\delta)=\langle\mathbf{E}^{*}_{\text{in}}|\mathbf{E}^{-}\rangle=t(\delta)-1$. Here, we used the fact that, for each defect at transverse position $\mathbf{r}_h$, the projection $\langle\mathbf{E}_{\text{in}}|\mathbf{E}_{\text{defect}}\rangle$ only selects from Eq. 4.18 the component with $\mathbf{k}_{\text{xy}}=0$, thus not depending on the value of $\mathbf{r}_h$. At the same time, we observe that the fraction of defects emerges as $P_{\text{h}}=\sum_h d^2/L^2$, while in the last step we assume $P_{\text{h}}\ll 1$, thus defining the self-energy $\Sigma_{\text{h}}(\delta)=P_{\text{h}}/\chi(0,\delta)$. In Fig. 4.6, we numerically validate the analytic prediction in Eq. 4.20, by solving the coupled-dipole equations for a finite 2D atomic array with (randomly positioned) holes.

As expressed by Eq. 4.20, the real part Re $\Sigma_{\text{h}}(\delta)$ of the self-energy introduces an energy shift of the total resonance frequency of the collective mode $|E\rangle$ of the 2D array. At the same time, its imaginary part represents the emergence of losses (from the perspective of the single-mode $|E\rangle$), due to the energy irradiated into the other collective modes (mainly non-radiative, when $d\ll\lambda_0$). One can easily notice, indeed, that the quantity $-2\text{Im}\ \Sigma_{\text{h}}(\delta)=P_{\text{h}}\Gamma_{\text{d}}(\delta)$ is the straightforward extension of $\Gamma_{\text{d}}(\delta)$ (rep-

resenting the rate of excitation of the transverse modes through a single defect, as shown in Eq. 4.16) to the case of multiple defects.

4.3.2.3 Final remarks on a 2D array with defects

We want to conclude this section by highlighting some implications of our findings, beyond the analysis of the refractive index. In the context of atomic arrays it is generally accepted that low lattice constants can mitigate the effects of experimental, inelastic losses Γ' (that we assume are independent of the lattice constant d), by enhancing the fraction $\Gamma(0)/\Gamma' \propto (\lambda_0/d)^2$ of elastic over inelastic response. In a real experimental setting, however, some lattice sites remain likely unfilled, leading to a fraction of defects $P_\mathrm{h} \neq 0$ that might be low but still non-null. In sight of our observations, the relevant figure of merit for the elastic optical response of the 2D atomic array then reads (at low lattice constants $d \ll \lambda_0$)

$$\frac{\Gamma(0)}{\Gamma' - 2\mathrm{Im}\ \Sigma_\mathrm{h}(\delta)} \sim \frac{d}{P_\mathrm{h}\lambda_0}, \tag{4.21}$$

where we used the fact that $\Gamma(0) \propto \Gamma_0(\lambda_0/d)^2$ and $\Sigma_\mathrm{h}(\delta) \sim \Gamma_0(\lambda_0/d)^3 P_\mathrm{h}$ (as shown in Section 4.3.1). This proves the counter-intuitive result that low lattice constants might instead be detrimental in real implementations of atomic arrays, approximately when $d/\lambda_0 \lesssim P_\mathrm{h}$.

4.4 The onset of quantum chemistry

As mentioned before, our primary goal is to understand the behavior of the refractive index at densities corresponding to the onset of quantum chemistry, when the lattice constant is still large compared to the Bohr radius, i.e. $d \gg a_0$. We favor this approach because chemistry can be considered weak and can thus be treated perturbatively, which allows one to avoid the well-known theoretical and computational challenges of quantum chemistry of solids. Studying this regime also enables one to continue to treat multiple scattering non-perturbatively, which is key to understanding the limits of refractive index.

In the regime of pure optics that we studied so far, our analysis was dealing with generic two-level emitters, uniquely characterized by their resonant frequency ω_0 and spontaneous emission rate Γ_0. Within the weak chemistry limit, one has to choose the individual atomic building block of the lattice. We take hydrogen atoms, which have the advantage that the

single hydrogen atom is an exactly solvable quantum mechanics problem. Our analysis must indeed be interpreted as a simplified, very minimal model of the onset of chemistry, to highlight the first-order corrections to quantum optics. In fact, despite the specificity of considering hydrogen, we will see that the main mechanisms that limit the refractive index involve the emergence of quantum magnetism, chemistry-induced electronic density-density correlations, and tunneling dynamics of photo-excited electrons. These are rather general features in materials, which may plausibly give our model broader qualitative validity.

To be specific, we consider a rectangular lattice with constant d in the transverse plane and $d_z = 2.5d$ along the direction of light propagation, avoiding the effects of the evanescent coupling discussed in Section 4.2.3. For an isolated hydrogen atom, the transition wavelength from the 1s to $2p_x$ level is $\lambda_0 \approx 121$ nm and the corresponding spontaneous emission rate is $\Gamma_0 \approx 2\pi \times 100$ MHz. Of course, neither hydrogen nor any other material is energetically stable for arbitrary values of d, d_z. In our simplified model, we assume that the nuclei can be arbitrarily fixed for this thought experiment, while more realistic routes are discussed in Section 4.5.

4.4.1 Definition of the Hamiltonian

The Hamiltonian of Eq. 4.1 characterizes the quantum optics limit of atoms that are very far apart, compared to the spatial extension of their orbitals. In this situation, the atoms are point-like scatterers, which respond to light via their electric dipole moment.

Here, we are specifically interested in the regime of $a_0 \ll d \ll \lambda_0$. The atoms can still be fairly considered as separated objects, and we can approximate the electronic orbitals as those of isolated atoms. At the same time, the optical response is still dominated by the electric dipole moment of the atoms, since higher multipolar orders would only start to contribute at distances d comparable to the extension of the orbitals (roughly, $\sim a_0$) [144].

Nonetheless, as the tails of the orbitals bound to neighbouring nuclei start to overlap, one can identify electron hopping as a first, fundamental correction to Eq. 4.1. To model this process in our simplified scenario of hydrogen atoms, we only need to account for one electron per nucleus, which can either be in the 1s or $2p_x$ state, as characterized by the creation $\hat{b}^\dagger_{\nu i\sigma}$ and annihilation $\hat{b}_{\nu i\sigma}$ fermionic operators (defined in Eq. 4.1) of an electron with spin σ, occupying the orbital ν of atom i. At the first order, the tunneling $t_\nu \hat{b}^\dagger_{\nu i\sigma}\hat{b}_{\nu j\sigma}$, between two neighbouring $\langle ij\rangle$ sites, can be restricted

only to atoms belonging to the same 2D layer, thanks to our geometrical configuration $d_z \gg d$. This assumption strongly simplifies our calculations, allowing us to study the onset of chemistry only within the 2D arrays, to quantify how it breaks the single-mode nature of their optical response. Finally, when two electrons occupy the orbitals ν and ν' of the same atom, one need to pay an energetic penalty $U_{\nu\nu'}$, due to their Coulomb repulsion. At the same time, one needs to enforce Pauli exclusion, which forbids two electrons having the same quantum state. We can thus write the total Hamiltonian for our model as

$$\hat{\mathcal{H}}_{\rm tot} \approx \hat{\mathcal{H}}_{\rm QO} + \sum_n \hat{\mathcal{H}}_{\rm QC}^{{\rm 2D},n}, \tag{4.22}$$

where the terms $\hat{\mathcal{H}}_{\rm QC}^{{\rm 2D},n}$, represent the onset of chemistry within each n-th 2D array $\mathcal{L}_n$, reading

$$\begin{aligned}\hat{\mathcal{H}}_{\rm QC}^{\rm 2D,n} &= -\sum_{\langle ij\rangle\in\mathcal{L}_n}\sum_{\nu\sigma} t_\nu\left(\hat{b}^\dagger_{\nu i\sigma}\hat{b}_{\nu j\sigma} + h.c.\right) + \sum_{i\in\mathcal{L}_n} U_{ss}\hat{n}_{si\uparrow}\hat{n}_{si\downarrow} \\ &+ \sum_{i\in\mathcal{L}_n} U_{sp}(\hat{n}_{pi\uparrow}+\hat{n}_{pi\downarrow})(\hat{n}_{si\uparrow}+\hat{n}_{si\downarrow}).\end{aligned} \tag{4.23}$$

where we define the population operators $\hat{n}_{\nu i\sigma} = \hat{b}^\dagger_{\nu i\sigma}\hat{b}_{\nu i\sigma}$. The Hamiltonian in Eq. 4.23 (with the addition of the term $\hat{\mathcal{H}}_0$ of Eq. 4.1, which quantifies the bare orbital energies) represents the well-established two-band Fermi-Hubbard model, at half filling (due to our choice of neutral, hydrogen atoms). Here, we neglect the repulsion term U_{pp} because we are explicitly interested in the linear-optics regime of single excitation.

We now want to estimate the tunneling rates in Eq. 4.23, as a function of the lattice constant d. To this aim, we notice that $2t_s$ corresponds to the energy splitting between the two states of the ground-state manifold of the H_2^+ hydrogen molecule ion, which are approximately given by the odd/even superpositions of a 1s orbital on the two nuclei a and b, $|1s\rangle_a \mp |1s\rangle_b$, at large nuclear separation. A similar reasoning relates $2t_p$ to the p_x-state manifold of H_2^+. The energy curves of H_2^+ can be calculated with very high numerical precision (we use the numerical data of [236]) obtaining the black (t_s) and red (t_p) curves of Fig. 4.7-a. Finally, the Coulomb-repulsion energies $U_{\nu\nu'}$ can be calculate from the known orbital wave functions $\varphi_\nu(\mathbf{r}_i)$, as

$$U_{ss} = \frac{q^2}{4\pi\epsilon_0}\int d\mathbf{r}_1 d\mathbf{r}_2 \frac{1}{|\mathbf{r}_1-\mathbf{r}_2|}\varphi_{1s}^2(\mathbf{r}_1)\varphi_{1s}^2(\mathbf{r}_2), \tag{4.24}$$

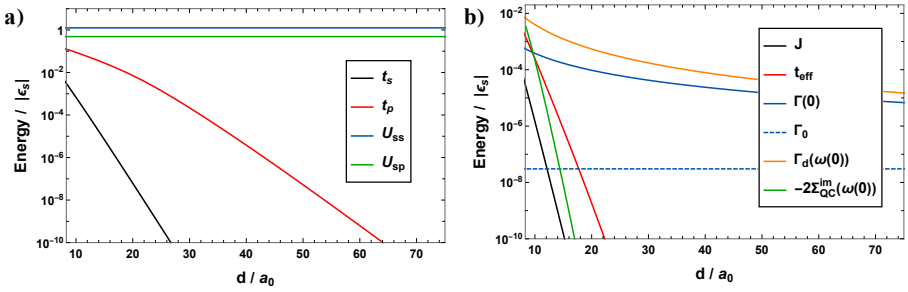

Figure 4.7: Estimation of the relevant energies and rates. a) Numerical values of the tunneling rates t_s (black) and t_p (red) used in our calculations for the ground and excited state electrons, respectively, as a function of scaled lattice constant d/a_0. These rates are inferred from the spectrum of the H_2^+ hydrogen molecule ion. We also plot the on-site interaction energies U_{ss} (blue) and U_{sp} (green), as calculated from the isolated hydrogen atom. Energies are shown in units of the Rydberg constant $|\epsilon_s|$. b) Heisenberg interaction strength J (black) and p-orbital impurity tunneling rate $t_{\rm eff}$ (red) as a function of lattice constant, and in units of the Rydberg constant. The solid and dashed blue lines indicate the collective emission rate $\Gamma(0)$ of an ideal 2D lattice in the quantum optics limit, and the emission rate Γ_0 of an isolated hydrogen atom, respectively. The orange line represents the resonant emission rate $\Gamma_{\rm d}(\delta = \omega(0))$ related to a selectively driven atom in an array, as discussed in Section 4.3.1. The green curve captures the effective dissipation rate in the optical response of a 2D array, due to quantum chemistry. On resonance, this is quantified by $-2\mathrm{Im}\,\Sigma_{\rm QC}(\delta = \omega(0))$.

and

$$U_{sp} = \frac{q^2}{4\pi\epsilon_0}\int d\mathbf{r}_1 d\mathbf{r}_2 \frac{1}{|\mathbf{r}_1 - \mathbf{r}_2|}\varphi_{1s}^2(\mathbf{r}_1)\varphi_{2p_x}^2(\mathbf{r}_2), \tag{4.25}$$

which can be solved analytically by expanding the Coulomb potential in spherical harmonic functions. One obtains $U_{ss} = 5|\epsilon_s|/4$ (blue line of Fig. 4.7-a) and $U_{sp} = 118|\epsilon_s|/243$ (green line), where $\epsilon_s \approx -13.6$ eV is the hydrogen ground-state energy.

The Fermi-Hubbard model in Eq. 4.23 certainly over-simplifies the full quantum chemistry problem of an array of hydrogen atoms. Perhaps most prominently, the on-site interaction energies $U_{\nu\nu'}$, as estimated above, are on the order of the ionization energy of hydrogen itself, which implies that higher bands should be needed to accurately reproduce the full electronic wave functions of the array. Nonetheless, state-of-the-art computational quantum chemistry calculations [237] on the ground state of a 1D hydrogen chain at large lattice constants suggest that the Fermi-Hubbard model well describes the key physics. Although such a direct comparison in 2D is beyond numerical capabilities, we take the 1D results as sufficient justifica-

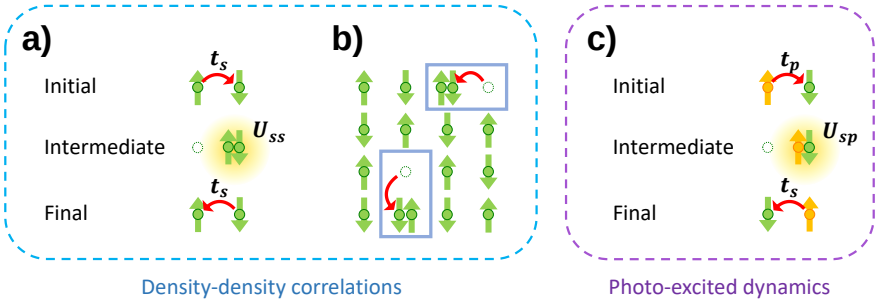

Figure 4.8: Illustration of the relevant perturbative processes in the two-band, Fermi-Hubbard model. a) Mechanism giving rise to anti-ferromagnetic Heisenberg spin interactions between nearest-neighbour electrons in their s-orbitals. An electron tunnels to its nearest neighbour, producing an intermediate state with large energy $E = U_{ss}$ (due to on-site interactions), and forcing an electron to tunnel back. This process is only allowed provided the two electrons have different spins, due to Pauli exclusion. b) The Heisenberg spin interaction leads to an anti-ferromagnetic Néel order for the many-body ground state, as qualitatively illustrated here by the checkerboard pattern of up and down spins of the s-orbital electrons. At next order in perturbation theory, the intermediate state illustrated in (a) manifests itself in the many-body ground state through the appearance of bound holon-doublon pairs (the pairs of sites outlined by rectangles), which reflect the electronic density-density correlations generated by the interactions. These pairs consist of a holon (dashed circle), i.e. a nucleus without an electron, and a neighbouring doublon with two electrons. c) An analogous process to (a) can occur if an electron on one site is in its p-orbital (with the p-orbital state indicated by orange) and a neighbour is in its s-orbital (indicated by green). Note that going from the initial to the final state, both the spin and orbital degrees of freedom between the sites have been exchanged.

tion for the reduction to the 2D Fermi-Hubbard model.

Starting from Eq. 4.23, we can identify two relevant physical aspects, that we introduce here below. In the next section, we will discuss in detail how they affect the optical response.

- **Dynamics in the low-energy sector.** The dynamics and the physical properties encoded in Eq. 4.23 can be conveniently studied by further simplifying our Hamiltonian. To do so, we realize from Fig. 4.7-a that the on-site interaction terms U_{ss}, U_{sp} greatly exceed the tunneling rates t_s, t_p, in the regime of interest of $d \gg a_0$ (roughly, when $d \gtrsim 10a_0$). The Hilbert space thus separates into a low-energy manifold consisting of one electron per site, and a high-energy manifold where two electrons occupy the same nucleus. The dynamics within the low-energy sector is characterized by perturbative, virtual processes

which involve higher-energy states. Specifically, within second-order perturbation theory, an electron can tunnel to a neighbour nucleus to create a virtual state with higher energy, followed by tunneling of an electron back to the empty site. The relevant situations are then illustrated in Fig. 4.8. Specifically, in Fig. 4.8-a we show the case of an electron in its s-orbital hopping into a site already occupied by an electron in its s-orbital, with an energy price of $E = U_{ss}$. Due to Pauli exclusion, this process is restricted to electrons having opposite spins, and it gives rise to anti-ferromagnetic Heisenberg interactions of strength $J = 4t_s^2/U_{ss}$ (black curve of Fig. 4.7-b) between the spin degrees of freedom of nearest neighbour electrons. Another relevant case is that depicted in Fig. 4.8-c. There, a p-orbital electron can first tunnel to a nearest neighbour already containing an s-orbital electron, to create a high-energy intermediate state of energy $E = U_{sp}$. The s-orbital can then tunnel back to replace the p-orbital on its original site, with an overall rate of $t_{\text{eff}} = 2t_s t_p/U_{sp}$ (red curve of Fig. 4.7-b). This includes as well the analogous case of a s-orbital electrons tunneling to a site occupied by a p-orbital electron, which then replaces the first electron in its original site.

The emerging Hamiltonian for the low-energy sector is given by the *so-called* tJ model, reading

$$\hat{\mathcal{H}}_{\text{QC}}^{\text{2D,n}} \approx \underbrace{J \sum_{\langle ij\rangle \in \mathcal{L}_n} \hat{\mathbf{S}}_i \cdot \hat{\mathbf{S}}_j}_{\hat{\mathcal{H}}_J} \underbrace{-t_{\text{eff}} \sum_{\langle ij\rangle \in \mathcal{L}_n} \sum_{\sigma\sigma'} \left(\hat{b}_{pi\sigma}^\dagger \hat{b}_{pj\sigma} \hat{b}_{sj\sigma'}^\dagger \hat{b}_{si\sigma'} + h.c. \right)}_{\hat{\mathcal{H}}_t}, \tag{4.26}$$

which can be formally derived from Eq. 4.23 by projecting the dynamics into the low-energy manifold via a Schrieffer-Wolff transformation [238]. Here, the (isotropic) Heisenberg interaction $\hat{\mathcal{H}}_J$ reflects the onset of quantum magnetism due to quantum chemistry, by coupling the spin operators $\hat{S}_i^\alpha = \sum_{\sigma\sigma'} \hat{b}_{si\sigma}^\dagger \tau_{\sigma\sigma'}^\alpha \hat{b}_{si\sigma'}/2$, where τ^α is the α-th Pauli matrix. As a result, the global state of the spins in the ground state has anti-ferromagnetic Néel order.

- **Holon-doublon pairs.** Now, we neglect the dynamics involving an excited electron in its p-orbital, and we focus more in detail on the ground-state properties within the manifold where all electrons are in their s-orbitals. Specifically, while $\hat{\mathcal{H}}_J$ describes the perturbative effect of tunneling within the low-energy manifold of one electron per nucleus, at next order of perturbation theory the intermediate states

in Fig. 4.8-a lead to a total ground state illustrated in Fig. 4.8-b, where there is a small probability $\sim (t_s/U_{ss})^2$ to find holon-doublon pairs consisting of two electrons on one nucleus (doublon) and no electrons on a nearest neighbour (holon). More precisely, one can calculate the fraction of sites occupied by holons or doublons via the slave-fermion formalism introduced in [239]. In the thermodynamic limit, the number of holon-doublon pairs over the total number of lattice sites is given by

$$P_{\mathrm{hd}} \approx 2.58 \left(\frac{t_s}{U_{ss}}\right)^2 . \tag{4.27}$$

These holon-doublon pairs are a manifestation of density-density correlations that emerge due to quantum chemistry. To make this statement more concrete, we consider, from the full Hamiltoninan Eq. 4.23, the terms that only involve s-orbital electrons, and we study the system in its ground state. At any perturbative order, the electron-density operator $\hat{\mathcal{D}}_j = \sum_{\nu\sigma} \hat{n}_{\nu j\sigma}$ must have a homogeneous, mean value of one electron in each lattice site, i.e. $\langle\hat{\mathcal{D}}_j\rangle = 1$, $\forall j$, due to both the half-filling condition $\sum_j \langle\hat{\mathcal{D}}_j\rangle = N$ and the full translational symmetry, which guarantees the homogeneity $\langle\hat{\mathcal{D}}_j\rangle = \langle\hat{\mathcal{D}}_i\rangle$, $\forall i, j$. Within the low-energy sector (by definition), this operator has zero variance $\langle\hat{\mathcal{D}}_i^2\rangle - \langle\hat{\mathcal{D}}_i\rangle^2 = 0$. At higher perturbative orders, however, due to the virtual processes of Fig. 4.8-a, the variance around the (homogeneous) mean value becomes non-zero. This means that a non-null probability exists, per lattice site, of encountering either a holon or a doublon, which can be described with the population P_{hd}. At the same time, this is accompanied with the emergence of spatial correlations $\langle\hat{\mathcal{D}}_i\hat{\mathcal{D}}_j\rangle - \langle\hat{\mathcal{D}}_i\rangle\langle\hat{\mathcal{D}}_j\rangle \neq 0$ for nearest neighbours.

4.4.2 Optical response at the onset of chemistry

Here, we analyze in detail how we expect that the onset of chemistry can alter the optical response of each 2D atomic layer. We begin by recalling the main result in the quantum optics limit of Section 4.2.3, involving only the $\hat{\mathcal{H}}_{\mathrm{QO}}$ term of Eq. 4.22. In particular, for weak light at normal incidence, a 2D array behaves as a single-mode system, where the light excites only a single collective mode $|E\rangle$, *and* this collective mode only re-radiates light elastically at a rate $\Gamma(\mathbf{k}_{\mathrm{xy}} = 0)$ back in the same $\mathbf{k}_{\mathrm{xy}} = 0$ direction (either forward or backward). This single-mode nature of the quantum optics limit

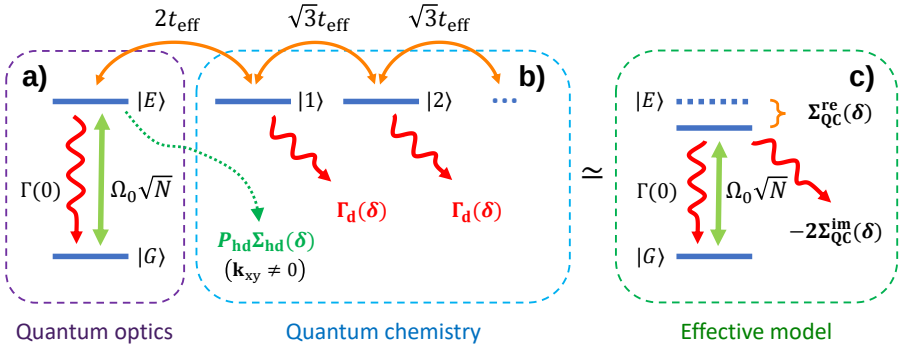

Figure 4.9: Model of optical response of a 2D atomic array including the onset of chemistry. a) In the quantum optics regime, a large refractive index is achieved due to the single-mode response of an individual 2D layer, where weak incident light only couples the many-electron ground state $|G\rangle$ to a single collective excited state $|E\rangle$, and this state emits elastically back into the same optical mode at a rate $\Gamma(0)$. b) Quantum chemistry allows for inelastic or spatial multi-mode emission. Spatial multi-mode emission into directions $\mathbf{k}_{\text{xy}} \neq 0$ arises from light scattering off of electronic density-density correlations, in the form of holon-doublon pairs (dashed green arrow). Hopping of the photo-excited electron at a rate $\sim t_{\text{eff}}$ couples the excited states to a continuum of additional states $|n\rangle$, labeled by an integer n that describes the degree to which the hopping disturbs the anti-ferromagnetic Néel order of the electron spins, as described further in the main text. This process, along with the effective decay rate $\Gamma_{\text{d}}(\delta) = -2\text{Im}\ 1/\chi(0,\delta)$ of the excited electron, lead to inelastic emission. c) The various quantum chemistry processes illustrated in Fig. 4.9-b give rise to a modified optical response of the 2D layer, which can be captured by a complex self energy $\Sigma_{\text{QC}}(\delta)$ of the excited state $|E\rangle$. The real and imaginary parts describe an chemistry-induced energy shift and effective inelastic decay rate, respectively.

is illustrated in Fig. 4.9-a (dashed purple box), and produces the large, purely real refractive index of a 3D lattice. One effect that emerges due to quantum chemistry is the appearance of anti-ferromagnetic Néel ordering in the spin component $|\sigma\rangle$ of the many-electron ground state $|G\rangle$, as discussed in Section 4.4.1. This same spin wave function is inherited by $|E\rangle$, as the exciting light does not affect spin. The Néel ordering in itself thus does not alter the refractive index.

In contrast, the excited electron dynamics and the density-density correlations break the single mode response by allowing for inelastic or spatial multi-mode emission processes, as illustrated in Fig. 4.9-b (dashed blue box). Specifically, they give rise to optical processes analogous to those discussed in Section 4.3, which can be incorporated into a frequency-dependent effective level shift and inelastic decay rate of the excited state, as charac-

terized respectively by the real and imaginary parts of a self-energy term $\Sigma_{\mathrm{QC}}(\delta)$ (see Fig. 4.9-c). We now discuss these processes more in detail.

4.4.2.1 Dynamics of photo-excited electron

In this subsection, we neglect density-density correlations (i.e. assuming exactly one electron per site), and focus on the effect of photo-excited electron dynamics as described by the tJ-model Hamiltonian of Eq. 4.26. Instead of dealing directly with $\hat{\mathcal{H}}_{\mathrm{tJ}}$, we will work with the simpler $\mathrm{tJ_z}$ model, which is known to capture well the dynamics at short times [240]. In the $\mathrm{tJ_z}$ model, only the z components of the spins are assumed to interact, which is enforced by replacing the Heisenberg coupling $\hat{\mathcal{H}}_J$ with the anti-ferromagnetic, Ising coupling $\hat{\mathcal{H}}_{J_z} = \sum_{\langle ij\rangle\in\mathcal{L}_n} S_i^z S_j^z$. In this case, the classical anti-ferromagnetic Néel order describes exactly the global spin ground state configuration $|\sigma\rangle$ of the electronic ground state $|G\rangle$ and excited state $|E\rangle$, as illustrated in Fig. 4.10-a,b. The excited state is an equal superposition of the excited p-orbital being located at different sites, as we qualitatively show in Fig. 4.10-b by depicting two representative configurations in the overall superposition.

We thus want to derive the index of the system evolving under Eq. 4.22 with the replacement chemistry described by the $\mathrm{tJ_z}$-model of Eq. 4.26 (with only $\hat{\mathbf{z}}$-spins interacting). We also assume that due to the small magnitude of J (compared to both $\Gamma(0)$ and t_{eff}, as seen in Fig. 4.7-b), the energies E_σ of different spin configurations will be non-zero but negligible from the standpoint of the dynamical evolution $e^{-iE_\sigma t}$, so that $\hat{\mathcal{H}}_{J_z}$, although defining the spin ground state, doesn't directly affect the dynamics. Furthermore, we ignore the contributions of $\hat{\mathcal{H}}_{\mathrm{drive}}$ beyond the matrix element connecting $|G\rangle$ and $|E\rangle$, as all other contributions only lead to multi-photon corrections in the refractive index that are nonlinear in the field intensity.

The first non-trivial effect beyond the quantum optics limit arises from $\hat{\mathcal{H}}_{\mathrm{t}}$ acting on $|E\rangle$. As illustrated in Fig. 4.10-b, we can express the state $|E\rangle = \left(\sum_j |\mathbf{r}_j\rangle/\sqrt{N}\right)\otimes|\sigma\rangle$ as an equal-weight superposition, where $|\mathbf{r}_j\rangle$ denotes that the excited p-orbital is located at site $\mathbf{r}_j$ and $|\sigma\rangle$ is the ground-state spin configuration. The Hamiltonian $\hat{\mathcal{H}}_{\mathrm{t}}$ allows the excited electron to exchange both its orbital and spin degrees of freedom with any nearest neighbor, thus coupling $|E\rangle$ to the new normalized state

$$|1\rangle = \frac{1}{2\sqrt{N}}\sum_j \sum_{\boldsymbol{\delta}_1=\pm d\widehat{\mathbf{x}},\pm d\widehat{\mathbf{y}}} |\mathbf{r}_j+\boldsymbol{\delta}_1\rangle|\sigma_{j,\boldsymbol{\delta}_1}\rangle, \tag{4.28}$$

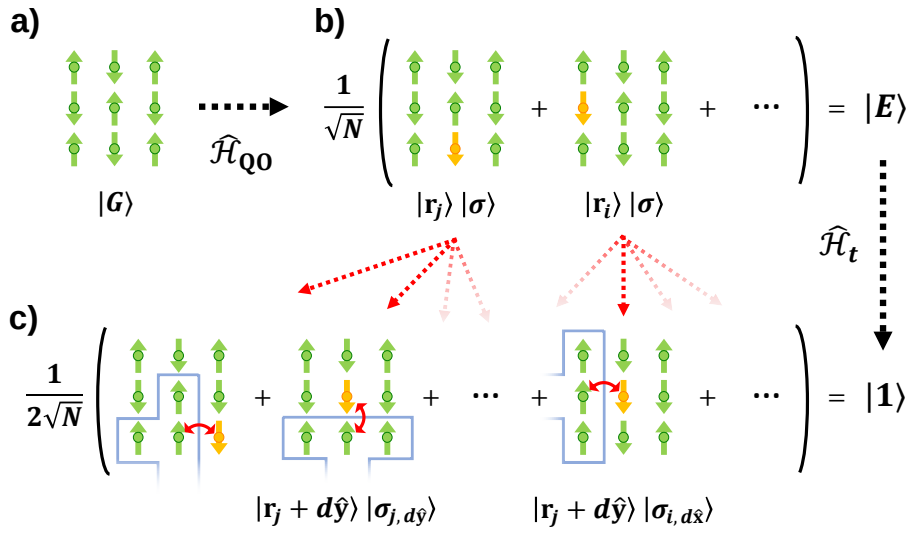

Figure 4.10: Physics of the $\mathrm{tJ_z}$ model. a) The many-body ground state of the 2D array consists of a single s-orbital electron per site (green), with classical anti-ferromagnetic Néel order of the spins, as indicated by the arrows. b) A single incident photon excites the array into the superposition state $|E\rangle$, where any electron at site i is equally excited to a p-orbital (yellow) without changing the spin. c) Dynamics of the excited electron via the Hamiltonian $\hat{\mathcal{H}}_t$ couples the state $|E\rangle$ to the state $|1\rangle$, a superposition state of all possibilities where the p-orbital can exchange orbital and spin degrees of freedom with an s-orbital electron in a neighbouring site (solid red arrows). This dynamics breaks the perfect anti-ferromagnetic order for the s-orbital electrons inside the blue boxes. Certain configurations making up the superposition are labeled and described further in the main text.

where $|\mathbf{r}_j + \boldsymbol{\delta}_1\rangle$ describes the position of the p-orbital following a move in the nearest neighbor direction $\boldsymbol{\delta}_1$ and $|\sigma_{j,\boldsymbol{\delta}_1}\rangle$ is the spin state following the corresponding spin exchange. All spin states are orthogonal to one another $\langle\sigma_{j,\boldsymbol{\delta}_1}|\sigma_{j',\boldsymbol{\delta}_1'}\rangle = \delta_{j,j'}\delta_{\boldsymbol{\sigma}_1,\boldsymbol{\sigma}_1'}$, and the state $|1\rangle$ is entangled in the orbital and spin degrees of freedom. The matrix element of the interaction is $\langle 1|\hat{\mathcal{H}}_{\mathrm{t}}\,|E\rangle = -2t_{\mathrm{eff}}$.

A key consequence of the above discussion is that the dynamics of $\hat{\mathcal{H}}_{\mathrm{t}}$ results in distinguishable spin backgrounds, even when the p-orbital winds up on the same final site. This is illustrated in Fig. 4.10-b, where we explicitly show two positions $|\mathbf{r}_j\rangle$ and $|\mathbf{r}_i = \mathbf{r}_j - d\hat{\mathbf{x}} + d\hat{\mathbf{y}}\rangle$ of the p-orbital in the state $|E\rangle$, and in Fig. 4.10-c, where we draw the new orbital states $|\mathbf{r}_j + d\hat{\mathbf{y}}\rangle$ following an upward move and $|(\mathbf{r}_j - d\hat{\mathbf{x}} + d\hat{\mathbf{y}}) + d\hat{\mathbf{x}})\rangle = |\mathbf{r}_j + d\hat{\mathbf{y}}\rangle$ following a rightward move, respectively. Despite the orbital wave functions being the

same, the orthogonality of the associated spin wave functions $|\sigma_{j,d\widehat{\mathbf{y}}}\rangle$ and $|\sigma_{i,d\widehat{\mathbf{x}}}\rangle$ is particularly easy to see by examining the blue boxes enclosing the s-orbital electrons where the original perfect Néel order has been broken as a result of the p-orbital motion. Note that should broken order be left behind once the p-orbital relaxes by photon emission, the photon emission will be inelastic and thus contributes an imaginary component to the refractive index.

To calculate the effect on the index, we must understand how state $|1\rangle$ further evolves under excited-state hopping dynamics and dipole-dipole interactions, as contained in the approximate Hamiltonian $\hat{\mathcal{H}}_{\rm t} + \hat{\mathcal{H}}_0 + \hat{\mathcal{H}}_{\rm dip-dip}$ (from above, recall that we ignore $\hat{\mathcal{H}}_{J_z}$ and $H_{\rm drive}$ in subsequent evolution). These processes are pictorially described in Fig. 4.9-a, by orange ($\hat{\mathcal{H}}_{\rm t}$) and red, wavy arrows ($\hat{\mathcal{H}}_0 + \hat{\mathcal{H}}_{\rm dip-dip}$). Due to the different scalings of the interactions seen in Fig. 4.7-b, we consider simpler limits where either $\hat{\mathcal{H}}_{\rm t}$ or $\hat{\mathcal{H}}_0 + \hat{\mathcal{H}}_{\rm dip-dip}$ completely dominates. In any case, from the standpoint of $|E\rangle$, these dynamics couple this state to a continuum, leading for example, to an effective decay rate other than the preferred elastic emission channel, decreasing in optical response. Our goal is to quantify this in terms of a "self-energy" contribution to state $|E\rangle$.

- **Case when $\hat{\mathcal{H}}_0 + \hat{\mathcal{H}}_{\rm dip-dip}$ dominates.** We first consider when $\hat{\mathcal{H}}_0 + \hat{\mathcal{H}}_{\rm dip-dip}$ dominates subsequent evolution of $|1\rangle$. Since $\hat{\mathcal{H}}_0 + \hat{\mathcal{H}}_{\rm dip-dip}$ does not couple to spins, the various states in $|1\rangle$ with different spin backgrounds $|\sigma_{j,\boldsymbol{\delta}_1}\rangle$ always retain orthogonality in subsequent evolution under $\hat{\mathcal{H}}_0 + \hat{\mathcal{H}}_{\rm dip-dip}$. This implies that the excited p-orbital $|\mathbf{r}_j + \boldsymbol{\delta}_1\rangle$ in $|1\rangle$ is "distinguishable" in complete analogy to the situation studied in Section 4.3.1, where we considered an array in the quantum optics limit with a single atom selectively driven by an external source. In particular, each orbital configuration $|\mathbf{r}_j + \boldsymbol{\delta}_1\rangle$ represents an excitation deposited on a selected atom, which can spread inside the array through the propagator $\hat{G}_\chi(\delta) = -(\hat{\mathcal{H}}_0 + \hat{\mathcal{H}}_{\rm dip-dip})^{-1}$ (in the rotating frame of the incident light) of Eq. 4.13. One of the consequences is an effective decay rate $\Gamma_{\rm d}(\delta) = -2\mathrm{Im}\ 1/\chi(0,\delta)$ as seen by the distinguishable excitation, which is depicted by red, wavy arrows in Fig. 4.9-b from the state $|1\rangle$. This analogy is manifestly seen once we use the Nakajima-Zwanzig formalism [241] to integrate out the excited states $|\mathbf{r}_j + \boldsymbol{\delta}_1\rangle$ and the continuum to which they couple, to produce an effective non-Hermitian dynamics on state $|E\rangle$. The resulting complex self-energy, encoding the coherent energy shift and decay rate due to this coupling to a continuum, is given

by $\Sigma_t(\delta) = \langle E|\hat{\mathcal{H}}_{\rm t}\hat{G}_\chi(\delta)\hat{\mathcal{H}}_{\rm t}\,|E\rangle = -4t_{\rm eff}^2\chi(0,\delta)$ [229, 241, 242]. The appearance of the susceptibility χ defined by a *classical* optics calculation confirms the analogy. To conclude, in Appendix D.2.1 we report an alternative approach to calculate the same self-energy $\Sigma_{\rm t}(\delta)$, by directly solving the equations of motion at the steady-state.

- **Case when $\hat{\mathcal{H}}_t$ dominates.** We now consider the opposite limit where $\hat{\mathcal{H}}_{\rm t}$ dominates the subsequent dynamics of the state $|1\rangle$. Besides returning back to $|E\rangle$, $\hat{\mathcal{H}}_{\rm t}$ connects $|1\rangle$ to an additional orthogonal state $|2\rangle$ characterized by $n = 2$ non-trivial hops of the p-orbital relative to its position in the original state $|E\rangle$,

$$|2\rangle = \frac{1}{2\sqrt{3N}}\sum_j \sum_{\boldsymbol{\delta}_{1,2}=\pm d\hat{\mathbf{x}},\pm d\hat{\mathbf{y}}} (1-\delta_{\boldsymbol{\delta}_1,-\boldsymbol{\delta}_2})\,|\mathbf{r}_j+\boldsymbol{\delta}_1+\boldsymbol{\delta}_2\rangle|\sigma_{j,\boldsymbol{\delta}_1,\boldsymbol{\delta}_2}\rangle. \tag{4.29}$$

  The corresponding matrix element is $\langle 2|\hat{\mathcal{H}}_{\rm t}|1\rangle = -\sqrt{3}t_{\rm eff}$. The state $|2\rangle$ has an increased number of nearest neighbors with broken Néel ordering, with the spin states $|\sigma_{j,\boldsymbol{\delta}_1,\boldsymbol{\delta}_2}\rangle$ being orthogonal to one another and to the spin states in $|1\rangle$ and $|E\rangle$. For a larger number of hops $n > 2$, a standard approximation is to assume that spin backgrounds are always distinguishable [243, 244]. Then, the problem reduces to hopping on a Bethe lattice and the matrix elements are $\langle n+1|\hat{\mathcal{H}}_{\rm t}|n\rangle = -\sqrt{3}t_{\rm eff}$ for $n \geq 1$ (see Appendix D.2.2).

  Intuitively, the effect of hopping over the states $|n\rangle$ will dominate the effective dissipation seen by the state $|E\rangle$ when $t_{\rm eff} \gg \Gamma_{\rm d}(\delta)$. As shown in Fig. 4.7, in the relevant range of lattice constants $d \gg a_0$, this regime never occurs when illuminating the system exactly at the resonance $\delta = \omega(0)$. However, hopping to other states $|n\rangle$ can become important for other near-resonant driving frequencies $\delta \neq \omega(0)$. Hopping on the Bethe lattice has been previously solved in [245], with the main results summarized in Appendix D.2.2. In particular, one finds that these dynamics contribute an imaginary self-energy to the the excited state $|E\rangle$, reading $\Sigma_{\rm t}(\delta) = -4it_{\rm eff}$. This intuitively states that the effective decay rate from $|E_{\mathbf{k}_{\rm xy}=0}\rangle$ to the continuum of states $|n\rangle$ is proportional to the hopping matrix element itself.

Up to now, we have considered the limits where either $\hat{\mathcal{H}}_t$ or $\hat{\mathcal{H}}_{\rm dip-dip}$ dominates the dynamics from the state $|1\rangle$. To include both effects, we can

use the simplified, phenomenological formula

$$\Sigma_{\mathrm{t}}(\delta) = \frac{4t_{\mathrm{eff}}^2\chi(\delta,0)}{it_{\mathrm{eff}}\chi(\delta,0)-1}, \tag{4.30}$$

which interpolates between the results obtained in the two limits. This is the main result of this section, as it reduces all of the chemistry-induced photon-excited electron dynamics to an effective complex self-energy correction to the excited state $|E\rangle$.

4.4.2.2 Density-density correlations

We now ignore the p-orbital dynamics of $\hat{\mathcal{H}}_t$, and consider just the effect of ground-state density-density correlations under the quantum optics Hamiltonian $\hat{\mathcal{H}}_{\mathrm{QO}}$. The holon (nucleus with no electron) and doublon (approximately a negatively charged hydrogen ion) have a completely different response to light and in particular do not efficiently couple to light near resonance with the neutral hydrogen transition. At large d/a_0, we can thus model the optical response of the holon-doublon pair in the otherwise perfect array as a *classical* array of point dipoles with two consecutive empty sites. The breaking of discrete translational symmetry by these two sites induces light scattering from the incident direction into random ones, effectively leading to an imaginary contribution to the index.

Specifically, we want to quantify the optical properties of an array with a fraction $P_{\mathrm{hd}} \ll 1$ of holon-doublon pairs, as defined in Section 4.4.1 (i.e. number of pairs over the total number of lattice sites). Assuming that the density of pairs is low enough that the emission from different pairs is uncorrelated, we can proceed in an analogous fashion to Section 4.3.2.2, where we calculated the optical response of an array with a small fraction P_{h} of random holes. A naive guess would be to simply replace $P_{\mathrm{h}} \to 2P_{\mathrm{hd}}$ in Eq. 4.20 to account for the fraction of sites occupied by holons or doublons. However, the fact that a holon-doublon pair occupies neighboring sites means that their scattering is correlated, and leads to a modest correction that we now derive. To properly address this, we begin by solving a 2D array with a pair of neighboring defects at positions $\mathbf{r}_{h^\pm}$, similarly to the single-defect case, defining the Rabi frequency $\Omega_{\mathsf{hd}}(\delta)/2$, which self-consistently drives the two defects to ensure $\tilde{c}_{h^\pm}(t) = -c_{\mathrm{E}}(\delta)$. At the steady state, one obtains $\tilde{c}_j(\delta) = [\chi(\mathbf{r}_j - \mathbf{r}_{h^+},\delta) + \chi(\mathbf{r}_j - \mathbf{r}_{h^-},\delta)]\Omega_{\mathsf{hd}}(\delta)/2$. The transmission and reflection coefficients for a low density of defects $P_{\mathrm{hd}} \ll 1$ can be calculated by directly generalizing the procedure of Section 4.3.2.2, leading to a structural form identical to Eq. 4.20, with the replacement of the single-hole

self-energy $\Sigma_{\rm h}(\delta)$ with the holon-doublon self-energy

$$\Sigma_{\rm hd}(\delta) = \sum_{\widehat{\mathbf{a}}=\widehat{\mathbf{x}},\widehat{\mathbf{y}}} \frac{P_{\rm hd}}{\chi(0,\delta)+\chi(d\widehat{\mathbf{a}},\delta)}, \tag{4.31}$$

which is averaged over the two possible orientations $\widehat{\mathbf{a}} = \widehat{\mathbf{x}}, \widehat{\mathbf{y}}$ of the pairs. The imaginary component of $\Sigma_{\rm hd}(\delta)$ characterizes an effective dissipation arising from the scattering of normally incident light $\mathbf{k}_{\rm xy} = 0$ into random other directions. Similarly to what shown for the single-defect case of Fig. 4.6, we have numerically calculated the classical transmission and reflection of finite-size 2D arrays with a fixed fraction of nearest-neighbour atoms removed (with a random orientation of the pair axis), finding a great agreement between the numerics and our analytical solution.

The difference in orientations arises from the anisotropic band structure of Fig. 4.4-b. In response to a plane wave near resonance $\delta \approx \omega(0)$ with the $\mathbf{k}_{\rm xy} = 0$ mode, the pair of defects will strongly scatter into the isoenergetic modes that satisfy $\omega(\mathbf{k}_{\rm xy}) \approx \omega(0)$ (black dashed line), which are roughly characterized by $|k_{\rm x}| \sim$ const $\ll \pi/d$, and $|k_{\rm y}| \leq \pi/d$. When the connecting vector between the pair of sites is along $\widehat{\mathbf{x}}$, the relevant Bloch modes cannot resolve the two defects placed at a distance d, and intuitively one expects the total scattering cross section to resemble that of a single defect. On the contrary, when the connecting vector is along $\widehat{\mathbf{y}}$, the Bloch modes can resolve the sites, and one expects a scattering cross section roughly twice that of a single defect. To check this intuition, we compute the resonant cross section of a pair of nearest defects (at $\delta = \omega(0)$) from the optical theorem, analogously to Section 4.3.2.1. We obtain $\sigma_{\rm hd}^{\rm x,y} = (\sigma_0/2)(\Gamma_0/\Omega_0^2)\sum_{\pm} {\rm Im}\ (\Omega_{\rm hd}/2)\tilde{c}_{h^{\pm}}$, when the pair is aligned either along $\widehat{\mathbf{x}}$ or $\widehat{\mathbf{y}}$. By numerically evaluating the susceptibilities $\chi(d\widehat{\mathbf{x}}, \delta = \omega(0))$ and $\chi(d\widehat{\mathbf{y}}, \delta = \omega(0))$ with the method of Appendix D.1, we find that the number of lattice sites affected by the holon-doublon pair (as defined in Section 4.3.2.1) is $N_{\rm hd}^{\rm x} \simeq N_{\rm h}$ for the $\widehat{\mathbf{x}}$ alignment, and $N_{\rm hd}^{\rm y} \simeq 1.8 N_{\rm h}$ otherwise, with an average value of $\langle N_{\rm hd}\rangle \sim 1.4 N_{\rm h}$. Here, $N_{\rm h}$ is the single-defect solution of Eq. 4.17, while the resonant cross section of a holon-doublon can be related to the self-energy via $P_{\rm hd}\langle N_{\rm hd}\rangle = -2{\rm Im}\ \Sigma_{\rm hd}/\Gamma(0)$, at $\delta = \omega(0)$.

4.4.3 The limit to the index by quantum chemistry

From the previous subsections, we can assign a total complex self-energy $\Sigma_{\rm QC}(\delta) = \Sigma_{\rm t}(\delta) + \Sigma_{\rm hd}(\delta)$ for the collective mode $|E\rangle$ of a 2D array, which

includes the effects of both the p-orbital dynamics $\Sigma_{\mathsf{t}}(\delta)$ (via Eq. 4.30) and the density-density correlations $\Sigma_{\mathsf{hd}}(\delta)$ (via Eq. 4.31). The frequency-dependent resonance shift Re $\Sigma_{\mathsf{QC}}(\delta)$ and inelastic losses $-2\mathrm{Im}\ \Sigma_{\mathsf{QC}}(\delta)$ alter the linear reflection and transmission coefficients in response to a normally incident field, to $r(\delta) = i\Gamma(0)/[-2\delta + 2\omega(0) + 2\Sigma_{\mathsf{QC}}(\delta) - i\Gamma(0)]$ and $t(\delta) = 1 + r(\delta)$. A non-zero loss $-2\mathrm{Im}\ \Sigma_{\mathsf{QC}}(\delta) > 0$ generally results in a loss of coherently scattered energy $|r|^2+|t|^2< 1$. It should also limit the maximum index achievable. This can easily be seen in the limit of large $-2\mathrm{Im}\ \Sigma_{\mathsf{QC}}(\delta)/\Gamma(0) \gg 1$, where $r(\delta) \sim 0$ and $t(\delta) \sim 1$.

The derivation of the refractive index of a 3D lattice, based upon multiple scattering between 2D arrays, follows in a manner analogous to that presented in Section 4.2.3. In particular, recall that we obtained the dispersion relation $J(k_z)$ of Eq. 4.9 for a 3D system by diagonalizing the Hamiltonian $H^{1\mathrm{D}}_{\mathrm{dip-dip},ij}$ of Eq. 4.8 describing field-mediated interactions between planes. Within the limits that we consider quantum chemistry, one can repeat the calculation with the modification of the intra-plane matrix element $H^{1\mathrm{D}}_{\mathrm{dip-dip},ii} \to H^{1\mathrm{D}}_{\mathrm{dip-dip},ii} + \Sigma_{\mathrm{QC}}(\delta)$ to include chemistry effects. This modifies the dispersion relation of Eq. 4.9 into the nonlinear form $J(k_z) \to J(k_z) + \Sigma_{\mathrm{QC}}(J(k_z))$.

By choosing an aspect ratio of $d_z/d = 2.5$, we can ensure that the contribution of the evanescent field to the band (i.e. $J_{\mathsf{ev}}(k_z)$, as defined in Eq. 4.10) is negligible in the range of interest $d/a_0 \gg 1$, guaranteeing that the modified dispersion relation Eq. 4.9 is readily invertible (see Appendix C.3 for more quantitative details). By defining the complex refractive index as $n(\delta) = k_z(\delta)/k_0$, we obtain

$$n(\delta) = \frac{1}{k_0 d_z} \arccos\left[\cos(k_0 d_z) + \frac{\Gamma(0)\sin(k_0 d_z)}{2\delta - 2\omega(0) - 2\Sigma_{\mathsf{QC}}(\delta)}\right]. \tag{4.32}$$

One can prove that the definition of index leading to Eq. 4.32 correctly describes the optical properties within the framework of classical macroscopic electrodynamics. For example, in Section 4.4.4.1 we show that the formula of $n(\delta)$ correctly describes the reflection and transmission of a finite-length 3D system when inserted into standard Fresnel coefficient formulas for a dielectric slab, as long as the wavelength of light cannot resolve the atomic positions, i.e. when $k_0 d_z \ll 1$ and $|n(\delta)k_0 d_z|< 1$.

The expression shown in Eq. 4.32 represents our final formal result, where we are able to transition from the quantum optics to (weak) quantum chemistry limit, while calculating the refractive index in a manner that still retains non-perturbative multiple scattering of light. In order to appreciate

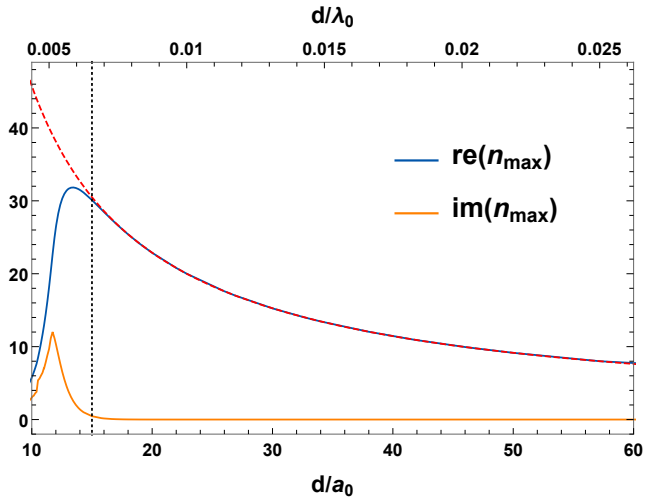

Figure 4.11: Maximum (real) refractive index. Approximate calculation of maximum real part of the refractive index (solid, blue line, maximized over the detuning δ), as a function of lattice constant, including the effects of quantum chemistry $\Sigma_{\mathrm{QC}}(\delta)$, without additional experimental noise $\Gamma' = 0$. The dashed black curve represents the result $n = \lambda_0/(2d_z)$ in the quantum optics limit, while the red curve shows the imaginary part of the index.

its non-perturbative nature, we can examine the requirements for Eq. 4.32 to reduce to usual perturbative theories of optical response, such as the Drude-Lorentz model. As shown in Section 4.4.4.2, this occurs when the inelastic losses due to quantum chemistry become so intense as to strongly suppress the effects of multiple scattering, specifically, when $-2\mathrm{Im}\ \Sigma_{\mathrm{QC}}(\delta)/\Gamma(0) > 1$ and $k_0 d_z \ll 1$. This observation helps to qualitatively understand why perturbative theories work so well when quantum chemistry interactions become strong, as is the case for real solids.

We use Eq. 4.32 to calculate the complex refractive index, as a function of the lattice constant $a_0 \ll d \ll \lambda_0$, choosing the detuning δ which maximizes its real part. In the numerical implementation, we must avoid the range of frequencies associated with the bandgap, where there are no propagating modes, i.e. the range of values of $J(k_z)$ that have no solution for any k_z. It can readily be checked that even if the losses are explicitly set to zero ($\mathrm{Im}\ \Sigma_{\mathrm{QC}} = 0$), within the bandgap region, Eq. 4.32 would predict a complex index, incorrectly suggesting a lossy medium. We emphasize that this issue is simply associated with how to define a proper macroscopic index in the bandgap regime, whereas the microscopic dispersion relation $J(k_z)$ remains correct.

The results of Eq. 4.32 are shown in Fig. 4.11, where the blue line shows the maximum real part of the index, while the orange line represents the associated imaginary part (i.e. at the same frequency δ). The red, dashed line shows the ideal quantum optics scaling of $n_{\max} = \lambda_0/(2d_z)$ obtained in Eq. 4.11. One can see that the model predicts a possible real part of the index as large as $\max n_{\mathrm{re}} \approx 30$ around $d \approx 15a_0$, accompanied by a small imaginary part describing losses $n_{\mathrm{im}} \lesssim 1$, for an optimal lattice constant. As one further decreases the lattice constant, one first sees a decrease in the real part of the index and an increase in the imaginary part, followed by a decrease in both, even as the effects of quantum chemistry continuously increase, as characterized by $\Sigma_{\mathrm{QC}}(\delta)$. This reflects our earlier observation that a huge inelastic loss rate should make an individual 2D layer increasingly transparent. Finally, when the lattice constants are $d \gtrsim 30a_0$, the presence of $\Sigma_{\mathrm{QC}}(\delta) \approx 0$ is negligible. Due to this reason, given Eq. 4.32, any lattice constant $30a_0 \lesssim d < \lambda_0$ would guarantee a (purely real) near-zero index $n_{\min} \approx 0$ (as shown in Section 4.2.3), regardless of chemistry.

4.4.4 Recovering classical optics

The refractive index defined in Eq. 4.32 includes, non-perturbatively, the multiple scattering, between each 2D atomic array, of the light propagating in the longitudinal $\hat{\mathbf{z}}$ direction. As anticipated in Section 4.4.3, the onset of chemistry introduces some fundamental losses which allow to perturbatively recover the standard laws of macroscopic, classical optics, due to the suppression of multiple scattering along $\hat{\mathbf{z}}$. Here, we analytically prove the emergence of the Fresnel equations for the reflection and transmission of a finite slab (as discussed in Section 3.2.2.1), as well as the appearance of the usual smooth-field theories introduced in Section 2.1.

4.4.4.1 Emergence of Fresnel equations

In Eq. 4.32, we define the refractive index for the 3D lattice via a Bloch band structure calculation. In this appendix, we prove that this definition of index correctly reproduces various predictive properties of optical response, within classical macroscopic electrodynamics. In particular, we on one hand will calculate by microscopic approaches the reflection and transmission through a finite-length 3D system, and on the other hand see that this agrees with the standard Fresnel equations for a dielectric slab.

First of all, we recall that from the standpoint of classic optics, given a dielectric slab of length L and (complex) refractive index $n(\delta)$, the Fresnel equations predict a transmission $t_{\mathrm{Fr}}(\delta)$ and a reflection $r_{\mathrm{Fr}}(\delta)$ that were

explicitly shown in Eq. 3.6. We now consider a 3D crystal composed of a number M of 2D atomic arrays, separated by the distance d_z and illuminated at normal incidence. In the regime where the evanescent field can be neglected, each 2D array is characterized by the reflection and transmission coefficients $r(\delta) = i\Gamma(0)/[-2\delta + 2\omega(0) + 2\Sigma_{QC}(\delta) - i\Gamma(0)]$ and $t(\delta) = 1 + r(\delta)$. To our analysis, it is convenient to write $r(\delta)$ and $t(\delta)$ as functions of the index $n(\delta) = k_z(\delta)/k_0$. This is accomplished by using Eq. 4.32 to replace the dependency on δ with that on n, thus obtaining the functions $r(n)$ and $t(n)$.

The multiple scattering problem through multiple layers reduces to a 1D problem that can be efficiently and exactly solved by the transfer-matrix formalism [246]. In particular, the Chebyshev's identity can be used to calculate the (exact) total transmission and reflection of the stack of M, 2D arrays, which read [247]

$$\begin{aligned} t_M(n) &= \frac{e^{ik_0 d_z} t(n)}{u_M(n) - e^{ik_0 d_z} t(n) u_{M-1}(n)}, \\ r_M(n) &= \frac{e^{2ik_0 d_z} r(n) u_M(n)}{u_M(n) - e^{ik_0 d_z} t(n) u_{M-1}(n)}, \end{aligned} \tag{4.33}$$

where we define the function $u_M(n) = \sin(Mnk_0 d_z)/\sin(nk_0 d_z)$.

Starting from Eq. 4.33, we define the total length L and replace the number of layers with $M \to L/d_z$. Eventually, we can expand the resulting expressions as a Taylor series in $k_0 d_z \ll 1$, with the supplementary assumption that $|n(\delta)k_0 d_z| < 1$, but also keeping in mind that $k_0 L$ can be arbitrarily large. The two requirements $k_0 d_z \ll 1$ and $|n(\delta)k_0 d_z| < 1$ correspond to the physical regime where light cannot resolve the space between each single 2D atomic layer. This condition is naturally satisfied at low lattice constant due to the losses $-2\text{Im}\ \Sigma_{QC}(\delta)$, which reduce the index to $|n(\delta)k_0 d_z| < 1$ for any frequency δ. By performing such Taylor expansion, one recovers the Fresnel predictions of Eq. 3.6, at the zero-th order in $k_0 d_z \ll 1$. Further numerical evidence of the agreement with Fresnel equations is provided in Appendix C.2.2.

4.4.4.2 Emergence of Drude-Lorentz theory

At high densities, the losses introduced by quantum chemistry strongly suppress the effects of multiple scattering, preventing the appearance of ultra-high indices. In that regime, one expects that usual mean-field theories (such as the DL model) can well describe the physical phenomena.

Specifically, we are interested in a system which exhibits one single, dominant resonance ω_{res}, and which is illuminated by near-resonant light with $|\omega_{\mathrm{L}} - \omega_{\mathrm{res}}| \ll \omega_{\mathrm{res}}$. We recall from Eq. 2.5 that, in this limit, the DL model predicts the index

$$n = \sqrt{1 + \frac{f_{\mathrm{res}}\omega_{\mathrm{P}}^2}{\omega_{\mathrm{res}}^2 - \omega_{\mathrm{L}}^2 - i\gamma'\omega_{\mathrm{L}}}} \approx \sqrt{1 - \frac{f_{\mathrm{res}}\omega_{\mathrm{P}}^2/\omega_{\mathrm{res}}}{2(\omega_{\mathrm{L}} - \omega_{\mathrm{res}}) + i\gamma'}}, \tag{4.34}$$

where ω_{P} and γ' are respectively the plasma frequency and the damping rate, while f_{res} is the *so-called* oscillator strength which depends on the choice of the resonant transition. Here, we show that the refractive index of an atomic lattice, as predicted by Eq. 4.32, reduces to Eq. 4.34 at high densities, due to the losses induced by quantum chemistry. To this aim, we first re-write Eq. 4.32 as

$$\cos(k_0 d_z n(\delta)) = \cos(k_0 d_z) + \frac{\Gamma(0)\sin(k_0 d_z)}{2\delta - 2\omega(0) - 2\Sigma_{\mathrm{QC}}(\delta)}. \tag{4.35}$$

At low lattice constants, we can expand this equation up to the second order in $k_0 d_z \ll 1$. To do so, one needs to fulfill the condition $|k_0 d_z n(\delta)| < 1$, which is guaranteed by the suppression of multiple scattering induced by $-2\mathrm{Im}\ \Sigma_{\mathrm{QC}}(\delta) \gtrsim \Gamma(0) > \Gamma_0$ (this also guarantees the closure of the optical bandgap). This procedure permits to directly recover Eq. 4.34, by defining $\omega_{\mathrm{res}} = \omega_0 + \omega(0) + \mathrm{Re}\ \Sigma_{\mathrm{QC}}(\delta)$, $\gamma' = -2\mathrm{Im}\ \Sigma_{\mathrm{QC}}(\delta)$ and $f_{\mathrm{res}}\omega_{\mathrm{P}} = \sqrt{6\pi\omega_{\mathrm{res}}\Gamma_0/(k_0^3 d^2 d_z)}$. To trace this latter back to the usual definition of the plasma frequency, we can focus on the simple case of a transition between the ground and the first excited state of a hydrogen atom, observing that the factor $1/(d^2 d_z) = N/V$ represents the electronic density. Then, we can compute the atomic dipole moment as $|\mathbf{d}_0| = q|\langle\psi_{2p_x}|\hat{\mathbf{x}}|\psi_{1s}\rangle| = \beta q_{\mathrm{e}} a_0$, and plug it into the definition of the decay rate $\Gamma_0 = k_0^3|\mathbf{d}_0|^2/(3\pi\hbar\epsilon_0)$. There, we recall that q_{e} denotes the electron charge, while $\beta \approx 0.53$ is a proportionality factor, related to the choice of the $1s \rightarrow 2p_{\mathrm{x}}$ hydrogen transition. Finally, by noticing that in our regime both $\omega(0)$ and $\mathrm{Re}\ \Sigma_{\mathrm{QC}}(\delta)$ represent small displacements compared to ω_0, we can write $\omega_{\mathrm{res}} \sim \omega_0 = (3/4)\hbar/(2m_{\mathrm{e}}a_0^2)$, where m_{e} is the electron mass. This leads to $\omega_{\mathrm{P}} = \sqrt{N q_{\mathrm{e}}^2/(m_{\mathrm{e}}\epsilon_0 V)}$, which is the standard formula discussed in Section 2.1.1 for the plasma frequency, along with $f_{\mathrm{res}} = \beta\sqrt{3/4} \approx 0.46$. Within the limits studied here, we note that the typically phenomenological decay rate γ' appearing in the Drude-Lorentz model can be quantitatively connected to specific quantum mechanical processes as encoded in

the imaginary part of the self-energy $\Sigma_{\mathrm{QC}}(\delta)$.

Finally, it is interesting to notice that the first correction that emerges from this picture is the shift of the resonant frequency $\omega_0 \to \omega_0 + \omega(0)$, due to near-field interactions and multiple scattering. Notably, at low lattice constants $d \ll \lambda_0$ the numerical value $\omega(0)/\Gamma_0 \approx -0.0136(\lambda_0/d)^3 = -3.37(d/d_z)\eta$ [150] (with $\eta = N/(k_0^3 V)$) is surprisingly close to what predicted by the LL model discussed in Section 2.1.3. We recall, indeed, that this latter represents an established (but approximated) method to partially include near-field corrections, which predicts a density-dependent resonance shift $\omega_{\mathrm{LL}}/\Gamma_0 = -\pi\eta$, for an isotropic distribution of atoms (see Eq. 2.13). Although it would be hard to infer some general and solid conclusions from this relation, we think that the agreement $\omega(0)/\omega_{\mathrm{LL}} \approx 1.07(d/d_z)$ (up to the spatial anisotropy factor d/d_z characterizing our geometry) represents an interesting observation.

4.5 A new route to extreme indices?

From an applied perspective, rather than focus on how large the real part of the index can be, a more relevant question might be how small the loss can be, $\min\, n_{\mathrm{im}}$, given a target value of the real part of the index n_{re}. To this aim, it is instructive to generalize Eq. 4.32 to a more realistic experimental scenario, including a phenomenological inelastic loss term Γ' to the self-energy, $\Sigma_{\mathrm{QC}}(\delta) \to \Sigma_{\mathrm{QC}}(\delta) - i\Gamma'/2$, which accounts for other effects beyond the quantum chemistry interactions that we explicitly considered up to now.

In Fig. 4.12, we thus quantify how robust the near-zero (Fig. 4.12-a) and ultra-high (Fig. 4.12-b) indices are to the hypothetical additional dissipation rates $\Gamma'/\Gamma_0 = 0.01,\ 0.1,\ 1,\ 10^2,\ 10^3$ (from the bottom, solid brown curve to the top, solid magenta curve). To do so, we numerically compute the minimum value of the losses n_{im} for a target value n_{re}, optimizing over the lattice constant d and detuning δ. As a reference, the black, solid line represent the case where $\Gamma' = 0$ (this curve doesn't appear in Fig. 4.12-a, as in that case one would obtain exactly $n = 0$, at lattice constants where chemistry does not play any role). For the same reasons discussed in Section 4.4.3, when optimizing over δ, we avoid the range of frequencies that would be associated to an optical bandgap when $\Gamma' = 0$. This guarantees that the complex index of refraction is a well-defined quantity, but also reduces the performance of the numerical optimization.

Finally, the dotted lines portray simple approximate scalings that can be inferred in the same regime of $k_0 d_z \ll 1$ and $|nk_0 d_z| < 1$ that was considered

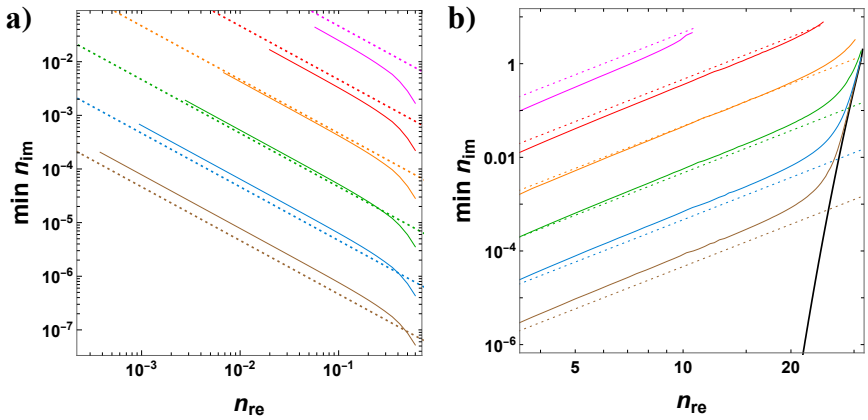

Figure 4.12: Minimum losses in experimental scenarios. Given any fixed value of the real index n_{re}, we plot the minimum imaginary part n_{im}, obtainable with proper choices of d and δ (colored, solid lines). Specifically, in (a) we consider the case of a near-zero index $n_{re} \sim 0$, while in (b) we focus on ultra-high values $n_{re} \gg 1$. The curves (from brown at the bottom, to magenta on top) refer to increasing values of the additional inelastic losses $\Gamma' = 0.01,\ 0.1,\ 1,\ 10,\ 10^2,\ 10^3$. The black solid line shows the case $\Gamma' = 0$, which is purely limited by the intrinsic effects of $\Sigma_{QC}(\delta)$. The dotted, colored lines represent the asymptotic scalings $n_{im} \propto n_{re}^{-1}\Gamma'/\Gamma_0$ for the near-zero index in (a) and $n_{im} \propto n_{re}^{3}\Gamma'/\Gamma_0$ for the ultra-high index in (b).

in Section 4.4.4. These are given by $n_{im} \propto n_{re}^{-1}\Gamma'/\Gamma_0$ for the near-zero index and $n_{im} \propto n_{re}^{3}\Gamma'/\Gamma_0$ for the ultra-high index.

To calculate them, we start by deriving from Eq. 4.32 the equation

$$2\tilde{\delta} + \frac{\tilde{\gamma}\cos(k_0 d_z)}{\sin(k_0 d_z n_{re})\sinh(k_0 d_z n_{im})} = \tilde{\gamma}\cot(k_0 d_z n_{re})\coth(k_0 d_z n_{im}), \tag{4.36}$$

where $\tilde{\delta} = [\delta - \omega(0) - \text{Re}\,\Sigma_{QC}(\delta)]/\Gamma(0)$ and $\tilde{\gamma} = [\Gamma' - 2\text{Im}\,\Sigma_{QC}(\delta)]/\Gamma(0)$. In the regime of low losses $k_0 d_z n_{im} \ll 1$, we can solve Eq. 4.36 to obtain $n_{im} \approx \tilde{\gamma}[\cos(k_0 d_z n_{re}) - \cos(k_0 d_z)]/[2k_0 d_z \tilde{\delta}\sin(k_0 d_z n_{re})]$. Inspired by the numerical, brute-force optimization of $\min n_{im}$, we then observe that the minimal losses are always obtained when the lattice constant is roughly fixed around $d \approx d_{QC} \approx 15a_0$. This value roughly represents the lattice constant where quantum chemistry starts to play a major role (as shown by the dotted, vertical line in Fig. 4.11), so that $d \approx d_{QC}$ then minimizes the parameter $\tilde{\gamma}$ in Eq. 4.32, for any fixed value of Γ'. Given $d = d_{QC}$, the value of n_{re} is varied by changing δ on a fixed curve. As we are in the regime of low losses $n_{im} \ll 1$ and negligible quantum chemistry, we can approximate

$\tilde{\delta}$ with the band structure of Eq. 4.9, i.e. $\tilde{\delta} \approx [J(n_{\mathrm{re}}k_0) - \omega(0)]/\Gamma(0)$, evaluated $d = d_{\mathrm{QC}}$. This proves to be a good approximation as long as $n_{\mathrm{im}} \ll n_{\mathrm{re}}$. Finally, after expanding for $k_0 d_z \ll 1$ (given $n_{\mathrm{re}} k_0 d_z < 1$), one obtains

$$n_{\mathrm{im}} \approx \frac{\Gamma'}{\Gamma_0}\left(\frac{d_z}{d}\right)\left(\frac{k_0^3 d_{\mathrm{QC}}^3}{12\pi}\right)\left(\frac{1}{n_{\mathrm{re}}} - 2n_{\mathrm{re}} + n_{\mathrm{re}}^3\right), \tag{4.37}$$

where we use the fact that $d = d_{\mathrm{QC}} \approx 15a_0$ (i.e. right before quantum chemistry) to approximate $\tilde{\gamma} \approx \Gamma'/\Gamma(0)$.

From the above discussions, it is clear that in principle one possible approach to achieve high-index materials is to realize high-density arrays of well-positioned, sufficiently homogeneous quantum emitters [4]. The maximum index would be achieved at a distance between emitters right before the electronic orbital wave functions between nearest neighbor emitters begins to appreciably overlap. Although we know of no specific platform that would immediately allow for an extreme and low-loss index, we note that there has been steady progress to deterministically position emitters, such as by self-organization [248] or ion beam implantation [249]. We also note that in principle, quantum emitters already exist with sufficiently small values of Γ' (where we allow Γ' to incorporate non-radiative decay, additional undesired radiative decay paths, dephasing, and inhomogeneous broadening) that an ultra-high index might be possible, if they could be arranged into arrays.

For example, single color centers in diamond (such as silicon-vacancy centers) exhibit inelastic rates as low as $\Gamma' \sim \Gamma_0$ [249, 250], and inhomogeneous broadening levels at low temperatures in the range of $\Gamma'/\Gamma_0 \sim 10$-100 [249, 251, 252]. Single quantum dots can offer almost lifetime-limited linewidths with $\Gamma' \ll \Gamma_0$ [253, 254], although some technological improvement is still required to reduce the amount of inhomogeneous broadening in ensembles. Separately, since the key underlying ingredient for high index is a near-ideal single-mode response of a single 2D layer, 2D materials supporting excitonic resonances could also be a suitable platform. In particular, 2D transition metal dichalcogenides have been observed to exhibit nearly perfect reflection on resonance [255–257], due to the high radiative efficiency of excitons in such systems. If such individual layers with sufficiently low loss could be stacked with controllable spacings between layers [223, 258], both a ultra-high and a near-zero index should exist until quantum chemistry between layers becomes appreciable and the index reduces back to the value found in bulk 3D material.

4.6 Conclusions and outlook

In summary, we have shown that the magnitudes of refractive indices observed in known optical materials likely does not reflect a fundamental limit, and an ultra-high index, low-loss material should be allowed by the laws of nature. Our analysis also suggests why an answer to the problem surrounding the limits of refractive index has been elusive, as the answer seemingly requires one to understand the nature of non-perturbative multiple light scattering over a broad range of densities that spans across the quantum optics and quantum chemistry limits. Our work will hopefully stimulate new efforts to identify, design, and fabricate ultra-high index materials.

As we discussed in Section 1.1.2, the idea of using resonant scatterers to potentially realize extreme-index materials has been discussed before, typically in the context of small metallic nanoparticles or metal composites with plasmonic resonances. Compared to such works, two key differences of our work are that first, we consider isolated atoms as building blocks that are completely lossless and have a large scattering cross section decoupled from their physical size, and that second, by bringing the atoms progressively closer until quantum chemistry turns on, we can better address the fundamental limits of refractive index of a "real" material.

While our current analysis focused on a specific model in which the limits to index arise due to electronic density-density correlations and dynamics of excited electrons, it would be interesting in future work to examine other general material models. For example, are there paradigms in which the mechanisms discussed here can be strongly suppressed, leading to higher indices? In order to better answer such questions, and also to aid in the search or possible design of extreme-index materials, it might also be desirable to develop more general frameworks for the calculation of optical response in the regime of non-perturbative scattering, and which ideally might be integrated with state-of-the-art computational quantum chemistry. One promising approach might be to generalize the electromagnetic Green's function based methods to many-body condensed matter settings.

Finally, while our work specifically focused on the question of linear refractive index, it more generally suggests that there is a broad range of material densities where other important optical properties might have surprising behavior, due to strong multiple scattering. As one example, it would be interesting to develop similar theories for the limits of nonlinear optical response, and to address whether there exist mechanisms to enhance the nonlinear response beyond that of known materials.

In the context of atomic arrays, for instance, our analysis of the de-

fects might offer a possible pathway to study nonlinear phenomena. At the quantum level, the first manifestation of nonlinearity consists of an excited atom becoming transparent to a second incoming photon, suggesting that it might act similarly to a defect. It would be interesting to explore if the scattering cross section σ_{h} of a hole can provide the correct physical intuition for the two-photon correlations in a 2D atomic array, perhaps expanding our analysis to cubic 3D arrays by including the evanescent coupling between 2D layers.

5 - Atomic metalens of structured arrays

Chapter Contents

5.1 Introduction

As extensively discussed in the previous chapters, light-mediated dipole-dipole interactions can strongly modify the optical response of an atomic ensemble, leading to the emergence of cooperative effects which firmly differ from that of individual atoms [155, 163, 166, 167, 172–181, 259]. We showed that this is the case of ordered atomic arrays, [151, 152, 260–264] and we mentioned the great interest gathered by the theoretical possibility of building a perfect mirror out of a single 2D atomic array [149, 150], as experimentally addressed in [171]. In this context, further manipulation of light at the quantum level was proposed in recent years, by either exploiting the Rydberg blockade of ancillary atoms trapped next to the array [265–267], or by controlling the energy levels of the individual atoms via AC Stark shift [268–270]. In this chapter, we discuss the design of a structured optical device, specifically a microscopic lens, which solely exploits the cooperative response of arrays of two-level atoms, where the choice of tailored lattice constants allows to locally manipulate the properties of light.

5.1.1 From lenses to metalenses

Usual refractive lenses rely on local variations of the optical path inside the lens (where light experiences a higher, positive refractive index) to induce a spatially dependent phase shift. Thereby, the wavefront is shaped in such a way that the output beam focuses at a designed distance. In the last couple of decades, the idea emerged of designing optical devices by means of flat metasurfaces, which rely on the electromagnetic response of tailored nanostructures to locally impress abrupt phase shifts on the transmitted light [271–274]. In particular, flat metalenses can be designed to mimic the spatial phase pattern of a spherical lens [28, 29, 32, 275–283], and they have proven to exhibit good focusing properties as well as an ultra-thin thickness, up to fractions of a micron [33, 273].

Considering an input monochromatic light beam with wavevector $\mathbf{k} = (2\pi/\lambda_0)\widehat{\mathbf{z}} = k_0\widehat{\mathbf{z}}$, the system acts as a lens with focal length f as long as it imparts the phase profile

$$\phi_{\text{lens}}(r) = \text{mod}\left[k_0\left(f - \sqrt{r^2 + f^2}\right) + \phi_0, 2\pi\right] - \pi, \tag{5.1}$$

where we define the transverse coordinate $r = \sqrt{x^2 + y^2}$, while the parameter $-\pi < \phi_0 \leq \pi$ corresponds to the phase at the center of the lens [28, 279]. As discussed in Section 1.1.3, a metalens is usually composed of microscopic nano-elements, which act as discrete phase shifters, whose size is as small as few fractions of the wavelength λ_0 [33]. Here, we propose that an "atomic metalens" can be analogously conceived by means of actual atoms, with a well-defined dipole transition, arranged to form atomic arrays. Specifically, we show that any phase shift can be impressed (while maintaining high and directional transmission) by using at least two consecutive, 2D arrays with tailored (subwavelength) lattice constants.

5.1.2 Overview of experimental platforms

From an experimental perspective, color centers in diamond can offer a reliable framework for the implementation of such an atomic metalens. In particular, a single color center is known to behave as an atom-like emitter with well-defined selection rules and a dipolar response aligned along one of the four possible tetrahedral directions of the diamond lattice [220, 284–288]. Moreover, new technologies in the fabrication process promise to offer good control over the spatial position of single color centers [289–293], as well as the construction of almost defect-free arrays [294].

Hereafter, we select Silicon-Vacancy (SiV) centers as a plausible experimental reference. These latter can exhibit nearly lifetime-limited linewidths, as well as $\sim 70\%$ of emission into the zero-phonon line [249, 252, 295, 296]. Furthermore, we assume that the fabrication process permits to preferentially discriminate over the four possible orientations, so that all dipole transitions of the SiV centers can be considered as aligned along the same axis, that we define as $\widehat{\mathbf{x}}$ [297–300]. Although we consider color centers in diamond as a possible system to implement our scheme, the proposed protocol is more general. Specifically, it is based on the scattering properties of point-like dipoles, and it can be potentially tested with any experimental platform where a sufficient control can be ensured over the spatial positions of two-level, atom-like systems. In the context of solid-state systems, in the last years many efforts were put in controlling at the nanoscale the spatial positions of the single elements forming arrays of either quantum dots [221] or rare-earth-ion dopings [222], showing promising results, but limited to very small systems. At the same time, it was recently proven that cold atoms can be arranged in arrays of arbitrary shape [301–303], although with typical distances $\gtrsim \mu$m.

5.2 Theoretical formalism

We can now introduce the theoretical framework. We focus on a set of atom-like scatterers, embedded in a bulk, nonabsorbing material of positive refractive index n, which are characterized by a linear polarizability $\alpha_0 = -3\pi\epsilon_0/[(\Delta + i(1+\Gamma')/2)k_0^3]$ and a dipole matrix element $\mathbf{d}_0 = d_0\widehat{\mathbf{x}}$, aligned along a well-defined direction. Here, $\Delta \equiv (\omega - \omega_0)/\Gamma_0$ represents the dimensionless detuning between the frequency ω of the incident light and the atomic resonance ω_0, in units of the natural atomic linewidth Γ_0 in the bulk material, while $k_0 = 2\pi/\lambda_0 = n\omega_0/c$ denotes the resonant wavevector. For the specific reference of SiV centers, one has a resonant transition $2\pi c/\omega_0 = 737$nm and a decay rate $\Gamma_0/(2\pi) \simeq 94$MHz [249, 252], while the bulk index (diamond) reads $n \simeq 2.4$.

Throughout this chapter, we focus on the relevant case of resonant input light, i.e. $\Delta = 0$, but the extension to near-resonant light is straightforward. Moreover, we write all the frequencies and rates in units of Γ_0.

Finally, the term Γ' represents both non-radiative and non-elastic emission, and it also includes the possibility of inhomogeneous broadening of the atomic resonances [251] (some further discussion is provided in Appendix D.3). In particular, we define $\Gamma' = \Gamma_{\text{inel}} + \Gamma_{\text{inhom}}$, where we adopt

some experimentally inspired values of $\Gamma_{\text{inel}} \sim 3/4$ and $\Gamma_{\text{inhom}} \sim 5$.

We are interested in an atomic system arranged in a stack of M, 2D rectangular lattices, infinitely extending in the $\widehat{\mathbf{x}}$ and $\widehat{\mathbf{y}}$ directions, with constants $\xi_{\text{x}} = d_{\text{x}}/\lambda_0$ and $\xi_{\text{y}} = d_{\text{y}}/\lambda_0$, and separated by a longitudinal distance $\xi_{\text{z}} = d_{\text{z}}/\lambda_0$. The system is illuminated by a resonant, $\widehat{\mathbf{z}}$-directed, $\widehat{\mathbf{x}}$-polarized plane wave $\mathbf{E}_{\text{in}}(\mathbf{r}, z) = E_0 e^{ikz}\widehat{\mathbf{x}}$. In this regime, the coupled-dipole equations of Eq. 2.17 can be simplified by exploiting the symmetries of the lattice. In Section 2.3.2, we discussed in details the optical response of a 2D square array, where $\xi_{\text{x}} = \xi_{\text{y}}$. In this case, we are interested in the more general scenario of $\xi_{\text{x}} \neq \xi_{\text{y}}$, which nonetheless exhibits a qualitatively identical response. Specifically, a plane wave normally incident to an infinite 2D rectangular lattice still only excites one symmetric collective mode, characterized by the cooperative resonance $\omega_{\text{coop}}(\xi_{\text{x}}, \xi_{\text{y}})$ and cooperative decay rate $\Gamma_{\text{coop}}(\xi_{\text{x}}, \xi_{\text{y}})$ (in this chapter, we define the dimensionless rates $\Gamma_{\text{coop}} = \Gamma(0)/\Gamma_0$ and $\omega_{\text{coop}} = \omega(0)/\Gamma_0$). Each plane is thus reduced to just a single degree of freedom, characterized by the dipole moment d_m for all the atoms in the plane m. In general, this single mode can scatter light in all the directions, associated to an infinite number of diffraction orders. However, if we restrict to the regime of $\xi_{\text{x}} < 1$, $\xi_{\text{y}} < 1$ (i.e., zero-th diffraction order), the light can only be scattered (either in transmission or in reflection) into the same direction as the input light, while all the other orders become evanescent.

As discussed in Chapter 4, if one now assembles a stack of M infinite 2D atomic arrays, the optical response at normal incidence will be single-mode, allowing to rewrite Eq. 2.17 as a simpler set of coupled equations between the layers (we remind that we fix the resonant condition $\Delta = 0$)

$$\left[\omega_{\text{coop}} - \frac{i}{2}\left(\Gamma_{\text{coop}} + \Gamma'\right)\right] c_m - \sum_{m \neq j} \mathcal{G}_{mj} c_j = e^{2\pi i (m-1)\xi_{\text{z}}}, \tag{5.2}$$

whose dimensionless coefficients c_m are related to the atomic dipole moments d_m through $c_m = d_m \Gamma_0/(\Omega_0 |\mathbf{d}_0|)$ and where we define the the interaction matrix $\mathcal{G}_{mj} = \mathcal{G}^{\text{1D}}_{mj} + \mathcal{G}^{\text{ev}}_{mj}$. Here, the term $\mathcal{G}^{\text{1D}}_{mj} = i\Gamma_{\text{coop}} e^{2\pi i |m-j| \xi_{\text{z}}}/2$ represents that scattered light which propagates in the longitudinal $\widehat{\mathbf{z}}$ direction, while the term $\mathcal{G}^{\text{ev}}_{mj}$ stands for the evanescent interaction, which exponentially decreases with the distance between planes (its full expression can be found in Appendix E.1). We also notice that $\Gamma_{\text{coop}} = 3/(4\pi\xi_{\text{x}}\xi_{\text{y}})$ when $\xi_{\text{x}}, \xi_{\text{y}} < 1$ (which is the straightforward extension to $\xi_{\text{x}} \neq \xi_{\text{y}}$ of the parameter $\Gamma(0)/\Gamma_0$ shown in Eq. 4.3), while ω_{coop} can be numerically calculated with the prescriptions of [150, 225, 262, 304].

After solving for the excitation amplitudes c_n via Eq. 5.2, one can find the optical response. In particular, as detailed in Appendix C.2.1, the stack of M, 2D arrays is characterized by the total transmission and reflection

$$t = 1 + i\frac{\Gamma_{\text{coop}}}{2}\sum_{m=1}^{M} c_m\, e^{-2\pi i(m-1)\xi_z}, \qquad r = i\frac{\Gamma_{\text{coop}}}{2}\sum_{m=1}^{M} c_m\, e^{2\pi i(m-1)\xi_z}. \tag{5.3}$$

To conclude, hereafter we want to restrict to a regime where one has $\mathcal{G}^{\text{ev}}_{mj} \sim 0$ for any pair of planes. For rectangular lattices (in the regime of $\xi_x \ll 1$, $\xi_y \ll 1$), an approximate rule of thumb for $\mathcal{G}^{\text{ev}}_{mj} \sim 0$ to be satisfied is $\xi_z \gg \max[\xi_x, \xi_y]/(2\pi)$. However, as discussed in detail in Appendix E.1, when one approaches the condition $\xi_y \sim 1$, then some supplementary caution is required.

5.3 The building block: a phase shifter

We now discuss how to conceive the building blocks of an atomic metalens. A usual metalens is composed of nanostructures of the size of fractions of λ_0, and each of these blocks is designed to transmit as much light as possible and to induce a tunable phase shift. Hereafter, we show that these two properties can be similarly achieved by exploiting the collective response of an atomic array. We underline that we work in a regime where the evanescent interaction can be neglected, i.e. $\mathcal{G}^{\text{ev}}_{mj} \sim 0$. Finally, hereafter we will define the phase shift impressed upon transmission as $\phi \equiv \arg t$.

Given Eq. 5.2, one can easily calculate the complex transmission of a stack of M atomic layers. It is then easy to show that our goal cannot be obtained with one single layer of atoms. In that case, indeed, the solution of Eq. 5.2 satisfies the relation $t_{1\text{L}} + r_{1\text{L}} = 1$, which (together with $|t_{1\text{L}}|^2 + |r_{1\text{L}}|^2 = 1$) imposes $\cos(\phi_{1\text{L}}) = |t_{1\text{L}}|$, meaning that a perfect transmission is strictly associated with the fixed phase $\phi_{1\text{L}} = 0$.

On the contrary, a system with $M = 2$ atomic layers and $\mathcal{G}^{\text{ev}}_{mj} \sim 0$ is equivalent to a Fabry-Perot cavity, which can potentially fulfill our scope. This is represented in Fig. 5.1-a, where we plot the value of the phase $\phi_{2\text{L}} = \arg t_{2\text{L}}$ in the noiseless regime $\Gamma' = 0$. To this aim, we vary the three lattice constants $\xi_{x,y} < 0.1$ and $\xi_z < 0.5$ independently (same results are obtained if considering the full range $\xi_{x,y,z} < 1$), and we plot the phase shift as a

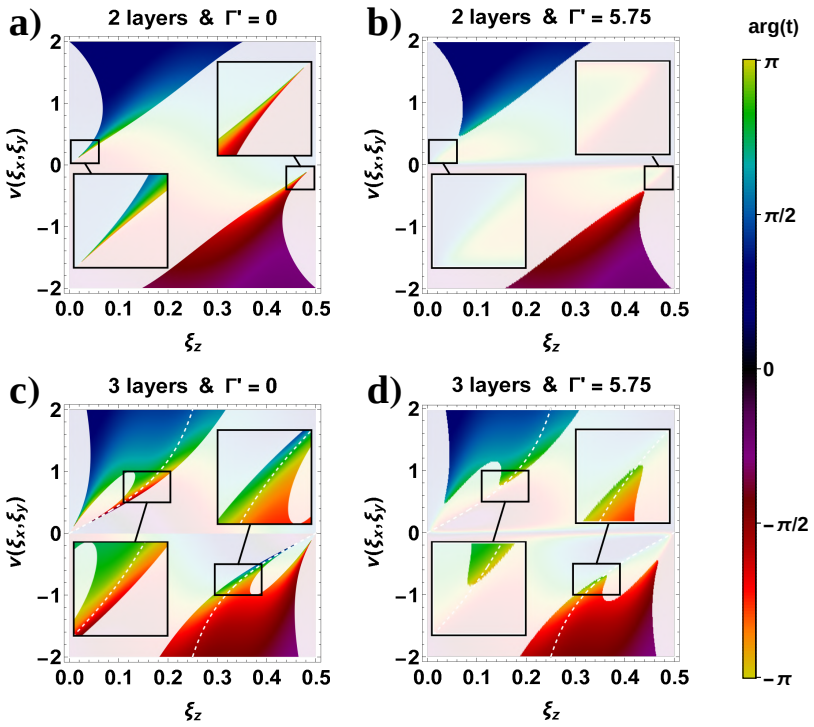

Figure 5.1: Phase shift of a multi-layer atomic array, as a function of $\nu(\xi_x,\xi_y) \equiv 2\omega_{coop}(\xi_x,\xi_y)/\Gamma_{coop}(\xi_x,\xi_y)$ and $\xi_z = z/\lambda_0$. (a,b) Phase shift $\phi_{2L} = \arg t_{2L}$ in the case of two atomic layers, given either $\Gamma' = 0$ (a) or $\Gamma' = 5.75$ (b). The transverse lattice constants are varied imposing the constraint $1 > \xi_{x,y} \geq \xi_{min} = 0.03$, which means that $\Gamma'/\Gamma_{coop}(\xi_x,\xi_y) \gtrsim 0.03$. When different pairs of ξ_x and ξ_y are associated to the same value of $\nu(\xi_x,\xi_y)$, but distinct $\Gamma_{coop}(\xi_x,\xi_y)$, the pair with the highest cooperative decay is selected. The colorbar depicts the value of the phase shift ϕ_{2L}. The region where $|t_{2L}|^2 < 0.5$ is represented by a white shaded area, while the insets show the relevant case of $\phi_{2L} \equiv \arg t_{2L} \sim \pm\pi$ and $|t_{2L}|^2 \geq 0.5$, whose bandwidth is infinitesimally small and breaks down in the noisy regime (b). (c,d) Same structure of subfigures (a) and (b), but for the three-layer case. The white dashed lines represent the path defined in Eq. 5.8. Here, the insets show the emergence of a new branch, where both the phase $\phi_{3L} = \pm\pi$ and the transmission $|t_{3L}|^2 \geq 0.5$ can be obtained over a much broader bandwidth (c), becoming more resistant to the noise (d).

function of ξ_z and the parameter $\nu(\xi_x,\xi_y) = 2\omega_{coop}(\xi_x,\xi_y)/\Gamma_{coop}(\xi_x,\xi_y)$, which provides the ratio of resonance frequency to cooperative linewidth of a single 2D array. Notably, we see that these parameters allow one to tune the transmission, although the input frequency is fixed to the bare atomic resonance. In particular, the white shaded area shows the region of low transmission, where $|t_{2L}|^2 < 0.5$. By suitably choosing ξ_x, ξ_y and ξ_z, one

can have both a sufficient transmission $|t_{2L}|^2 \geq 0.5$ and an arbitrary phase shift $-\pi < \phi_{2L} \leq \pi$. However, the bandwidth associated to $\phi_{2L} \to \pm\pi$ and $|t_{2L}|^2 \geq 0.5$ is asymptotically small [305], as can be observed in the insets of Fig. 5.1-a. This phenomenon makes the system around $\phi_{2L} \sim \pm\pi$ very fragile against the noise. To quantify this, we should first set a minimum inter-atomic distance $\xi_{\min} = 0.03$ (corresponding to $d = 10\text{nm}$ for SiV centers) that is realistically achievable [293, 306]. Otherwise, allowing the distance to become arbitrarily small allows the cooperative decay rate $\Gamma_{\text{coop}}(\xi_x, \xi_y)$ to become arbitrarily large and overtake any sources of noise. In Fig. 5.1-b, we then define $\Gamma' = 5.75$ and perform the same calculation of the phase shift. It can be seen that a large transmission $|t_{2L}|^2 \geq 0.5$ and full phase control can no longer be simultaneously achieved.

5.3.1 Fragility of two layers against nonradiative losses

Before describing our final approach, we devote this section to a more quantitative analysis of the fragility of two layers. Specifically, we analytically derive the qualitative conclusions of the previous subsection, and we accomplish this by re-writing in a Fabry-Perot fashion the results of Eq. 5.2 and Eq. 5.3 for two layers $M = 2$. For a reader specifically interested in our implementation of an atomic metalens, we suggest jumping to Section 5.3.2.

Starting from Eq. 5.2 and Eq. 5.3, we can define the resonant ($\Delta = 0$), single-layer reflection $r_{1L} = i\Gamma_{\text{coop}}/[2\omega_{\text{coop}} - i(\Gamma_{\text{coop}} + \Gamma')] \equiv \sqrt{R_{1L}}e^{i\phi^{R}_{1L}}$ and transmission $t_{1L} = 1 + r_{1L} \equiv \sqrt{T_{1L}}e^{i\phi^{T}_{1L}}$, where we recall that one has $-\pi/2 \leq \phi^{T}_{1L} \leq \pi/2$, as shown in Fig. 4.1-b. When $\mathcal{G}^{\text{ev}}_{mj} \sim 0$, the two-layer transmission derived from Eq. 5.3 can be equivalently written as

$$t_{2L}(\zeta) = \frac{T_{1L}}{1 - R_{1L}e^{2i\zeta}} e^{2i\phi^{T}_{1L}}, \qquad \zeta = 2\pi\xi_z + \phi^{R}_{1L}, \tag{5.4}$$

which is valid for both the noiseless $\Gamma' = 0$ and noisy $\Gamma' > 0$ case.

In particular, in the noiseless regime of $\Gamma' = 0$, one has $T_{1L} + R_{1L} = 1$. Thus, by tuning the distance ξ_z to satisfy $\zeta = 0$, the factor $T_{1L}/\left(1 - R_{1L}\right) = 1$ simplifies to unity, regardless of the single-layer properties. This corresponds to an ideal Fabry-Perot resonance, where the two-layer system becomes perfectly transmitting, while inheriting a completely tunable phase shift set by the single-layer transmission phase, i.e. $t_{2L}(0) = e^{2i\phi^{T}_{1L}}$.

Analogously, when $\Gamma' > 0$ the condition $\zeta = 0$ is satisfied as long as

$$\zeta = 0 \quad \longrightarrow \quad \tan(2\pi\xi_z) = \frac{1}{2\pi}\arctan\left(\frac{\nu}{1+\gamma'}\right), \tag{5.5}$$

where we define the ratio $\gamma'(\xi_x,\xi_y)=\Gamma'/\Gamma_{coop}(\xi_x,\xi_y)$, while we recall that $\nu(\xi_x,\xi_y)=2\omega_{coop}(\xi_x,\xi_y)/\Gamma_{coop}(\xi_x,\xi_y)$. This leads to the transmission on the Fabry-Perot resonance given by

$$|t_{2L}(0)|^2=\left(\frac{T_{1L}}{1-R_{1L}}\right)^2=\left[\frac{\nu^2+(\gamma')^2}{\gamma'(2+\gamma')+\nu^2}\right]^2, \qquad \phi_{2L}^{T}(0)=\arg t_{2L}(0)=2\arctan\left(\frac{\nu}{\gamma'(1+\gamma')+\nu^2}\right). \tag{5.6}$$

We recall that in our situation we have a fixed value of $\Gamma'=5.75$, while the lattice constants are constrained by $\xi_{x,y}\geq\xi_{min}\simeq 0.03$, leading to the maximum cooperative rate $\Gamma_{coop}^{max}=\Gamma_{coop}(\xi_{min},\xi_{min})\simeq 225$. This implies that $\gamma'\geq\gamma'_{min}=\Gamma'/\Gamma_{coop}^{max}\simeq 0.03$.

First of all, we want to quantify how the noise affects the system around $\phi_{2L}^{T}(0)\approx\pm\pi$, via analytic optimization. To this aim, in this paragraph we assume that γ' and ν can be independently optimized, although in general this is not true, as they are correlated by the choice of the lattice constants $\xi_{x,y}$. Nonetheless, this ensures that any physical scenario cannot perform better than what we calculate. We now ask what is the closest phase to $\phi_{2L}^{T}(0)\approx\pm\pi$ that can be achieved, and what is its associated transmission. To compute so, we first notice from Eq. 5.6, that $\phi_{2L}^{T}(0)\to\pm\pi$ when $|\nu|+(1+\gamma')(\gamma'/|\nu|)\simeq|\nu|+\gamma'/|\nu|\to 0$. We thus minimize $|\nu|+\gamma'/|\nu|$, with the constrain $\gamma'\geq\gamma'_{min}$. The optimal solution is given by $\gamma'=\gamma'_{min}$ and $\nu=\pm\sqrt{\gamma'_{min}}$, leading to $\phi_{2L}^{T}(0)\simeq\pm 2\arctan\left(1/\left(2\sqrt{\gamma'_{min}}\right)\right)\approx\pm 0.8\pi$ and $|t_{2L}(0)|^2=(4+\gamma'_{min})^2/(6+\gamma'_{min})^2\approx 0.4$, where we used $\gamma'_{min}\ll 1$. At the same time, a supplementary question is how close the phase can be to $\phi_{2L}^{T}(0)\approx\pm\pi$, when constraining the transmission to be higher than a fixed value, namely $|t_{2L}(0)|^2\geq 0.5$. We obtain the solution $\phi_{2L}^{T}(0)\approx\pm 2\arctan\left(0.4/\left(\sqrt{\gamma'_{min}}\right)\right)\approx\pm 0.7\pi$, whose inadequate value further confirms the fragility against the noise.

A radically different result emerges when studying the response of the system around the phases $\phi_{2L}^{T}(0)\approx\pm\pi/2$. The reason why this value is interesting will become clearer in the next section. Differently from the previous analysis (where we argued that even the best-case scenario had low performance), here we provide some reasonable argument to conclude that a relatively good result can be obtained with realistic settings. To this aim, we numerically observe that a choice of $\xi_{x,y}$ exists that guarantees both $\nu=\pm 1$ and $\gamma'\approx 2\gamma'_{min}\ll 1$, given our choice of $\xi_{min}=0.03$. In general, we have numerical reasons to believe that analogous results should

still be obtainable given a broad range of values of $\xi_{\min} \ll 1$, by fixing, for example, one of the lattice constant to $\xi_{\min}$ and then tuning the other. In any case, plugging $\nu = \pm 1$ into Eq. 5.6 and using $\gamma' \ll 1$, we obtain $\phi_{2\mathrm{L}}^{\mathrm{T}}(0) \simeq \pm(\pi/2 - \gamma') \approx \pm 0.45\pi$ and $|t_{2\mathrm{L}}(0)|^2 \simeq 1 - 4\gamma' \approx 0.81$. The higher resistance to the noise can be understood by observing from Fig. 5.1-a that the bandwidth where a single cavity transmits at least half of the light and imparts a phase of $\phi_{2\mathrm{L}} \sim \pm\pi/2$ is much broader than that associated to $\phi_{2\mathrm{L}} \sim \pm\pi$.

5.3.2 Robust scheme with three layers

The addition of a third atomic layer solves the problem of the previous section. The system, indeed, becomes analogous to a row of two subsequent cavities, which can be designed to impress a phase of $\phi_{2\mathrm{L}} \sim \pm\pi/2$ each, so that the total phase shift will be twice this quantity $\phi_{3\mathrm{L}} \sim 2\phi_{2\mathrm{L}}$. As discussed in the previous section, differently from $\phi_{2\mathrm{L}} \sim \pm\pi$, a single cavity can impart phases $\phi_{2\mathrm{L}} \sim \pm\pi/2$ while exhibiting much higher resistance to noise. This result is evident from Fig. 5.1-c,d, where the insets highlight the regime of $\phi_{3\mathrm{L}} \sim \pm\pi$ and $|t_{3\mathrm{L}}|^2 \geq 0.5$ over a large bandwidth, for both the noiseless (c) and noisy case (d).

In sight of these observations, we construct the building blocks of the atomic metalens with a three-layer atomic array. First, we focus on the ideal case $\Gamma' = 0$. Ignoring the evanescent interaction, the transmission reads

$$t_{3\mathrm{L}} = \frac{\nu^3}{2e^{4\pi i\xi_z}(-i+\nu) + (-i+\nu)^3 + e^{8\pi i\xi_z}(i+\nu)}. \tag{5.7}$$

The system is equivalent to a three-mirror etalon, so that it can be fully transparent when properly engineering the layer distance ξ_z [307]. In what follows, we take the following parameterization of ξ_z as a function of the lattice constants $\xi_{x,y}$

$$\begin{aligned} \xi_z(\xi_x, \xi_y) &= -\frac{\mathrm{mod}\,[g(\xi_x,\xi_y), 2\pi]}{6\pi} + \frac{5 - \mathrm{sign}[\nu(\xi_x,\xi_y)]}{12}, \\ g(\xi_x, \xi_y) &= \arg\left[-8\left(\frac{\nu+i}{\nu - i\sqrt{4+3\nu^2}}\right)^3\right] \in (-\pi, \pi], \end{aligned} \tag{5.8}$$

which is represented by the dashed, white line of Fig. 5.1-c,d. In the noiseless case, this choice of $\xi_z(\xi_x, \xi_y)$ leads to $t_{3\mathrm{L}}(\xi_x, \xi_y) = \exp[ig(\xi_x, \xi_y)]$, so that the transparency condition $|t_{3\mathrm{L}}|^2 = 1$ is ensured, while the phase shift reads

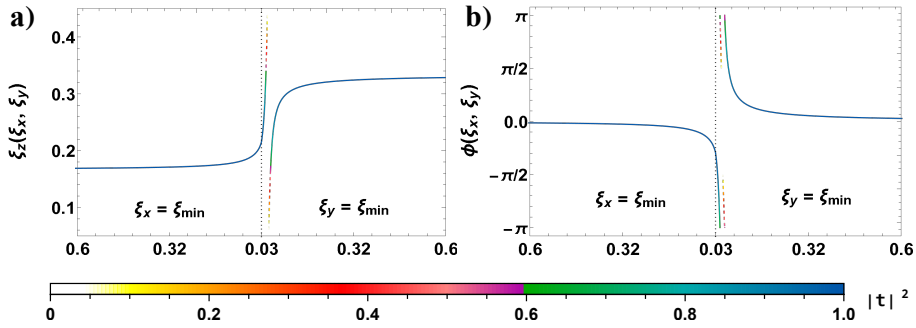

Figure 5.2: Longitudinal lattice constant ξ_z and phase shift $\phi_{3L} = \arg t_{3L}$ as a function of ξ_x and ξ_y, given $\Gamma' = 5.75$. In the subfigure (a) we show the phase shift $\phi_{3L}(\xi_x, \xi_y) \equiv \arg t_{3L}$ of a three-layer atomic array, when choosing ξ_z as in Eq. 5.8. The latter is reported in the subfigure (b). The system transmission is given by Eq. 5.7, where the noise is included by the substitution $\nu(\xi_x, \xi_y) \to \nu(\xi_x, \xi_y) - i\Gamma'/\Gamma_{coop}(\xi_x, \xi_y)$. On the horizontal axis, the transverse lattice constants ξ_x and ξ_y are varied along the path composed of the two straight lines $\xi_x = \xi_{min} \cup \xi_{min} \leq \xi_y < 1$ (left side of the plots) and $\xi_y = \xi_{min} \cup \xi_{min} \leq \xi_x < 1$ (right side of the plots), where $\xi_{min} = 0.03$. The color scheme depicts the corresponding absolute value of transmission $|t_{3L}|^2$. The solid part of the curves show the range of parameters that we consider for the design of our atomic metalens, corresponding to $-\pi < \phi(\xi_x, \xi_y) \leq \pi$, $1/6 \leq \xi_z(\xi_x, \xi_y) \leq 1/3$ and $|t_{3L}|^2 \gtrsim 0.6$.

$\phi_{3L}(\xi_x, \xi_y) \equiv \arg t_{3L}(\xi_x, \xi_y) = g(\xi_x, \xi_y)$. Then, by properly tuning $\xi_x < 1$ and $\xi_y < 1$ to explore any value of $\nu(\xi_x, \xi_y) \in \mathbb{R}$, one can design the lattice to impress any phase $-\pi < \phi_{3L}(\xi_x, \xi_y) \leq \pi$.

In the noisy case $\Gamma' = 5.75$, the transmission of Eq. 5.7 is modified by the substitution $\nu(\xi_x, \xi_y) \to \nu(\xi_x, \xi_y) - i\Gamma'/\Gamma_{coop}(\xi_x, \xi_y)$. In particular, assuming the minimum distance $\xi_{min} = 0.03$, we can vary the transverse lattice constants along the two straight lines $\xi_x = \xi_{min}$, $1 > \xi_y \geq \xi_{min}$ and $1 > \xi_x \geq \xi_{min}$, $\xi_y = \xi_{min}$, while still choosing $\xi_z(\xi_x, \xi_y)$ as in Eq. 5.8. As shown in Fig. 5.2-a, this allows to both tune the phase in the full range $-\pi < \phi_{3L}(\xi_x, \xi_y) \leq \pi$ and keep a sufficiently high transmission $|t_{3L}|^2 \gtrsim 0.6$. The corresponding values of the longitudinal lattice constant $\xi_z(\xi_x, \xi_y)$ are shown in Fig. 5.2-b, and span the range $1/6 \leq \xi_z(\xi_x, \xi_y) \leq 1/3$. Due to this reason, the maximum thickness of the atomic metalens is $\Delta z = 2\lambda_0 \xi_z^{max} = 2\lambda_0/3$, corresponding to $\Delta z \simeq 205$nm for SiV centers.

5.4 Atomic metalens

In the previous section, we showed how a three-layer atomic lattice can be engineered to impress an arbitrary phase shift, while guaranteeing high

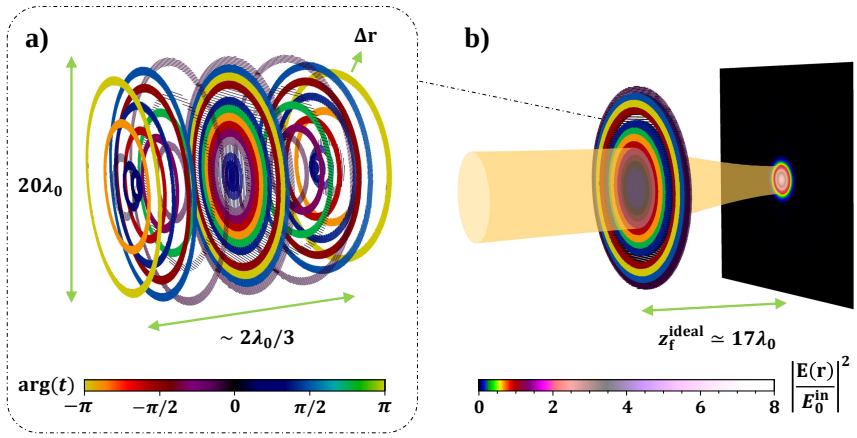

Figure 5.3: Structure of an atomic metalens, with focal length $f = 20\lambda_0$ and radius $R_{\text{lens}} = 10\lambda_0$. (a) 3D representation of the atomic metalens, where each point depicts the position of one atom. This atomic metalens is composed of 15 concentric rings of thickness $\Delta r = 2\lambda_0/3$, with a buffer-zone parameter $\alpha = 0.2$. The lens has a width of $\Delta z \approx 2\lambda_0/3$, much thinner than the total diameter of $20\lambda_0$. The atoms belonging to the j-th ring have the same lattice constants ξ_{x}^j, ξ_{y}^j and ξ_{z}^j, which are uniquely associated to the phase shift $\phi_j = \phi(\Delta r(2j-1)/2)$ of Eq. 5.1 (with $\phi_0 \simeq -2.06$), through the curves $\phi_j = \phi(\xi_{\text{x}}^j, \xi_{\text{y}}^j)$ and $\xi_{\text{z}}^j = \xi_{\text{z}}(\xi_{\text{x}}^j, \xi_{\text{y}}^j)$ shown in Fig. 5.2. The color of the atoms in each ring reflects the value of ϕ_j, as described by the colorbar at the bottom. b) Focusing of a $\hat{\mathbf{x}}$-polarized, resonant, input Gaussian beam with $w_0^{\text{in}} = 4\lambda_0$, due to the atomic metalens. The orange, shaded area shows the theoretical beam waist $w(z)$. The metalens is designed to focus the beam at a distance $z_f^{\text{ideal}} \simeq 17\lambda_0$. This defines the focal plane, where we numerically reconstruct the total intensity $I(\mathbf{r})/I_0^{\text{in}} = |\mathbf{E}(\mathbf{r})/E_0^{\text{in}}|^2$ via the input-output formalism of Eq. 2.17, in the noisy regime of $\Gamma' = 5.75$. The value of $I(\mathbf{r})$ is portrayed with the color scheme shown by the colorbar at the bottom. Further results from the coupled-dipole simulations are shown in Fig. 5.4.

transmission in presence of non-radiative noise. Here, we want to describe how such a system can be used as a building block of an atomic metalens.

The main idea is to design a pattern of lattice constants ξ_{x} and ξ_{y} which vary in space in such a way that the induced phase shift of the system $\phi_{3\text{L}}(\xi_{\text{x}}, \xi_{\text{y}})$ mimics the ideal phase shift $\phi_{\text{lens}}(r)$ of a thin lens (i.e. Eq. 5.1). Specifically, we divide the transverse plane into concentric rings $j = 1, 2...$ of radius $r_j = j\,\Delta r$ (see Fig. 5.3-a), and we associate to each ring the central phase shift $\phi_j \equiv \phi_{\text{lens}}(\Delta r\,(2j-1)/2)$, by using Eq. 5.1. Here, we recall that the initial phase shift ϕ_0 is a free parameter. At this point, we impose $\phi_{3\text{L}}(\xi_{\text{x}}^j, \xi_{\text{y}}^j) = \phi_j$, and extract the lattice constants ξ_{x}^j and ξ_{y}^j by numerically inverting the solid line of Fig. 5.2-a. Exploiting Eq. 5.8, we then define the

longitudinal distance between the layers $\xi_{\mathsf{z}}^j = \xi_{\mathsf{z}}(\xi_{\mathsf{x}}^j, \xi_{\mathsf{y}}^j)$, as in Fig. 5.2-b. For each j-th ring we can thus construct a three-layer lattice with constants ξ_{x}^j, ξ_{y}^j and ξ_{z}^j, whose atoms are constrained by the condition $r_{j-1} \leq r < r_j$. The final metalens is then the union of these discrete building blocks, as shown in Fig. 5.3. By choosing $\Delta r \lesssim \lambda_0$, we ensure that the discretization scale is of the same order of a common metalens [33, 277].

Given this scheme, at the interface between different rings the lattice constants can change abruptly. The sharp, finite size of the rings can potentially give rise to phenomena of light diffraction into unwanted modes, which should be avoided as they might lower the efficiency. To this aim, in the $\widehat{\mathbf{x}}, \widehat{\mathbf{y}}$-plane we introduce a small *buffer zone* between two consecutive rings, which extends over the first fraction $0 \leq \alpha < 1$ of each ring (i.e. the region $r_{j-1} \leq r < r_{j-1} + \alpha\Delta r$). In this buffer zone, the atoms are placed at intermediate positions between those of the consecutive rings, thus mitigating the undesired effects. The definition of such connecting regions is not strict, and many variants might be tested. Our approach is described in detail in Appendix E.2, and we numerically found that it can boost the efficiency of up to $\sim 3\%$. To conclude, we remark that for each target focal length f, our atomic metalens is defined up to three free parameters, which are the overall phase shift $-\pi < \phi_0 \leq \pi$, the ring thickness Δr, and the buffer fraction $0 \leq \alpha < 1$.

5.4.1 Numerical simulations

To check our design, we need to calculate the efficiency of the atomic metalens. Once we fix the atomic positions, we illuminate the system at normal incidence with a $\widehat{\mathbf{x}}$-polarized, resonant, input Gaussian beam focused at the lens position and defined by the beam waist w_0^{in} and the focal intensity $I_0^{\mathsf{in}} = |E_0^{\mathsf{in}}|^2/(2\mu_0 c)$. This reads $\mathbf{E}_{\mathsf{in}}(\mathbf{r}, z) = E_0^{\mathsf{in}}[w_0^{\mathsf{in}}/w(z)] \exp[-|\mathbf{r}|^2/w(z)^2 + ik_0 z + i\varphi(\mathbf{r}, z, w_0^{\mathsf{in}})]\widehat{\mathbf{x}}$, where $w(z) = w_0^{\mathsf{in}}\sqrt{1 + (z/z_{\mathsf{R}})^2}$ describes the transverse extension of the beam, while we have $\varphi(\mathbf{r}, z, w_0^{\mathsf{in}}) = -\arctan(z/z_{\mathsf{R}}) + k_0 r^2/[2R(z)]$, with $z_{\mathsf{R}} = k_0(w_0^{\mathsf{in}})^2/2$ and the radius of curvature $R(z) = z[1 + (z_{\mathsf{R}}/z)^2]$. Moreover, we want to fulfill the condition $w_0^{\mathsf{in}} > \lambda_0$, to avoid nonparaxial effects. We perform exact simulations of the linear optical response, reconstructing the total field $\mathbf{E}(\mathbf{r}, z)$ (input plus scattered) via the input-output formalism of Eq. 2.17. We want to compare it with the theoretical prediction of the field transmitted by an ideal lens of focal length f. This is given by the Gaussian beam $\mathbf{E}_{\mathsf{ideal}}(\mathbf{r}, z)$, characterized by the beam waist $w_0^{\mathsf{ideal}} = \mathcal{M} w_0^{\mathsf{in}}$, focal position $z_f^{\mathsf{ideal}} = (1 - \mathcal{M}^2) f$ and focal intensity $I_0^{\mathsf{ideal}} = I_0^{\mathsf{in}}/\mathcal{M}^2$, where the parameter $\mathcal{M} = f/\sqrt{f^2 + k_0^2 (w_0^{\mathsf{in}})^4/4}$

is the *so-called* magnification of the lens, which ensures the conservation of energy $\int|\mathbf{E}_{\text{ideal}}|^2 d\mathbf{r} = \int|\mathbf{E}_{\text{in}}|^2 d\mathbf{r} = \pi(E_0^{\text{in}} w_0^{\text{in}})^2/2$.

We analyze the projection of the transmitted field onto the ideal Gaussian mode, which reads $\langle\mathbf{E}_{\text{ideal}}|\mathbf{E}\rangle = \int \mathbf{E}^*_{\text{ideal}} \cdot \mathbf{E}\, d\mathbf{r} / \int|\mathbf{E}_{\text{ideal}}|^2 d\mathbf{r}$, as defined in Appendix A and further discussed in Appendix E.3. In the far field $z \gg \lambda_0$ this quantity does not depend on the observation point and we can use it to define the efficiency $\eta = |\langle\mathbf{E}_{\text{ideal}}|\mathbf{E}\rangle|^2$, which describes the fraction of power that is transmitted into the target solution. Similarly, we define another quantity of interest, that is the overlap between the transmitted field and the input field $\epsilon = |\langle\mathbf{E}_{\text{in}}|\mathbf{E}\rangle|^2$, which quantifies how strongly the atomic system is manipulating the light. Obviously, one aims to operate in a regime where $\eta \sim 1$, while $\epsilon \ll 1$. As our definition of efficiency is theoretically strict, we also estimate the more experimentally friendly signal-to-background ratio, which compares the power transmitted into the target mode P_η to the total transmitted power P_{out}. This reads P_η/P_{out}, where $P_\eta = \eta \int|\mathbf{E}_{\text{ideal}}|^2 d\mathbf{r}/(2\mu_0 c) = \eta\pi(E_0^{\text{in}} w_0^{\text{in}})^2/(4\mu_0 c)$, while we numerically compute $P_{\text{out}} = \int|\mathbf{E}|^2 d\mathbf{r}/(2\mu_0 c)$ by reconstructing the total field at the focal plane $z = z_{\text{f}}^{\text{ideal}}$.

To show the potential of our scheme, we can now discuss a full-scale simulation of an illustrative atomic metalens, characterized by the focal length $f = 20\lambda_0$ and the radius $R_{\text{lens}} = 10\lambda_0$, illuminated by an input Gaussian beam of waist $w_0^{\text{in}} = 4\lambda_0$. These simulations involve on the order of $N \sim 5 \times 10^5$ atoms, which is between one and two orders of magnitude larger than coupled-dipole models of atoms in literature [154, 157–159, 165, 166, 169, 170, 173–176]. The techniques by which we accomplish this are described in Appendix E.4.

The predicted magnification reads $\mathcal{M} = w_0^{\text{ideal}}/w_0^{\text{in}} \simeq 0.37$, associated to an ideal intensity enhancement of $I_0^{\text{ideal}}/I_0^{\text{in}} \simeq 7.32$. The free parameters of the lens were numerically chosen to maximize η in the noisy regime, and read $\Delta r = 2\lambda_0/3$, $\phi_0 \simeq -2.06$, and $\alpha = 0.2$. The results are shown in Fig. 5.4, where we plot the intensity of the total field $I(\mathbf{r})/I_0^{\text{in}} = |\mathbf{E}(\mathbf{r})/E_0^{\text{in}}|^2$, calculated on the horizontal plane $y = 0$ (top row) and at the expected focal plane $z = z_f^{\text{ideal}} \simeq 17\lambda_0$ (bottom row). The latter shows the focal spot, whose size is often used as an experimental benchmark of the lens efficiency. The column on the left (Fig. 5.4-a,c), shows the ideal values that one would expect for a textbook thin lens, i.e. $\mathbf{E}_{\text{ideal}}$. This is compared to the numerical simulations of the atomic metalens, calculated for the noisy case $\Gamma' = 5.75$ (right column, Fig. 5.4-b,d). Very similar plots are obtained when studying the noiseless case $\Gamma' = 0$, or when plotting the intensity on the plane $x = 0$. We benchmark the optical response of

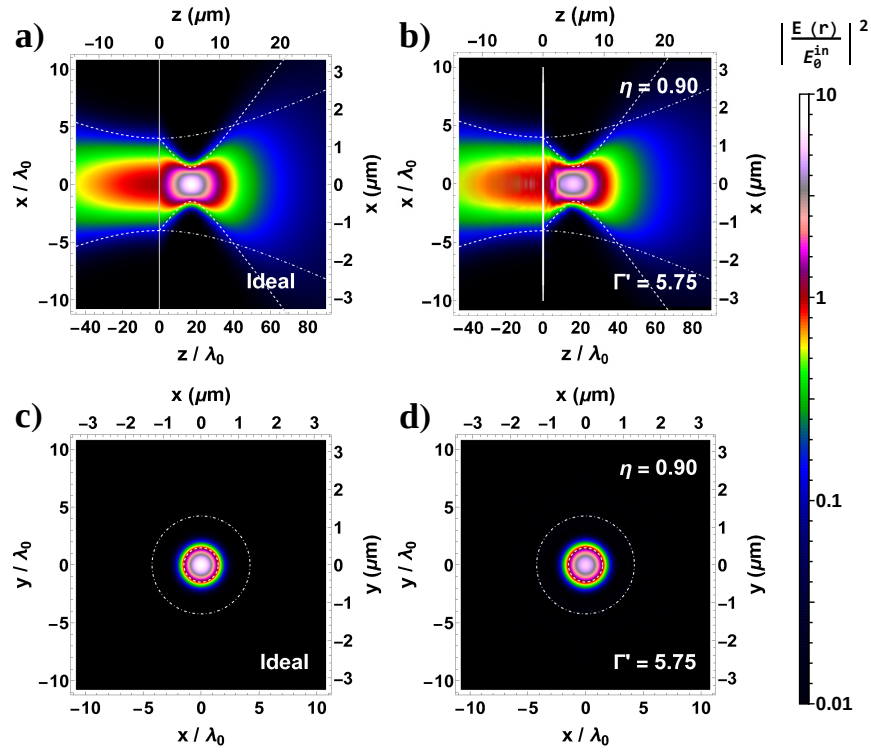

Figure 5.4: Performance of an atomic metalens with focal length $f = 20\lambda_0$, radius $R_{\text{lens}} = 10\lambda_0$, and parameters $\Delta r = 2\lambda_0/3$, $\phi_0 \simeq -2.06$, and $\alpha = 0.2$, illuminated by a resonant Gaussian beam with waist $w_0^{\text{in}} = 4\lambda_0$. The figures show the intensity of the total field $I(\mathbf{r}) \propto |\mathbf{E}(\mathbf{r})/E_0^{\text{in}}|^2$, calculated on the planes $y = 0$ (top row, subfigures a,b) and $z = z_f^{\text{ideal}} \simeq 17\lambda_0$ (bottom row, subfigures c,d). The subplots (a,c) represent the ideal case of a perfect lens, while the subplots (b,d) show the results of the numerical simulations with $\Gamma' = 5.75$. The dashed, white lines represent the ideal value of the beam extension $w(z)$, while the dot-dashed, white lines show the beam waist of the input beam without the lens. The efficiency of the noisy $\Gamma' = 5.75$ case, estimated from the simulations, reads $\eta \simeq 0.9$. Almost identical plots are obtained when plotting the intensity on the plane $x = 0$, as well as when simulating the noiseless case $\Gamma' = 0$ (although in that situation the efficiency is higher, reading $\eta \simeq 0.95$). Both the noisy and the noiseless simulations show a high signal-to-background ratio, given by $P_\eta/P_{\text{out}} > 0.98$. The number of simulated atoms is $N \simeq 4.6 \times 10^5$.

the atomic metalens from our simulations, finding an efficiency $\eta \simeq 0.95$ and an intensity enhancement at the focal point of $I_0/I_0^{\text{in}} \simeq 6.03$, in the noiseless regime. Similarly, in the noisy case of $\Gamma' = 5.75$ we obtain the values $\eta \simeq 0.90$ and $I_0/I_0^{\text{in}} \simeq 5.60$. These high efficiencies can be compared with the relatively low overlap between the output field and the input

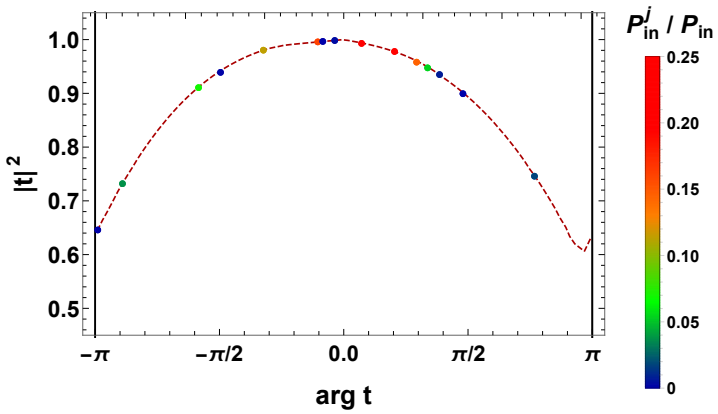

Figure 5.5: Transmission of a three-layer lattice as a function of the induced phase, given $\Gamma' = 5.75$. The dashed, red line represents the relation between $|t_{3L}|^2$ and $\arg t_{3L}$, when varying the lattice constants following our scheme. In particular, we recall that the transverse lattice constants are chosen on the path composed of the two straight lines $\xi_x = \xi_{min} \cup \xi_{min} \leq \xi_y < 1$ and $\xi_y = \xi_{min} \cup \xi_{min} \leq \xi_x < 1$, where $\xi_{min} = 0.03$, while the longitudinal lattice constant $\xi_z(\xi_x, \xi_y)$ is defined by Eq. 5.8. The colored points represent the actual values for each ring of the lens in Fig. 5.4. Their color is associated to the intensity of the input beam integrated over the area of each of those rings, divided by the input power $P_{in} = \int |\mathbf{E}_{in}|^2 d\mathbf{r}/(2\mu_0 c) = \pi(w_0^{in} E_0^{in})^2/(4\mu_0 c)$.

beam, which reads $\epsilon \simeq 0.42$ (for both $\Gamma' = 0.0$ and $\Gamma' = 5.75$). Finally, both the noisy and the noiseless cases exhibit a high signal-to-background ratio, reading $P_\eta / P_{out} > 0.98$.

To understand how the non-radiative noise affects the efficiency in Fig. 5.5, we plot the expected transmission $|t_{3L}|^2$ of the rings composing the metalens, as a function of the ring phase $\phi_{3L} = \arg t_{3L}$, in presence of noise. In the noiseless case, the transmission would always be 100%, but when $\Gamma' = 5.75$, some phases are associated to a much lower transmission, up to $|t_{3L}|^2 \approx 0.6$, around $\phi_{3L} \simeq \pm\pi$. If we consider the rings that compose our atomic metalens (colored points of Fig. 5.5) we observe that some rings can transmit more light than others, because of the presence of Γ'. The rings, however, are not homogeneously illuminated, meaning that some of them receives more energy than others. One can check that the reduction in efficiency in the noisy system (i.e. the ratio between the noisy and noiseless efficiencies), agrees well with the average of the loss of each ring, weighted by the intensity illuminating the ring. This naive model should explain why we observe that the detrimental effect of Γ' can strongly depend on the phase parameter ϕ_0 of Eq. 5.1 (which describes the phase at the center of

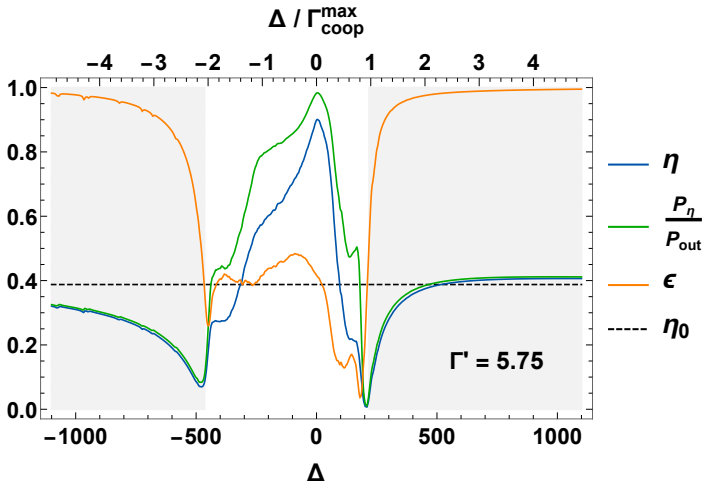

Figure 5.6: Spectral response of the atomic metalens, with focal length $f = 20\lambda_0$, radius $R_{\text{lens}} = 10\lambda_0$, and parameters $\Delta r = 2\lambda_0/3$, $\phi_0 \simeq -2.06$, and $\alpha = 0.2$. The curves represent the efficiency (η, blue), signal-to-background ratio (P_η/P_{out}, green) and overlap with the input beam (ϵ, orange). The dashed, black, horizontal line shows the value of the overlap between the input and the ideal field $\eta_0 = |\langle \mathbf{E}_{\text{ideal}} | \mathbf{E}_{\text{in}} \rangle|^2$. The simulation is performed for the noisy case $\Gamma' = 5.75$. The gray region empirically corresponds to the regime where the metalens becomes transparent and stops to efficiently focus the light. The detuning $\Delta = (\omega - \omega_0)/\Gamma_0$ is expressed both in units of Γ_0 (label below) and in units of $\Gamma^{\text{max}}_{\text{coop}} = \Gamma_{\text{coop}}(\xi_{\text{min}}, \xi_{\text{min}}) \simeq 225$ (label above).

the lens). Indeed, due to the exponential decay of the energy of the input Gaussian beam, the rings with small radius receives much more energy, meaning that one should roughly aim to maximize the transmission of the first ring, i.e. $|t_{3\text{L}}(\phi_1)|^2 = |t_{3\text{L}}(\phi(\Delta r/2))|^2$.

5.4.2 Spectral properties

Although we design our atomic metalens to optimally focus resonant light $\Delta = (\omega - \omega_0)/\Gamma_0 = 0$, it is interesting to explore the bandwidth where the efficiency retains high. Intuitively, we expect the bandwidth of the response to be of the same order of the maximum cooperative decay rate allowed in our system, i.e. $\Gamma^{\text{max}}_{\text{coop}} = \Gamma_{\text{coop}}(\xi_{\text{min}}, \xi_{\text{min}}) \simeq 225$ (in units of Γ_0).

This intuition well reflects what we numerically observe in Fig. 5.6, where we plot the spectrum of efficiency η (blue), signal-to-background ratio P_η/P_f (green) and overlap with the input mode ϵ (orange). This is calculated when illuminating the atomic metalens with a Gaussian beam of waist $w_0^{\text{in}} = 4\lambda_0$, in the noisy regime of $\Gamma' = 5.75$. As expected, when

$|\Delta/\Gamma^{\max}_{\text{coop}}| \gg 1$ the metalens shows the features of a transparent system, i.e. $\mathbf{E} \sim \mathbf{E}_{\text{in}}$, meaning that $\epsilon \sim 1$, while the efficiency tends to the overlap between the ideal and the input mode, i.e. $\eta \sim \eta_0 = |\langle \mathbf{E}_{\text{ideal}} | \mathbf{E}_{\text{in}} \rangle|^2 \approx 0.4$ (approximately marked with a gray region in the plot). On the contrary, the behaviour inside the white area is irregular, but we can identify a bandwidth of $\sim \Gamma^{\max}_{\text{coop}}$ where the efficiency η retains relatively high. For SiV centers, this would correspond to a value of $\sim (2\pi) \times 21$GHz. Finally, we stress that the value of $\Gamma^{\max}_{\text{coop}}$ is related to our particular choice of ξ_{min}, to guarantee $\Gamma^{\max}_{\text{coop}} \gg \Gamma'$. We can thus identify a trade-off between the tightness of the bandwidth and the resistance to noise, meaning that some applications which require smaller bandwidths, but can tolerate lower efficiencies, can opt for higher values of ξ_{min}.

5.4.3 Noise and imperfections

Up to now, we only included in our model the presence of some intrinsic, minimal losses, roughly characterized by the inelastic rate $\Gamma' = 5.75$. Here, we want to investigate the detrimental effects of experimental imperfections, which can deviate from that basic description.

First, we study the response in presence of much larger losses $\Gamma' \gg 1$. To this aim, it is instructive to focus on the response of the single building blocks of the metalens. In particular, in the noiseless case $\Gamma' = 0$ our scheme allows to have a perfect transmission $|t|^2 = 1$ for any chosen phase. This is not true anymore when $\Gamma' \neq 0$, as some choices of the phase become associated to lower transmission, especially around $\arg t \sim \pm\pi$. In Fig. 5.7-a, we show the relation between the phase $\arg t$ (on the horizontal axis) and the absolute transmission $|t|^2$ (color scheme), when considering increasing values of Γ' (vertical axis, in log scale). The plot is obtained by varying the lattice constant as defined by our protocol, i.e. scanning the transverse constants along the path $\xi_{\text{x}} = \xi_{\text{min}}$, $1 > \xi_{\text{y}} \geq \xi_{\text{min}}$ and $1 > \xi_{\text{x}} \geq \xi_{\text{min}}$, $\xi_{\text{y}} = \xi_{\text{min}}$, while fixing ξ_{z} to fulfill Eq. 5.8. For values $\Gamma'/\Gamma^{\max}_{\text{coop}} \gtrsim 0.04$, the system starts to manifest low transmissions $|t|^2 \lesssim 0.5$. The deleterious process becomes even stronger for values $\Gamma'/\Gamma^{\max}_{\text{coop}} \gtrsim 0.15$, where some phases cannot be engineered anymore (black areas in the plot). For our particular choice of $\xi_{\text{min}} = 0.03$, this threshold corresponds to $\Gamma' \gtrsim 30$, although this can be generally mitigated by decreasing ξ_{min}.

In Fig. 5.7-b, we discuss the overall response of our atomic metalens, for noise levels up to $\Gamma'/\Gamma^{\max}_{\text{coop}} \simeq 2 \times 10^2$, i.e. $\Gamma' \simeq 10^5$. The blue line depicts the efficiency η, the orange line the overlap ϵ and the green line the signal-to-background ratio P_η/P_{out}. Roughly, the system becomes trans-

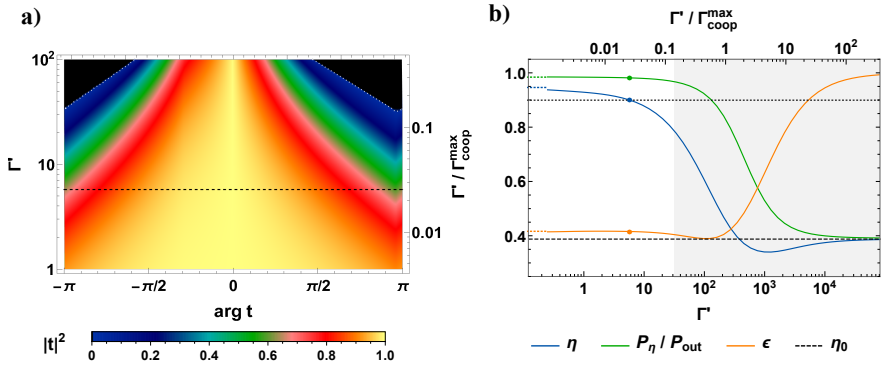

Figure 5.7: Resistance to nonradiative losses. a) Transmission $|t_{3L}|^2$ of a 3-layer array, as defined in Eq. 5.7, given increasing levels Γ'. For each value of Γ' (vertical axis), we choose ξ_x, ξ_y and ξ_z following our proposed protocol, which allows to associate a unique transmission $|t_{3L}|^2$ (color scheme) to each phase $\arg t_{3L}$ (horizontal axis). An almost identical plot is obtained if numerically optimizing $(\xi_x,\ \xi_y,\ \xi_z) \geq \xi_{min} = 0.03$ to ensure the maximum transmission. The black, dashed line highlights the particular case $\Gamma' = 5.75$. The black regions (bounded by dotted, white lines) identify values of $\arg t$ that cannot be obtained with any configuration of ξ_x, ξ_y and ξ_z, given that level of noise Γ'. b) Efficiency as a function of Γ', given an atomic metalens with focal length $f = 20\lambda_0$, radius $R_{lens} = 10\lambda_0$, and construction parameters $\Delta r = 2\lambda_0/3$, $\phi_0 \simeq -2.06$, and $\alpha = 0.2$, illuminated by a Gaussian beam with $w_0^{in} = 4\lambda_0$. The lines show the efficiency η (blue), signal-to-background ratio P_η/P_{out} (green), overlap ϵ (orange) and base-line efficiency $\eta_0 = |\langle \mathbf{E}_{ideal}|\mathbf{E}_{in}\rangle|^2$ (black, dashed line). The colored, dotted lines represent the values at $\Gamma' = 0$, while the colored points show the case of $\Gamma' = 5.75$. Finally, the black, dotted line depicts the threshold of 0.9, while the shaded, gray region portrays the regime where some phases cannot be engineered anymore by the single building blocks, i.e. the appearance of black areas in subfigure (a).

parent above the threshold $\Gamma'/\Gamma^{max}_{coop} \gtrsim 0.5$, which would correspond to $\Gamma' \gtrsim 10^2$. Notably, the efficiency retains acceptable $\eta \gtrsim 0.5$ beyond the threshold of $\Gamma'/\Gamma^{max}_{coop} \approx 0.15$ where some phases cannot be engineered anymore (gray, shaded region). This happens because the initial phase shift $\phi_0 \simeq -2.06$ allows us to concentrate the majority of the optical response far from the phases $|\phi| \sim \pi$, which are less robust to noise. This is a general recipe to maximize the efficiency, but we expect that an atomic metalens with a higher numerical aperture would hardly exhibit a good efficiency above $\Gamma'/\Gamma^{max}_{coop} \approx 0.15$. Nonetheless, for certain application, a high efficiency is unnecessary, and one only needs to identify the focal spot over the background of transmitted light [308]. As one can see from Fig. 5.7-b, the signal-to-background ratio P_η/P_{out} retains relatively high up to much higher losses, so that $P_\eta/P_{out} \gtrsim 0.9$ up to $\Gamma'/\Gamma^{max}_{coop} \approx 0.8$ (i.e. $\Gamma' \simeq 10^2$)

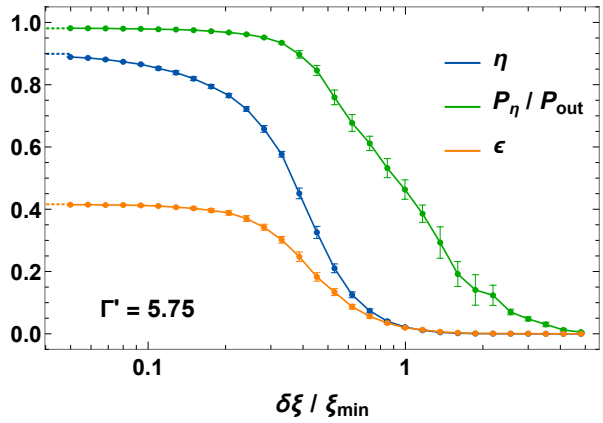

Figure 5.8: Resistance to random spatial displacement. The data are calculated for the atomic metalens with focal length $f = 20\lambda_0$, radius $R_{\text{lens}} \simeq 9\lambda_0$, and construction parameters $\Delta r = 2\lambda_0/3$, $\phi_0 \simeq -2.06$, and $\alpha = 0.2$, illuminated by a Gaussian beam with $w_0^{\text{in}} = 4\lambda_0$. The horizontal axis represents the amount of disorder $\delta\xi = \delta d/\lambda_0$. This is defined by randomly displacing the position of each atom inside a sphere of radius δd, centered at the original position. The curves represent the efficiency (η, blue), signal-to-background ratio (P_η/P_{out}, green) and overlap with the input beam (ϵ, orange). Each point is calculate by averaging over 10 random configurations, and the error bars represent one standard deviation. The simulation is performed for the noisy case $\Gamma' = 5.75$.

and $P_\eta/P_{\text{out}} \gtrsim 0.5$ up to $\Gamma'/\Gamma_{\text{coop}}^{\text{max}} \approx 5$ (i.e. $\Gamma' \simeq 10^3$).

Finally, we discuss the effect of disorder in the atomic positions, defined by randomly displacing each position inside a 3D sphere of radius $\delta\xi = \delta d/\lambda_0$, given a uniform distribution. In Fig. 5.8, we represent the values of efficiency (blue), signal-to-background ratio (green) and overlap with the input mode (orange) as a function of increasing disorder $\delta\xi$. As intuitively expected, when the displacement is comparable to ξ_{min}, then the efficiency is strongly undermined, with $\eta \to 0$. In that regime, the transmitted light is so randomly altered, that it does not overlap anymore with the input field either and $\epsilon \to 0$. This introduces a trade-off in the choice of ξ_{min}, as low values enhance the resistance to losses, but they make the system more fragile against imperfect positioning. Nonetheless, the signal-to-noise ratio still exhibit robust properties, with $P_\eta/P_{\text{out}} \gtrsim 0.6$ up to $\delta\xi \sim 0.7\xi_{\text{min}}$.

5.5 Conclusions and outlook

We have argued that it is possible to build an atomic metalens composed of atomic arrays with lattice constants ξ_x, ξ_y and ξ_z that vary in space, in order

to ensure a proper phase modulation and a good transmission. The spatial variation of the lattice constants is discretized over scales $\lesssim \lambda_0$, which roughly correspond to the discretization lengths of common metalenses [28, 33, 277]. We have shown that two atomic layers would be enough in the ideal, lossless regime, but they fail when the intrinsic losses are accounted for. On the contrary, the addition of a third layer makes the scheme more robust and resistant to losses. We tested the behaviour of an exemplary atomic metalenses, by numerically solving the coupled-dipole equations, which describe exactly the optical, linear response. To this aim, we chose a situation where the atomic metalens is substantially altering the mode of the light, up to the limitations of our computational resources. We observed good efficiencies and signal-to-background ratios, even in presence of losses.

The possibility of using atomic arrays to build up a device as complex as a lens is a fascinating idea. Differently from some other proposals [268, 269], we engineer the cooperative response by fixing tailored values of the lattice constants, without the necessity of selectively driving the individual atoms with external laser fields, to keep the lens working. If one considers a solid-state system, such as color centers in diamond, this approach would turn the atomic system into a static, passive, optical element, whose properties are set during the fabrication process, such as the majority of usual metalenses. Similarly to these latter, our atomic metalens would be characterized by a subwavelength thickness (reading $\simeq 2\lambda_0/3$), and it wouldn't intrinsically require a much thicker substrate (typically ~ 1mm, for common metalenses [33]). At the same time, our scheme shares with metalenses the possibility to polarize and spectrally filter the focused light, given that the atomic system is meant to respond only to one transverse polarization [309] and within a small bandwidth $\sim 10^2\Gamma_0$ (i.e. tens of GHz for typical electronic transitions).

The atomic nature of our metalens can provide further tools to dynamically control the optical properties. As an example, AC Stark shift has been proposed as a path to control the response of atomic arrays [268, 269], and we estimate that in our scheme this phenomenon could be exploited to fine-tune the wavelength of maximum efficiency, by a factor of few GHz. Similarly, it has been shown that the atomic, optical response can be dynamically tuned by addressing supplementary atomic level, potentially modifying their refractive index [310], or the dispersion relation in ordered arrays [311].

Our calculations are performed in the classical regime of linear optical response. Nonetheless, at the quantum level, atoms can be engineered to exhibit strong nonlinearities. Given a system of two atomic arrays in series, it was recently discussed the possibilities of either enhancing the non-

linear, collective effects [312], or even designing a non-reciprocal optical response [313]. Similarly, large interest was raised by the possibility of dynamically inhibiting the atomic response by exploiting Rydberg blockade [265–267, 314]. This can be activated in the quantum regime, potentially allowing to create a quantum superposition of different macroscopic optical responses. Finally, for the specific case of solid-state systems such as color centers in diamond, further physical effects can be exploited to tune the resonance frequency of individual color centers, such as two-photon Raman transitions [315] or strain control [316–319].

Our proposal is based on the design of atomic arrays that can impress an arbitrary phase shift, along with high transmission. These building blocks can potentially offer a broader range of optical applications. As an example, they exhibit the typical requirements to encode a phase-only, computer-generated hologram [320–322]. To this aim, one would need to arrange the atomic arrays into subwavelength $\lesssim \lambda_0$ quadratic pixels, whose phase shift encodes the hologram, rather than concentric rings. Moreover, one could also explore other combinations of lattice constants associated to a lower transmission, given that holograms can be more efficiently encoded when engineering both amplitude and phase [320, 321, 323].

Part III

Discussion

6 - Overall conclusions

The promising role of photonics in modern and future technologies [324] has motivated in the recent years a deeper analysis of the intrinsic bounds to the index of refraction, from either a fundamental [4, 80] or more applied [55–57] perspective. Given the implicit limits imposed on photonic devices [140], it is indeed surprising that no complete answer exists to an apparently basic question: why is the refractive index always of order one?

To tackle this question, we embarked on an unconventional path, starting from an idealized description of the dilute, quantum optical regime, and then drawing a continuous line which would potentially connect its predictions to those of solid-state materials. To do so, we had to explore in detail a vast, intermediate region where the inter-atomic distances are much smaller than the extent of optical cross sections of the atoms, but nonetheless considerably larger than the size of atomic orbitals. Under these conditions, the atoms can be considered as point-like light scatterers, but the multiple scattering of light occurring between them must be treated non-perturbatively.

Our results open several questions on a number of fronts. First, they suggest that the refractive index of a disordered atomic medium is intrinsically limited by electrodynamics, due to a combination of near-field coupling and random atomic positions. These properties effectively induce an intrinsic inhomogeneous broadening, which limits the number of near-resonant atoms to few atoms per cubic wavelength, regardless of the physical density. The existence of such a process has compelling implications for those quantum technologies based on atomic ensembles. In fact, on the back of our findings, it has been shown that this phenomenon can represent an intrinsic dephasing mechanism for collective, spin-wave excitations [259, 325], decreasing the performance of light-matter interfaces based on this paradigm. At the same time, we notice that the magnitude of the OD encodes fundamental error bounds for many applications [14, 218, 219], and a constraint on the maximum imaginary part of the index limits the minimum system sizes that are compatible with high fidelities.

Furthermore, the detrimental effect of this inhomogeneous broadening scales as the average near-field intensity $\sim 1/\langle\rho\rangle^3 \approx \eta$. In three-dimensional ensembles, this equates the additive enhancement of the optical response with increasing densities $\eta = N/(k_0^3 V)$, and this balance leads to the saturation of the optical response. For 2D geometries, this would not hold

true anymore, as the inhomogeneous broadening $\sim 1/\langle\rho\rangle^3$ would eventually overcome the additive response $\sim 1/\langle\rho\rangle^2$, leading to the counter-intuitive prediction that the atomic medium would become progressively transparent at higher densities. As numerical simulations strongly support this interpretation, two-dimensional slabs of cold atoms (such as those studied in [158]) would then represent a straightforward ground to experimentally test our theory.

This raises wider questions on the role of dimensionality in dense, disordered, atomic media. It is well known, for example, that this should represent a decisive parameter for the appearance of Anderson localization of light [182, 183, 204, 215–217]. Can our RG formalism provide key insights to the challenging question of whether an Anderson localization transition exists in a 3D ensemble? Some recent experiments with silica particles [326] and titanium powders [327, 328] show evidences in this direction, suggesting that the near-field couplings provide a competing channel for the energy transport, which suppresses localization. One can wonder if a similar description can be applied to atomic ensembles. Our RG theory could then not only describe this property at the steady-state (due to a renormalized, lower density of near-resonant atoms), but it might also provide a framework to estimate the complex structure of this hypothetical near-field channel. To this aim, a suggestive strategy would consist of addressing the transport dynamics with the insights gained from studying the spread of correlations during the RG flow. More generally, the problem of optical trapping is strictly related to the concepts of subradiance [329, 330] and superradiance [331]. We have numerical evidences that the correlations built by the RG can be used to approximately reproduce the decay-rate distribution of superradiant eigenmodes in spherical atomic clouds. The possibility of relating this observation with light transport via near-field couplings is certainly an intriguing perspective.

Differently from the disordered case, we found that in 3D atomic arrays a high optical response is favoured by the perfect interference patterns stemming from the multiple scattering of light. Specifically, this applies to the subwavelength, quantum optics regime of atoms acting as point-like scatterers, with characteristic lattice constants $a_0 \ll d < \lambda_0$. In this situation, the optical behaviour reduces to a single-mode problem [332], leading to an enhanced, purely real, refractive index which grows as $n \approx \lambda_0/(2d)$. Similarly, we predict that a lossless NZI is theoretically possible in the same regime. Both these findings suggest that extreme indices of refraction are not prohibited by the laws of physics, as long as one deals with resonant and low-loss objects (such as atoms) whose optical response

is narrow-band enough, in agreement with [3].

Aiming to highlight the extreme limits to the index, we designed our lattice geometry to enhance this single-mode response, by choosing a distance $d_z \gg d$ between the 2D arrays, larger than their transverse lattice constant d. This allows us to neglect the coupling between 2D layers mediated by the evanescent field, stemming from the non-radiative diffraction orders. Similarly to what mentioned for the disordered case, this phenomenon can nonetheless represent a competing transport channel, whose effects in the ordered case would be similar to having a tight-binding, hopping term on top of the radiative Hamiltonian. We have argued that this phenomenon can make the dispersion relation non-invertible, meaning that the incident light at some given frequencies can potentially excite a superposition of two modes, in relation to these two transport processes. It would be interesting to provide a full characterization of this regime. Specifically, if such superposition is nearly equal, then the index would not be a well-defined concept. In practice, however, since one wavevector is much larger than the other, then one would expect that the lower k_z would get predominantly excited, due to mode-matching considerations, which in turn would define the index. In any case, it would be compelling to provide a deeper description of the physical meaning of these evanescent-field phenomena, for example whether they continuously transform into quasi-particle excitations in the limit of a dense, conventional solid.

At very close distances $d \ll \lambda_0$, it is well known that the atomic scattering can be described by a series of multipole orders, by expanding the response for values of d much larger than the atomic orbitals $\sim a_0$. In our analysis, we retain only the first-order (electric-dipole) term, by focusing on the regime $d > 10a_0$. We also neglect further well-known perturbative processes stemming from those energy non-conserving terms in the electric-dipole Hamiltonian, such as van Der Waals and Casimir interactions between ground-state atoms, or (Rydberg-like) blockade effects between excited states [333]. This latter, indeed, would only be relevant in the non-linear, multi-excitation case, while the first would produce an overall shift of ground-state energy, which would not affect our conclusions. In this context, the first corrections that we identify are related to electron tunneling between neighbouring, overlapping orbitals, which we argue can suppress the enhanced refractive index back to unity.

Introducing the onset of quantum chemistry in the framework of non-perturbative multiple light scattering is a new, fascinating paradigm, which would deserve further studies. In particular, it would be interesting to identify the immediate, second-order corrections to our description, once one

approaches $d \sim a_0$ and our perturbative treatment of chemistry is not valid anymore. At the same time, one might investigate if other processes can be engineered to suppress the detrimental mechanisms discussed, to obtain higher refractive indices. More ambitiously, it would be desirable to develop a more general framework to predict the optical response in the regime of non-perturbative light scattering. One possible approach would consist of generalizing the methods based on the electromagnetic Green's function to many-body, condensed-matter settings, aiming to describe on the same non-perturbative and second-quantized ground, both the multiple scattering of light and the many-body dynamics of the electrons.

To conclude, our work provided various insights on the linear optical behaviour in presence of strong multiple scattering of light. One might wonder if similar approaches might be used to characterize the nonlinear regime. From a technological standpoint, indeed, it would be equally relevant to understand the mechanisms limiting the nonlinear properties of materials. From a more applied perspective, one might investigate if strong multiple scattering could lead to an enhanced nonlinear response, in analogy to what observed for the refractive index of an atomic lattice. More specifically, in the disordered case we hypothesize that our RG theory could provide useful tools to extend the diagrammatic treatment of nonlinearities (see [205] for the dilute case) to the strong-scattering scenario of dense media. A possible approach would consist of first summing via RG the interactions between nearby pairs, and then treating the remaining interactions perturbatively. In the case of atomic lattices, on the contrary, our analysis of the defects might represent a potential starting point, since the first manifestation of nonlinearity is given by an excited atom acting as a defect for a second incoming photon. Similarly to [232, 233], we showed the importance of near-field effects, which lead to the counter-intuitive result of a defect having a bigger scattering cross section than a unit cell.

Finally, we mention that engineering the nonlinear, inter-atomic interactions could be a fascinating outlook also for our proposal of an atomic metalens, as it might be use to induce specific and on-demand optical effects on top of the lens. In the context of atomic arrays, for instance, it was either proposed how to tailor a non-reciprocal response [313], or shown how to experimentally inhibit the optical response at the quantum level [334]. All these properties can potentially apply to the building blocks of our atomic metalens, paving the way to their possible use in the metalens context.

Appendix

A - Optical mode projection

Here, we discuss the projection of a light field into a well-defined optical mode, to infer the transmission and reflection of Eq. 3.2 and Eq. 3.3.

A.1 Definition of the mode projection

We start by considering generic, monochromatic field $\mathbf{E}^{\pm}$ with wavevector $|\mathbf{k}_{\mathrm{xyz}}|= k_0 = 2\pi/\lambda_0$, where the sign $\pm$ selects only the forward or backward components $\pm k_{\mathrm{z}}$, along the $\widehat{\mathbf{z}}$ direction. Hereafter, we focus on the case of forward-propagating light $\mathbf{E} = \mathbf{E}^{+}$ in the far field $k_0 z \gg 1$ (where evanescent components are suppressed). Analogous conclusions can be derived for the backward case $\mathbf{E}^{-}$, given $k_0 z \ll -1$. We can write

$$\mathbf{E}(\mathbf{r}_{\perp}, z) = \int_{|\mathbf{k}_{\mathrm{xy}}|\leq k_0} \frac{d\mathbf{k}_{\mathrm{xy}}}{(2\pi)^2}\, \mathbf{E}(\mathbf{k}_{\mathrm{xy}}) e^{i\mathbf{k}_{\mathrm{xy}}\cdot\mathbf{r}_{\perp}} e^{ik_{\mathrm{z}}(\mathbf{k}_{\mathrm{xy}})z},$$

$$\mathbf{E}(\mathbf{k}_{\mathrm{xy}}) = E_{\mathrm{x}}(\mathbf{k}_{\mathrm{xy}})\widehat{\mathbf{x}} + E_{\mathrm{y}}(\mathbf{k}_{\mathrm{xy}})\widehat{\mathbf{y}} - \left[\frac{k_{\mathrm{x}}E_{\mathrm{x}}(\mathbf{k}_{\mathrm{xy}})}{k_{\mathrm{z}}(\mathbf{k}_{\mathrm{xy}})} + \frac{k_{\mathrm{y}}E_{\mathrm{y}}(\mathbf{k}_{\mathrm{xy}})}{k_{\mathrm{z}}(\mathbf{k}_{\mathrm{xy}})}\right]\widehat{\mathbf{z}}. \tag{A.1}$$

where $k_{\mathrm{z}}(\mathbf{k}_{\mathrm{xy}}) = \sqrt{k_0^2 - |\mathbf{k}_{\mathrm{xy}}|^2}$. We are interested in calculating the flux of energy Φ across the $z \gg \lambda_0$, $\widehat{\mathbf{x}}, \widehat{\mathbf{y}}$-plane. For any polarized light beam, we can define $E_{\mathrm{y}}(\mathbf{r}_{\perp}, z) = 0$ without loss of generality, by labelling $\widehat{\mathbf{x}}$ the polarization axis and $\widehat{\mathbf{y}}$ its orthogonal component. We thus calculate Φ from the surface integral of the $\widehat{\mathbf{z}}$-component of the Poynting vector

$$\frac{\Phi}{2} = \int_{k_0 z \gg 1} d\mathbf{r}_{\perp} E_{\mathrm{x}}(\mathbf{r}_{\perp}, z) H_{\mathrm{y}}^{*}(\mathbf{r}_{\perp}, z) = \int_{|\mathbf{k}_{\mathrm{xy}}|\leq k_0} \frac{d\mathbf{k}_{\mathrm{xy}}}{(2\pi)^2} E_{\mathrm{x}}(\mathbf{k}_{\mathrm{xy}}) H_{\mathrm{y}}^{*}(\mathbf{k}_{\mathrm{xy}}), \tag{A.2}$$

which shows that Φ doesn't depend on z in the far field $k_0 z \gg 1$. There, we made use of the far-field condition to restrict to $|\mathbf{k}_{\mathrm{xy}}| \leq k_0$, while the initial factor of 2 comes from time average. The magnetic field can be calculated by means of the Maxwell's equation and using $\nabla \cdot \mathbf{E} = 0$, obtaining

$$H_{\mathrm{y}}^{*}(\mathbf{k}_{\mathrm{xy}}) = \left(\frac{1}{ck_0\mu_0}\right)\left[k_{\mathrm{z}}(\mathbf{k}_{\mathrm{xy}}) + \frac{k_{\mathrm{x}}^2}{k_{\mathrm{z}}(\mathbf{k}_{\mathrm{xy}})}\right] E_{\mathrm{x}}^{*}(\mathbf{k}_{\mathrm{xy}}) \tag{A.3}$$

We finally obtain

$$\Phi = \frac{2}{c\mu_0} \int_{|\mathbf{k}_{\mathrm{xy}}|\leq k_0} \frac{d\mathbf{k}_{\mathrm{xy}}}{(2\pi)^2} \frac{k_{\mathrm{z}}(\mathbf{k}_{\mathrm{xy}})}{k_0} |\mathbf{E}(\mathbf{k}_{\mathrm{xy}})|^2, \tag{A.4}$$

where we used $|E_{\mathrm{x}}(\mathbf{k}_{\mathrm{xy}})|^2 = k_{\mathrm{z}}(\mathbf{k}_{\mathrm{xy}})^2|\mathbf{E}(\mathbf{k}_{\mathrm{xy}})|^2/[k_{\mathrm{x}}^2 + k_{\mathrm{z}}(\mathbf{k}_{\mathrm{xy}})^2]$. Inspired by this analysis, we can define the projection of a field $\mathbf{E}(\mathbf{r}_\perp, z)$ onto the spatial mode $\mathbf{E}_{\mathrm{mode}}(\mathbf{r}_\perp, z)$ as

$$\langle \mathbf{E}_{\mathrm{mode}}|\mathbf{E}\rangle = \mathcal{N}_{\mathrm{mode}} \int_{|\mathbf{k}_{\mathrm{xy}}|\leq k_0} \frac{d\mathbf{k}_{\mathrm{xy}}}{(2\pi)^2} \frac{k_{\mathrm{z}}(\mathbf{k}_{\mathrm{xy}})}{k_0} \mathbf{E}^*_{\mathrm{mode}}(\mathbf{k}_{\mathrm{xy}}) \cdot \mathbf{E}(\mathbf{k}_{\mathrm{xy}}), \tag{A.5}$$

which is normalized to the detection mode, i.e. $\mathcal{N}_{\mathrm{mode}} = 2/(c\mu_0\Phi_{\mathrm{mode}})$.

A.2 Mode decomposition

The physical meaning of this equation can be explained by decomposing the fields into a complete set of plane waves, whose wavevector $\mathbf{k}_{\mathrm{xy}} = k_0(\cos\phi_k \sin\theta_k \widehat{\mathbf{x}} + \sin\phi_k \sin\theta_k \widehat{\mathbf{y}})$ is written in spherical coordinates

$$\mathbf{u}^{k_0}_{\theta_k,\phi_k,\alpha}(\mathbf{r}_\perp, z) = \widehat{\mathbf{e}}^{\alpha}_{\theta_k,\phi_k} e^{ik_0(\cos\phi_k \sin\theta_k x + \sin\phi_k \sin\theta_k y + \cos\theta_k z)}, \tag{A.6}$$

where we introduce the polarization basis defined by the two independent versors $\widehat{\mathbf{e}}^1_{\theta_k,\phi_k} = \sin\phi_k\widehat{\mathbf{x}} - \cos\phi_k\widehat{\mathbf{y}}$, parallel to the $\widehat{\mathbf{x}},\widehat{\mathbf{y}}$-plane, and $\widehat{\mathbf{e}}^2_{\theta_k,\phi_k} = \cos\phi_k\cos\theta_k\widehat{\mathbf{x}} + \sin\phi_k\cos\theta_k\widehat{\mathbf{y}} - \sin\theta_k\widehat{\mathbf{z}}$, orthogonal to $\widehat{\mathbf{e}}^1_{\theta_k,\phi_k}$ and to $\mathbf{k}_{\mathrm{xyz}} = \mathbf{k}_{\mathrm{xy}} + k_{\mathrm{z}}(\mathbf{k}_{\mathrm{xy}})\widehat{\mathbf{z}}$ [152]. We can re-write the expression in Eq. A.1 as

$$\mathbf{E}(\mathbf{r}_\perp, z) = \frac{k_0^2}{(2\pi)^2} \sum_{\alpha=1,2} \int_{S^+} d\Omega_k \; \tilde{E}^{\alpha}(\theta_k,\phi_k) \; \mathbf{u}^{k_0}_{\theta_k,\phi_k,\alpha}(\mathbf{r}_\perp, z) \tag{A.7}$$

where we made use of the integral equation

$$\int_{|\mathbf{k}_{\mathrm{xy}}|\leq k_0} \frac{d\mathbf{k}_{\mathrm{xy}}}{k_0 k_{\mathrm{z}}(\mathbf{k}_{\mathrm{xy}})} f(\mathbf{k}_{\mathrm{xy}}) = \int_{S^+} d\Omega_k f(\theta_k,\phi_k), \tag{A.8}$$

with S^+ representing the positive $k_{\mathrm{z}} > 0$ hemisphere. We also defined

$$\frac{k_{\mathrm{z}}(\mathbf{k}_{\mathrm{xy}})}{k_0}\mathbf{E}(\mathbf{k}_{\mathrm{xy}}) = \sum_{\alpha=1,2} \tilde{E}^{\alpha}(\theta_k,\phi_k)\widehat{\mathbf{e}}^{\alpha}_{\theta_k,\phi_k} = \tilde{\mathbf{E}}(\theta_k,\phi_k). \tag{A.9}$$

In sight of these definitions, the projection Eq. A.5 becomes

$$\langle \mathbf{E}_{\mathrm{mode}}|\mathbf{E}\rangle = \mathcal{N}_{\mathrm{mode}} \int_{S^+} d\Omega_k \; \tilde{\mathbf{E}}^*_{\mathrm{mode}}(\theta_k,\phi_k) \cdot \tilde{\mathbf{E}}(\theta_k,\phi_k), \tag{A.10}$$

which clarifies the correct physical meaning of the projection, given that the choice $\mathbf{E}_{\mathrm{mode}} = \mathbf{u}^{k_0}_{\theta'_k,\phi'_k,\alpha'}$ leads to the correct coefficient $\langle \mathbf{u}^{k_0}_{\theta'_k,\phi'_k,\alpha'}|\mathbf{E}\rangle \propto$

$\tilde{E}^{\alpha'}(\theta'_k, \phi'_k)$, up to the factor $\mathcal{N}_{\text{mode}}$, which is undefined for a plane wave.

A.2.1 Paraxial limit

Its physical interpretation further simplifies in the paraxial limit, where the detection mode $\mathbf{E}_{\text{mode}}$ has non-null Fourier components only when $k_z(\mathbf{k}_{xy}) \approx k_0$. Starting from Eq. A.5 and using $k_z(\mathbf{k}_{xy}) \approx k_0$, one has

$$\langle \mathbf{E}_{\text{mode}} | \mathbf{E} \rangle \simeq \mathcal{N}_{\text{mode}} \int_{k_0 z \gg 1} d\mathbf{r}_\perp \; \mathbf{E}^*_{\text{mode}}(\mathbf{r}_\perp, z) \cdot \mathbf{E}(\mathbf{r}_\perp, z), \tag{A.11}$$

where we used the fact that the evanescent components are null in the far field [152, 170, 234, 235]. This simplified equation is commonly used to describe the coupling between a free-space light beam and a single-mode fiber [156, 157]. Any complete set $\mathbf{E}^\alpha_{mn}$ of solutions to the paraxial wave equation (α defines two orthogonal polarizations in the $\widehat{\mathbf{x}}, \widehat{\mathbf{y}}$ plane), satisfy the correct relations using the scalar product of Eq. A.11

$$\begin{aligned} &\text{Orthogonality:} && \langle \mathbf{E}^\alpha_{mn} | \mathbf{E}^{\alpha'}_{m'n'} \rangle = \delta_{m,m'} \delta_{n,n'} \delta_{\alpha,\alpha'}, \\ &\text{Completeness:} && \sum_{m,n} [\mathbf{E}^\alpha_{mn}(\mathbf{r}_\perp, z)]^* \cdot \mathbf{E}^\alpha_{mn}(\mathbf{r}'_\perp, z') \propto \delta(\mathbf{r}_\perp - \mathbf{r}'_\perp), \end{aligned} \tag{A.12}$$

meaning that any generic paraxial field can be written as a linear combination $\mathbf{E} = \sum_{m,n,\alpha} \mathcal{C}^\alpha_{mn} \mathbf{E}^\alpha_{mn}$, so that the projection defined in Eq. A.11 correctly yields $\langle \mathbf{E}^\alpha_{mn} | \mathbf{E} \rangle = \mathcal{C}^\alpha_{mn}$.

A.3 Projection of the scattered field

We want to apply our definition of the projection to the field scattered by an atomic dipole $\mathbf{d}_j = \mathbf{d}_0 \beta_j$, which reads

$$\mathbf{E}^j_{\text{sc}}(\mathbf{r}_\perp, z) = E_0 \left(\frac{3\pi}{k_0} \right) \frac{\Gamma_0}{\Omega_0} \bar{\bar{\mathbf{G}}}(\mathbf{r}_\perp - \mathbf{r}^j_\perp, z - z_j) \cdot \mathbf{d}_j. \tag{A.13}$$

The Green's function can be written in Fourier space as [150, 152, 262]

$$\begin{aligned} &\bar{\bar{\mathbf{G}}}(\mathbf{r}_\perp - \mathbf{r}^j_\perp, z - z_j, \omega_0) \\ &\quad = \int_{\mathbb{R}^2} \frac{d\mathbf{k}_{xy}}{(2\pi)^2} \left[\left(\frac{i}{2k_0^2} \right) \frac{\bar{\bar{\mathcal{K}}}(\mathbf{k}_{xy}, \omega_0)}{k_z(\mathbf{k}_{xy})} \right] e^{i\mathbf{k}_{xy} \cdot (\mathbf{r}_\perp - \mathbf{r}^j_\perp) + i|z - z_j| k_z(\mathbf{k}_{xy})}, \end{aligned} \tag{A.14}$$

where

$$\bar{\bar{\mathcal{K}}}(\mathbf{k}_{\mathrm{xy}},\omega_0)=\begin{pmatrix} k_0^2-k_{\mathrm{x}}^2 & -k_{\mathrm{x}}k_{\mathrm{y}} & -s\ k_{\mathrm{x}}k_{\mathrm{z}}(\mathbf{k}_{\mathrm{xy}}) \\ -k_{\mathrm{x}}k_{\mathrm{y}} & k_0^2-k_{\mathrm{y}}^2 & -s\ k_{\mathrm{y}}k_{\mathrm{z}}(\mathbf{k}_{\mathrm{xy}}) \\ -s\ k_{\mathrm{x}}k_{\mathrm{z}}(\mathbf{k}_{\mathrm{xy}}) & -s\ k_{\mathrm{y}}k_{\mathrm{z}}(\mathbf{k}_{\mathrm{xy}}) & k_0^2-k_{\mathrm{z}}(\mathbf{k}_{\mathrm{xy}})^2 \end{pmatrix}, \tag{A.15}$$

where $s=\mathrm{sign}(z-z_j)$. In our case, we are studying forward-propagating light in the regime where $z>z_j$ (similar conclusions apply for the opposite case). From Eq. A.5 we have

$$\begin{aligned}&\langle\mathbf{E}_{\mathrm{mode}}|\mathbf{E}^j_{\mathrm{sc}}\rangle \\ &\propto\frac{i}{2k_0^3}\int_{|\mathbf{k}_{\mathrm{xy}}|\le k_0}\frac{d\mathbf{k}_{\mathrm{xy}}}{(2\pi)^2}\left(\tilde{\mathbf{E}}^*_{\mathrm{mode}}(\mathbf{k}_{\mathrm{xy}})\cdot\bar{\bar{\mathcal{K}}}(\mathbf{k}_{\mathrm{xy}})\cdot\mathbf{d}_j\right)e^{-i\mathbf{k}_{\mathrm{xy}}\cdot\mathbf{r}^j_\perp-ik_{\mathrm{z}}(\mathbf{k}_{\mathrm{xy}})z_j} \\ &=\frac{i}{2k_0}\mathbf{E}^*_{\mathrm{mode}}(\mathbf{r}^j_\perp,z_j)\cdot\mathbf{d}_j.\end{aligned} \tag{A.16}$$

where we exploited $\tilde{\mathbf{E}}^*_{\mathrm{mode}}(\mathbf{k}_{\mathrm{xy}})\cdot\bar{\bar{\mathcal{K}}}(\mathbf{k}_{\mathrm{xy}})\cdot\mathbf{d}_j=k_0^2\tilde{\mathbf{E}}^*_{\mathrm{mode}}(\mathbf{k}_{\mathrm{xy}})\cdot\mathbf{d}_j$, due to Eq. A.1 and Eq. A.15. If one chooses the detection mode $\mathbf{E}_{\mathrm{mode}}=\mathbf{E}_{\mathrm{gauss}}$ as a paraxial, Gaussian beam of waist w_0, travelling in the $\hat{\mathbf{z}}$ direction, then $\mathcal{N}_{\mathrm{gauss}}=2/(\pi w_0^2E_0^2)$, so that

$$\langle\mathbf{E}_{\mathrm{gauss}}|\mathbf{E}^j_{\mathrm{sc}}\rangle=\frac{3i}{(k_0w_0)^2}\frac{\mathbf{E}^*_{\mathrm{gauss}}(\mathbf{r}^j_\perp,z_j)\cdot\mathbf{d}_0}{E_0}\left(\frac{\Gamma_0}{\Omega_0}\beta_j\right), \tag{A.17}$$

where we recall that, in our notation, we have $\mathbf{d}_j=\beta_j\mathbf{d}_0$, where β_j is the excited-state coefficient of the j-th atom. This defines the transmission coefficient of Eq. 3.2. Similarly, the reflection can be inferred by projecting onto the backward mode $\mathbf{E}^*_{\mathrm{gauss}}$, to obtain Eq. 3.3.

B - Analysis of the RG scheme

Here, we provide a more detailed and formal description of the RG algorithm. The first part of this technical subsection is meant to ensure that the scheme could be fully reproducible. In the second part, we discuss the problem of assigning new positions to the renormalized atoms. Finally, we analyze the optical cross section of an atomic pair.

B.1 Definition of the RG algorithm

We assume that we have an ensemble of N randomly positioned atoms. As shown in Eq. 3.4, each pair of atoms interacts through the coupling $G_{ij} = (3\pi/k_0)\widehat{\mathbf{x}} \cdot \bar{\bar{\mathbf{G}}}(\boldsymbol{\rho}_{ij}, \omega_0) \cdot \widehat{\mathbf{x}}$, where $\boldsymbol{\rho}_{ij} \equiv k_0(\mathbf{r}_i - \mathbf{r}_j)$. The $1/\rho_{ij}^3$ near-field component of G_{ij} is given by Eq. 3.7. This near-field interaction is purely real, and describes a coherent interaction between dipoles.

Let us now consider a generic step of the RG flow, where the atomic ensemble is already composed of effective atoms characterized by different atomic resonances and a specific set of allowed near-field interactions. This system is described by the $N \times N$ matrix $\mathcal{M} = \text{diag}(\boldsymbol{\omega}) - \tilde{G}$, where the elements $\tilde{G}_{ij}$ read $\tilde{G}_{ij} = \mathcal{L}_{ij} G_{ij}^{\text{near}} + (G_{ij} - G_{ij}^{\text{near}})$. Numerically, this matrix is initialized according to $\boldsymbol{\omega}^{\text{init.}} = (0, \dots, 0)$ and $\mathcal{L}_{ij}^{\text{init.}} = 1 - \delta_{ij}$, stating that all atoms are resonant at the frequency ω_0 and cannot self-interact.

At each step of the RG flow, we evaluate the list of couplings $\mathcal{K}_{ij} = \mathcal{L}_{ij}|G_{ij}^{\text{near}}|/(|\delta\omega_{ij}|+1)$ (where $\delta\omega_{ij} = (\omega_i - \omega_j)/2$), ordering them from the largest to smallest in amplitude. Nominally, we should select the most strongly interacting pair and renormalize the pair properties, but the computational cost of this approach would be unfeasible for large atom number. Due to this reason, we start from the most strongly interacting pair (say, i, j), select it, and remove from the list all other pairs containing one of those atoms (e.g. i, k or j, k). We then proceed iteratively, until we select N_{step} most strongly interacting pairs. We choose N_{step} to be a small fraction of the total atom number N (approximately $\sim 2.5\%$), since the maximum number of possible disjoint pairs scales as $N/2$. We have checked that the results are insensitive to different choices. Given each pair (i, j) of the selected set, we diagonalize $\mathcal{M}_{\text{pair}}$, and define its eigenvalues as the new effective resonances $\omega_\pm = \langle\omega\rangle_{ij} \mp \sqrt{\delta\omega_{ij}^2 + (G_{ij}^{\text{near}})^2}$, where $\langle\omega\rangle_{ij} = (\omega_i + \omega_j)/2$. We then substitute the initial frequencies (ω_i, ω_j) with the new two effective resonances in $\boldsymbol{\omega}$, randomly choosing the labels.

We need to impose that the pair does not interact anymore through the

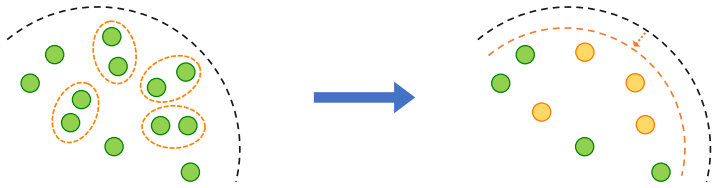

Figure B.1: RG scheme based upon re-positioning atoms. Due to the finite size of the sample, if one defines the positions of the new effective atoms as being at the midpoint between the original pair, then, at each RG step, the cloud effectively shrinks, resulting in a distortion of the ensemble.

near field, meaning that we must replace $\mathcal{L}_{ij}^{\text{old}} = 1$ with $\mathcal{L}_{ij}^{\text{new}} = 0$. At the same time, at any given stage of the RG flow, the resonance frequencies of any pair of effective atoms i and j might have been derived from a set of previous RG steps involving a set of atoms with indices $\{I'\}$ and $\{J'\}$, respectively. If the sets $\{I'\}$ and $\{J'\}$ have some non-zero intersection, then atoms i and j must be omitted from a subsequent frequency renormalization step. Not doing this would violate the principle of RG, that we are integrating or "freezing" out the degrees of freedom with the strongest interactions. Numerically, we efficiently enforce this constraint by replacing $\mathcal{L}_{ik}^{\text{new}} = \mathcal{L}_{jk}^{\text{new}} = \mathcal{L}_{ki}^{\text{new}} = \mathcal{L}_{kj}^{\text{new}} = \mathcal{L}_{ik}^{\text{old}}\mathcal{L}_{jk}^{\text{old}}$, $\forall k$, anytime a pair (i, j) is renormalized. Since $\mathcal{L}$ has (at any step) zero-valued diagonal elements, this directly ensures that $\mathcal{L}_{ij}^{\text{new}} = 0$. After all atoms of the step have been renormalized, we re-evaluate the new set of $\mathcal{K}$ parameters, and repeat the scheme. When all pairs exhibit $\mathcal{K} \leq \mathcal{K}_{\text{cut-off}} = 1$, we stop the RG flow, obtaining an ensemble of N inhomogeneously broadened atoms. Given a fixed value of the density η, we repeat this process for ≈ 100 different spatial configurations, in order to build up the final distribution $P(\omega_{\text{eff}})$.

We extract the optical properties from the renormalized ensemble by applying Eq. 3.4, modified in order to account for the the new $N \times N$ matrix $\mathcal{M}$ emerging from the RG scheme. This reads

$$(-\Delta + \omega_i)\, c_i(\Delta) - \sum_{j=1}^{N} \left[G_{ij} - (1 - \mathcal{L}_{ij})\, G_{ij}^{\text{near}}\right] c_j(\Delta) = \frac{E_{\text{in}}(\mathbf{r}_i, \omega_0)}{E_0}. \tag{B.1}$$

B.2 Choice of the effective positions

In the previous section, we described how the optical response of a pair of atoms separated by a distance $\rho_{ij} \ll 1$ is characterized by two effective

resonance frequencies, corresponding to the real parts of the eigenvalues of the two-atom system. The two collective modes are intrinsically delocalized in space (being formed by atoms with two different positions $\mathbf{r}_{i,j}$). As this delocalization is difficult to incorporate into the RG scheme, we instead attribute each of these two resonance frequencies to a new effective atom, with well-defined position.

In our scheme, the new effective atomic positions are assigned to those of the original pair, $\mathbf{r}_{i,j}$ (randomly between the two possible permutations). A more natural choice, given that the two renormalized atoms are non-interacting, might be to place them at the midpoint $(\mathbf{r}_i + \mathbf{r}_j)/2$ between the two original atoms, but here we discuss the problem with that approach.

Specifically, for a finite-size sample, the atoms closest to the perimeter of the sample will only renormalize with atoms that are closer to the interior. As illustrated in Fig. B.1, this means that step by step, the shape of the cloud tends to shrink. This effectively distorts the ensemble and results in a higher density, and higher interaction strengths in the next step of RG.

B.3 Cross section of an atomic pair

The optical response of an identical atomic pair is characterized by a symmetric and an anti-symmetric normal mode. Here, we will study the scattering cross sections of such modes, in the limit of near-positioned atoms.

First of all, let us write the dimensionless positions (in units of k_0^{-1}) of the two atoms of the pair as

$$\boldsymbol{\rho}_1 = -\boldsymbol{\rho}_2 = \frac{\rho_{12}}{2}\left(\cos\theta\,\widehat{\mathbf{x}} + \sin\theta\cos\phi\,\widehat{\mathbf{y}} + \sin\theta\sin\phi\,\widehat{\mathbf{z}}\right), \tag{B.2}$$

where $\rho_{12} \ll 1$. The scattering cross section can be derived by means of the *so-called* optical theorem [230, 231, 335–338], which reads

$$\sigma_{\mathrm{sc}}^{\mathrm{pair}}(\Delta) = \frac{\sigma_{\mathrm{sc}}}{2}\mathrm{Im}\sum_{j=1}^{2}\frac{E_{\mathrm{in}}^{*}(\boldsymbol{\rho}_j)}{E_0}c_j(\Delta) \tag{B.3}$$

where $\sigma_{\mathrm{sc}} = 3\lambda_0^2/(2\pi)$ is the resonant cross section of a single, isolated, electric dipolar atom, while the dimensionless coefficients $c_j = \Gamma_0\beta_j/\Omega_0$ are defined as in Eq. 3.4, starting from the excited-state coefficients β_j of Eq. 2.17 or, equivalently, from the atomic dipole moments $\mathbf{d}_j = \beta_j\mathbf{d}_0$.

By plugging the solutions of Eq. 3.4 into Eq. B.3, one obtains a total cross section characterized by the two resonances $\omega_\pm$, which are respectively associated to the symmetric and anti-symmetric modes, so that

the resonant scattering cross sections of these two modes can be defined as $\sigma_{\mathsf{sc}}^{\pm} \equiv \sigma_{\mathsf{sc}}^{\mathsf{pair}}(\omega_{\pm})$. In the limit where $\rho_{12} \ll 1$, the two resonances $\omega_{\pm} = \mp \mathsf{Re}\ G_{12} \sim \mp 1/\rho_{12}^3$ are well-separated and can be efficiently resolved, leading to

$$\frac{\sigma_{\mathsf{sc}}^{\pm}}{\sigma_{\mathsf{sc}}} \simeq \frac{(\mathbf{E}_{12}^{*} \cdot \mathbf{v}_{\pm})(\mathbf{E}_{12} \cdot \mathbf{v}_{\pm})}{\Gamma_{\pm}}, \tag{B.4}$$

where we defined $\mathbf{E}_{12} \equiv \{E_{\mathsf{in}}(\boldsymbol{\rho}_1), E_{\mathsf{in}}(\boldsymbol{\rho}_2)\}/E_0$, as well as the eigenstates $\mathbf{v}_{\pm} = \{1, \pm 1\}/\sqrt{2}$ and the decay rates $\Gamma_{\pm} = 1 \pm 2\mathsf{Im}\ G_{12}$.

Assuming that the input field is either a $\widehat{\mathbf{x}}$-polarized, $\widehat{\mathbf{z}}$-directed Gaussian beam with $w_0 \gg \lambda_0$ and focal point at $\mathbf{r} = 0$, or equivalently a $\widehat{\mathbf{x}}$-polarized, $\widehat{\mathbf{z}}$-directed a plane wave, one can evaluate the cross sections in the limit of $\rho_{12} \ll 1$, obtaining

$$\frac{\sigma_{\mathsf{sc}}^{+}}{\sigma_{\mathsf{sc}}} \simeq 1, \qquad \frac{\sigma_{\mathsf{sc}}^{-}(\theta,\phi)}{\sigma_{\mathsf{sc}}} \simeq \frac{f(\theta,\phi)}{g(\theta)}, \tag{B.5}$$

where $f(\theta,\phi) \equiv (\sin\theta \sin\phi)^2$ and $g(\theta) \equiv [2 - \cos^2\theta]/5$.

As expected, the symmetric mode exhibits a perfect electric dipolar behaviour, characterized by the same scattering cross section of one single, isolated atom. On the contrary, the complex multipolar nature of the anti-symmetric mode leads to a more complicated scattering cross section, which depends on the mutual orientation of the initial pair. This suggests considering the average resonant cross section over all possible orientations of a pair, obtaining

$$\left\langle \frac{\sigma_{\mathsf{sc}}^{-}}{\sigma_{\mathsf{sc}}} \right\rangle = \frac{1}{4\pi} \int_0^{\pi} d\theta \int_0^{2\pi} d\phi\ \frac{\sigma_{\mathsf{sc}}^{-}(\theta,\phi)}{\sigma_{\mathsf{sc}}} \sin\theta \simeq 0.94 \sim 1, \tag{B.6}$$

which shows that, on average, the multipolar anti-symmetric mode will scatter light very similarly to a point-like, dipolar atom.

During the RG flow, one can also encounter pairs of effective atoms that have a detuning of $\delta\omega_{12} = (\omega_1 - \omega_2)/2$ with respect to each other. In order for these pairs to strongly interact and be renormalized, the pairwise interaction parameter should satisfy $\mathcal{K}_{12} > 1$, which is roughly equivalent to $|\delta\omega_{12}/G_{12}^{\mathsf{near}}| \ll 1$. In this limit, one can readily extend the previous calculation to the case of two different atoms. In particular, after averaging the resonant cross-section of the (nearly) anti-symmetric, multipolar mode

over all possible orientations, one finds

$$\left\langle \frac{\sigma_{\mathsf{sc}}^{-}(\zeta)}{\sigma_{\mathsf{sc}}} \right\rangle = \frac{5}{2}\left[1-(3\zeta^2+1)\frac{\operatorname{arctanh}\left(\frac{1}{\sqrt{5\zeta^2+2}}\right)}{\sqrt{5\zeta^2+2}}\right], \tag{B.7}$$

where $\zeta \equiv \delta\omega_{12}/(\rho_{12}G_{12}^{\mathsf{near}})$, and which satisfies

$$0.94 \lesssim \left\langle \frac{\sigma_{\mathsf{sc}}^{-}(\zeta)}{\sigma_{\mathsf{sc}}} \right\rangle \leq 1. \tag{B.8}$$

Thus, we see that the multipolar mode of a pair of inequivalent atoms can also be well-approximated in its optical response by a single, electric dipolar atom.

C - Optical properties of a 3D atomic array

In this appendix, we provide some supplementary information on the optical, linear response of a 3D atomic array. We start by addressing the refractive index in the regime $\lambda_0/2 \leq d_z < \lambda_0$ that was not explored in Section 4.2.3. Afterwards, we explicitly report our method to calculate the index from the phase of transmission, as obtained from numerical simulations. Finally, we discuss the regimes where the evanescent interaction between different 2D layers can or cannot be ignored.

C.1 Maximum index when $\lambda_0/2 \leq d_z < \lambda_0$

Here, we calculate the index in the regime of $\lambda_0/2 < d_z < \lambda_0$. In this section, we focus on the lossless regime $\Gamma' = 0$ and we ignore the evanescent field between layers. The band structure of Eq. C.1 reduces to

$$J(k_z) = \omega(0) + \frac{\Gamma(0)}{2} \frac{\sin(k_0 d_z)}{\cos(k_z d_z) - \cos(k_0 d_z)}. \tag{C.1}$$

To obtain this, we recall that we work in the "single-mode" scenario where all diffraction orders but $\mathbf{k}_{xy} = 0$ are evanescent, i.e. when $d < \lambda_0$. In this situation (and as long as the evanescent fields are suppressed), we can associate the wavevector of the Bloch mode to the index of refraction, reading $n(\delta) = k_z(\delta)/k_0$, assuming that $k_{\text{light}} \approx k_0$. This happens because the light at a fixed δ excites one precise Bloch mode, with its wavevector $k_z(\delta)$ describing the phase of propagation per unit length.

In Chapter 4, we explicitly focus on the regime $d_z < \lambda_0/2$, where we can write:

$$n(\delta) = \frac{1}{k_0 d_z} \arccos\left[\cos(k_0 d_z) + \frac{\Gamma(0)\sin(k_0 d_z)}{2\delta - 2\omega(0)}\right], \tag{C.2}$$

by directly inverting Eq. C.1 within the first Brillouin zone. Considering the Bloch mode at the edge of the Brillouin zone, we have then the maximum index $n_{\text{max}} = \lambda_0/(2d_z)$. As one can see, this latter prediction should not be extended to lattice constants above $d_z > \lambda_0/2$, as it would lead to the conclusion that the maximum index is below unity.

The condition $d = \lambda_0/2$ represents the threshold between two regimes, where the light-lines (i.e. $k_z = \pm(\delta + \omega_0)/c \approx \pm k_0$) are either outside

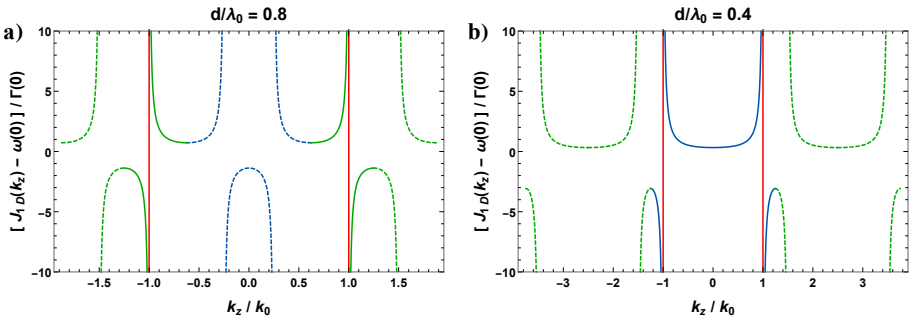

Figure C.1: Band structure for lattice constants above and below the threshold $d = \lambda_0/2$, compared to the light-cone. The light cone is given by the red, solid line, and it appears vertical since we are in the near-resonant regime $|\delta| \ll \omega_0$, i.e. $k_{\text{light}} \approx k_0$. The blue (dashed and solid) curves describe the dispersion relation inside the first Brillouin zone $|k_z| \leq \pi/d_z$, while the green lines are two extended Brillouin zones. The solid lines are those modes effectively excited by the incoming light, corresponding to the Bloch modes nearer to the light-cone.

($d_z > \lambda_0/d_z$) or inside ($d_z < \lambda_0/d_z$) the first Brillouin zone, as represented in Fig. C.1 for the two cases of $d_z = 0.8\lambda_0$ (a) and $d_z = 0.4\lambda_0$ (b). In particular, in the first case, the input light excites the modes belonging to the extended Brillouin zones $\pi/d_z \leq |k_z| \leq 2\pi/d_z$, which are nearer to the light-cone. This is a standard result in the field of photonic crystals, where higher frequencies excite higher bands with wavevectors belonging to extended Brillouin zones [246, 339]. This leads to the index

$$n(\delta) = \frac{1}{k_0 d_z}\left\{-\arccos\left[\cos(k_0 d_z) + \frac{\Gamma(0)\sin(k_0 d_z)}{2\delta - 2\omega(0)}\right] + 2\pi\right\}, \qquad \text{(C.3)}$$

whose maximum value reads $n_{\text{max}} = \lambda_0/d_z$.

In Fig. C.2, we compare these predictions (green lines) with the numerical estimation of the refractive index from the phase of transmission, given a finite-length system (blue points). The agreement is excellent, both spectrally (Fig. C.2-a) or only considering the maximum index (Fig. C.2-b). Here, the numerics are calculated using the method reported in the next section, i.e. Section C.2.

The discontinuity at $d_z = \lambda_0/2$ in the behaviour of $\max n$, is associated to the exceptional point at $d_z = \lambda_0/2$ where the band in Eq. C.1 becomes flat $J_{1D}(k_z) = \omega(0)$. Physically, this represents the condition of perfect Bragg reflection at normal incidence, where perfect destructive interference cancels the forward propagation of light, so that the object becomes fully reflective.

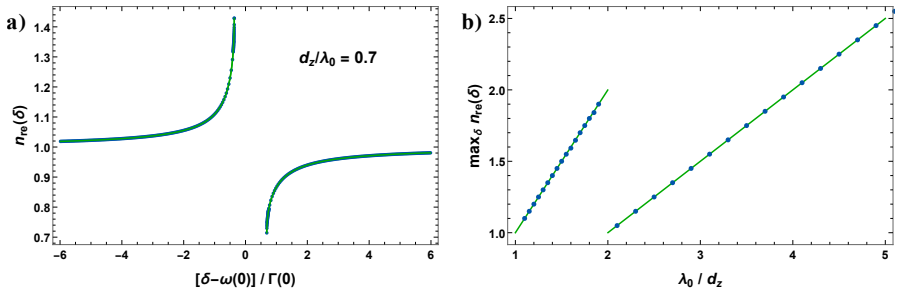

Figure C.2: Refractive index of a 3D lattice. a) Spectrum of the index given $d_z = 0.7\lambda_0$. Here, we fix $d_z = 2.5d$ to suppress the evanescent field, so that Eq. C.1 is valid. b) Maximum index as a function of the lattice constant d_z. In both cases, the green lines represent the predictions of Eq. C.2 (for $d < \lambda_0/2$) and Eq. C.3 (for $d > \lambda_0/2$).

C.2 Numerical simulations of the index

In this section, we define our numerical method to calculate the refractive index of an ordered 3D atomic lattice, composed of a finite number M of transverse 2D arrays. For any detuning δ, we can numerically calculate the transmission $t(\delta)$ and reflection $r(\delta)$ from the coupled-dipole formalism.

C.2.1 Transmission and reflection

In our regime $d_z \leq d < \lambda_0$ of single-mode response, the result is the natural extension of the single-layer case shown in Eq. 4.7. Specifically, the total wavefunction has the form $|\psi_{3D}\rangle = c_G|G\rangle + \sum_j c_E^j|E_j\rangle$, where $c_G \approx 1$ and $|E_j\rangle$ is the collective mode associated with the 2D plane at position z_j. We can use it to compute the field from the output equation of Eq. 4.2. We are interested in the far-field transmission and reflection, so that the observation point is far $|k_0(z - z_j)| \gg 1$ from the position z_j of any layer. Recalling $\mathbf{E}_{in}(z) = E_0 e^{ik_0 z}\hat{\mathbf{x}}$, we get

$$\mathbf{E}(z) = \langle\psi_{3D}|\hat{\mathbf{E}}\,|\psi_{3D}\rangle = \Big[\, E^+(z) + E^-(z) \,\Big]\hat{\mathbf{x}}, \tag{C.4}$$

where the $|\psi_{3D}\rangle$ is calculated at the steady state from Eq. 4.8. Here, we decomposed the field into the forward- and backward-propagating terms

$$\frac{E^+(z)}{E_0} = e^{ik_0 z} + i\frac{\Gamma(0)}{2}\sum_{z_m<z} e^{ik_0(z-z_m)}c_E^m(\delta), \tag{C.5}$$

and

$$\frac{E^{-}(z)}{E_0} = i\frac{\Gamma(0)}{2}\sum_{z_m>z} e^{-ik_0(z-z_m)}c_{\mathrm{E}}^{m}(\delta). \tag{C.6}$$

We can then define the transmission and reflection coefficients as

$$t \equiv \lim_{z\to+\infty}\frac{E^{+}(z)}{E_{\mathsf{in}}(z)}, \qquad r \equiv \lim_{z\to-\infty}\frac{E^{-}(z)}{E_{\mathsf{in}}^{*}(z)}. \tag{C.7}$$

C.2.2 Index from the phase of transmission

Once one knows the transmission, they can in principle attempt to infer the index from the phase accumulated in the medium. This was the spirit of the numerical calculations performed in Chapter 3. Formally, the transmission and the index are related by the macroscopic Fresnel equation. As discussed in Section 3.2.2.1, this accounts for the effects of multiple bouncing inside the medium by reflection at the interfaces with free space. For a system of length L, we recall that this reads

$$t_{\mathsf{Fr}} = \left[\frac{4n}{(1+n)^2-(n-1)^2t_{\mathsf{ph}}^2}\right]t_{\mathsf{ph}}, \tag{C.8}$$

where $t_{\mathrm{ph}} = \exp\left(i\left(n-1\right)k_0L\right)$. In Chapter 3, we approximated the total transmission with only $\sim t_{\mathsf{ph}}$ to speed up the calculations. As we checked in Section 3.2.2.1, we were allowed to do so by the high, on-resonance absorption $n_{\mathrm{im}} \gg 0$, which suppressed multiple bouncing of light between the two interfaces of the atomic medium with free space.

In the case of an ordered lattice of (ideal, lossless) atoms, we predict from the dispersion relation a purely real index, so we do not expect this approximation to be valid. Nonetheless, if one studies the phase $\arg t_{\mathrm{Fr}}$ as a function of the total length $L = Md_{\mathrm{z}}$, then can notice that the pre-factor inside the square brackets of Eq. C.8 only contributes with small oscillations around the behaviour of $\arg t_{\mathrm{ph}}$. This is exemplified in Fig. C.3, where we use the dispersion relation of Eq. C.2 to predict the index n_{theo} (given $d = d_{\mathrm{z}} = \lambda_0/60$ and $\delta \simeq 1.5\omega(0)$), as a function of the number of layers M. Then we plug this value into Eq. C.8 to define t_{Fr} (blue line) as well as its simplified version t_{ph} (orange line). The phase analysis of Fig. C.3-a clearly show how $\arg t_{\mathrm{ph}}$ largely characterizes the behaviour of $\arg t_{\mathrm{Fr}}$. Finally, we use the coupled-dipole equations to numerically compute the transmission (as discussed in Section C.2.1), finding a perfect agreement with the Fresnel equations where $n = n_{\mathrm{theo}}$ is defined from the band dispersion.

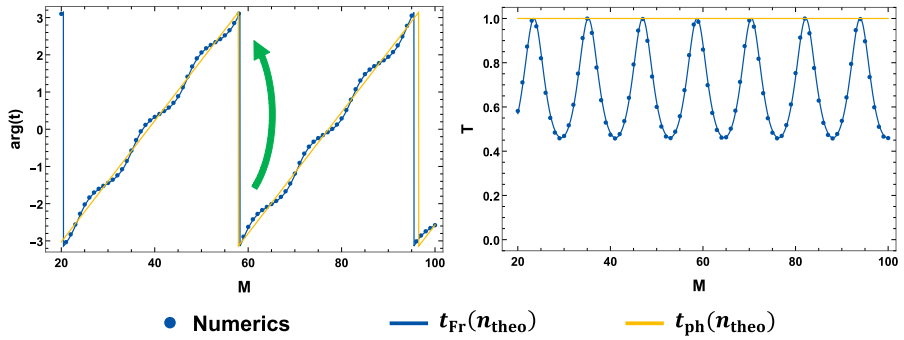

Figure C.3: Comparison between the Fresnel prediction t_{Fr} and the full numerics, given $d_z = d = \lambda_0/60$ and $\delta \simeq 1.5\omega(0)$. The detuning is chosen to be in a regime where the band is invertible. First, we compute the transmission by numerically solving the coupled-dipole equations, for an increasing number of transverse layers M, as described in Section C.2.1. We plot with blue points the resulting phase $\arg t$ (a) and absolute value $T = |t|^2$. We want to compare this transmission with that predicted by the Fresnel theory, i.e. t_{Fr}. We thus use the dispersion relation Eq. C.2 to predict the index n_{theo} and we plug this latter into Eq. C.8, obtaining the blue curves. Finally, with orange lines we represent the value of the simplified model t_{ph}, where the transmission only corresponds to a phase.

These observations motivate the definition of the following algorithm, to extract the index from the numerical simulations of the transmission. We anticipate that we extensively checked our theoretical predictions by comparing it with the results of this algorithm, used as a black box (as in Fig. C.2).

- For each value of the detuning δ, we numerically calculate the transmission for many, increasing values of M, from the coupled-dipole equations. For each value of M, we evaluate the phase $\phi = \arg t$.
- For each pair of consecutive points (e.g. $\tilde{M}$ and $\tilde{M}+1$), we compute the phase difference $\Delta\phi_{\tilde{M}} = \phi_{\tilde{M}+1} - \phi_{\tilde{M}}$.
- If $|\Delta\phi_{\tilde{M}}| > \pi$, we vertically shift all the following points $M \geq \tilde{M}+1$ by a factor $\pm 2\pi$, choosing the sign that minimizes $|\Delta\phi_{\tilde{M}} \pm 2\pi|$. This happens because the phase function $\arg t$ is only defined modulo 2π, which we must correct (green arrow in Fig. C.3-a).
- We fit the final line with $\phi = aM + b$, and then define the real index as $n_{\mathrm{re}} = a/(k_0 d_z) + 1$.

The necessity of imposing the condition $|\Delta\phi_{\tilde{M}}| > \pi$, to identify the jumps, arises because these jumps are typically slightly different than exactly

2π, since we can only discretely increase M and due to the small fluctuations of the pre-factor in the square brackets of Eq. C.8. Moreover, since we expect that $n_{\mathrm{re}} \leq \lambda_0/(2d_z)$, we obtain that the vertical space between consecutive, numerical points should remain bounded by $|\phi_{M+1} - \phi_M| \lesssim \pi$, meaning that we should easily identify the discontinuous jumps anytime we witness $|\phi_{M+1} - \phi_M| > \pi$. Numerically, we found that the threshold $|\Delta\phi_{\tilde{M}}| > \pi$ gives consistent and robust results.

C.3 Invertibility of the optical band structure

In this section, we discuss the effect of the evanescent interaction between atomic layers, which can make the optical band structure non-invertible. We start from the band structure of the 3D system $J(k_z)$, as described in Eq. C.1 and Eq. 4.10. We are interested in the limit $d_z \ll \lambda_0$ and $d_z \geq d$. By Taylor expanding in the ratio $|\cos(k_z d_z)/\cosh(|\mathbf{g}_{mn}| d_z)| \ll 1$, one can simplify the evanescent contribution to the band into $J_{\mathrm{ev}}(k_z) \simeq (\lambda_0/d_z)[-A(d_z/d) + B(d_z/d)\cos(k_z d_z)]$, where we define the coefficients

$$A(\mu) = \sum_{\substack{m\in\mathbb{Z}\\ n\in\mathbb{Z}\\ (m,n)\neq(0,0)}} \frac{m^2\mu}{\sqrt{m^2+n^2}}\left[1 - \tanh\left(2\pi\mu\sqrt{m^2+n^2}\right)\right],$$
$$B(\mu) = \sum_{\substack{m\in\mathbb{Z}\\ n\in\mathbb{Z}\\ (m,n)\neq(0,0)}} \frac{m^2\mu}{\sqrt{m^2+n^2}}\left[\frac{\tanh\left(2\pi\mu\sqrt{m^2+n^2}\right)}{\cosh\left(2\pi\mu\sqrt{m^2+n^2}\right)}\right]. \tag{C.9}$$

which only depend on the aspect-ratio of the lattice $\mu = d_z/d$. This allows to easily calculate the properties of the band in an analytic fashion. In particular, hereafter we focus on the quantum optics regime, i.e. when no quantum chemistry is present. The presence of a local maximum around $|k_z| \lesssim \pi/d_z$ is responsible for the non-invertible behavior of the band. In the limit $k_0 d_z \ll 1$, the condition for this local maximum to exist becomes

$$\frac{d}{\lambda_0} < \frac{d}{d_z}\sqrt{\frac{2B(d_z/d)}{\pi}} \simeq 2\sqrt{\frac{2d}{\pi d_z}}e^{-\pi d_z/d}, \tag{C.10}$$

which defines the regime where the band is non-invertible. This threshold is represented by the white, dashed line of Fig. C.4-a, where we illustrate the condition as a function of λ_0/d and d_z/d. In the same figure, we perform

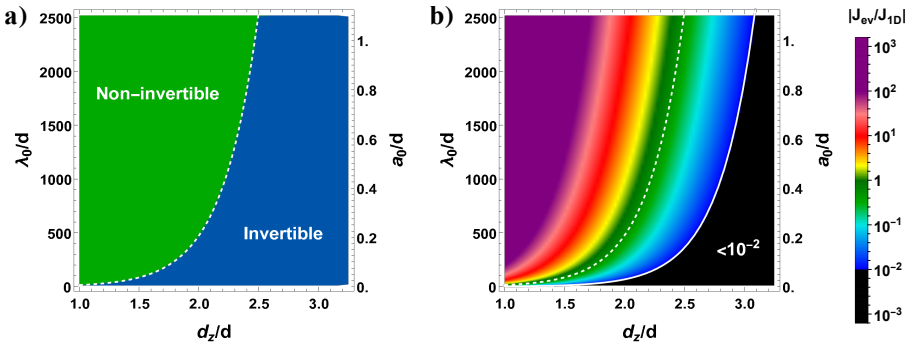

Figure C.4: Contribution of the evanescent fields to the band dispersion of a 3D lattice. a) Regimes where the band is either invertible (blue region) or not (green region), as a function of the aspect ratio d_z/d and the longitudinal lattice constant d_z/λ_0. The data are calculated by fully numerically computing the band and explicitly looking for local maxima at some $|k_z| < \pi/d_z$. The white, dashed line represents the analytic bound of Eq. C.10. b) Ratio between the evanescent and radiative contributions to the band structure, i.e. $|J_{ev}/J_{1D}|$, calculated at $k_z = \pi/d_z$. When $d_z \ll \lambda_0$, one can prove that this corresponds to the maximum value $\max_{k_z}|J_{ev}/J_{1D}|$. The dashed, white line is the same invertibility boundary as before, which is equivalent to $|J_{ev}/J_{1D}| \lesssim 1/2$. The solid, white line shows the analytic prediction for the threshold where $|J_{ev}/J_{1D}| \leq 10^{-2}$. In both plots the value of J_{ev} is computed numerically from its exact formula of Eq. 4.10.

an exact numerical calculation of the band structure, and indicate with blue and green the regions of parameter space where the band structure is invertible and non-invertible, respectively.

The condition above describes when $J_{ev}(k_z)$ is so strong to radically alter the band, making it non-invertible. In turns, this means that even in the regime where the band is invertible, the contribution could still be non-negligible, albeit small. To quantify this, we calculate the ratio between the evanescent $J_{ev}(k_z)$ and the radiative $J_{1D}(k_z) = \sin(k_0 d_z)/[\cos(k_z d_z) - \cos(k_0 d_z)]$ contributions. This quantity in principle depends on the wavevector k_z, so we consider the maximum value $\max_{k_z}|J_{ev}/J_{1D}|$. When $d_z \ll \lambda_0$, this ratio is maximized by $k_z = \pi/d_z$ so that we obtain $\max|J_{ev}/J_{1D}| \simeq (\lambda_0/d_z)^2 B(d_z/d)/\pi$. Comparing this with Eq. C.10, one can deduce that the band becomes non-invertible if $|J_{ev}/J_{1D}| \gtrsim 1/2$. In Fig. C.4-b, we represent the value of this maximum ratio as a function of the aspect ratio d_z/d and lattice constant d. The black region represents the regime where $|J_{ev}/J_{1D}| \geq 10^{-2}$, which allows us to ignore the evanescent contribution. For our choice of the aspect ratio $d_z/d = 2.5$, this is true as long as $d/a_0 \gtrsim 6$.

To conclude, we mention that in Appendix E.1 we extend the analysis

of the evanescent interaction to the case of a rectangular array with lattice constants $d_{\mathrm{x,y,z}}$ that are different in all the three spatial directions. This discussion finds application in the context of the "atomic metalens" that we propose in Chapter 5.

D - Dissipation processes in 2D arrays

In this appendix, we group some further analysis of dissipation processes in a 2D (square and subwavelength), atomic array spanning the $\widehat{\mathbf{x}}$ and $\widehat{\mathbf{y}}$ directions. With the term "dissipation", we also denote the excitations of non-radiative modes inside the 2D array. These, indeed, can be seen as emergent losses to the single-mode response expected for an ideal array, where all the energy is either reflected or transmitted in the $\widehat{\mathbf{z}}$ direction. We thus start by further analyzing the optical scenario of an atom selectively driven, which can excite such modes. Then, we discuss more in detail the dynamics under the 2D tJz model, that we use in Section 4.4 to model the onset of chemistry. We show that the associated physical phenomena provide indeed a natural source of selective atomic excitation. Finally, we discuss the possible presence of supplementary, unidentified environmental factors (namely, inelastic losses and inhomogeneous broadening of the atomic resonances), arguing that they can be modeled with a non-radiative decay rate Γ'.

D.1 Distinguishable atom in a 2D array

In this appendix, we detail how to numerically calculate the susceptibility $\chi(\mathbf{r}_j-\mathbf{r}_h,\delta)=c_j(\delta)/\Omega_h$ from the steady-state solutions $c_j(\delta)$ of an infinite 2D array of lattice constant d, where one atom at position $\mathbf{r}_h$ is selectively driven by a near-resonant Rabi frequency Ω_h, detuned by a factor $\delta=\omega_L-\omega_0$. We recall that the atomic wave function is given by $|\psi_{\mathrm{2D}}(t)\rangle = c_{\mathrm{G}}(t)|G\rangle+\sum_j c_j\hat{b}^\dagger_{pj}\hat{b}_{sj}|G\rangle$, and the other atoms $\mathbf{r}_j\neq\mathbf{r}_h$ can still be excited via dipole-dipole interactions with the driven atom, via Eq. 4.1.

We numerically simulate a finite 2D square array of lateral size $2l$ and lattice constant d. For simplicity, the selectively driven atom is placed at the center $\mathbf{r}_h=0$. To mimic the infinite size of the array, we introduce a smooth cut-off of non-radiative decay $\Gamma'_{\text{cut-off}}(R=\sqrt{x^2+y^2})$, which decreases the response of the system around the boundaries. This allows as well to avoid finite-size, hardcore interfaces. Specifically, we define

$$\Gamma'_{\text{cut-off}}(R)=\begin{cases}0 & \text{if } R\leq R_{\text{cut-off}}\\ 3\Gamma(0)\left(\dfrac{R-R_{\text{cut-off}}}{R_{\text{cut-off}}/2}\right)^2 & \text{if } R>R_{\text{cut-off}}\end{cases}. \tag{D.1}$$

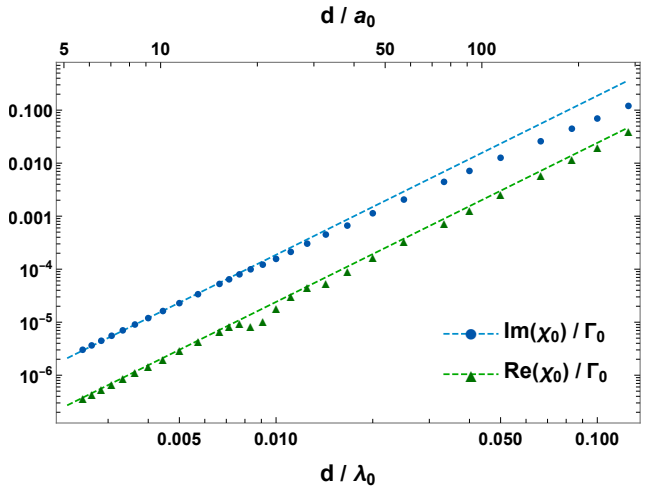

Figure D.1: Plot of the resonant susceptibility of the selectively driven atom $\chi_0 = \chi(0, \delta = \omega(0))$ vs d. The blue points (green triangles) represent, in log-log scale, the value of its imaginary (real) part, while the dashed blue and green lines show the asymptotic scalings Im $\chi_0/\Gamma_0 \sim 187(d/\lambda_0)^3$ and Re $\chi_0/\Gamma_0 \sim 24(d/\lambda_0)^3$.

On top of that, we fix $R \leq l = (3/2)R_{\text{cut-off}}$. This way, the cut-off is zero at $R = R_{\text{cut-off}}$, and up to $\Gamma'_{\text{cut-off}}(l) = 3\Gamma(0)$ at the boundaries $R = l$. We opt for a quadratic power-law scaling to ensure that also the impedance mismatch can both vary smoothly, and also exhibit small values in the relevant region around $R_{\text{cut-off}}$.

Due to the finite size of the system, we are effectively computing the optical response by discretely sampling Bloch wavevectors, rather than accounting for the full continuum. The smallest wavevector that we are implicitly considering can be roughly estimated by $|\mathbf{k}_{\text{xy}}^{\text{min}}| \approx \pi/R_{\text{cut-off}}$. We thus impose in our numerics that $R_{\text{cut-off}} \geq \lambda_0/2$, aiming to well capture at least those modes outside the light cone $|\mathbf{k}_{\text{xy}}| = k_0$. For lattice constants as small as $d \simeq \lambda_0/400$, this condition implies atomic numbers as large as $N \approx 4 \times 10^5$, which represents the maximal size that we can simulate. For larger lattice constants $d \gtrsim \lambda_0/150$, however, our numerics can tolerate larger systems, and in that case we impose $N \geq 4 \times 10^4$, to reduce the extent of our numerical approximations.

Our results are exemplified in Fig. D.1, where we numerically calculate the resonant susceptibility of the selectively driven atom $\chi_0 = \chi(0, \delta = \omega(0))$. Specifically, the blue points and the green triangles show the imaginary and real part of χ_0, along with their asymptotic values Im $\chi_0/\Gamma_0 \sim 187(d/\lambda_0)^3$ (dashed blue line) and Re $\chi_0/\Gamma_0 \sim 24(d/\lambda_0)^3$ (dashed blue

line), which confirm the scaling $\chi_0 \sim \Gamma_0 (d/\lambda_0)^3$.

D.2 Dynamics under the 2D, tJz model

In this section, we provide more insights into one of the two fundamental processes which limit the refractive index of a 3D atomic array, as discussed in Section 4.4.1. Specifically, we study the dissipation mechanisms (within each 2D layer), due to the evolution of a photo-excited electron under the tJz Hamiltonian, which models the onset of chemistry. This is characterized by two limits, where the hopping rate of the electron is either much smaller (Appendix D.2.1) or much larger (Appendix D.2.2) than the optical dynamics.

D.2.1 Adiabatic elimination

Here, we explicitly show a procedure (alternative to that of the main text) to calculate the corrections to the optical response of a 2D atomic array due to the photo-excitation dynamics described of Section 4.4.2.1. Specifically, we are interested in the single-hop case where $\hat{\mathcal{H}}_t |E\rangle$ results in the state $|1\rangle$, and in its subsequent evolution under $\hat{\mathcal{H}}_0 + \hat{\mathcal{H}}_{\mathrm{dip-dip}}$, as defined in Eq. 4.1 of the main text. Here, we ignore the further, multi-hop dynamics due to $\hat{\mathcal{H}}_t$, which would give rise to the state $\hat{\mathcal{H}}_t |1\rangle \propto |2\rangle$ and so on. The opposite case, where $\hat{\mathcal{H}}_t$ dominates over $\hat{\mathcal{H}}_{\mathrm{dip-dip}}$, is described in the next appendix. Furthermore, we recall that we also neglect the contribution of $\hat{\mathcal{H}}_{\mathrm{drive}}$ to the evolution of $|1\rangle$, as it would describe nonlinear, multi-photon processes, that go beyond the analysis of the refractive index.

For simplicity, here we adopt the formalism of Section 4.2.1, where we separate the orbital and spin degrees of freedom. In this language, the collective excited state reads $|E\rangle = \left(\sum_j^N |\mathbf{r}_j\rangle / \sqrt{N}\right) \otimes |\sigma\rangle$, where $|\mathbf{r}_j\rangle$ means that the atom at position j is excited, while $|\sigma\rangle$ is the antiferromagnetic, ground state of the spins. One has that $\hat{\mathcal{H}}_t(|\mathbf{r}_j\rangle \otimes |\sigma\rangle) = -t_{\mathrm{eff}} \sum_{\langle i \rangle_j}^4 |\mathbf{r}_i\rangle \otimes |\sigma_{ij}\rangle$, where $\langle i \rangle_j$ represent the sum over the four neighbour sites of j, while $|\sigma_{ij}\rangle$ is the spin ground state with the spins at sites i and j exchanged. We can explicitly write $\hat{\mathcal{H}}_t |E\rangle = -2t_{\mathrm{eff}} |1\rangle = -2t_{\mathrm{eff}} \sum_j^N \sum_{\langle i \rangle_j}^4 |\mathbf{r}_i\rangle \otimes |\sigma_{ij}\rangle / \sqrt{4N}$. The total state involved in the photonic dynamics of $|E\rangle$, its hopping into $|1\rangle$ and its evolution due to $\hat{\mathcal{H}}_{\mathrm{dip-dip}}$ reads

$$|\psi_{\mathrm{2D}}\rangle = |G\rangle + c'_{\mathrm{E}} |E\rangle + \sum_{k=1}^{N} \sum_{j=1}^{N} \sum_{\langle i \rangle_j}^{4} c_{k(ij)} |\mathbf{r}_k\rangle \otimes |\sigma_{ij}\rangle \,, \tag{D.2}$$

where each (ij) in $c_{k(ij)}$ identifies a different, distinguishable, spin background, while the label k represent the site of the excited atom. In this state, we approximated the ground-state coefficient as ≈ 1, since we are in the low excitation limit. The relevant, non-null matrix elements of the Hamiltonian are given by

$$
\begin{aligned}
&1. \qquad \langle E|\hat{\mathcal{H}}_{\text{drive}}\,|G\rangle = -\Omega_0,\\
&2. \qquad \langle E|\hat{\mathcal{H}}_0 + \hat{\mathcal{H}}_{\text{dip-dip}}\,|E\rangle = -\delta + \omega(0) - \frac{i}{2}\Gamma(0),\\
&3. \qquad \Big(\langle \mathbf{r}_k|\otimes\langle\sigma_{ij}|\Big)\hat{\mathcal{H}}_{\text{t}}\,|E\rangle = -\delta_{ki}\frac{2t_{\text{eff}}}{\sqrt{4N}},\\
&4. \qquad \Big(\langle \mathbf{r}_k|\otimes\langle\sigma_{ij}|\Big)\hat{\mathcal{H}}_0 + \hat{\mathcal{H}}_{\text{dip-dip}}\Big(\,|\mathbf{r}_a\rangle\otimes|\sigma_{bc}\rangle\,\Big)\\
&\qquad\quad = \delta_{ib}\delta_{jc}\left[(\delta_{ak}-1)\,G_{ak} - \delta_{ak}\left(\delta + \frac{i}{2}\Gamma_0\right)\right].
\end{aligned}
\tag{D.3}
$$

In sight of this, the steady-state coefficients are described by

$$
\left[-\delta + \omega(0) - \frac{i}{2}\Gamma(0)\right] c'_{\text{E}} - \frac{2t_{\text{eff}}}{\sqrt{4N}}\sum_{j=1}^{N}\sum_{\langle i\rangle_j}^{4} c_{i(ij)} = \Omega_0, \tag{D.4}
$$

together with the set of equations

$$
\left[-\delta - \frac{i}{2}\Gamma_0\right] c_{k(ij)} - \sum_{n\neq k} G_{kn}c_{n(ij)} = \delta_{ki}\frac{2t_{\text{eff}}}{\sqrt{4N}}c'_{\text{E}}. \tag{D.5}
$$

Specifically, Eq. D.5 explicitly shows that each spin background (ij) independently undergoes its own dynamics due to $\hat{\mathcal{H}}_0+\hat{\mathcal{H}}_{\text{dip-dip}}$. The formula in Eq. D.5 is equivalent to the application of Eq. 2.17 to an atomic array where the single site $k=i$ is selectively driven by $\Omega_i = 2t_{\text{eff}}c'_{\text{E}}/\sqrt{4N}$, whose solution was discussed in Section 4.3.1, reading $c_{i(ij)} = \chi(0,\delta)2t_{\text{eff}}c'_{\text{E}}/\sqrt{4N}$. These values can be plug into Eq. D.4 to recover

$$
\left[-\delta + \omega(0) - \frac{i}{2}\Gamma(0) + \Sigma_{\text{t}}(\delta)\right] c'_{\text{E}} = \Omega_0, \tag{D.6}
$$

defining the complex self-energy $\Sigma_t(\delta) = -4t_{\text{eff}}^2\chi(0,\delta)$.

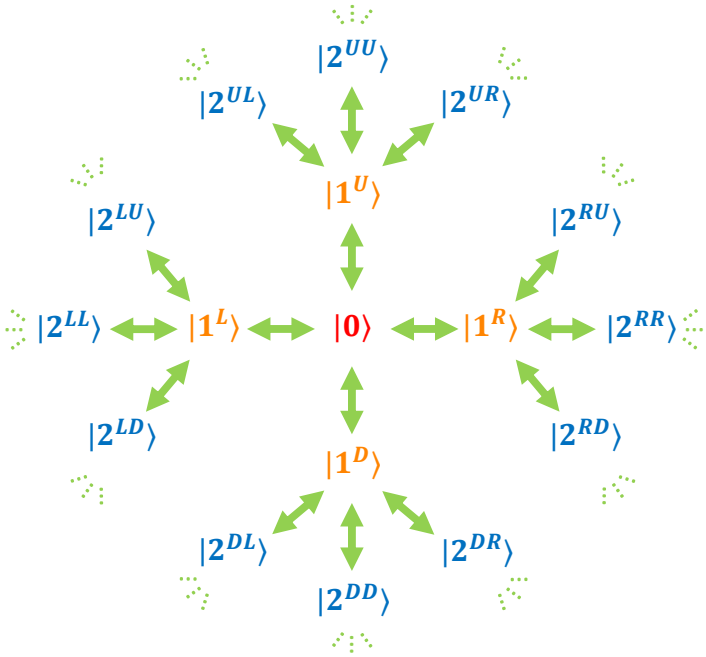

Figure D.2: Behavior of the hopping dynamics due to $\hat{\mathcal{H}}_{\mathrm{t}}$, depicted as a Bethe lattice. Evolution of the initial excited p-orbital $|0\rangle$, to states $|n^{ab\cdots}\rangle$. Here, the non-negative integer n denotes the number of hops, while $a, b, \ldots \in \{U, D, L, R\}$ denotes the direction (up, down, left, right) of each hop.

D.2.2 Hopping on a Bethe lattice

In this section, we derive the contribution to the self-energy $\Sigma_{\mathrm{t}}(\delta) \approx -4it_{\mathrm{eff}}$ of the excited state $|E\rangle$, which arises from the dynamics of the p-orbital hopping $\hat{\mathcal{H}}_{\mathrm{t}}$. As can be seen from Eq. 4.28 and Eq. 4.29 in the main text, the states involved in up to $n = 2$ hops are orthogonal due to their different spin backgrounds, and can be labeled according to the original position (when $n = 0$) $\mathbf{r}_j$ of the p-orbital, the four possible moves $\boldsymbol{\delta}_1 = \pm d\hat{\mathbf{x}}, \pm d\hat{\mathbf{y}}$ to a nearest neighbor at $n = 1$, and the three possible moves (besides returning to $\mathbf{r}_j$) $\boldsymbol{\delta}_2 \neq \boldsymbol{\delta}_1$ at $n = 2$. As the dynamics under $\hat{\mathcal{H}}_{\mathrm{t}}$ is the same for each $\mathbf{r}_j$ up to translation, in what follows we will forget about this label and simply denote the initial position as $|0\rangle$. For a better visualization, we will also switch to the labels U, D, L, R (up, down, left, right) for the possible values of $\boldsymbol{\delta}_i$. In Fig. D.2 we thus show how $\hat{\mathcal{H}}_{\mathrm{t}}$ has matrix elements (green arrows) between the initial state $|0\rangle$ and the superposition state $|1\rangle = \left(|1^U\rangle + |1^D\rangle + |1^L\rangle + |1^R\rangle\right)/2$ following $n = 1$ hops, and how $|1\rangle$ is connected in turn by $\hat{\mathcal{H}}_{\mathrm{t}}$ to the various configurations $|2^{ab}\rangle$ (with

$a, b \in \{U, D, L, R\}$) comprising the state $|2\rangle$. The corresponding matrix elements are $\langle 1|\hat{\mathcal{H}}_{\rm t}|0\rangle = -2t_{\rm eff}$ and $\langle 2|\hat{\mathcal{H}}_{\rm t}|1\rangle = -\sqrt{3}t_{\rm eff}$.

While this description up to $n = 2$ is exact, a standard approximation for larger n is to assume that the nature of the hopping from $|1\rangle$ to $|2\rangle$ generalizes to any $|n\rangle$ to $|n+1\rangle$ [243, 244]. In particular, one assumes that $\hat{\mathcal{H}}_{\rm t}$ connects a particular configuration $|n^{ab\cdots}\rangle$ to three possible new configurations $|(n+1)^{ab\cdots}\rangle$, and furthermore that all possible generated states have orthogonal spin backgrounds, i.e. the configurations satisfy the orthogonality condition $\langle m^{ab\cdots}|n^{a'b'\cdots}\rangle = \delta_{m,n}\delta_{a,a'}\delta_{b,b'}\delta_{\cdots}$. This makes the problem equivalent to hopping on a so-called Bethe lattice [245].

Within this approximation, the Hamiltonian $\hat{\mathcal{H}}_{\rm t}$ takes the form

$$\hat{\mathcal{H}}_{\rm t} \approx \hat{\mathcal{H}}_{\rm Bethe} \equiv -2t_{\rm eff}\,|1\rangle\langle 0| - \sqrt{3}t_{\rm eff}\sum_{n>0}|n+1\rangle\langle n| + h.c., \tag{D.7}$$

where we define the normalized states $|n\rangle = \sum_{ab\cdots}|n^{ab\cdots}\rangle/(2\sqrt{3^{n-1}})$, which are an equal superposition of all possible configurations at a given n. The eigenenergies and eigenstates of $\hat{\mathcal{H}}_{\rm Bethe}$ can be written in the form

$$\begin{aligned} \mathcal{E}(\theta) &= -2\sqrt{3}t_{\rm eff}\cos(\theta), \\ |\psi(\theta)\rangle &= \sqrt{\frac{2}{\pi}}\left[\frac{\sqrt{3}}{2}\sin(\gamma)\,|0\rangle + \sum_{n=1}^{\infty}\sin(n\theta+\gamma)\,|n\rangle\right], \end{aligned} \tag{D.8}$$

where $\tan(\gamma) = 2\tan(\theta)$. The density of states can be also calculated, obtaining the value [243, 245]

$$\rho(\mathcal{E}) = \frac{2}{\pi t_{\rm eff}}\frac{\sqrt{24-(\mathcal{E}/t_{\rm eff})^2}}{16-(\mathcal{E}/t_{\rm eff})^2} = -\frac{3}{2\pi}\sin^2(\gamma)\frac{d\theta}{d\mathcal{E}}. \tag{D.9}$$

Starting from the quasi-bound state $|0\rangle$ initially, the decay rate $\Gamma_{\rm Bethe}$ out of this state into the continuum of the band can be estimated by Fermi's golden rule as

$$\begin{aligned} \frac{\Gamma_{\rm Bethe}}{t_{\rm eff}} &= \frac{2\pi}{t_{\rm eff}}\int_{-2\sqrt{3}t_{\rm eff}}^{2\sqrt{3}t_{\rm eff}} d\mathcal{E}\;\rho(\mathcal{E})\left|\langle\psi(\mathcal{E})|\hat{\mathcal{H}}_{\rm Bethe}\,|0\rangle\right|^2 \\ &= \frac{24}{\pi}\int_0^{\pi} d\theta\;\sin^2(\gamma)\sin^2(\theta+\gamma) = \frac{864}{\pi}\int_0^1 du\;\frac{\sqrt{u^3(1-u)}}{(1+3u)^2} = 8. \end{aligned} \tag{D.10}$$

This allows us to define the contribution to the self-energy of the state $|E\rangle$

as $\Sigma_{\mathrm{t}}(\delta) \approx -4it_{\mathrm{eff}}$.

D.3 Non-radiative noise in a 2D array

Here, we discuss our model of inelastic noise in a 2D atomic array as a supplementary, non-radiative decay rate. In the expression of the atomic polarizability $\alpha_0 = -3\pi\epsilon_0/\{[\Delta + i(1+\Gamma')/2]k_0^3\}$, we define a generic non-radiative decay rate Γ' (in units of the natural atomic linewidth Γ_0), which accounts for the energy that is lost in non-radiative processes. This includes both inelastic scattering of light (such as losses into phononic side-bands), as well as inhomogeneous broadening of the atomic resonance frequencies. In particular, we consider $\Gamma' = \Gamma_{\mathrm{inel}} + \Gamma_{\mathrm{inhom}}$.

While the interpretation of inelastic scattering is straightforward, it is not obvious *a priori* that the inhomogeneous broadening can have very similar effects to non-radiative decay. In a 1D atomic array, for instance, this would not generally be true, as the randomness in the atomic frequencies can lead to peculiar effects such as Anderson localization [340, 341]. On the contrary, it is experimentally known that the inhomogeneous broadening of both 3D atomic ensembles (such as Doppler broadening [165–168]) or two-level emitters in solid-state systems (including color centers in diamond [249, 251, 252, 342]) usually acts by inelastically broadening the overall linewidth (without contributing to the resonant scattering), behaving as a supplementary, non-radiative term.

Mathematically, one can model the inhomogeneous broadening of such an open ensemble by assuming that each atom of the lattice has a shifted resonance $\tilde{\omega}_i$, distributed according to a well-defined probability distribution $P_{\mathrm{inhom}}(\tilde{\omega})$. Here, for simplicity, we focus on a Lorentzian distribution of width $\sigma_{\mathrm{Lorentz}}$ (in units of Γ_0), i.e. $P_{\mathrm{inhom}}(\tilde{\omega}) = \sigma_{\mathrm{Lorentz}}/\left[\pi(\sigma_{\mathrm{Lorentz}}^2 + \tilde{\omega}^2)\right]$. The coupled-dipole equations, then, are modified by substituting $\alpha_0 \to \alpha(\tilde{\omega}_i)$, in Eq. 2.17, so that each atom is characterized by a different polarizability $\alpha(\tilde{\omega}_i) = -3\pi\epsilon_0/\{[\Delta - \tilde{\omega}_i + i\,(1+\Gamma_{\mathrm{inel}})/2]\,k_0^3\}$. In our model, we assume that we can average the atomic response over disorder first, before solving the multiple-scattering problem. We obtain an average atomic polarizability, which reads

$$\begin{aligned}\alpha_0 = \langle\alpha(\tilde{\omega})\rangle &= -\frac{3\pi\epsilon_0}{k_0^3}\int \frac{P_{\mathrm{inhom}}(\tilde{\omega})}{\Delta - \tilde{\omega} + i(1+\Gamma_{\mathrm{inel}})/2}\,d\tilde{\omega} \\ &= -\frac{3\pi\epsilon_0}{k_0^3}\frac{1}{\Delta + i(1+\Gamma_{\mathrm{inel}}+2\sigma_{\mathrm{Lorentz}})/2},\end{aligned} \tag{D.11}$$

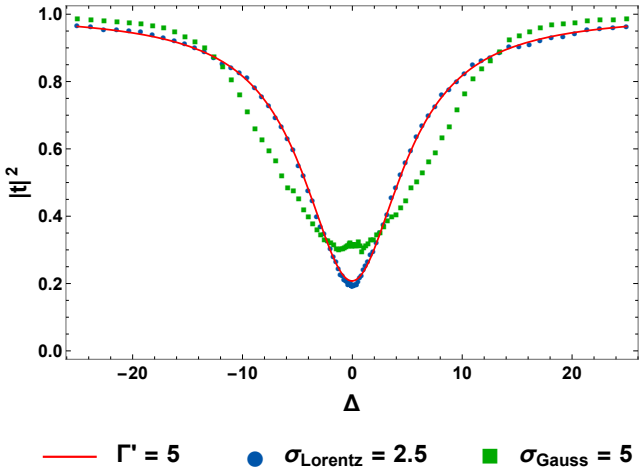

Figure D.3: Effects of inhomogeneous broadening on a 2D atomic array, given $\Gamma_{\text{inel}} = 0$. Transmission spectrum of a finite 2D square lattice with transverse dimensions $\Delta x = \Delta y = 6.4\lambda_0$ and lattice constants $\xi_x = \xi_y = 0.2$, illuminated by a Gaussian beam of waist $w_0 = \Delta x/4$. The detuning Δ is expressed in units of Γ_0. The blue points (green squares) are calculated by solving the inhomogeneous version of the coupled-dipole equations Eq. 2.17 with $\alpha_0 \to \alpha(\tilde{\omega}_i)$, and considering atomic resonance frequencies $\tilde{\omega}_i$ randomly sampled from a Lorentzian (Gaussian) distribution of width $\sigma_{\text{Lorentz}} = 2.5$ (standard deviation $\sigma_{\text{Gauss}} = 5$). The red line shows the predictions of Eq. 2.17, when removing the inhomogeneous broadening $\omega_i = \omega_0$ but adding a non-radiative decay rate $\Gamma' = \Gamma_{\text{inhom}} = 5$. The data are averaged over ~ 100 configurations.

so that one can define $\Gamma_{\text{inhom}} = 2\sigma_{\text{Lorentz}}$.

The validity of this assumption, in the regime under analysis, is reasonable, but not obvious. In Fig. D.3, we check its soundness by evaluating the spectrum of transmission $t(\Delta)$ of a 2D square lattice of transverse dimensions $\Delta x = \Delta y = 6.4\lambda_0$ and lattice constant $\xi_x = \xi_y = 0.2$, illuminated by a Gaussian beam of waist $w_0 = \Delta x/4$ (here, $t(\Delta)$ is calculated by projecting the output field of Eq. 2.17 onto the same mode as the input beam, as in Eq. E.8 of Appendix E.3). Assuming $\Gamma_{\text{inel}} = 0$, we compare the results of Eq. 2.17 when $\Gamma' = \Gamma_{\text{inhom}} = 5$ (red line), with those obtained by considering a Lorentzian distribution of width $\sigma_{\text{Lorentz}} = 2.5$ (blue points), observing a great agreement. As a reference, with green points we also show the case when the resonances $\tilde{\omega}_i$ are sampled from a Gaussian distribution of standard deviation $\sigma_{\text{Gauss}} = 5$.

E - Analysis of the atomic metalens

In this appendix, we provide further insights into our definition and numerical validation of an atomic metalens. We start by properly discussing the validity of neglecting the evanescent coupling between the 2D arrays. Then, we detail our definition of buffer zones, where atoms are placed in an intermediate position at the interface between two consecutive rings. To continue, we report our method to extract the efficiency of the atomic metalens from the numerics. Finally, we mention some computational challenges in the numerical validation of our scheme, via large-scale simulations.

E.1 Neglecting the evanescent interaction

Here, we discuss the validity of the approximation $\mathcal{G}^{\text{ev}}_{nm} \sim 0$, $\forall n, m$, when applying our protocol to define an atomic metalens. In Section C.3, a similar analysis was provided, restricted to the case where each 2D layer was composed of a square array with $d_{\text{x}} = d_{\text{y}} = d$, and mainly focused on the role of the evanescent field in the dispersion relation (in the limit of an infinite number of 2D layers, $M \to \infty$). In this section, we instead study the direct coupling between two neighbouring, 2D arrays at distance d_{z}, and we extend the discussion to $d_{\text{x}} \neq d_{\text{y}}$.

Considering $\hat{\mathbf{x}}$-polarized atomic dipoles, the interaction of Eq. 5.2 between two different 2D arrays reads $\mathcal{G}_{nm} = \mathcal{G}^{\text{1D}}_{nm} + \mathcal{G}^{\text{ev}}_{nm}$, where the evanescent term can be explicitly written as

$$\mathcal{G}^{\text{ev}}_{nm} = \frac{\Gamma_{\text{coop}}}{2} \sum_{\substack{a\in\mathbb{Z}\\ b\in\mathbb{Z}\\ (a,b)\neq(0,0)}} \frac{1-(a/\xi_{\text{x}})^2}{\kappa_{\text{z}}(a,b)} e^{-2\pi|m-n|\xi_{\text{z}}\kappa_{\text{z}}(a,b)}, \tag{E.1}$$

where $\kappa_{\text{z}}(a,b) = \sqrt{(a/\xi_{\text{x}})^2 + (b/\xi_{\text{y}})^2 - 1}$, and where we recall that $\xi_{\text{x,y,z}} = d_{\text{x,y,z}}/\lambda_0 < 1$, while $\Gamma_{\text{coop}} = \Gamma(0)/\Gamma_0 = 3/(4\pi\xi_{\text{x}}\xi_{\text{y}})$. Differently from the infinite-range terms $\mathcal{G}^{\text{1D}}_{nm} = i\Gamma_{\text{coop}}e^{2\pi i|m-n|\xi_{\text{z}}}/2$, the magnitude of the evanescent interaction $\mathcal{G}^{\text{ev}}_{nm}$ decreases exponentially with the distance $\sim |n-m|\xi_{\text{z}}$ between the two planes. Due to this reason, we can focus on the worst-case scenario of two nearest-neighbor planes.

The asymptotic behaviour at small lattice constants $\xi_{\text{x}} \ll 1$ and $\xi_{\text{y}} \ll 1$ can be studied by considering the first terms in the sum of Eq. E.1. In particular, if we retain the terms with either $a = \pm(1,2)$ and $b = 0$ or $a = 0$ and $b = \pm(1,2)$, for $|\mathcal{G}^{\text{ev}}_{12}| < |\mathcal{G}^{\text{1D}}_{12}|$ to be satisfied one obtains the following

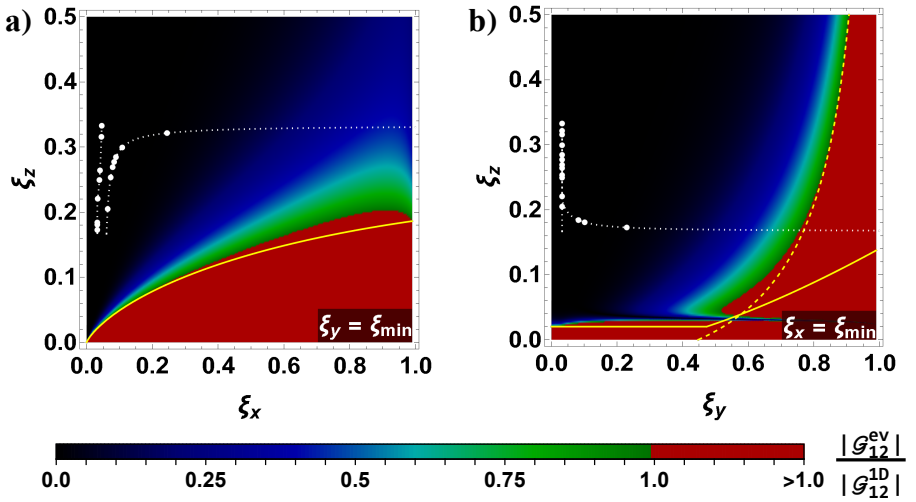

Figure E.1: Strength of the evanescent interaction in our scheme. Magnitude of $|\mathcal{G}_{12}^{\text{ev}}|/|\mathcal{G}_{12}^{\text{1D}}|$, for two nearest-neighbor planes, where the evanescent interaction is maximum. The red color describes the region where the approximation $|\mathcal{G}_{12}^{\text{ev}}| \sim 0$ breaks down. In the two panels, we explore the two branches of the path chosen for our scheme, reading $\xi_y = \xi_{\text{min}} \cup \xi_{\text{min}} \leq \xi_x < 1$ (a) and $\xi_x = \xi_{\text{min}} \cup \xi_{\text{min}} \leq \xi_y < 1$ (b), where $\xi_{\text{min}} = 0.03$. The evanescent interaction is calculated from the full equation Eq. E.1. The white, dotted line represents the possible values of $\xi_z(\xi_x, \xi_y)$, as defined in Eq. 5.8, while the white points show the actual values that we used to design the lens of Fig. 5.4, which all fall in a regime where $\mathcal{G}_{12}^{\text{ev}} \sim 0$. The yellow, either solid and dashed lines respectively show the asymptotic bounds of Eq. E.2 and Eq. E.3.

bounds (expanded, respectively, in $\xi_x \ll 1$ and $\xi_y \ll 1$)

$$\xi_z \gtrsim \frac{\xi_x}{2\pi} \log\left(\frac{1+\sqrt{1+4\xi_x}}{\xi_x}\right), \qquad \xi_z \gtrsim \frac{\xi_y}{2\pi} \log\left(\xi_y + \sqrt{\xi_y + \xi_y^2}\right), \tag{E.2}$$

which roughly correspond to the rule of thumbs $\xi_z \gg \max[\xi_x, \xi_y]/(2\pi)$. On top of this, since we are considering $\hat{\mathbf{x}}$-polarized dipoles, the terms with $a = 0$ and $b = \pm 1$ explode when $\xi_y \to 1$, meaning that the evanescent interaction dominates in that regime. In particular, this leads to the supplementary condition for $\mathcal{G}_{12}^{\text{ev}}$ to be negligible (in the regime of $\xi_y \to 1$)

$$\xi_z > \frac{\xi_y}{2\pi\sqrt{1-\xi_y^2}} \log\left(\frac{2\xi_y}{\sqrt{1-\xi_y^2}}\right). \tag{E.3}$$

The validity of the approximation $\mathcal{G}_{12}^{\text{ev}} \sim 0$ in our scheme is shown in Fig. E.1.

Here, we plot the ratio $|\mathcal{G}_{12}^{\text{ev}}|/|\mathcal{G}_{12}^{\text{1D}}|$, when exploring the two branches $\xi_y = \xi_{\text{min}} \cup \xi_{\text{min}} \leq \xi_x < 1$ (Fig. E.1-a) and $\xi_x = \xi_{\text{min}} \cup \xi_{\text{min}} \leq \xi_y < 1$ (Fig. E.1-b) of the path adopted in our scheme, while arbitrarily varying ξ_z. The red regions represents regimes where our approximation breaks down, while the other colors show various degrees of validity of our assumption (from the highest, in black, to the lowest, in green). The white points show the values of the lattice constants that were actually used to design the lens in Fig. 5.4, which fall in a regime where our approximation $|\mathcal{G}_{12}^{\text{ev}}| \ll |\mathcal{G}_{12}^{\text{1D}}|$ is perfectly justified. On the contrary, the dotted white lines show all the possible values that one might potentially need when designing a generic lens with our prescription (in sight of Eq. 5.8, which defines $\xi_z(\xi_x, \xi_y)$). As one can see in Fig. E.1-b, the main problem is associated with those phases $\phi(\xi_x, \xi_y)$ that require $\xi_y \gtrsim 0.7$, which violate the bound of Eq. E.3 (yellow, dashed line). Nonetheless, as shown in Fig. 5.2-a, this happens only for phases $\phi(\xi_x, \xi_y) \sim 0$, and two easy solutions would be to either leave the related ring empty (which would correspond to approximating the requested phase with exactly $\phi(\xi_x, \xi_y) = 0$), or to introduce a cut-off on the minimum absolute value of the phase.

E.2 Buffer zones

Here, we describe in detail our definition of the buffer zone between consecutive rings of an atomic metalens, which is aimed to avoid an abrupt change of lattice constants at the interfaces.

This scheme takes advantage of the fact that, in our approach, often one of the two lattice constant does not change between two consecutive rings, having either $\xi_x^j = \xi_x^{j-1} = \xi_{\text{min}}$ or $\xi_y^j = \xi_y^{j-1} = \xi_{\text{min}}$ (as discussed in Fig. 5.2). The full algorithm is described below.

- Given each ring j, its first $0 \leq \alpha < 1$ fraction is reserved as a buffer zone (green and orange regions of Fig. E.2), aimed to connect the j-th lattice with the previous one in a smoother way. Hereafter, we describe how a generic j-th buffer (separating the $(j-1)$-th and the j-th ring) is constructed.

- First of all, the system checks if either $\xi_x^j = \xi_x^{j-1} = \xi_{\text{min}}$ or $\xi_y^j = \xi_y^{j-1} = \xi_{\text{min}}$ are satisfied. If none of them is fulfilled, then the algorithm ignores that buffer (as in the orange regions of Fig. E.2).

- Let us assume that one has $\xi_y^j = \xi_y^{j-1} = \xi_{\text{min}}$, as in the green regions of Fig. E.2. The opposite case is a straightforward extension, which

can be described by simply reversing the references to the vertical and horizontal coordinates.

- In this regime, the lattices are organized in columns spaced by either ξ_{x}^{j-1} and ξ_{x}^{j}. The algorithm defines $x_{\mathrm{max}} = \max x_{j-1} + (3/4)\xi_{\mathrm{x}}^{j-1}$, where x_{j-1} identify the horizontal positions of the columns of the $(j-1)$-th ring. If there are columns of the j-th ring having $x_j > x_{\mathrm{max}}$, then those columns are ignored in the following steps (as in the black box of Fig. E.2).

- At this point, the algorithm counts the number of columns in either the j-th or the $(j-1)$-th ring, satisfying the condition $0 \leq x_{j,j-1} \leq x_{\mathrm{max}}$. Then, it identifies which of the two rings has less columns. For the sake of simplicity, we will assume it to be the j-th ring, but the algorithm deals with the opposite case in a similar manner. For each column i of this ring, the code searches the horizontally nearest column k among the ones of the $(j-1)$-th ring, i.e. the one minimizing the quantity $|x_j^i - x_{j-1}^k|$.

- Given this pair of columns, the algorithm connects them by drawing a straight line, and then placing atoms with a vertical spacing $\xi_{\mathrm{y}}^{j} = \xi_{\mathrm{y}}^{j-1} = \xi_{\mathrm{min}}$. For a line to be drawn, the condition $y_j^i > y_{j-1}^k$ must be fulfilled, in order to avoid negative slopes. When the number of columns in the two original rings are different, some columns must remain unconnected, as highlighted by the purple box in Fig. E.2.

- For what concerns the $\widehat{\mathbf{z}}$ position, all the atoms of the j-th buffer are associated to the lattice constant ξ_{z}^{j}, meaning that the columns are actually connected only in the $\widehat{\mathbf{x}}, \widehat{\mathbf{y}}$-plane. We tested the idea of fully connecting them in 3D, but this choice seems not to improve the efficiency.

E.3 Definition of the efficiency

In our simulations of an atomic metalens, we consider a finite ensemble of N, $\widehat{\mathbf{x}}$-polarizable atomic dipoles, with resonant frequency ω_0 and embedded in a non-absorbing, bulk material of index n. Due to the presence of the bulk material, the resonant wavevector is defined as $k_0 = 2\pi/\lambda_0 = n\omega_0/c$. This atomic system is illuminated by a resonant, $\widehat{\mathbf{x}}$-polarized Gaussian beam

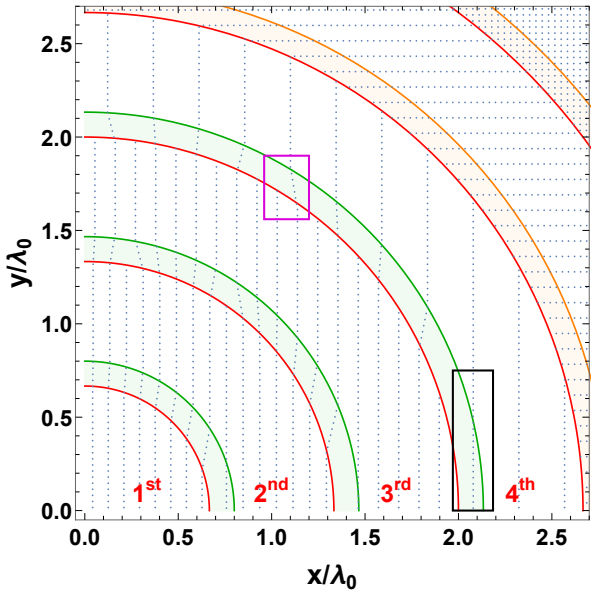

Figure E.2: Example of "buffer zones" between two consecutive rings, in the $\widehat{\mathbf{x}}, \widehat{\mathbf{y}}$-plane. The blue points show the atomic positions, while each ring is identified by a red line, as well as an ordinal number, still in red. The first $\alpha = 0.2$ fraction of each ring is dedicated to the buffer zones, which are represented by either green or orange regions. In particular, the green areas describe the case where one of the two conditions $\xi_{\mathrm{x}}^{j} = \xi_{\mathrm{x}}^{j-1} = \xi_{\mathrm{min}}$ or $\xi_{\mathrm{y}}^{j} = \xi_{\mathrm{y}}^{j-1} = \xi_{\mathrm{min}}$ are satisfied, which allows to smoothly connect the neighbouring rings. On the contrary, the case where none of these two conditions is fulfilled is shown by the orange zones, which are simply treated as normal parts of the corresponding ring. The black and purple boxes identify two peculiar instances, as described in the main text.

of waist w_0^{in}. We recall that it reads $\mathbf{E}_{\mathrm{in}}(\mathbf{r}, z) = \mathbf{E}_{\mathrm{gauss}}(\mathbf{r}, z, w_0^{\mathrm{in}})$, with

$$\mathbf{E}_{\mathrm{gauss}}(\mathbf{r}, z, w_0) = E_0^{\mathrm{in}} \frac{w_0}{w(z)} \exp\left[-\left(\frac{r}{w(z)}\right)^2 + ik_0 z + i\varphi(\mathbf{r}, z, w_0) \right] \widehat{\mathbf{x}}, \tag{E.4}$$

where $w(z) = w_0^{\mathrm{in}} \sqrt{1 + (z/z_{\mathrm{R}})^2}$ is the waist of the beam, while $\varphi(\mathbf{r}, z, w_0^{\mathrm{in}}) = -\arctan(z/z_{\mathrm{R}}) + k_0 r^2/[2R(z)]$, with $z_{\mathrm{R}} = k_0 (w_0^{\mathrm{in}})^2/2$ and radius of curvature $R(z) = z[1 + (z_{\mathrm{R}}/z)^2]$.

The total field $\mathbf{E}(\mathbf{r}, z)$ can be reconstructed by means of the coupled-dipole equations of Eq. 2.17. This numerical prediction must be then compared to the theoretical output field that one would expect for an ideal lens of focal length f. When the focal plane of the input beam is on the lens, this latter is given by $\mathbf{E}_{\mathrm{ideal}}(\mathbf{r}, z) = \mathbf{E}_{\mathrm{gauss}}(\mathbf{r}, z - z_f^{\mathrm{ideal}}, w_0^{\mathrm{ideal}})/\mathcal{M}$, where

one has

$$\frac{w_0^{\text{ideal}}}{w_0^{\text{in}}} = \mathcal{M} = \frac{f}{\sqrt{f^2 + k_0^2 (w_0^{\text{in}})^4/4}}, \qquad z_f^{\text{ideal}} = \left(1 - \mathcal{M}^2\right) f. \tag{E.5}$$

Here, $\mathcal{M}$ is the *so-called* magnification of the lens, and describes energy conservation [37]. The ideal increase in the beam intensity at the focal spot (over the intensity $I_0^{\text{in}} = |E_0^{\text{in}}|^2/(2\mu_0 c)$) is instead given by $I_0^{\text{ideal}}/I_0^{\text{in}} = 1/\mathcal{M}^2$. We can calculate the efficiency η of the atomic metalens by evaluating the overlap between this ideal solution and the total field. In the paraxial limit, we use Eq. A.11 to define $\eta = |\langle \mathbf{E}_{\text{ideal}} | \mathbf{E} \rangle|^2$, where

$$\langle \mathbf{E}_{\text{ideal}} | \mathbf{E} \rangle = t_0 + \frac{3i}{(k_0 w_0^{\text{in}})^2} \sum_{j=1}^{N} \frac{E_{\text{ideal}}^*(\mathbf{r}_j, z_j)}{E_0^{\text{in}}} \left(\frac{\Gamma_0}{\Omega_0^{\text{in}}} \beta_j \right), \tag{E.6}$$

due to Eq. A.17. Here,we have

$$t_0 = \langle \mathbf{E}_{\text{ideal}} | \mathbf{E}_{\text{in}} \rangle = \frac{2\pi w_0^{\text{in}} w_0^{\text{ideal}} \exp\left(2i\pi z_f^{\text{ideal}}/\lambda_0\right)}{\pi \left[(w_0^{\text{in}})^2 + (w_0^{\text{ideal}})^2\right] + i z_f^{\text{ideal}} \lambda_0}. \tag{E.7}$$

Here, we recall that $\mathcal{N}_{\text{gauss}}^{\text{in}} = 2/[\pi (w_0^{\text{in}} E_0^{\text{in}})^2]$. Similarly, we define the overlap $\epsilon = |\langle \mathbf{E}_{\text{in}} | \mathbf{E} \rangle|^2$ between the output and the input mode, where

$$\langle \mathbf{E}_{\text{in}} | \mathbf{E} \rangle = 1 + \frac{3i}{(k_0 w_0^{\text{in}})^2} \sum_{j=1}^{N} \frac{E_{\text{in}}^*(\mathbf{r}_j, z_j)}{E_0^{\text{in}}} \left(\frac{\Gamma_0}{\Omega_0^{\text{in}}} \beta_j \right). \tag{E.8}$$

E.4 Numerical methods

In Section 5.4, we discussed the results of our large-scale numerical simulations of coupled-dipole equations. Here, we briefly describe some technical expedients that allowed us to implement such numerical calculations.

We numerically simulate the optical response of the system by solving the coupled-dipole equations of Eq. 5.2 and Eq. 5.3, whose complexity scales as $\sim N^2$, where N is the number of atomic dipoles. The input Gaussian beam must have a waist w_0 much smaller than the radius R_{lens} of the atomic metalens, to avoid scattering from the edges or non-negligible fractions of light passing outside the lens. Due to the paraxial approximation, however, this imposes the constraint $\lambda_0 \ll w_0^{\text{in}} \ll R_{\text{lens}}$. Furthermore, to counteract the effects of the noise Γ', one must work with small lattice constants, thus

explaining the necessity of simulating up to $N \sim 5 \times 10^5$ atomic dipoles, between one and two orders of magnitude larger than typical theoretical studies [154, 157–159, 165, 166, 169, 170, 173–176]. To accomplish this task, we exploit the fact that the system is symmetric for $\widehat{\mathbf{x}} \to -\widehat{\mathbf{x}}$ and $\widehat{\mathbf{y}} \to -\widehat{\mathbf{y}}$, which implies that the each dipole d_j is equal to those of the atoms at the mirrored positions. The actual degrees of freedom are given by the number of atoms satisfying $x_j \geq 0$ and $y_j \geq 0$, which are roughly $\tilde{N} \sim N/4$. The coupled dipole equations can be then simplified by accounting only for these atoms, and then considering as if each of them scattered light from the mirrored positions as well. This allows us to simulate up to $N \sim 5 \times 10^5$ two-level atoms, by solving a system of *only* $\tilde{N} \sim 1.2 \times 10^5$ degrees of freedom, which still requires notable computational efforts. The most compelling problem is the amount of Random Access Memory (RAM) needed to elaborate the simulation. We design the code in such a way that the maximum allocation of memory is given by the construction of the $\tilde{N} \times \tilde{N}$ Green's function matrix. By defining it as a matrix of Complex{Float32} (64 bit) rather than the custom Complex{Float64} (128 bit), we cut the memory consumption to $\sim 200 - 300$ GB of RAM. We checked that we were still working with enough numerical precision, by comparing the simulations of smaller systems, performed with both choices of the variable definition.

Bibliography

[1] J. Bezanson *et al.*, "Julia: A fresh approach to numerical computing", *SIAM review*, vol. 59, no. 1, pp. 65–98, 2017. Cited at page xiii.

[2] J. D. Joannopoulos *et al.*, *Photonic Crystals: Molding the Flow of Light*. Princeton University Press, 2nd ed., 2008. Cited at pages 3 and 14.

[3] H. Shim, Z. Kuang, and O. D. Miller, "Optical materials for maximal nanophotonic response", *Optical Materials Express*, vol. 10, pp. 1561–1585, 7/2020. Cited at pages 3, 7, 11 and 137.

[4] J. B. Khurgin, "Expanding the Photonic Palette: Exploring High Index Materials", *ACS Photonics*, vol. 9, no. 3, pp. 743–751, 2022. Cited at pages 3, 7, 11, 12, 14, 24, 25, 26, 108 and 135.

[5] O. P. Rustgi, J. S. Nodvik, and G. L. Weissler, "Optical constants of germanium in the region 0-27 ev", *Physical Review*, vol. 122, pp. 1131–1134, 5/1961. Cited at pages 4, 25 and 41.

[6] H. R. Philipp and H. Ehrenreich, "Optical properties of semiconductors", *Physical Review*, vol. 129, pp. 1550–1560, 2/1963. Cited at pages 4, 25 and 41.

[7] W. C. Walker and J. Osantowski, "Ultraviolet optical properties of diamond", *Physical Review*, vol. 134, p. A153, 4/1964. Cited at pages 4, 25 and 41.

[8] P. L. Lamy, "Optical constants of crystalline and fused quartz in the far ultraviolet", *Applied Optics*, vol. 16, p. 2212, 8/1977. Cited at pages 4, 25 and 41.

[9] D. E. Aspnes and A. A. Studna, "Dielectric functions and optical parameters of Si, Ge, GaP, GaAs, GaSb, InP, InAs, and InSb from 1.5 to 6.0 eV", *Physical Review B*, vol. 27, p. 985, 1/1983. Cited at pages 4, 11, 25 and 41.

[10] S. G. Warren, "Optical constants of ice from the ultraviolet to the microwave", *Applied Optics*, vol. 23, p. 1206, 4/1984. Cited at pages 4, 25 and 41.

[11] A. D. Papadopoulos and E. Anastassakis, "Optical properties of diamond", *Physical Review B*, vol. 43, pp. 5090–5097, 2/1991. Cited at pages 4, 25 and 41.

[12] R. Kitamura, L. Pilon, and M. Jonasz, "Optical constants of silica glass from extreme ultraviolet to far infrared at near room temperature", *Applied Optics*, vol. 46, pp. 8118–8133, 11/2007. Cited at pages 4, 25 and 41.

[13] M. O. M. O. Scully and M. S. Zubairy, *Quantum optics*. Cambridge University Press, 1997. Cited at page 4.

[14] K. Hammerer, A. S. Sørensen, and E. S. Polzik, "Quantum interface between light and atomic ensembles", *Rev. Mod. Phys.*, vol. 82, pp. 1041–1093, 4/2010. Cited at pages 5, 21, 26, 67 and 135.

[15] A. Szabo and N. S. Ostlund, *Modern Quantum Chemistry: Introduction to Advanced Electronic Structure Theory. Revised*. Dover Publications, 1989. Cited at page 5.

[16] W. M. Foulkes *et al.*, "Quantum Monte Carlo simulations of solids", *Reviews of Modern Physics*, vol. 73, p. 33, 1/2001. Cited at page 5.

[17] R. O. Jones, "Density functional theory: Its origins, rise to prominence, and future", *Reviews of Modern Physics*, vol. 87, p. 897, 8/2015. Cited at page 5.

[18] J. Paier *et al.*, "Cu2ZnSnS4 as a potential photovoltaic material: A hybrid Hartree-Fock density functional theory study", *Physical Review B*, vol. 79, p. 115126, 3/2009. Cited at page 5.

[19] J. Sun *et al.*, "Ab initio investigations of optical properties of the high-pressure phases of ZnO", *Physical Review B*, vol. 71, p. 125132, 3/2005. Cited at page 5.

[20] W. S. Werner, K. Glantschnig, and C. Ambrosch-Draxl, "Optical Constants and Inelastic Electron-Scattering Data for 17 Elemental Metals", *Journal of Physical and Chemical Reference Data*, vol. 38, p. 1013, 12/2009. Cited at page 5.

[21] M. Segev, Y. Silberberg, and D. N. Christodoulides, "Anderson localization of light", *Nature Photonics*, vol. 7, pp. 197–204, 3/2013. Cited at page 7.

[22] I. M. Vellekoop and A. P. Mosk, "Focusing coherent light through opaque strongly scattering media", *Optics Letters*, vol. 32, p. 2309, 8/2007. Cited at page 7.

[23] J. Bertolotti and O. Katz, "Imaging in complex media", *Nature Physics*, vol. 18, pp. 1008–1017, 9/2022. Cited at pages 7 and 28.

[24] S. Gigan, "Imaging and computing with disorder", *Nature Physics*, vol. 18, pp. 980–985, 9/2022. Cited at pages 7 and 28.

[25] G. R. Fowles, *Introduction to modern optics*. Dover Publications, 1989. Cited at pages 7, 9, 22 and 24.

[26] I. Liberal and N. Engheta, "Near-zero refractive index photonics", *Nature Photonics*, vol. 11, pp. 149–158, 3/2017. Cited at pages 7, 10 and 13.

[27] N. Kinsey *et al.*, "Near-zero-index materials for photonics", *Nature Reviews Materials*, vol. 4, pp. 742–760, 9/2019. Cited at pages 7 and 10.

[28] M. Khorasaninejad *et al.*, "Metalenses at visible wavelengths: Diffraction-limited focusing and subwavelength resolution imaging", *Science*, vol. 352, pp. 1190–1194, 6/2016. Cited at pages 8, 16, 112 and 130.

[29] A. Arbabi *et al.*, "Subwavelength-thick lenses with high numerical apertures and large efficiency based on high-contrast transmitarrays", *Nature Communications*, vol. 6, pp. 1–6, 5/2015. Cited at pages 8, 16 and 112.

[30] J. Engelberg *et al.*, "Near-IR wide-field-of-view Huygens metalens for outdoor imaging applications", *Nanophotonics*, vol. 9, pp. 361–370, 2/2020. Cited at page 8.

[31] P. J. Reardon and R. A. Chipman, "Maximum power of refractive lenses: a fundamental limit", *Optics Letters*, vol. 15, p. 1409, 12/1990. Cited at page 7.

[32] F. Aieta *et al.*, "Aberration-free ultrathin flat lenses and axicons at telecom wavelengths based on plasmonic metasurfaces", *Nano Letters*, vol. 12, pp. 4932–4936, 9/2012. Cited at pages 8 and 112.

[33] J. Engelberg and U. Levy, "The advantages of metalenses over diffractive lenses", *Nature Communications*, vol. 11, 12/2020. Cited at pages 8, 15, 16, 112, 122 and 130.

[34] E. Di Fabrizio *et al.*, "High-efficiency multilevel zone plates for keV X-rays", *Nature*, vol. 401, pp. 895–898, 10/1999. Cited at page 8.

[35] J. B. Pendry, "Negative Refraction Makes a Perfect Lens", *Physical Review Letters*, vol. 85, p. 3966, 10/2000. Cited at page 9.

[36] J. Koglin, U. Fischer, and H. Fuchs, "Material contrast in scanning near-field optical microscopy at 1–10 nm resolution", *Physical Review B*, vol. 55, p. 7977, 3/1997. Cited at page 9.

[37] B. E. A. Saleh and M. C. Teich, *Fundamentals of Photonics*. John Wiley & Sons, Inc., 10/1991. Cited at pages 9, 10, 24 and 172.

[38] D. E. Chang, V. Vuletić, and M. D. Lukin, "Quantum nonlinear optics - photon by photon", *Nature Photonics*, vol. 8, pp. 685–694, 8/2014. Cited at pages 9 and 21.

[39] S. Rebić *et al.*, "Large Kerr nonlinearity with a single atom", *Journal of Optics B*, vol. 1, p. 490, 8/1999. Cited at page 9.

[40] J. T. Shen and S. Fan, "Strongly correlated two-photon transport in a one-dimensional waveguide coupled to a two-level system", *Physical Review Letters*, vol. 98, p. 153003, 4/2007. Cited at page 9.

[41] I. Schuster *et al.*, "Nonlinear spectroscopy of photons bound to one atom", *Nature Physics*, vol. 4, pp. 382–385, 4/2008. Cited at page 9.

[42] E. Urban *et al.*, "Observation of Rydberg blockade between two atoms", *Nature Physics*, vol. 5, pp. 110–114, 1/2009. Cited at page 9.

[43] S. J. Masson and A. Asenjo-Garcia, "Atomic-waveguide quantum electrodynamics", *Physical Review Research*, vol. 2, p. 043213, 11/2020. Cited at page 9.

[44] D. G. Baranov *et al.*, "All-dielectric nanophotonics: the quest for better materials and fabrication techniques", *Optica*, vol. 4, pp. 814–825, 7/2017. Cited at pages 9 and 10.

[45] S. Jahani and Z. Jacob, "All-dielectric metamaterials", *Nature Nanotechnology*, vol. 11, pp. 23–36, 1/2016. Cited at pages 9 and 16.

[46] M. L. Brongersma, Y. Cui, and S. Fan, "Light management for photovoltaics using high-index nanostructures", *Nature Materials*, vol. 13, pp. 451–460, 4/2014. Cited at page 9.

[47] I. I. Smolyaninov *et al.*, "Far-field optical microscopy with a nanometer-scale resolution based on the in-plane image magnification by surface plasmon polaritons", *Physical Review Letters*, vol. 94, p. 057401, 2/2005. Cited at page 9.

[48] A. Darafsheh *et al.*, "Optical super-resolution by high-index liquid-immersed microspheres", *Applied Physics Letters*, vol. 101, p. 141128, 10/2012. Cited at page 9.

[49] A. Darafsheh *et al.*, "Optical super-resolution imaging by high-index microspheres embedded in elastomers", *Optics Letters*, vol. 40, pp. 5–8, 1/2015. Cited at page 9.

[50] X. Zhu *et al.*, "Resonant laser printing of structural colors on high-index dielectric metasurfaces", *Science Advances*, vol. 3, 5/2017. Cited at page 9.

[51] B. J. Lin, "Optical lithography - present and future challenges", *Comptes Rendus Physique*, vol. 7, pp. 858–874, 10/2006. Cited at page 10.

[52] S. M. Barnett, B. Huttner, and R. Loudon, "Spontaneous emission in absorbing dielectric media", *Physical Review Letters*, vol. 68, pp. 3698–3701, 6/1992. Cited at page 10.

[53] F. J. Schuurmans, P. De Vries, and A. Lagendijk, "Local-field effects on spontaneous emission of impurity atoms in homogeneous dielectrics", *Physics Letters A*, vol. 264, pp. 472–477, 1/2000. Cited at page 10.

[54] K. Kim *et al.*, "Limitations and Opportunities for Optical Metafluids to Achieve an Unnatural Refractive Index", *ACS Photonics*, vol. 4, pp. 2298–2311, 9/2017. Cited at page 10.

[55] F. Naccarato *et al.*, "Searching for materials with high refractive index and wide band gap: A first-principles high-throughput study", *Physical Review Materials*, vol. 3, p. 044602, 4/2019. Cited at pages 10, 26 and 135.

[56] A. A. Shubnic *et al.*, "High refractive index and extreme biaxial optical anisotropy of rhenium diselenide for applications in all-dielectric nanophotonics", *Nanophotonics*, vol. 9, pp. 4737–4742, 11/2020. Cited at pages 10, 26 and 135.

[57] B. Unal, "Fundamental Limits of Nonlinear Optical Effects for Metalens Design with High Index Optical Materials", *Triton Systems Inc.*, 2021. Cited at pages 10, 26 and 135.

[58] K. Sato and S. Adachi, "Optical properties of ZnTe", *Journal of Applied Physics*, vol. 73, p. 926, 6/1998. Cited at page 11.

[59] E. Shkondin *et al.*, "Large-scale high aspect ratio Al-doped ZnO nanopillars arrays as anisotropic metamaterials", *Optical Materials Express*, vol. 7, pp. 1606–1627, 5/2017. Cited at page 11.

[60] J. R. DeVore, "Refractive Indices of Rutile and Sphalerite", *JOSA*, vol. 41, pp. 416–419, 6/1951. Cited at page 11.

[61] H. R. Phillip and E. A. Taft, "Kramers-Kronig Analysis of Reflectance Data for Diamond", *Physical Review*, vol. 136, p. A1445, 11/1964. Cited at page 11.

[62] J. Y. Kim *et al.*, "Highly tunable refractive index visible-light metasurface from block copolymer self-assembly", *Nature Communications*, vol. 7, 9/2016. Cited at pages 11 and 15.

[63] R. Verre *et al.*, "Transition metal dichalcogenide nanodisks as high-index dielectric Mie nanoresonators", *Nature Nanotechnology*, vol. 14, pp. 679–683, 5/2019. Cited at page 11.

[64] S. Lee, "Colloidal superlattices for unnaturally high-index metamaterials at broadband optical frequencies", *Optics Express*, vol. 23, pp. 28170–28181, 11/2015. Cited at pages 11 and 15.

[65] C. E. Ekuma *et al.*, "Optical properties of PbTe and PbSe", *Physical Review B*, vol. 85, p. 085205, 2/2012. Cited at page 11.

[66] F. Weiting and Y. Yixun, "Temperature effects on the refractive index of lead telluride and zinc selenide", *Infrared Physics*, vol. 30, pp. 371–373, 1/1990. Cited at page 11.

[67] J. Shin, J. T. Shen, and S. Fan, "Three-dimensional metamaterials with an ultrahigh effective refractive index over a broad bandwidth", *Physical Review Letters*, vol. 102, p. 093903, 3/2009. Cited at pages 11 and 14.

[68] M. Choi *et al.*, "A terahertz metamaterial with unnaturally high refractive index", *Nature*, vol. 470, pp. 369–373, 2/2011. Cited at pages 11 and 15.

[69] A. Pimenov and A. Loidl, "Experimental demonstration of artificial dielectrics with a high index of refraction", *Physical Review B*, vol. 74, p. 193102, 11/2006. Cited at pages 11 and 15.

[70] A. Rohatgi, *Webplotdigitizer: Version 4.5*. ankitrohatgi@hotmail.com, 2021. Cited at pages 11 and 13.

[71] M. N. Polyanskiy, *Refractive index database*. CC0 1.0, 2022. Cited at pages 11 and 13.

[72] S. Tan *et al.*, "Terahertz metasurfaces with a high refractive index enhanced by the strong nearest neighbor coupling", *Optics Express*, vol. 23, pp. 29222–29230, 11/2015. Cited at pages 11 and 15.

[73] X. Jing *et al.*, "Design of ultrahigh refractive index metamaterials in the terahertz regime", *Superlattices and Microstructures*, vol. 109, pp. 716–724, 9/2017. Cited at page 11.

[74] T. Chang *et al.*, "Broadband giant-refractive-index material based on mesoscopic space-filling curves", *Nature Communications*, vol. 7, pp. 1–7, 8/2016. Cited at pages 11 and 24.

[75] X. Chen *et al.*, "Robust method to retrieve the constitutive effective parameters of metamaterials", *Physical Review E*, vol. 70, p. 7, 7/2004. Cited at pages 11 and 13.

[76] M. Lobet *et al.*, "Momentum considerations inside near-zero index materials", *Light: Science & Applications*, vol. 11, pp. 1–8, 4/2022. Cited at pages 10 and 12.

[77] R. Fox, C. G. Kuper, and S. G. Lipson, "Faster-than-light group velocities and causality violation", *Proceedings of the Royal Society A*, vol. 316, pp. 515–524, 5/1970. Cited at page 10.

[78] A. C. Turner *et al.*, "Tailored anomalous group-velocity dispersion in silicon channel waveguides", *Optics Express*, vol. 14, pp. 4357–4362, 5/2006. Cited at page 10.

[79] M. H. Javani and M. I. Stockman, "Real and Imaginary Properties of Epsilon-Near-Zero Materials", *Physical Review Letters*, vol. 117, p. 107404, 9/2016. Cited at page 10.

[80] H. Shim, F. Monticone, and O. D. Miller, "Fundamental Limits to the Refractive Index of Transparent Optical Materials", *Advanced Materials*, vol. 33, p. 2103946, 10/2021. Cited at pages 10, 24, 25 and 135.

[81] O. Reshef *et al.*, "Direct Observation of Phase-Free Propagation in a Silicon Waveguide", *ACS Photonics*, vol. 4, pp. 2385–2389, 10/2017. Cited at pages 10 and 13.

[82] S. Yun *et al.*, "Low-loss impedance-matched optical metamaterials with zero-phase delay", *ACS Nano*, vol. 6, pp. 4475–4482, 5/2012. Cited at pages 10, 13 and 15.

[83] R. W. Ziolkowski, "Propagation in and scattering from a matched metamaterial having a zero index of refraction", *Physical Review E*, vol. 70, p. 12, 10/2004. Cited at page 10.

[84] M. Silveirinha and N. Engheta, "Tunneling of electromagnetic energy through subwavelength channels and bends using ϵ-near-zero materials", *Physical Review Letters*, vol. 97, p. 157403, 10/2006. Cited at pages 10 and 12.

[85] R. Liu *et al.*, "Experimental demonstration of electromagnetic tunneling through an epsilon-near-zero metamaterial at microwave frequencies", *Physical Review Letters*, vol. 100, p. 023903, 1/2008. Cited at page 10.

[86] X. Huang *et al.*, "Dirac cones induced by accidental degeneracy in photonic crystals and zero-refractive-index materials", *Nature Materials*, vol. 10, pp. 582–586, 5/2011. Cited at pages 10, 12 and 14.

[87] B. Edwards *et al.*, "Experimental verification of epsilon-near-zero metamaterial coupling and energy squeezing using a microwave waveguide", *Physical Review Letters*, vol. 100, p. 033903, 1/2008. Cited at pages 10, 12 and 14.

[88] D. C. Adams *et al.*, "Funneling light through a subwavelength aperture with epsilon-near-zero materials", *Physical Review Letters*, vol. 107, p. 133901, 9/2011. Cited at pages 10, 12 and 13.

[89] D. Ploss *et al.*, "Young's Double-Slit, Invisible Objects and the Role of Noise in an Optical Epsilon-near-Zero Experiment", *ACS Photonics*, vol. 4, pp. 2566–2572, 10/2017. Cited at page 10.

[90] A. Alù and N. Engheta, "Light squeezing through arbitrarily shaped plasmonic channels and sharp bends", *Physical Review B*, vol. 78, p. 035440, 7/2008. Cited at page 12.

[91] B. Edwards *et al.*, "Reflectionless sharp bends and corners in waveguides using epsilon-near-zero effects", *Journal of Applied Physics*, vol. 105, p. 044905, 2/2009. Cited at page 12.

[92] M. G. Silveirinha and N. Engheta, "Theory of supercoupling, squeezing wave energy, and field confinement in narrow channels and tight bends using ϵ near-zero metamaterials", *Physical Review B*, vol. 76, p. 245109, 12/2007. Cited at page 12.

[93] A. Alù, M. G. Silveirinha, and N. Engheta, "Transmission-line analysis of ϵ -near-zero-filled narrow channels", *Physical Review E*, vol. 78, p. 016604, 7/2008. Cited at page 12.

[94] I. Liberal *et al.*, "Near-zero-index media as electromagnetic ideal fluids", *Proceedings of the National Academy of Sciences of the United States of America*, vol. 117, pp. 24050–24054, 9/2020. Cited at page 12.

[95] H. Li *et al.*, "Direct observation of ideal electromagnetic fluids", *Nature Communications*, vol. 13, pp. 1–8, 8/2022. Cited at page 12.

[96] J. Hao, W. Yan, and M. Qiu, "Super-reflection and cloaking based on zero index metamaterial", *Applied Physics Letters*, vol. 96, p. 101109, 3/2010. Cited at page 12.

[97] S. A. Ramakrishna *et al.*, "Imaging the near field", *Journal of Modern Optics*, vol. 50, no. 9, pp. 1419–1430, 2003. Cited at pages 12 and 14.

[98] A. Salandrino and N. Engheta, "Far-field subdiffraction optical microscopy using metamaterial crystals: Theory and simulations", *Physical Review B*, vol. 74, p. 075103, 8/2006. Cited at pages 12 and 14.

[99] Z. Jacob *et al.*, "Optical Hyperlens: Far-field imaging beyond the diffraction limit", *Optics Express*, vol. 14, pp. 8247–8256, 9/2006. Cited at pages 12 and 14.

[100] I. I. Smolyaninov, Y. J. Hung, and C. C. Davis, "Magnifying Superlens in the Visible Frequency Range", *Science*, vol. 315, pp. 1699–1701, 3/2007. Cited at pages 12 and 14.

[101] A. D. Rakić, "Algorithm for the determination of intrinsic optical constants of metal films: application to aluminum", *Applied Optics*, vol. 34, pp. 4755–4767, 8/1995. Cited at page 13.

[102] P. B. Johnson and R. W. Christy, "Optical Constants of the Noble Metals", *Physical Review B*, vol. 6, p. 4370, 12/1972. Cited at page 13.

[103] J. Gao *et al.*, "Experimental realization of epsilon-near-zero metamaterial slabs with metal-dielectric multilayers", *Applied Physics Letters*, vol. 103, p. 051111, 8/2013. Cited at page 13.

[104] G. V. Naik, V. M. Shalaev, and A. Boltasseva, "Alternative Plasmonic Materials: Beyond Gold and Silver", *Advanced Materials*, vol. 25, pp. 3264–3294, 6/2013. Cited at page 13.

[105] P. Moitra *et al.*, "Realization of an all-dielectric zero-index optical metamaterial", *Nature Photonics*, vol. 7, pp. 791–795, 8/2013. Cited at pages 13 and 14.

[106] Y. Li *et al.*, "On-chip zero-index metamaterials", *Nature Photonics*, vol. 9, pp. 738–742, 10/2015. Cited at pages 13 and 14.

[107] J. Valentine *et al.*, "Three-dimensional optical metamaterial with a negative refractive index", *Nature*, vol. 455, pp. 376–379, 8/2008. Cited at pages 13 and 15.

[108] D. Korobkin, G. Shvets, and Y. Urzhumov, "Enhanced near-field resolution in midinfrared using metamaterials", *JOSA B*, vol. 23, pp. 468–478, 3/2006. Cited at page 13.

[109] W. G. Spitzer, D. Kleinman, and D. Walsh, "Infrared Properties of Hexagonal Silicon Carbide", *Physical Review*, vol. 113, p. 127, 1/1959. Cited at page 13.

[110] T. Suzuki, T. Suzuki, and H. Asada, "Reflectionless zero refractive index metasurface in the terahertz waveband", *Optics Express*, vol. 28, pp. 21509–21521, 7/2020. Cited at pages 13 and 15.

[111] J. Kim *et al.*, "Optical properties of gallium-doped zinc oxide-a low-loss plasmonic material: First-principles theory and experiment", *Physical Review X*, vol. 3, p. 041037, 12/2014. Cited at page 13.

[112] S. Enoch *et al.*, "A Metamaterial for Directive Emission", *Physical Review Letters*, vol. 89, p. 213902, 11/2002. Cited at pages 12 and 14.

[113] L. Vegni and L. L. Spada, "Near-zero-index wires", *Optics Express*, vol. 25, pp. 23699–23708, 10/2017. Cited at page 12.

[114] J. B. Pendry, D. Schurig, and D. R. Smith, "Controlling electromagnetic fields", *Science*, vol. 312, pp. 1780–1782, 6/2006. Cited at page 12.

[115] U. Leonhardt, "Optical conformal mapping", *Science*, vol. 312, pp. 1777–1780, 6/2006. Cited at page 12.

[116] D. Schurig *et al.*, "Metamaterial electromagnetic cloak at microwave frequencies", *Science*, vol. 314, pp. 977–980, 11/2006. Cited at page 12.

[117] J. Wu *et al.*, "Epsilon-near-zero photonics: infinite potentials", *Photonics Research*, vol. 9, pp. 1616–1644, 8/2021. Cited at page 14.

[118] R. Tirole *et al.*, "Saturable time-varying mirror based on an ENZ material", *arXiv:2202.05937*, 2/2022. Cited at page 14.

[119] C. Elloh *et al.*, "Gausson parameter dynamics in ENZ-material based waveguides using moment method", *Optik*, vol. 227, p. 165273, 2/2021. Cited at page 14.

[120] C. Fruhling *et al.*, "Understanding all-optical switching at the epsilon-near-zero point: a tutorial review", *Applied Physics B*, vol. 128, pp. 1–12, 1/2022. Cited at page 14.

[121] A. Alù *et al.*, "Epsilon-near-zero metamaterials and electromagnetic sources: Tailoring the radiation phase pattern", *Physical Review B*, vol. 75, p. 155410, 4/2007. Cited at page 14.

[122] J. Bohn *et al.*, "Spatiotemporal refraction of light in an epsilon-near-zero indium tin oxide layer: frequency shifting effects arising from interfaces", *Optica*, vol. 8, pp. 1532–1537, 12/2021. Cited at page 14.

[123] A. Boltasseva *et al.*, "Adiabatic frequency shifting in epsilon-near-zero materials: the role of group velocity", *Optica*, vol. 7, pp. 226–231, 3/2020. Cited at page 14.

[124] Y. Zhou *et al.*, "Broadband frequency translation through time refraction in an epsilon-near-zero material", *Nature Communications*, vol. 11, pp. 1–7, 5/2020. Cited at page 14.

[125] Y. Kiasat *et al.*, "Epsilon-Near-Zero (ENZ)-based Optomechanics", *arXiv:2203.07525*, 3/2022. Cited at page 14.

[126] V. Pacheco-Peña *et al.*, "Mechanical 144 GHz beam steering with all-metallic epsilon-near-zero lens antenna", *Applied Physics Letters*, vol. 105, p. 243503, 12/2014. Cited at page 14.

[127] S. A. Schulz *et al.*, "Optical response of dipole antennas on an epsilon-near-zero substrate", *Physical Review A*, vol. 93, p. 063846, 6/2016. Cited at page 14.

[128] P. P. Iyer *et al.*, "Ultrawide thermal free-carrier tuning of dielectric antennas coupled to epsilon-near-zero substrates", *Nature Communications*, vol. 8, pp. 1–7, 9/2017. Cited at page 14.

[129] X. Hu *et al.*, "High-throughput search for lossless metals", *Physical Review Materials*, vol. 6, p. 065203, 6/2022. Cited at pages 14 and 16.

[130] J. B. Khurgin, "How to deal with the loss in plasmonics and metamaterials", *Nature Nanotechnology*, vol. 10, pp. 2–6, 1/2015. Cited at pages 14 and 16.

[131] E. J. R. Vesseur *et al.*, "Experimental verification of n=0 structures for visible light", *Physical Review Letters*, vol. 110, p. 013902, 1/2013. Cited at page 14.

[132] A. Ahmadi and H. Mosallaei, "Physical configuration and performance modeling of all-dielectric metamaterials", *Physical Review B*, vol. 77, p. 045104, 1/2008. Cited at page 14.

[133] J. T. Shen, P. B. Catrysse, and S. Fan, "Mechanism for designing metallic metamaterials with a high index of refraction", *Physical Review Letters*, vol. 94, p. 197401, 5/2005. Cited at page 15.

[134] A. Harumi *et al.*, "Reflectionless metasurface with high refractive index in the terahertz waveband", *Optics Express*, vol. 29, pp. 14513–14524, 5/2021. Cited at page 15.

[135] K. Ishihara and T. Suzuki, "Metamaterial Demonstrates Both a High Refractive Index and Extremely Low Reflection in the 0.3-THz Band", *Journal of Infrared, Millimeter, and Terahertz Waves 2017 38:9*, vol. 38, pp. 1130–1139, 7/2017. Cited at page 15.

[136] X. Jing *et al.*, "Design of ultrahigh refractive index metamaterials in the terahertz regime", *Superlattices and Microstructures*, vol. 109, pp. 716–724, 9/2017. Cited at page 15.

[137] S. Banerji *et al.*, "Imaging with flat optics: Metalenses or diffractive lenses?", *Optica*, vol. 6, pp. 805–810, 6/2019. Cited at pages 15 and 16.

[138] N. Meinzer, W. L. Barnes, and I. R. Hooper, "Plasmonic meta-atoms and metasurfaces", *Nature Photonics*, vol. 8, pp. 889–898, 11/2014. Cited at page 16.

[139] R. Paniagua-Domínguez *et al.*, "A Metalens with a Near-Unity Numerical Aperture", *Nano Letters*, vol. 18, pp. 2124–2132, 3/2018. Cited at page 16.

[140] D. A. B. Miller, "Why optics needs thickness", *Science*, vol. 379, pp. 41–45, 1/2023. Cited at pages 16 and 135.

[141] M. Pan *et al.*, "Dielectric metalens for miniaturized imaging systems: progress and challenges", *Light: Science & Applications*, vol. 11, pp. 1–32, 6/2022. Cited at page 16.

[142] F. Andreoli *et al.*, "Maximum Refractive Index of an Atomic Medium", *Physical Review X*, vol. 11, p. 011026, 2/2021. Cited at page 17.

[143] A. Andryieuski *et al.*, "Water: Promising Opportunities For Tunable All-dielectric Electromagnetic Metamaterials", *Scientific Reports 2015 5:1*, vol. 5, pp. 1–9, 8/2015. Cited at page 22.

[144] R. Loudon, *The Quantum Theory of Light*. Oxford University Press, 3rd ed., 2000. Cited at pages 23 and 88.

[145] N. W. Ashcroft and D. N. Mermin, *Solid state physics*. Saunders College Publishing, 1976. Cited at page 23.

[146] A. D. Rakić *et al.*, "Optical properties of metallic films for vertical-cavity optoelectronic devices", *Applied Optics*, vol. 37, pp. 5271–5283, 8/1998. Cited at pages 24 and 25.

[147] F. Bassani *et al.*, *Electronic States and Optical Transitions in Solids*. Pergamon, 1975. Cited at page 26.

[148] D. E. Chang *et al.*, "Colloquium: Quantum matter built from nanoscopic lattices of atoms and photons", *Reviews of Modern Physics*, vol. 90, p. 031002, 8/2018. Cited at pages 27 and 34.

[149] R. J. Bettles, S. A. Gardiner, and C. S. Adams, "Enhanced Optical Cross Section via Collective Coupling of Atomic Dipoles in a 2D Array", *Physical Review Letters*, vol. 116, p. 103602, 3/2016. Cited at pages 27, 32, 37, 70, 74 and 111.

[150] E. Shahmoon *et al.*, "Cooperative Resonances in Light Scattering from Two-Dimensional Atomic Arrays", *Physical Review Letters*, vol. 118, p. 113601, 3/2017. Cited at pages 27, 32, 37, 70, 74, 106, 111, 114 and 143.

[151] A. Asenjo-Garcia *et al.*, "Exponential Improvement in Photon Storage Fidelities Using Subradiance and "Selective Radiance" in Atomic Arrays", *Physical Review X*, vol. 7, p. 31024, 8/2017. Cited at pages 27, 32, 33, 34, 36, 73, 74 and 111.

[152] M. T. Manzoni *et al.*, "Optimization of photon storage fidelity in ordered atomic arrays", *New Journal of Physics*, vol. 20, p. 83048, 8/2018. Cited at pages 27, 36, 46, 75, 86, 111, 142 and 143.

[153] J. Pellegrino *et al.*, "Observation of Suppression of Light Scattering Induced by Dipole-Dipole Interactions in a Cold-Atom Ensemble", *Physical Review Letters*, vol. 113, p. 133602, 9/2014. Cited at pages 27, 32, 43 and 48.

[154] S. D. Jenkins *et al.*, "Collective resonance fluorescence in small and dense atom clouds: Comparison between theory and experiment", *Physical Review A*, vol. 94, p. 023842, 8/2016. Cited at pages 27, 32, 43, 48, 123 and 173.

[155] S. D. Jenkins *et al.*, "Optical Resonance Shifts in the Fluorescence of Thermal and Cold Atomic Gases", *Physical Review Letters*, vol. 116, 5/2016. Cited at pages 27, 32, 48 and 111.

[156] S. Jennewein *et al.*, "Coherent Scattering of Near-Resonant Light by a Dense Microscopic Cold Atomic Cloud", *Physical Review Letters*, vol. 116, p. 233601, 6/2016. Cited at pages 27, 32, 43, 48, 86 and 143.

[157] S. Jennewein *et al.*, "Propagation of light through small clouds of cold interacting atoms", *Physical Review A*, vol. 94, no. 5, 2016. Cited at pages 27, 32, 43, 48, 86, 123, 143 and 173.

[158] L. Corman *et al.*, "Transmission of near-resonant light through a dense slab of cold atoms", *Physical Review A*, vol. 96, p. 53629, 11/2017. Cited at pages 27, 32, 43, 44, 48, 123, 136 and 173.

[159] S. Jennewein *et al.*, "Coherent scattering of near-resonant light by a dense, microscopic cloud of cold two-level atoms: Experiment versus theory", *Physical Review A*, vol. 97, 5/2018. Cited at pages 27, 32, 43, 44, 48, 123 and 173.

[160] J. Van Bladel, "Some Remarks on Green's Dyadic for Infinite Space", *IRE Transactions on Antennas and Propagation*, vol. 9, no. 6, pp. 563–566, 1961. Cited at page 29.

[161] K. M. Chen, "A Simple Physical Picture of Tensor Green's Function in Source Region", *Proceedings of the IEEE*, vol. 65, no. 8, pp. 1202–1204, 1977. Cited at page 29.

[162] D. E. Aspnes, "Local-field effects and effective-medium theory: A microscopic perspective", *American Journal of Physics*, vol. 50, pp. 704–709, 8/1982. Cited at page 29.

[163] J. Keaveney *et al.*, "Cooperative Lamb Shift in an Atomic Vapor Layer of Nanometer Thickness", *Physical Review Letters*, vol. 108, p. 173601, 4/2012. Cited at pages 30, 32 and 111.

[164] S. E. Schnatterly and C. Tarrio, "Local fields in solids: Microscopic aspects for dielectrics", *Reviews of Modern Physics*, vol. 64, no. 2, pp. 619–622, 1992. Cited at page 31.

[165] B. Zhu *et al.*, "Light scattering from dense cold atomic media", *Physical Review A*, vol. 94, p. 023612, 8/2016. Cited at pages 31, 43, 44, 123, 165 and 173.

[166] J. Javanainen *et al.*, "Shifts of a resonance line in a dense atomic sample", *Physical Review Letters*, vol. 112, 3/2014. Cited at pages 31, 32, 43, 56, 111, 123, 165 and 173.

[167] S. L. Bromley *et al.*, "Collective atomic scattering and motional effects in a dense coherent medium", *Nature Communications*, vol. 7, pp. 1–7, 3/2016. Cited at pages 31, 32, 111 and 165.

[168] T. Bienaimé, N. Piovella, and R. Kaiser, "Controlled Dicke subradiance from a large cloud of two-level systems", *Physical Review Letters*, vol. 108, p. 123602, 3/2012. Cited at pages 31 and 165.

[169] J. Javanainen and J. Ruostekoski, "Light propagation beyond the mean-field theory of standard optics", *Optics Express*, vol. 24, p. 993, 1/2016. Cited at pages 31, 43, 44, 56, 123 and 173.

[170] L. Chomaz *et al.*, "Absorption imaging of a quasi-two-dimensional gas: a multiple scattering analysis", *New Journal of Physics*, vol. 14, p. 055001, 5/2012. Cited at pages 31, 43, 44, 46, 86, 123, 143 and 173.

[171] J. Rui *et al.*, "A subradiant optical mirror formed by a single structured atomic layer", *Nature*, vol. 583, pp. 369–374, 7/2020. Cited at pages 32, 37, 70 and 111.

[172] J. T. Manassah, "Cooperative radiation from atoms in different geometries: decay rate and frequency shift", *Advances in Optics and Photonics*, vol. 4, p. 108, 6/2012. Cited at pages 32 and 111.

[173] H. Dobbertin, R. Löw, and S. Scheel, "Collective dipole-dipole interactions in planar nanocavities", *Physical Review A*, vol. 102, p. 031701, 9/2020. Cited at pages 32, 43, 56, 111, 123 and 173.

[174] N. J. Schilder *et al.*, "Polaritonic modes in a dense cloud of cold atoms", *Physical Review A*, vol. 93, p. 063835, 6/2016. Cited at pages 32, 43, 111, 123 and 173.

[175] N. J. Schilder *et al.*, "Homogenization of an ensemble of interacting resonant scatterers", *Physical Review A*, vol. 96, p. 013825, 7/2017. Cited at pages 32, 43, 44, 46, 111, 123 and 173.

[176] N. Schilder *et al.*, "Near-Resonant Light Scattering by a Subwavelength Ensemble of Identical Atoms", *Physical Review Letters*, vol. 124, p. 073403, 2/2020. Cited at pages 32, 43, 111, 123 and 173.

[177] R. H. Dicke, "Coherence in Spontaneous Radiation Processes", *Physical Review*, vol. 93, pp. 99–110, 1/1954. Cited at pages 32 and 111.

[178] M. Gross and S. Haroche, "Superradiance: An essay on the theory of collective spontaneous emission", *Physics Reports*, vol. 93, pp. 301–396, 12/1982. Cited at pages 32, 52, 73 and 111.

[179] S. J. Roof *et al.*, "Observation of Single-Photon Superradiance and the Cooperative Lamb Shift in an Extended Sample of Cold Atoms", *Physical Review Letters*, vol. 117, p. 073003, 8/2016. Cited at pages 32 and 111.

[180] M. O. Araújo *et al.*, "Superradiance in a Large and Dilute Cloud of Cold Atoms in the Linear-Optics Regime", *Physical Review Letters*, vol. 117, p. 073002, 8/2016. Cited at pages 32 and 111.

[181] Y. He *et al.*, "Geometric control of collective spontaneous emission", *Physical Review Letters*, vol. 125, p. 213602, 11/2020. Cited at pages 32 and 111.

[182] S. Skipetrov and I. Sokolov, "Absence of Anderson Localization of Light in a Random Ensemble of Point Scatterers", *Physical Review Letters*, vol. 112, p. 023905, 1/2014. Cited at pages 32, 44, 67 and 136.

[183] S. E. Skipetrov and I. M. Sokolov, "Search for Anderson localization of light by cold atoms in a static electric field", *Physical Review B*, vol. 99, 4/2019. Cited at pages 32, 67 and 136.

[184] T. Gruner and D. G. Welsch, "Green-function approach to the radiation-field quantization for homogeneous and inhomogeneous Kramers-Kronig dielectrics", *Physical Review A*, vol. 53, no. 3, pp. 1818–1829, 1996. Cited at page 32.

[185] H. T. Dung, L. Knöll, and D. G. Welsch, "Resonant dipole-dipole interaction in the presence of dispersing and absorbing surroundings", *Physical Review A*, vol. 66, no. 6, p. 16, 2002. Cited at pages 32 and 73.

[186] T. Caneva *et al.*, "Quantum dynamics of propagating photons with strong interactions: A generalized input-output formalism", *New Journal of Physics*, vol. 17, 10/2015. Cited at page 32.

[187] A. Asenjo-Garcia *et al.*, "Atom-light interactions in quasi-one-dimensional nanostructures: A Green's-function perspective", *Physical Review A*, vol. 95, p. 033818, 3/2017. Cited at pages 32 and 78.

[188] L. Knoll, S. Scheel, and D.-G. Welsch, "QED in dispersing and absorbing media", *arXiv:0006121v5*, 6/2000. Cited at page 34.

[189] J. D. Jackson, *Classical Electrodynamics*. John Wiley & Sons, 3rd ed., 1998. Cited at page 41.

[190] G. Grynberg *et al.*, *Introduction to Quantum Optics*. Cambridge University Press, 2010. Cited at pages 41 and 45.

[191] M. Fleischhauer and S. F. Yelin, "Radiative atom-atom interactions in optically dense media: Quantum corrections to the Lorentz-Lorenz formula", *Physical Review A*, vol. 59, pp. 2427–2441, 3/1999. Cited at page 43.

[192] W. Guerin, M. T. Rouabah, and R. Kaiser, "Light interacting with atomic ensembles: collective, cooperative and mesoscopic effects", *Journal of Modern Optics*, vol. 64, pp. 895–907, 5/2017. Cited at pages 43 and 44.

[193] J. Keaveney *et al.*, "Maximal Refraction and Superluminal Propagation in a Gaseous Nanolayer", *Physical Review Letters*, vol. 109, p. 233001, 12/2012. Cited at pages 43 and 48.

[194] L. S. Levitov, "Delocalization of vibrational modes caused by electric dipole interaction", *Physical Review Letters*, vol. 64, p. 547, 1/1990. Cited at pages 43, 53 and 62.

[195] D. S. Fisher, "Random antiferromagnetic quantum spin chains", *Physical Review B*, vol. 50, pp. 3799–3821, 8/1994. Cited at page 43.

[196] K. Damle, O. Motrunich, and D. A. Huse, "Dynamics and transport in random antiferromagnetic spin chains", *Physical Review Letters*, vol. 84, pp. 3434–3437, 4/2000. Cited at page 43.

[197] O. Motrunich *et al.*, "Infinite-randomness quantum Ising critical fixed points", *Physical Review B*, vol. 61, pp. 1160–1172, 1/2000. Cited at page 43.

[198] G. Refael and J. E. Moore, "Entanglement entropy of random quantum critical points in one dimension", *Physical Review Letters*, vol. 93, p. 260602, 12/2004. Cited at page 43.

[199] F. Iglói and C. Monthus, "Strong disorder RG approach of random systems", *Physics Reports*, vol. 412, pp. 277–431, 6/2005. Cited at page 43.

[200] R. Vosk and E. Altman, "Many-body localization in one dimension as a dynamical renormalization group fixed point", *Physical Review Letters*, vol. 110, p. 067204, 2/2013. Cited at page 43.

[201] G. Refael and E. Altman, "Strong disorder renormalization group primer and the superfluid-insulator transition", *Comptes Rendus Physique*, vol. 14, pp. 725–739, 10/2013. Cited at page 43.

[202] A. Lagendijk and B. A. Van Tiggelen, "Resonant multiple scattering of light", *Physics Report*, vol. 270, pp. 143–215, 5/1996. Cited at pages 44 and 46.

[203] N. Fayard *et al.*, "Intensity correlations between reflected and transmitted speckle patterns", *Physical Review A*, vol. 92, p. 033827, 9/2015. Cited at pages 44 and 46.

[204] F. Cottier *et al.*, "Microscopic and Macroscopic Signatures of 3D Anderson Localization of Light", *Physical Review Letters*, vol. 123, 8/2019. Cited at pages 44, 67 and 136.

[205] T. Binninger *et al.*, "Nonlinear quantum transport of light in a cold atomic cloud", *Physical Review A*, vol. 100, 9/2019. Cited at pages 44, 67 and 138.

[206] B. Shapiro, "Large intensity fluctuations for wave propagation in random media", *Physical Review Letters*, vol. 57, pp. 2168–2171, 10/1986. Cited at page 46.

[207] D. E. Chang *et al.*, "Cavity QED with atomic mirrors", *New Journal of Physics*, vol. 14, p. 63003, 6/2012. Cited at page 47.

[208] K. B. Davis *et al.*, "Bose-Einstein condensation in a gas of sodium atoms", *Physical Review Letters*, vol. 75, pp. 3969–3973, 11/1995. Cited at page 47.

[209] M. H. Anderson *et al.*, "Observation of Bose-Einstein condensation in a dilute atomic vapor", *Science*, vol. 269, pp. 198–201, 7/1995. Cited at page 47.

[210] N. Allard and J. Kielkopf, "The effect of neutral nonresonant collisions on atomic spectral lines", *Reviews of Modern Physics*, vol. 54, pp. 1103–1182, 10/1982. Cited at page 48.

[211] M. Born and E. Wolf, *Principles of Optics*. Cambridge University Press, 7 ed., 1999. Cited at page 48.

[212] C. C. Kwong *et al.*, "Coherent light propagation through cold atomic clouds beyond the independent scattering approximation", *Physical Review A*, vol. 99, p. 043806, 4/2019. Cited at page 51.

[213] M. W. Sørensen and A. S. Sørensen, "Three-dimensional theory for light-matter interaction", *Physical Review A*, vol. 77, p. 013826, 1/2008. Cited at page 51.

[214] R. Friedberg, S. R. Hartmann, and J. T. Manassah, "Frequency shifts in emission and absorption by resonant systems ot two-level atoms", *Physics Reports*, vol. 7, pp. 101–179, 3/1973. Cited at page 51.

[215] L. Bellando *et al.*, "Cooperative effects and disorder: A scaling analysis of the spectrum of the effective atomic Hamiltonian", *Physical Review A*, vol. 90, p. 063822, 12/2014. Cited at pages 67 and 136.

[216] S. E. Skipetrov and J. H. Page, "Red light for Anderson localization", *New Journal of Physics*, vol. 18, 1/2016. Cited at pages 67 and 136.

[217] S. E. Skipetrov and I. M. Sokolov, "Ioffe-Regel criterion for Anderson localization in the model of resonant point scatterers", *Physical Review B*, vol. 98, p. 064207, 8/2018. Cited at pages 67 and 136.

[218] A. V. Gorshkov *et al.*, "Universal Approach to Optimal Photon Storage in Atomic Media", *Physical Review Letters*, vol. 98, p. 123601, 3/2007. Cited at pages 67 and 135.

[219] A. V. Gorshkov *et al.*, "Photon-photon interactions via Rydberg blockade", *Physical Review Letters*, vol. 107, p. 133602, 9/2011. Cited at pages 67 and 135.

[220] C. Bradac *et al.*, "Quantum nanophotonics with group IV defects in diamond", *Nature Communications*, vol. 10, pp. 1–13, 12/2019. Cited at pages 72 and 112.

[221] H. Lan and Y. Ding, "Ordering, positioning and uniformity of quantum dot arrays", *Nano Today*, vol. 7, pp. 94–123, 4/2012. Cited at pages 72 and 113.

[222] K. Groot-Berning *et al.*, "Deterministic single-ion implantation of rare-earth ions for nanometer-resolution color-center generation", *Physical Review Letters*, vol. 123, p. 106802, 9/2019. Cited at pages 72 and 113.

[223] A. K. Geim and I. V. Grigorieva, "Van der Waals heterostructures", *Nature*, vol. 499, pp. 419–425, 7/2013. Cited at pages 72 and 108.

[224] P. De Vries, D. V. Van Coevorden, and A. Lagendijk, "Point scatterers for classical waves", *Reviews of Modern Physics*, vol. 70, pp. 447–466, 4/1998. Cited at page 73.

[225] M. Antezza and Y. Castin, "Fano-Hopfield model and photonic band gaps for an arbitrary atomic lattice", *Physical Review A*, vol. 80, p. 013816, 8/2009. Cited at pages 73, 77 and 114.

[226] E. Sierra, S. J. Masson, and A. Asenjo-Garcia, "Dicke Superradiance in Ordered Lattices: Dimensionality Matters", *Physical Review Research*, vol. 4, p. 023207, 6/2022. Cited at page 74.

[227] L. Henriet *et al.*, "Critical open-system dynamics in a one-dimensional optical-lattice clock", *Physical Review A*, vol. 99, p. 023802, 2/2019. Cited at page 78.

[228] C. Itzykson and J. B. Zuber, *Quantum field theory*. McGraw-Hill International Book Co., 1980. Cited at page 80.

[229] G. Grosso and G. Pastori Parravicini, *Solid state physics*. Academic Press, 2000. Cited at pages 80 and 98.

[230] R. G. Newton, "Optical theorem and beyond", *American Journal of Physics*, vol. 44, pp. 639–642, 7/1976. Cited at pages 83 and 147.

[231] R. Alaee *et al.*, "Kerker effect, superscattering, and scattering dark state in atomic antennas", *Phys. Rev. Research*, vol. 2, p. 043409, 8/2020. Cited at pages 83 and 147.

[232] A. Cidrim *et al.*, "Photon Blockade with Ground-State Neutral Atoms", *Physical Review Letters*, vol. 125, p. 073601, 8/2020. Cited at pages 84 and 138.

[233] L. A. Williamson, M. O. Borgh, and J. Ruostekoski, "Superatom Picture of Collective Nonclassical Light Emission and Dipole Blockade in Atom Arrays", *Physical Review Letters*, vol. 125, p. 073602, 8/2020. Cited at pages 84 and 138.

[234] M. K. Tey *et al.*, "Interfacing light and single atoms with a lens", *New Journal of Physics*, vol. 11, p. 043011, 4/2009. Cited at pages 86 and 143.

[235] S. A. Aljunid *et al.*, "Phase shift of a weak coherent beam induced by a single atom", *Physical Review Letters*, vol. 103, p. 153601, 10/2009. Cited at pages 86 and 143.

[236] F. M. Fernández and J. Garcia, "Highly accurate potential energy curves for the hydrogen molecule ion", *ChemistrySelect*, vol. 6, pp. 9527–9534, 7/2021. Cited at page 89.

[237] M. Motta *et al.*, "Ground-State Properties of the Hydrogen Chain: Dimerization, Insulator-to-Metal Transition, and Magnetic Phases", *Physical Review X*, vol. 10, p. 031058, 9/2020. Cited at page 90.

[238] S. Bravyi, D. P. DiVincenzo, and D. Loss, "Schrieffer-Wolff transformation for quantum many-body systems", *Annals of Physics*, vol. 326, pp. 2793–2826, 10/2011. Cited at page 92.

[239] X. J. Han *et al.*, "Charge dynamics of the antiferromagnetically ordered Mott insulator", *New Journal of Physics*, vol. 18, p. 103004, 10/2016. Cited at page 93.

[240] D. GoleŽ *et al.*, "Mechanism of ultrafast relaxation of a photo-carrier in antiferromagnetic spin background", *Physical Review B*, vol. 89, p. 165118, 4/2014. Cited at page 95.

[241] F. Reiter and A. S. Sørensen, "Effective operator formalism for open quantum systems", *Physical Review A*, vol. 85, p. 032111, 3/2012. Cited at pages 97 and 98.

[242] G. M. Andolina *et al.*, "Can deep sub-wavelength cavities induce Amperean superconductivity in a 2D material?", *arXiv:2210.10371*, 10/2022. Cited at page 98.

[243] W. F. Brinkman and T. M. Rice, "Single-Particle Excitations in Magnetic Insulators", *Physical Review B*, vol. 2, p. 1324, 9/1970. Cited at pages 98 and 164.

[244] E. Dagotto, "Correlated electrons in high-temperature superconductors", *Reviews of Modern Physics*, vol. 66, p. 763, 7/1994. Cited at pages 98 and 164.

[245] G. D. Mahan, "Energy bands of the Bethe lattice", *Physical Review B*, vol. 63, p. 155110, 3/2001. Cited at pages 98 and 164.

[246] I. H. Deutsch *et al.*, "Photonic band gaps in optical lattices", *Physical Review A*, vol. 52, pp. 1394–1410, 8/1995. Cited at pages 104 and 152.

[247] P. Markos and C. M. Soukoulis, *Wave propagation: From electrons to photonic crystals and left-handed materials*. Princeton University Press, 4/2008. Cited at page 104.

[248] G. Rainò *et al.*, "Superfluorescence from lead halide perovskite quantum dot superlattices", *Nature*, vol. 563, pp. 671–675, 11/2018. Cited at page 108.

[249] T. Schröder *et al.*, "Scalable focused ion beam creation of nearly lifetime-limited single quantum emitters in diamond nanostructures", *Nature Communications*, vol. 8, pp. 1–7, 5/2017. Cited at pages 108, 113 and 165.

[250] L. J. Rogers *et al.*, "Electronic structure of the negatively charged silicon-vacancy center in diamond", *Physical Review B*, vol. 89, p. 235101, 6/2014. Cited at page 108.

[251] L. J. Rogers *et al.*, "Multiple intrinsically identical single-photon emitters in the solid state", *Nature Communications*, vol. 5, 8/2014. Cited at pages 108, 113 and 165.

[252] R. E. Evans *et al.*, "Narrow-Linewidth Homogeneous Optical Emitters in Diamond Nanostructures via Silicon Ion Implantation", *Physical Review Applied*, vol. 5, p. 044010, 4/2016. Cited at pages 108, 113 and 165.

[253] A. V. Kuhlmann *et al.*, "Transform-limited single photons from a single quantum dot", *Nature Communications*, vol. 6, pp. 1–6, 9/2015. Cited at page 108.

[254] F. T. Pedersen *et al.*, "Near Transform-Limited Quantum Dot Linewidths in a Broadband Photonic Crystal Waveguide", *ACS Photonics*, vol. 7, pp. 2343–2349, 9/2020. Cited at page 108.

[255] S. Zeytinolu *et al.*, "Atomically thin semiconductors as nonlinear mirrors", *Physical Review A*, vol. 96, p. 031801, 9/2017. Cited at page 108.

[256] G. Scuri *et al.*, "Large Excitonic Reflectivity of Monolayer MoSe2 Encapsulated in Hexagonal Boron Nitride", *Physical Review Letters*, vol. 120, p. 037402, 1/2018. Cited at page 108.

[257] P. Back *et al.*, "Realization of an Electrically Tunable Narrow-Bandwidth Atomically Thin Mirror Using Monolayer MoSe2", *Physical Review Letters*, vol. 120, p. 037401, 1/2018. Cited at page 108.

[258] K. S. Novoselov *et al.*, "2D materials and van der Waals heterostructures", *Science*, vol. 353, 7/2016. Cited at page 108.

[259] Y. He *et al.*, "Unraveling disorder-induced optical dephasing in an atomic ensemble", *arXiv:2101.10779*, 1/2021. Cited at pages 111 and 135.

[260] Z. Meir *et al.*, "Cooperative lamb shift in a mesoscopic atomic array", *Physical Review Letters*, vol. 113, p. 193002, 11/2014. Cited at page 111.

[261] R. J. Bettles, S. A. Gardiner, and C. S. Adams, "Cooperative ordering in lattices of interacting two-level dipoles", *Physical Review A*, vol. 92, p. 063822, 12/2015. Cited at page 111.

[262] J. Perczel *et al.*, "Photonic band structure of two-dimensional atomic lattices", *Physical Review A*, vol. 96, p. 063801, 12/2017. Cited at pages 111, 114 and 143.

[263] E. Munro *et al.*, "Population mixing due to dipole-dipole interactions in a one-dimensional array of multilevel atoms", *Physical Review A*, vol. 98, p. 033815, 9/2018. Cited at page 111.

[264] S. J. Masson *et al.*, "Many-Body Signatures of Collective Decay in Atomic Chains", *Physical Review Letters*, vol. 125, p. 263601, 12/2020. Cited at page 111.

[265] R. Bekenstein *et al.*, "Quantum metasurfaces with atom arrays", *Nature Physics*, vol. 16, pp. 676–681, 6/2020. Cited at pages 111 and 131.

[266] D. Fernández-Fernández and A. González-Tudela, "Tunable Directional Emission and Collective Dissipation with Quantum Metasurfaces", *Physical Review Letters*, vol. 128, p. 113601, 3/2022. Cited at pages 111 and 131.

[267] K. Brechtelsbauer and D. Malz, "Quantum simulation with fully coherent dipole-dipole interactions mediated by three-dimensional subwavelength atomic arrays", *Physical Review A*, vol. 104, p. 013701, 7/2021. Cited at pages 111 and 131.

[268] M. Zhou *et al.*, "Optical Metasurface Based on the Resonant Scattering in Electronic Transitions", *ACS Photonics*, vol. 4, pp. 1279–1285, 5/2017. Cited at pages 111 and 130.

[269] K. E. Ballantine and J. Ruostekoski, "Cooperative optical wavefront engineering with atomic arrays", *Nanophotonics*, vol. 10, pp. 1901–1909, 5/2021. Cited at pages 111 and 130.

[270] K. E. Ballantine and J. Ruostekoski, "Quantum Single-Photon Control, Storage, and Entanglement Generation with Planar Atomic Arrays", *PRX Quantum*, vol. 2, p. 040362, 12/2021. Cited at page 111.

[271] A. V. Kildishev, A. Boltasseva, and V. M. Shalaev, "Planar photonics with metasurfaces", *Science*, vol. 339, pp. 12320091–12320096, 3/2013. Cited at page 112.

[272] N. Yu and F. Capasso, "Flat optics with designer metasurfaces", *Nature Materials*, vol. 13, pp. 139–150, 1/2014. Cited at page 112.

[273] W. T. Chen, A. Y. Zhu, and F. Capasso, "Flat optics with dispersion-engineered metasurfaces", *Nature Reviews Materials*, vol. 5, pp. 604–620, 8/2020. Cited at page 112.

[274] W. T. Chen and F. Capasso, "Will flat optics appear in everyday life anytime soon?", *Applied Physics Letters*, vol. 118, p. 100503, 3/2021. Cited at page 112.

[275] D. Fattal *et al.*, "Flat dielectric grating reflectors with focusing abilities", *Nature Photonics*, vol. 4, pp. 466–470, 7/2010. Cited at page 112.

[276] A. B. Klemm *et al.*, "Experimental high numerical aperture focusing with high contrast gratings", *Optics Letters*, vol. 38, p. 3410, 9/2013. Cited at page 112.

[277] M. Khorasaninejad and F. Capasso, "Metalenses: Versatile multifunctional photonic components", *Science*, vol. 358, 12/2017. Cited at pages 112, 122 and 130.

[278] Z. Zhou *et al.*, "Efficient Silicon Metasurfaces for Visible Light", *ACS Photonics*, vol. 4, pp. 544–551, 3/2017. Cited at page 112.

[279] S. Shrestha *et al.*, "Broadband achromatic dielectric metalenses", *Light: Science and Applications*, vol. 7, 12/2018. Cited at page 112.

[280] G. Tkachenko *et al.*, "Optical trapping with planar silicon metalenses", *Optics Letters*, vol. 43, p. 3224, 7/2018. Cited at page 112.

[281] H. Liang *et al.*, "Ultrahigh Numerical Aperture Metalens at Visible Wavelengths", *Nano Letters*, vol. 18, pp. 4460–4466, 7/2018. Cited at page 112.

[282] H. Liang *et al.*, "High performance metalenses: numerical aperture, aberrations, chromaticity, and trade-offs", *Optica*, vol. 6, p. 1461, 12/2019. Cited at page 112.

[283] A. Martins *et al.*, "On Metalenses with Arbitrarily Wide Field of View", *ACS Photonics*, vol. 7, pp. 2073–2079, 8/2020. Cited at page 112.

[284] V. M. Acosta *et al.*, "Diamonds with a high density of nitrogen-vacancy centers for magnetometry applications", *Physical Review B*, vol. 80, 9/2009. Cited at page 112.

[285] C. Hepp *et al.*, "Electronic structure of the silicon vacancy color center in diamond", *Physical Review Letters*, vol. 112, p. 036405, 1/2014. Cited at page 112.

[286] T. Müller *et al.*, "Optical signatures of silicon-vacancy spins in diamond", *Nature Communications*, vol. 5, pp. 1–7, 2/2014. Cited at page 112.

[287] T. Iwasaki *et al.*, "Tin-Vacancy Quantum Emitters in Diamond", *Physical Review Letters*, vol. 119, p. 253601, 12/2017. Cited at page 112.

[288] M. E. Trusheim *et al.*, "Lead-related quantum emitters in diamond", *Physical Review B*, vol. 99, p. 075430, 2/2019. Cited at page 112.

[289] K. Ohno *et al.*, "Three-dimensional localization of spins in diamond using 12C implantation", *Applied Physics Letters*, vol. 105, p. 52406, 8/2014. Cited at page 112.

[290] I. Bayn *et al.*, "Generation of Ensembles of Individually Resolvable Nitrogen Vacancies Using Nanometer-Scale Apertures in Ultrahigh-Aspect Ratio Planar Implantation Masks", *Nano Letters*, vol. 15, pp. 1751–1758, 3/2015. Cited at page 112.

[291] J. M. Smith *et al.*, "Colour centre generation in diamond for quantum technologies", *Nanophotonics*, vol. 8, pp. 1889–1906, 11/2019. Cited at page 112.

[292] L. V. H. Rodgers *et al.*, "Materials challenges for quantum technologies based on color centers in diamond", *MRS Bulletin*, vol. 46, pp. 623–633, 7/2021. Cited at page 112.

[293] T. Y. Hwang *et al.*, "Sub-10 nm Precision Engineering of Solid-State Defects via Nanoscale Aperture Array Mask", *Nano Letters*, vol. 22, pp. 1672–1679, 2/2022. Cited at pages 112 and 117.

[294] N. H. Wan *et al.*, "Large-scale integration of artificial atoms in hybrid photonic circuits", *Nature*, vol. 583, pp. 226–231, 7/2020. Cited at page 112.

[295] S. Pezzagna *et al.*, "Nanoscale Engineering and Optical Addressing of Single Spins in Diamond", *Small*, vol. 6, pp. 2117–2121, 9/2010. Cited at page 113.

[296] E. Janitz, L. Childress, and M. K. Bhaskar, "Cavity quantum electrodynamics with color centers in diamond", *Optica*, vol. 7, pp. 1232–1252, 10/2020. Cited at page 113.

[297] J. Michl *et al.*, "Perfect alignment and preferential orientation of nitrogen-vacancy centers during chemical vapor deposition diamond growth on (111) surfaces", *Applied Physics Letters*, vol. 104, p. 102407, 3/2014. Cited at page 113.

[298] M. Lesik *et al.*, "Perfect preferential orientation of nitrogen-vacancy defects in a synthetic diamond sample", *Applied Physics Letters*, vol. 104, p. 113107, 3/2014. Cited at page 113.

[299] T. Fukui *et al.*, "Perfect selective alignment of nitrogen-vacancy centers in diamond", *Applied Physics Express*, vol. 7, p. 055201, 4/2014. Cited at page 113.

[300] H. Ozawa *et al.*, "Formation of perfectly aligned nitrogen-vacancy-center ensembles in chemical-vapor-deposition-grown diamond (111)", *Applied Physics Express*, vol. 10, p. 045501, 4/2017. Cited at page 113.

[301] D. Barredo *et al.*, "An atom-by-atom assembler of defect-free arbitrary two-dimensional atomic arrays", *Science*, vol. 354, pp. 1021–1023, 11/2016. Cited at page 113.

[302] D. Barredo *et al.*, "Synthetic three-dimensional atomic structures assembled atom by atom", *Nature*, vol. 561, pp. 79–82, 9/2018. Cited at page 113.

[303] K. N. Schymik *et al.*, "Enhanced atom-by-atom assembly of arbitrary tweezer arrays", *Physical Review A*, vol. 102, p. 063107, 12/2020. Cited at page 113.

[304] M. Antezza and Y. Castin, "Spectrum of Light in a Quantum Fluctuating Periodic Structure", *Physical Review Letters*, vol. 103, p. 123903, 9/2009. Cited at page 114.

[305] H. Zheng and H. U. Baranger, "Persistent quantum beats and long-distance entanglement from waveguide-mediated interactions", *Physical Review Letters*, vol. 110, p. 113601, 3/2013. Cited at page 117.

[306] R. Alaee *et al.*, "Quantum Metamaterials with Magnetic Response at Optical Frequencies", *Physical Review Letters*, vol. 125, p. 063601, 8/2020. Cited at page 117.

[307] H. van de Stadt and J. M. Muller, "Multimirror Fabry–Perot interferometers", *JOSA A*, vol. 2, p. 1363, 8/1985. Cited at page 119.

[308] J. van de Groep *et al.*, "Exciton resonance tuning of an atomically thin lens", *Nature Photonics*, vol. 14, pp. 426–430, 4/2020. Cited at page 128.

[309] B. X. Wang *et al.*, "Design of metasurface polarizers based on two-dimensional cold atomic arrays", *Optics Express*, vol. 25, pp. 18760–18773, 8/2017. Cited at page 130.

[310] R. A. McCutcheon and S. F. Yelin, "Limits and possibilities of refractive index in atomic systems", *Optics Communications*, vol. 505, p. 127583, 2/2022. Cited at page 130.

[311] R. Gutiérrez-Jáuregui and A. Asenjo-Garcia, "Coherent control in atomic chains: To trap and release a traveling excitation", *Physical Review Research*, vol. 4, p. 013080, 2/2022. Cited at page 130.

[312] S. P. Pedersen, L. Zhang, and T. Pohl, "Quantum nonlinear optics in atomic dual arrays", *arXiv:2201.06544*, 1/2022. Cited at page 131.

[313] N. Nefedkin, M. Cotrufo, and A. Alù, "Nonreciprocal total cross section of quantum metasurfaces", *Nanophotonics*, vol. 0, 1/2023. Cited at pages 131 and 138.

[314] M. Moreno-Cardoner, D. Goncalves, and D. Chang, "Quantum Nonlinear Optics Based on Two-Dimensional Rydberg Atom Arrays", *Physical Review Letters*, vol. 127, p. 263602, 12/2021. Cited at page 131.

[315] S. Sun *et al.*, "Cavity-Enhanced Raman Emission from a Single Color Center in a Solid", *Physical Review Letters*, vol. 121, p. 083601, 8/2018. Cited at page 131.

[316] Y. I. Sohn *et al.*, "Controlling the coherence of a diamond spin qubit through its strain environment", *Nature Communications*, vol. 9, pp. 1–6, 5/2018. Cited at page 131.

[317] S. Meesala *et al.*, "Strain engineering of the silicon-vacancy center in diamond", *Physical Review B*, vol. 97, p. 205444, 5/2018. Cited at page 131.

[318] B. Machielse *et al.*, "Quantum Interference of Electromechanically Stabilized Emitters in Nanophotonic Devices", *Physical Review X*, vol. 9, p. 031022, 8/2019. Cited at page 131.

[319] S. Maity *et al.*, "Coherent acoustic control of a single silicon vacancy spin in diamond", *Nature Communications*, vol. 11, p. 193, 12/2020. Cited at page 131.

[320] L. Huang, S. Zhang, and T. Zentgraf, "Metasurface holography: From fundamentals to applications", *Nanophotonics*, vol. 7, pp. 1169–1190, 6/2018. Cited at page 131.

[321] G. Jin, L. Cao, and Q. Jiang, "When metasurface meets hologram: principle and advances", *Advances in Optics and Photonics*, vol. 11, pp. 518–576, 9/2019. Cited at page 131.

[322] L. Huang *et al.*, "Three-dimensional optical holography using a plasmonic metasurface", *Nature Communications*, vol. 4, pp. 1–8, 11/2013. Cited at page 131.

[323] Q. Wang *et al.*, "Broadband metasurface holograms: toward complete phase and amplitude engineering", *Scientific Reports*, vol. 6, pp. 1–10, 9/2016. Cited at page 131.

[324] Z. Chen and M. Segev, "Highlighting photonics: looking into the next decade", *eLight*, vol. 1, pp. 1–12, 6/2021. Cited at page 135.

[325] S. Grava *et al.*, "Renormalization group analysis of near-field induced dephasing of optical spin waves in an atomic medium", *New Journal of Physics*, vol. 24, p. 013031, 1/2022. Cited at page 135.

[326] R. R. Naraghi *et al.*, "Near-Field Effects in Mesoscopic Light Transport", *Physical Review Letters*, vol. 115, p. 203903, 11/2015. Cited at page 136.

[327] L. A. Cobus, G. Maret, and A. Aubry, "Crossover from renormalized to conventional diffusion near the three-dimensional Anderson localization transition for light", *Physical Review B*, vol. 106, p. 014208, 7/2022. Cited at page 136.

[328] R. R. Naraghi and A. Dogariu, "Phase Transitions in Diffusion of Light", *Physical Review Letters*, vol. 117, p. 263901, 12/2016. Cited at page 136.

[329] P. Weiss *et al.*, "Subradiance and radiation trapping in cold atoms", *New Journal of Physics*, vol. 20, p. 063024, 6/2018. Cited at page 136.

[330] W. Guerin, M. O. Araújo, and R. Kaiser, "Subradiance in a Large Cloud of Cold Atoms", *Physical Review Letters*, vol. 116, p. 083601, 2/2016. Cited at page 136.

[331] P. Weiss *et al.*, "Superradiance as single scattering embedded in an effective medium", *Physical Review A*, vol. 103, p. 023702, 2/2021. Cited at page 136.

[332] Y. Solomons, R. Ben-Maimon, and E. Shahmoon, "Universal approach for quantum interfaces with atomic arrays", *arXiv:2302.04913*, 2/2023. Cited at page 136.

[333] S. Y. Buhmann and D. G. Welsch, "Dispersion forces in macroscopic quantum electrodynamics", *Progress in Quantum Electronics*, vol. 31, pp. 51–130, 1/2007. Cited at page 137.

[334] K. Srakaew *et al.*, "A subwavelength atomic array switched by a single Rydberg atom", *arXiv:2207.09383*, 7/2022. Cited at page 138.

[335] B. T. Draine, "The discrete-dipole approximation and its application to interstellar graphite grains", *The Astrophysical Journal*, vol. 333, p. 848, 10/1988. Cited at page 147.

[336] I. O. Sosa, C. Noguez, and R. G. Barrera, "Optical properties of metal nanoparticles with arbitrary shapes", *Journal of Physical Chemistry B*, vol. 107, pp. 6269–6275, 7/2003. Cited at page 147.

[337] A. B. Evlyukhin, C. Reinhardt, and B. N. Chichkov, "Multipole light scattering by nonspherical nanoparticles in the discrete dipole approximation", *Physical Review B*, vol. 84, p. 235429, 12/2011. Cited at page 147.

[338] A. B. Evlyukhin *et al.*, "Multipole analysis of light scattering by arbitrary-shaped nanoparticles on a plane surface", *JOSA B*, vol. 30, p. 2589, 10/2013. Cited at page 147.

[339] A. Yariv, C.-S. Hong, and P. Yeh, "Electromagnetic propagation in periodic stratified media. I - General theory", *JOSA*, vol. 67, pp. 423–438, 4/1977. Cited at page 152.

[340] P. W. Anderson, "Absence of diffusion in certain random lattices", *Physical Review*, vol. 109, no. 5, pp. 1492–1505, 1958. Cited at page 165.

[341] C. A. Müller and D. Delande, "Disorder and interference: localization phenomena", *arXiv:1005.0915*, 2010. Cited at page 165.

[342] Y. Rosenzweig, Y. Schlussel, and R. Folman, "Probing the origins of inhomogeneous broadening in nitrogen-vacancy centers with Doppler-free-type spectroscopy", *Physical Review B*, vol. 98, 7/2018. Cited at page 165.